NUREG/CP-0044
MEA-2014
Vol. 2

Proceedings of the International Atomic Energy Agency Specialists' Meeting on Subcritical Crack Growth

Sessions III, IV, and V

Held at Freiburg, Federal Republic of Germany
May 13-15, 1981

Edited by W. H. Cullen

Sponsored by
International Atomic Energy Agency
U.S. Nuclear Regulatory Commission

Proceedings prepared by
Materials Engineering Associates, Inc.

Available from

GPO Sales Program
Division of Technical Information and Document Control
U.S. Nuclear Regulatory Commission
Washington, DC 20555

Printed copy price: $9.00

and

National Technical Information Service
Springfield, VA 22161

NUREG/CP-0044
MEA-2014
Vol. 2

Proceedings of the International Atomic Energy Agency Specialists' Meeting on Subcritical Crack Growth

Sessions III, IV, and V

Held at Freiburg, Federal Republic of Germany
May 13-15, 1981

Date Published: May 1983

Edited by
W. H. Cullen

Sponsored by
International Atomic Energy Agency
U.S. Nuclear Regulatory Commission
Office of Nuclear Regulatory Research

Proceedings prepared by
Materials Engineering Associates, Inc.
9700B George Palmer Highway
Lanham, MD 20706

Under subcontract to:
ENSA, Inc.
3320 Bailey Avenue
Buffalo, NY 14215
NRC FIN B8133

ABSTRACT

This report is a compilation of papers which were presented at the IAEA Specialists' Meeting on Subcritical Crack Growth, held at the Fraunhofer-Institute for Fracture Mechanics, Freiburg, FRG, May 13-15, 1981. These papers describe the experimental procedures for and interpretation of results of fatigue crack growth rate testing of pressure vessel and piping steels in pressurized, high-temperature water.

CONTENTS

CONTENTS

Page

1. INTRODUCTION

Volume II of this two volume set contains the proceedings from Sessions III, IV, and V of the specialists' meeting. Volume I contains the proceedings of Sessions I and IIA and IIB, which are titled as follows:

SESSION I - CRACK GROWTH OF PV STEEL IN THE LOWER OXYGEN CONTENT WATER RELEVANT TO PRESSURIZED WATER REACTOR (PWR) CONDITIONS

SESSION IIA - CRACK GROWTH OF PV STEELS IN THE HIGH OXYGEN CONTENT WATER RELEVANT TO BOILING WATER REACTOR (BWR) CONDITIONS

SESSION IIB - PIPE WORK.

FRACTOGRAPHIC ANALYSIS IN THE UNDERSTANDING OF CORROSION FATIGUE MECHANISMS

by
Andrew McMinn
Springfields Nuclear Power Development Laboratories - UKAEA

Introduction

Fractography has found increased usefulness both in the field of industrial service failure analyses and also in the area of understanding the micro-mechanisms of failure, particularly the inter-relationships between environment, stress, microstructure and fracture surface characteristics. This paper deals only with the latter application of fractography and in particular to the understanding of the mechanisms of corrosion fatigue crack growth for ferritic pressure vessel steels and austenitic stainless steels in light water reactor environments. The major emphasis of the studies on corrosion fatigue of pressure vessel steels has been to obtain data to establish crack growth laws and little attention in the past has been given to the underlying mechanisms involved. However, recently there has been more emphasis placed on fractographic analysis due to international collaboration. The aims of fractography in this area are:

(a) Initially to characterise the fracture modes of specimens tested in typical water reactor environments at operating conditions. This can often be hampered by the presence of corrosion products on the fracture surface.

(b) Secondly, to explain the fatigue crack growth data obtained from experiments, especially to explain any anomalous behaviour.

(c) To formulate an understanding of the operative mechanisms of corrosion fatigue. This may be helped by comparison with 'reference fractographs' of fractures occurring under well characterised conditions where the mechanisms is well understood.

(d) To aid in the prediction of behaviour once mechanisms are understood.

Thus the major long term goal is to understand crack growth processes, so that the response of the material to practical combinations of mechanical loading and environment could be predicted. To achieve this fractographic analyses need to be used in conjunction with test results from programmes that include controlled variation of environmental and loading parameters.

In this paper some ideas on the mechanisms of corrosion fatigue are presented, to explain the fractographic evidence and the crack growth behaviour of steels tested in the author's laboratory. Three pressure vessel steels have been examined; a plain C-Mn steel, Ducol W30 and A533-B; in light water reactor environments, with varying pH, conductivity and oxygen content. Tests have been performed at several combinations of stress ratio (R) and cyclic frequency. Type 304 stainless steel has also been tested in a simulated PWR environment. All the experimental work was performed at ambient temperature, which is a particularly important factor when discussing mechanisms of corrosion fatigue. Fracture surfaces have been examined in the scanning electron microscope, which has now become the primary electron optical instrument for analysis, due to the ease of specimen preparation and its depth of field. As the specimens were tested at ambient temperature they were not covered by any tightly adherent oxide layer and so no special surface cleaning was necessary. Fracture surfaces were ultrasonically cleaned in acetone, dry stripped of loosely adherent oxide using acetate film and then sputter coated with gold/pallidium.

Carbon-Manganese Steel

This steel was tested in air and in an oxygenated (8 ppm) neutral water of low conductivity (0.08 μmho). The steel had a ferritic-pearlitic microstructure with an average grain size of 24 μm and a volume fraction of pearlite between 20 and 25%. The mechanical properties and chemical composition are given in Table 1.

When tested in air, crack growth rates were independent of frequency and stress ratio (R) and fracture surfaces showed ductile, transgranular striations over a wide range of cyclic stress intensity (ΔK). Two types of striations were observed, relatively large 'multiple' striations which consisted of several finer regular markings (see Fig. 1). The larger striation spacings corresponded well with an estimate of half the maximum crack tip opening displacement (CTOD) defined as:

$$\delta = 0.22 \frac{K^2_{max}}{E\sigma_y} \qquad (1)$$

where for C-Mn steel σ_y = yield stress = 340 MNm^{-2}

and E = 1.86×10^5 MNm^{-2}

The smaller striations showed a good correlation with the macroscopic crack growth rate (Fig. 2). Although not shown on Fig. 2, observations on this and other ferritic steels, reveal that at high crack growth rates the distinction between fine and large striations cannot easily be made. As crack growth rates approach the CTOD then striation spacings reflect both da/dN and $\delta/2$, and in some cases measured spacings are slightly lower than the da/dN and CTOD. At low growth rates where striations were not very well pronounced some intergranular fracture was observed ($\Delta K < 18$ $MNm^{-3/2}$).

The aqueous environment enhanced crack growth rates by up to an order of magnitude and the steel fractured predominantly by transgranular quasi-cleavage above $\Delta K = 25$ $MNm^{-3/2}$ and mainly by intergranular separation below $\Delta K = 20$ $MNm^{-3/2}$ (Figs. 3 and 4). Interspersed between these modes were ductile striated areas, and the transition region between modes ($\Delta K = 18$ to 25 $MNm^{-3/2}$) consisted of a mixed mode of fracture. The transition in fracture mode occurred over the ΔK range in which crack growth retardations and plateaux were experimentally observed (Fig. 5). Thus fractographic observation offers an explanation for anomalous crack growth behaviour, indicating that crack growth is faster if intergranular separation predominates.

The quasi-cleavage facets showed typical fan like 'river' markings, but in addition, often showed regular ductile markings parallel to the crack front. The spacing of these markings often corresponded to the local ductile striation size. Brittle striations, up to three times the size of ductile striations, were also observed on the cleavage facets (Fig. 6) and on grain boundaries in the intergranular fracture areas (Fig. 7). Stereo-fractography indicated that the quasi-cleavage facets were mainly orientated perpendicular to the stress axis. The degree of quasi-cleavage appeared to increase for lower cyclic frequencies and was co-incident with an increase in cyclic crack growth rate.

Ducol W30 Steel

This steel was tested in an identical water environment to the C-Mn steel. It had, however, a bainitic microstructure, which was interspersed by a small amount of cementite free ferrite. Mechnical properties and chemical analyses are again given in Table 1.

Fractographically the Ducol W30 steel showed very similar features to those obtained for the C-Mn steel, except that the degree of quasi-cleavage and intergranular separation were very markedly reduced. It thus appears that these fracture modes are microstructurally sensitive and are dependent on the ferrite microconstituent in the steel. Crack growth rates for Ducol W30 were generally slightly lower than for the C-Mn steel under identical testing conditions.

A533-B Steel

This steel was tested in air and in simulated PWR water environments of low and high pH, with low oxygen levels (< 0.1 ppm). Several sources of this steel have now been examined, all mainly having a uniform bainitic microstructure, with typical mechanical properties and chemical analysis being given in Table 1.

Crack growth in bainitic A533-B was always found to be by a ductile striation mechanism in air, the non striated areas failing by ductile tearing. No intergranular fracture was observed at low ΔK levels. Unlike the C-Mn steel, this striated mode was also the fracture mechanism when tested in aqueous environments. The one exception to this has been in low pH water, at low frequency (0.01 Hz), when transgranular quasi-cleavage was induced by lowering the cyclic frequency from 0.1 Hz. (See Fig. 8). This change in mode was also accompanied by an increase in crack growth rate (see Fig. 9). A less pronounced form of quasi-cleavage has also been observed in neutral water (pH = 7) of low oxygen content, but none at all in high pH water environments. This indicates that quasi-cleavage is not solely dependent on microstructure, but is also dependent on water chemistry.

Type 304 Stainless Steel

Tests have been performed both in air and in a simulated PWR environment, identical to that used for A533-B. Demineralised water was used and dosed with LiOH to give a pH = 10. Oxygen levels were kept below 0.1 ppm by purging with argon and then maintaining a constant argon overpressure. Tests were carried out on both unsensitised and sensitised (650°C for 1 hour) material.

The fracture surfaces of specimens tested in air were ductile, transgranular and striated. They were, however, quite distinct from the ferritic steels tested in air, in that striations were much more pronounced and covered a much greater part of the fracture surface. The fracture surfaces also had much more of a 'folded' or rumpled appearance (Fig. 10). Many step like features and twin boundaries were also observed.

At high R ratio (0.7), striations were not well defined below $\Delta K = 15$ $MNm^{-3/2}$ although there were many markings reflecting slip activity (Fig. 11). These slip markings were generally independent of the overall crack growth direction and often showed a fluted or herringbone type morphology. Measurement of these slip lines/striations showed that the spacings had a lower limit of 0.05 μm and even this was an order of magnitude greater than the overall crack growth rate. Larger markings generally had a spacing between 0.5 and 1.5 μm, which was much greater than da/dN, but in the region of the CTOD (see Fig. 12).

For low R ratios and ΔK levels in the region of 25 to 60 $MNm^{-3/2}$ striations were well accentuated and as for the ferritic steels were of two types (Fig. 13). The relatively large striation spacings again showed a good correlation with

an estimate of the maximum CTOD defined in equation 1. However, at smaller crack tip openings (lower ΔK) good agreement was found when the yield stress (σy) was used in equation 1, whilst at larger openings the striations were better described in terms of the ultimate tensile stress (σ_{UTS}). Fine regular striations observed within the larger markings, closely followed the crack growth rate (Fig. 12).

At high ΔK levels (> 50 MNm $^{-3/2}$) the fracture consisted increasingly of microvoid coalescence, but very little secondary cracking was observed.

Unlike the ferritic steels, this austenitic steel essentially showed the same crack growth behaviour in the PWR environment as in air. Crack growth rates were not enhanced by the aqueous environment, except when the mean stress was increased. This R ratio effect appeared to saturate at R = 0.7 and enhanced growth was only obtained if ΔK was > 10 MNm $^{-3/2}$. There was however little or no effect of test frequency on growth rates. Crack growth in both the unsensitised and sensitised material was identical under similar testing conditions.

The fracture surfaces of the specimens tested in the simulated PWR water environment were very similar to those tested in air. The fracture mode was transgranular with pronounced ductile striations over a large range of ΔK. Two types of striation were again observed, showing good correlation with the estimated CTOD and da/dN respectively. The distinction was only lost at large openings for R = 0 ($\Delta K > 50$ MNm $^{-3/2}$) where da/dN, CTOD and striation spacing (S), all tend towards a common value. At low ΔK levels and high R ratios striations reflecting the CTOD and approximately three orders of magnitude greater than da/dN were observed ($\Delta K = 6$ MNm$^{-3/2}$). The smallest striations observed had a spacing of 0.06 μm. A dependence very similar to that shown in Fig. 12 was obtained for striations formed in the corrosion fatigue test. Striations in fact appeared more pronounced than those observed in the air fractures at low ΔK (< 15 MNm$^{-3/2}$) levels. There was also more secondary branching observed in the water tested specimens.

A major difference in fracture mode was observed however between the air and aqueous fatigued specimens, with the presence of highly reflective, macroscopically flat facets on the fracture surfaces of water tested specimens for ΔK levels less than 40 MNm$^{-3/2}$ (Fig. 14). These facets were observed under high and low R conditions, and their area fraction increased with ΔK level. They were often several hundreds of microns long and were more prominant for low frequency (0.01 Hz) testing. The facets were generally smooth and undeformed but some showed small variations in macroscopic height. They were normally straight sided, but virtually no evidence of triple points indicated that the mode was not grain boundary fracture. The facets indicate separation along crystallographic planes and in many cases fine detail could be resolved. Intersecting parallel slip line markings were observed, and in several cases three sets of intersecting slip lines indexed the planes as (111) planes (Fig. 15). The fracture mode for the sensitised 304 was very similar, with striations and facets, although the presence of intergranular failure was undoubtedly observed due to the occurrence of a significant number of grain boundary triple junctions.

Fractography of Pressure Vessel Steels Tested at Elevated Temperatures

Although no corrosion fatigue tests have as yet been performed at elevated temperature in the author's laboratory, specimens from Westinghouse and AERE have kindly been supplied for examination. The results of these findings, together with fractographic evidence reported by other laboratories are discussed here.

Three specimens were supplied by Westinghouse, one from an A508 Cl 2 forging, one from an A533-B Cl 1 plate and one from a sub-arc weldment. All the specimens had been tested at low frequency (1 or 0.5 cpm) and high R ratio (0.7 or 0.75) in a simulated PWR water environment at 2000 lb/in^2 and 288°C. High crack growth rates, well above the ASME XI wet line had been reported by Bamford[1] for each of these specimens, except for the weldment, which after high initial crack growth showed crack retardation. The specimens were cleaned using a cathodic electrolytic technique using an electrolyte based on Endox 214**, which the author[2] has found to be particularly effective in removing the magnetite layer formed at 288°C.

It should be noted, however, that using the same technique the oxide films could not be removed from specimens tested in the AERE autoclaves. This indicates that the electrochemical conditions within the Westinghouse and AERE experimental facilities may be different and this is discussed in more detail by Scott[3]. For the three Westinghouse specimens examined the fracture mode was ductile and transgranular in all cases. The forging showed very pronounced continuous striations covering large areas (Fig. 16) whilst the striations in the plate and weld specimens were much less distinct. There was no evidence of any brittle fracture mode. However, some secondary cracking was observed in all cases, with evidence of microvoid formation in the weldment. In the case of the forging, striations were observed throughout the test ΔK range. At the lower ΔK levels, the striation spacing (s) reflected $\delta/2$ and exceeded da/dN by a factor of 5-10, whereas at the higher ΔK levels, s and da/dN were in agreement and were $< \delta/2$. The striations in the weldment were smaller than in the forging, and therefore consistent with the lower crack growth rates. The growth retardation was accompanied by a decrease in s, although s was > da/dN.

This work has confirmed the work of Bamford[4] who has reported that growth is by a ductile striation mode, with the striation spacings however showing agreement with the macroscopic crack growth measurements. Bamford has stated that enhanced growth rates obtained are not a result of environmentally induced intergranular or cleavage modes, although occasionally regions exhibiting a cleavage-like appearance are observed in plate specimens. These regions show river-like markings which emanate from a single source and also periodic markings, which are not as well developed as adjacent ductile striations. In weldments growth by a void coalescence mechanism was observed, the voids nucleating around coarse carbides in the weldment. Bamford has reported[5] that specimens tested at 93°C, display a mixture of cleavage and ductile striated growth, the cleavage being more pronounced than at 288°C.

Tests performed at Westinghouse on austenitic 304 and 316 stainless steels in a PWR environment at 288°C have shown that crack growth occurs entirely by a ductile striation mechanism. There is no evidence of facetting, as observed in room temperature tests in the author's laboratory.

In support of collaborative work aimed at understanding the mechanisms of corrosion fatigue, other laboratories have examined fracture surfaces of specimens tested at elevated temperature in PWR environments containing various oxygen levels. Both Hickling[6] and Kondo[7] have reported ductile striation growth, no effect on striations being observed for changes in oxygen level, even though a marked effect on growth rates was produced. Hickling observed considerable secondary cracking in tests that produced low crack growth rates and suggests that this could be responsible for the growth rate retardation.

** Trade name

The only other laboratory to report other than a ductile striation mode has been NRL, who have observed 'brittle' striations and quasi cleavage. Törroren[8] has performed tests at 1 Hz and 1 cpm in low oxygen water (< 2 ppb) at 288°C. At 1 Hz, the data show little enhancement over air data and crack propagation is by striations with extensive microcracking. However, at 1 cpm, enhanced crack growth rates were obtained, which corresponded to a quasi cleavage mode of fracture with little microbranching. At the start and finish of this test, little environmental enhancement was obtained and the fracture mode consisted of striations which were brittle in appearance.

Fatigue Propagation in Inert Environments

Fatigue crack growth in air or inert environments is characterised by ductile striation formation, which is often termed Stage II of a three stage process. Stage II denotes an intermediate growth rate region (10^{-8} - 10^{-5} m/cycle) where crack tip deformation spreads over several grains in a polycrystal giving plastic continuum behaviour. Stage I denotes the threshold region or low growth rate region (< 10^{-8} m/cycle), where deformation in the crack tip plastic zone is often on a scale less than the grain size and therefore crack advance is crystallographically controlled. Cracks propagate along one of the maximum shear planes or along grain boundaries favourably oriented to the principal stress. Stage III is the region of high growth rate (> 10^{-5} m/cycle) where material inhomogeneities such as inclusions and precipitates nucleate voids ahead of the crack tip, leading to crack advance by tearing and finally instability.

In Stage II, crack advance occurs by the simultaneous localised shear deformation of the two 45° maximum shear bands, leading to the creation of new crack surface by decohesion at the crack tip. This localised flow is by dislocation movement and accommodates the plastic CTOD, δ. Hence it follows that there should be a correlation between the amount of new crack surface (Δa) and therefore da/dN, with the CTOD. Results show (Figs. 2 and 12) that in Stage II, $da/dN < \delta/2$ (not δ since resharpening on stress reversal produces two equal crack faces). This lack of correlation between da/dN and $\delta/2$ is due to crack flank material being incorporated into the crack tip deformation. In the low growth rate region of Stage II, δ is small and the crack flank contribution dominates and $da/dN \ll \delta/2$ (say two orders of magnitude), whereas at the higher Stage II growth rates, δ consists mainly of new crack surface and therefore da/dN approaches $\delta/2$. An upper bound to Stage II growth is given by $\delta/2$, as this represents the largest amount of crack tip blunting that can be accommodated by this process of crack advance. In Stage III, da/dN can exceed $\delta/2$ since fracture processes ahead of the crack tip contribute to crack advance.

Striations from during tensile loading as a result of this localised shear process (as in stretch zones) and are accentuated by unloading and reversal of the shear flow. Striations do not necessarily represent the amount of new crack surface created each cycle, as they reflect the shear process that accommodates the crack tip opening. The observations of large striations correlating with $\delta/2$ and finer striations agreeing with da/dN, but with a lower limit of approx. 0.05 μm, indicates a complex process of striation formation. Consider the results for 304 stainless steel at R = 0 given in Fig. 12. At low growth rates (0.01 μm/cycle) one fine striation (0.05 μm) is created over a number of cycles, crack growth only being continuous if the crack tip shear planes accommodate a fraction of new crack surface each cycle. Over several cycles, the accumulated surface is enough to create a fine striation on unloading and the process is repeated. During each cycle the maximum CTOD (> 10^{-7}m) is achieved due to crack flank involvement but shearing

on several planes at the crack tip (several fine striations) is required before the CTOD is achieved at the tip, producing a large striation which may not always be distinct. At high growth rates (10^{-6} m/cycle) and larger CTOD, several flow bands operate and contribute to the CTOD which is achieved in one load increment. Thus crack growth can produce several fine striations, but the crack increment per cycle now approaches the maximum CTOD.

Intergranular fracture was the other failure mode observed in the ferritic steels when tested at low stress intensity levels ($\Delta K < 18$ MNm$^{-3/2}$). This indicates that Stage I growth is occurring, but as areas around the facets were striated, the actual failure mode is a mixed Stage I and Stage II mode. The onset of the intergranular path is associated with the reverse plastic zone size (ΔD) becoming less than the grain size. Equating the reverse plastic zone size, $\Delta D = 1/32\ (\Delta K/\sigma y)^2$ to the average grain size (24 μm) in the C-Mn steel, indicates that intergranular fracture should occur for $\Delta K < 9.4$ MNm$^{-3/2}$, which is much lower than the observed $\Delta K = 18$ MNm$^{-3/2}$. However, if the maximum grain size (90 μm) is equated to the plastic zone size, as it is in these grains that the plastic zone will be contained in first, then intergranular fracture would be expected at $\Delta K = 18.8$ MNm$^{-3/2}$. An empirical relation[9] that equates four times the average grain size to ΔD, also predicts intergranular separation below this level. The experimental evidence is, therefore, in very good agreement with this proposed mechanism for intergranular failure. This mechanism indicates that intergranular separation is only dependent on the mechanics of the process, but observation has shown that the intergranular mode is microstructurally dependent - not occuring in bainitic structures, and environmentally sensitive - the fraction of grain boundary separation increasing in aqueous environment. For the bainitic microstructure which is lath-like, the plastic zone size would have to be much smaller before Stage I growth would be produced, unless the prior austenite grain boundaries were involved. This does not appear to be the case. The environmental dependence suggests some supplementary mechanism, such as a particular absorbing species lowering the grain boundary energy, but this can only be inferred.

Environmental Crack Growth in Ferritic Steels

The enhancement of fatigue crack growth rates in ambient temperature aqueous environments, mechanistically involves two processes; anodic dissolution of bare or partially corroded metal at the crack tip, and hydrogen embrittlement, the hydrogen being cathodically produced on the crack flanks close to the tip. Dissolution involves changes in local crack tip geometry only, whereas hydrogen by diffusion can affect the material ahead of the crack tip.

Anodic dissolution occurs at the bare metal crack tip exposed each cycle on opening, and where slip lines rupture any protective oxide layers. This corrosive dissolution competes against the constant mechanical resharpening of the tip. If the dissolution dominates then crack blunting can occur, and the limit to dissolution enhanced growth is $\delta/2$ since dissolution is limited to the crack tip. If dissolution gave a larger effective opening, the crack would not resharpen on unloading and would become a notch. Thus in corrosion fatigue tests when $da/dN < \delta/2$, propagation is by the extension of a sharp crack and ductile striations are accentuated in the normal way during stress reversal and fracture surfaces are similar to those obtained in air environments during Stage II growth. Since dissolution is a time dependent process, then lowering the cyclic frequency allows the corrosion effects to act for longer, causing dissolution enhanced growth rates to increase. However, there is a specific frequency which results in the maximum effect of corrosion, causing $\delta/2$ to be attained. Support for this mechanics-limited dissolution-assisted growth mechanism comes from Atkinson and Lindley[10], who have shown that the critical frequency at which $\delta/2$ is reached lies between 0.1 and 0.01 Hz.

They have also shown that this frequency is higher at 90°C than at 25°C, which is consistent with higher dissolution rates.

Thus in the Stage II growth region when crack growth is controlled by anodic dissolution, then an upper bound to crack growth would be described by $\delta/2$. This bound would be frequency-independent, but dependent on stress ratio (R), since at any given ΔK level, the CTOD increases as the R ratio increases. This would only be true if the material/environment combination showed no susceptibility to stress corrosion cracking, since under these circumstances dissolution enhanced growth would not be limited by $\delta/2$. The limiting condition would then be the maintenance of a high aspect crack ratio, obtained by a high dissolution rate at the oxide ruptured crack tip and an adequate passivation rate on the crack sides. Prater[11] has shown that these conditions can be obtained when cycling carbon steel in aerated, high temperature water at low frequency. Selective dissolution then leads to fatigue crack growth by incremental stress corrosion cracking, which gives $da/dN \gg \delta/2$. Whether these conditions can be obtained for A533-B tested in simulated PWR water environments is open to debate and is the subject of Scott's paper at this meeting[3].

Much of the published data for crack growth in aqueous environments show an apparent threshold for the corrosion effect, which is believed to occur at the Stage I/Stage II transition. The dominant shear mode of opening and the small crack openings in Stage I, limits the liquid environmental access to the crack tip and therefore the Stage I/II transition gives an effective limit to dissolution enhanced growth.

Hydrogen assisted growth is the second mechanism by which growth rates are enhanced, but the process is not independent of dissolution assisted growth, since the hydrogen is only produced as a result of the crack tip anodic dissolution. The mechanism can however involve material ahead of the crack tip in the fracture process, by hydrogen absorption and diffusion, to produce embrittlement. Fractographically the mechanism is distinguished from dissolution assisted growth by the presence of grain boundary or quasi cleavage facets often showing brittle striations. It occurs in low pH aqueous environments and in susceptible steels, such as ferritic-pearlitic steels, where cleavage occurs through the ferrite grains. A typical cleavage facet showing brittle striations is shown in Fig. 6, which indicates that the facets are created incrementally. There is evidence of ductile tearing normal to the crack front, which suggests that micro-cracks form ahead of the crack and link together and with the crack front by ductile tearing. This is analogous to Stage III fracture and can produce crack advance in excess of $\delta/2$. However, the size of the brittle striations (approx. 4 μm) are small compared with the size of an embrittled zone ahead of the crack based on a simple diffusion model (approx. 150 μm for 0.01 Hz). This indicates that the microfracture ahead of the crack is governed by some interaction between the hydrogen concentration gradient and the stress field ahead of the crack, there being some critical criteria for brittle striation formation. The striation marking the arrest of the crack at each cycle indicates that shear deformation is occurring, which supports Laird's view that the mechanism of ductile and brittle striation formation is very similar[12].

The fractographic evidence and the effect of cyclic frequency on growth rates support a discontinuous mechanism for hydrogen embrittlement. Hydrogen is readily absorbed onto the clean metal surface exposed on the tensile part of each cycle and it then diffuses into the metal to form a cluster in the tri-axially stressed region ahead of the crack, leading to microcrack formation, which link with the main crack front to give crack advance. It is difficult

to delineate an upper bound to hydrogen assisted growth, but this proposed mechanism indicates that an upper limit could be given by the cyclic plastic zone size. For this model, a reduction in the rise time or an increase in the R ratio would promote embrittlement by increasing the time for hydrogen diffusion and by increasing the size of the plastic zone at a given ΔK level, respectively.

Atkinson and Lindley[10] have tested A533-B in hydrogen and found a peak acceleration on reducing the frequency, supporting a hydrogen diffusion controlled mechanism. The critical frequency reduced on increasing the temperature, due to increased hydrogen mobility, indicating that hydrogen assisted growth may not be a problem at operating temperatures for PWR pressure vessels, because of diffusion away from the crack tip.

The threshold for hydrogen assisted growth is less clear than for dissolution controlled growth, since limited environmental access to the tip may not stop hydrogen diffusion from the crack flanks if any electro-chemical reaction can be sustained there. This lack of a threshold is observed in the work of Vosikovsky[13], in which hydrogen assisted growth dominates due to the application of a cathodic potential.

This hydrogen assisted crack growth mechanism is supported by Cullen and Torronen[14] for enhanced crack growth in a PWR environment at 288°C. They have fractographic evidence in support of the model, since they observe quasi-cleavage facets and brittle striations. They suggest that a lack of environmental enhancement at low ΔK levels may be due to the time required to attain an acidic environment at the crack tip. They also believe that at high ΔK values, where a retardation of the environmental influence is seen, that crack growth rates exceed the rate of hydrogen evolution and absorption and therefore the embrittling effect cannot be achieved. It is also possible that the electro-chemical conditions associated with a long crack may change the potential and reduce the evolution of hydrogen.

Environmental Crack Growth in Austenitic Steels

Fatigue crack growth experiments have been performed by Bamford on types 304 and 316 stainless steels exposed to a simulated PWR environment at 288°C[15]. Results have shown no enhancement of growth rates due to the PWR environment at low R ratios and no effect of test frequency or specimen orientation. A dependence on stress ratio was observed however, with growth rates increasing with R ratio. Fractography revealed that growth occurred by a ductile striation mechanism. Identical crack growth behaviour has been demonstrated by the author in a simulated PWR environment at ambient conditions, but fractography has revealed the presence of crystallographic facets. This additional fracture mode was environmentally sensitive but independent of mean stress and as such did not affect crack growth rates. These facets have, however, been observed on air fatigued fracture surfaces of type 304 and 316 stainless steel by de Vries[16] and Priddle and Walker[17]. Determination of the facet orientations by means of selected area channelling patterns has been carried out by de Vries. He observed that facets on samples tested at R= 0.05 had orientations near (110), (111), (112) and (114), but at higher stress ratios a larger fraction of (111) facets were observed. Intersecting parallel slip line markings were observed on these facets, and the facets were smooth. Evidence of slip lines on the facets indicates a substantial amount of plastic deformation. Facets on fracture surfaces of fatigue tested (R = 0.3, 140 Hz) type 316 stainless steel have been analysed by Priddle and Walker, who concluded that the facets were (111) cleavage facets, associated with reduced plasticity as evidenced by a reduction in slip lines. The fraction of cleavage facets

varied with ΔK and a peak occurred at a ΔK level that corresponded to the alternating plastic zone size equalling the grain diameter. The cleavage was considered as part of the fatigue process and not fast fracture, as crack front marking showed facets where the crack had stopped halfway across the facet.

The mechanism by which these facets are produced is open to debate as the experimental evidence is not totally in accord. Facets were not observed at the author's laboratory for air fatigued specimens, unlike de Vries and Priddle who observed them in air at ambient temperature. Facets of various orientations were identified by de Vries, whereas Priddle only observed (111) type facets. The mechanism proposed by Priddle, in that cleavage is occurring on {111} planes is debatable, since cleavage is not expected to occur in ductile fcc metals like austenitic stainless steels. Lynch[18] has however proposed a mechanism for cleavage in ductile materials. His results suggest that cleavage fracture is not an 'atomically brittle' process, but occurs by alternate slip at crack tips in conjunction with the formation of very small voids ahead of cracks. Lynch proposed that environmentally induced cleavage of normally ductile materials can be explained on the basis that chemisorption of environmental species facilitates nucleation of dislocations at the crack tip. This mechanism appears attractive for explaining any hydrogen induced fracture in austenitic steel, since the greater solubility of hydrogen in austenite than ferrite, would tend to rule out any mechanism based on embrittlement of material ahead of the crack tip. However, unlike Lynch who observed cleavage fracture on {100} planes in fcc metals, fracture planes for specimens tested in a simulated PWR environment were identified by analysis of slip traces as {111} planes, which is the slip or twin plane. This tends to indicate that cleavage is not occurring.

The proposed mechanism for the environmentally sensitive fracture observed at room temperature is again thought to be dissolution assisted. The emergence of slip steps at the crack tip allow dissolution to occur, but since environmental growth rates are not enhanced above growth rates in air, then little dissolution is occurring and passivation dominates. However, there exists in the material crystallographic planes which have specific surface energies that allow selective dissolution to occur. It is thought that this selective dissolution may be associated with the twin boundaries and further work is underway to examine this.

Conclusions

Fractographic examination of specimens tested in simulated LWR environments is steadily increasing enabling the fracture modes of several materials, including plate, forging, weld and heat affected zones, to be characterised. In general fractography has been able to explain data trends and has also given an understanding of the operative corrosion fatigue mechanisms.

Fatigue crack growth in air at ambient temperature has been seen to be by a ductile striation formation mechanism. A model has been described which shows that striation formation is a result of localised shear processes at the crack tip and correlations existing between the crack tip opening displacement, crack growth rate and striation spacing have been explained. The presence of some limited intergranular separation has been linked to Stage I crack growth, where deformation in the crack tip plastic zone is on a scale less than the grain size and is therefore crystallographically controlled.

Environmental crack growth in ferritic steels at ambient temperature has been described by a model involving both anodic dissolution and hydrogen embrittlement. Observation of quasi-cleavage facets and brittle striations in the ferritic-

pearlitic C-Mn steel suggests that this steel is susceptible to hydrogen embrittlement, the hydrogen being produced in the complementary cathodic reaction to the anodic dissolution process at the crack tip. Bainitic A533-B appears less susceptible to hydrogen assisted growth and dissolution is the dominant process, with growth in general being by a ductile striation mechanism. It has been proposed that for a dissolution dominated mechanism, the crack tip opening displacement would be an upper bound to crack growth and a threshold determined by environmental access would exist. For any growth dominated by a hydrogen mechanism these limites are more difficult to postulate, but it is possible that the cyclic plastic zone size may delinate an upper bound to growth.

Crack growth in austenitic steels in an inert environment is by ductile striation formation, the striations being much more developed than in the ferritic steels. An additional mode of failure of crystallographic facets were observed and seen to be environmentally sensitive. Some facets were identified by analysis of slip traces as {111} planes. It is thought that this environmentally sensitive fracture is again due to a dissolution process, with selective dissolution occuring along particular crystallographic planes.

Thus although fractography has led to an understanding of corrosion fatigue mechanisms, further work is needed in this area before fractography meets the objective of predicting the behaviour of material to practical combinations of mechanical loading and environment.

REFERENCES

1. BAMFORD W H. Transactions of the ASME, J of Engineering Materials and Technology 101 (1979) p.182-190.

2. McMINN A. SNL Report ND-R-526(S), 1980.

3. SCOTT P M and TRUSWELL A E. This Conference.

4. BAMFORD W H, MOON D M and CESCHINI L J. Heavy Section Steel Technology Programme Quarterly Progress Report, April-June 1979, ORNL-NUREG-TM-347.

5. BAMFORD W H and MOON D M. "Some mechanistic observations on the crack growth characteristics of pressure vessel and piping steels in PWR environments". presented at NACE meeting, Corrosion 79, March 1979.

6. HICKLING J. International Cyclic Crack Growth Rate Group Meeting, Harwell, UK. 15-16 May 1980.

7. KONDO T. Ref. 6.

8. TORRONEN, K. Ref. 6.

9. BIRBECK G B, INCKLE A E and WALDRON W J. J of Mat. Sci. Vol. 6, 1971, p.319-325.

10. ATKINSON J D and LINDLEY T C. The Influence of Environment on Fatigue. I.Mech.E/SEE Joint Conf. London 1977.

11. PRATER T A, FORD F P and COFFIN L F. Conf. on Micromechanisms of Crack Extension Cambridge. 31 March-2 April 1980.

12. LAIRD C. ASTM STP 415, 1967, p.247-309.

13. VOSIKOVSKY O. J of Eng. Mat. and Tech, 97, 1975, p.298.

14. CULLEN W H and TORRONEN K. NRL Report 4298, NUREG/CR-1576, September 1980.

15. BAMFORD W H. J of PV Technology, February 1979, Vol. 101, p.73-79.

16. DE VRIES M I and MASTENBROEK. J of Mat. Sci., 12, 1977, p.1700.

17. PRIDDLE E K and WALKER F E. J of Mat. Sci., 11, 1976, P.386.

18. LYNCH S P. Ref. 11.

TABLE 1

Chemical composition (wt.%) and mechanical properties of steels examined

	C-Mn steel	Ducol W30	A533-B	Type 304 stainless
Carbon	0.13	0.166	0.19	0.07
Manganese	1.35	1.6	1.25	1.30
Chromium	< 0.1	0.7	0.13	18.68
Nickel	< 0.1	0.1	0.68	10.75
Molybdenum	< 0.01	0.21	0.49	
Vanadium	< 0.015			
Silicon			0.205	0.25
Sulphur			0.013	0.019
Phosphorus			0.017	0.019
Cobalt			0.013	0.012
Tantalum			0.002	0.01
Tensile Strength MPa	570		579-585	578
Yield strength (0.2% offset) MPa	340		395-435	269
% Elongation			29	67.5
% reduction of area	60		66	

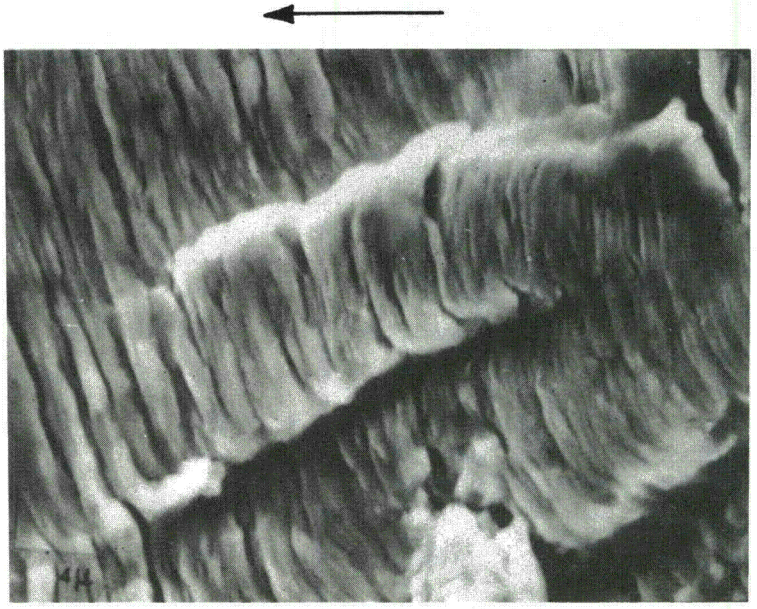

FIG. 1 MULTIPLE AND SINGLE STRIATIONS FORMED IN THE C-Mn STEEL AT ΔK = 35 MN $m^{-3/2}$ (x 5k)

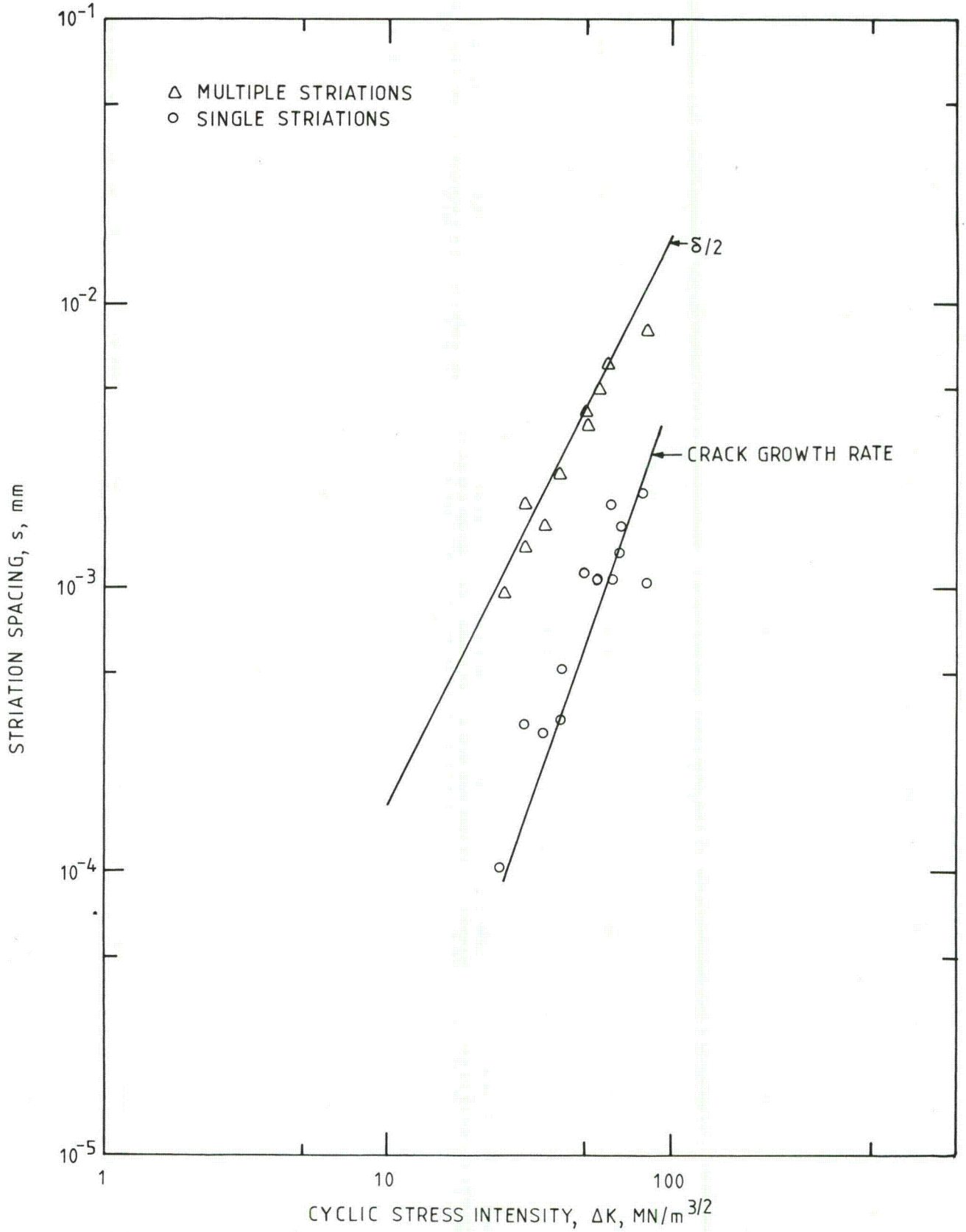

FIG.2. CORRELATION BETWEEN STRIATION SPACINGS, CRACK GROWTH RATE AND CRACK TIP OPENING DISPLACEMENT FOR THE C-Mn STEEL TESTED IN AIR AT R=0

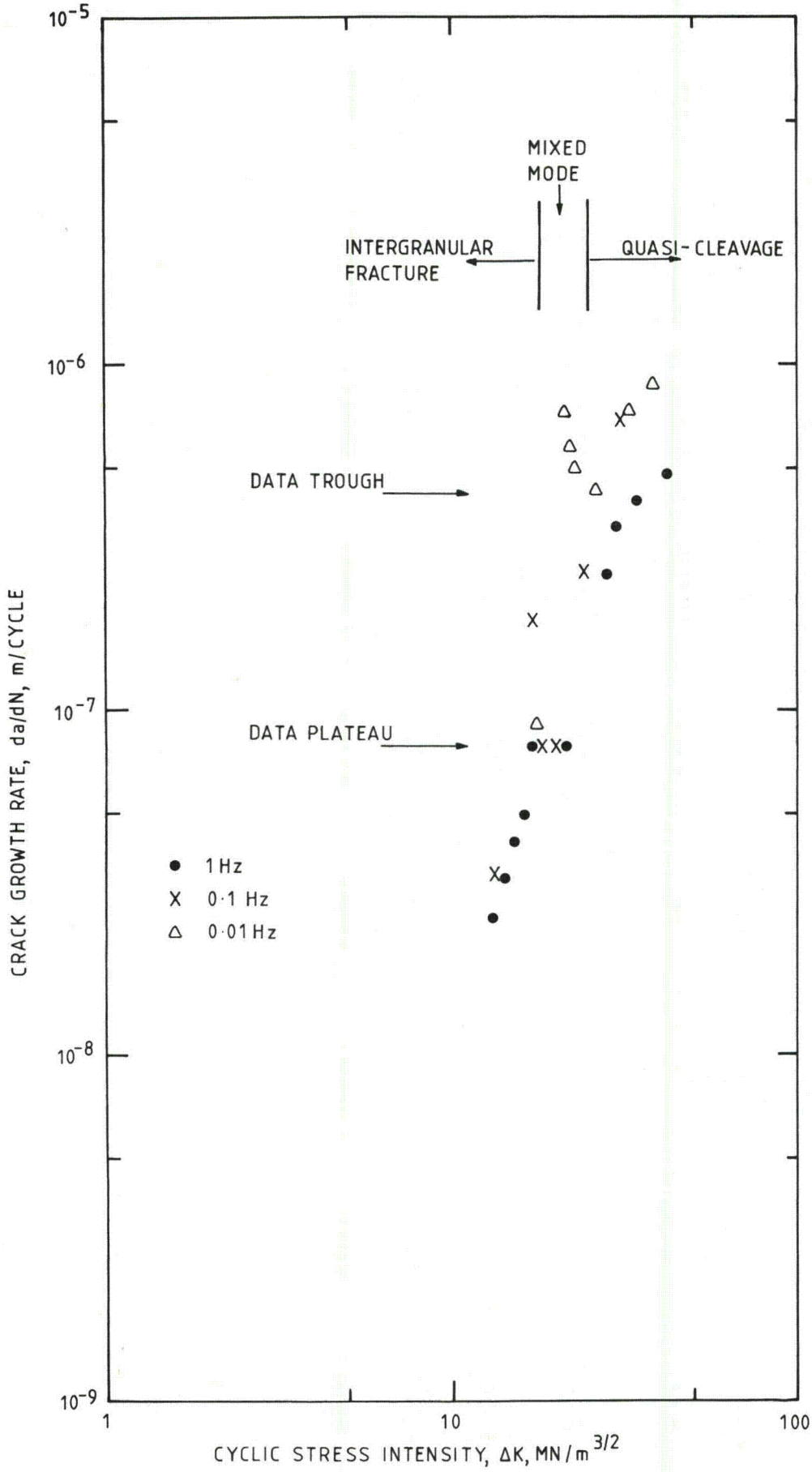

FIG.5. CORRELATION BETWEEN CRACK GROWTH RATE AND FRACTURE MODE FOR THE C-Mn STEEL TESTED IN AN AQUEOUS ENVIRONMENT AT R=0·5

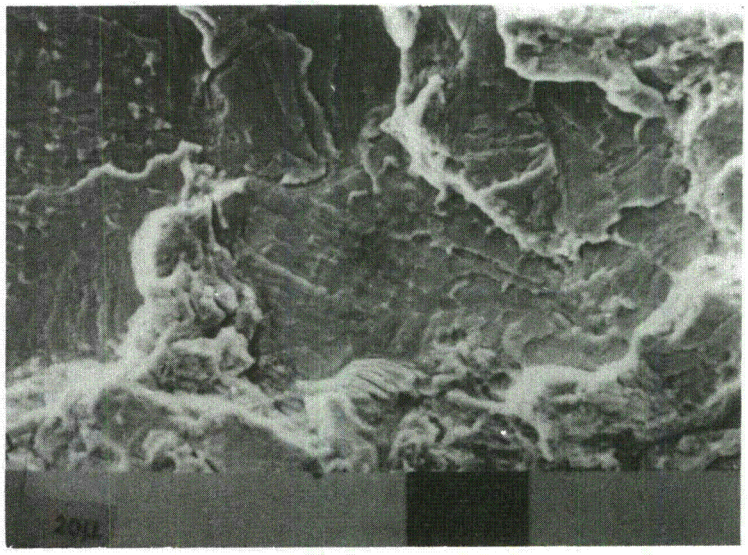

FIG. 3 TRANSGRANULAR QUASI-CLEAVAGE OBSERVED IN THE C-Mn STEEL TESTED IN AN AQUEOUS ENVIRONMENT (ΔK = 45 MN $m^{-3/2}$, 0.01 Hz)

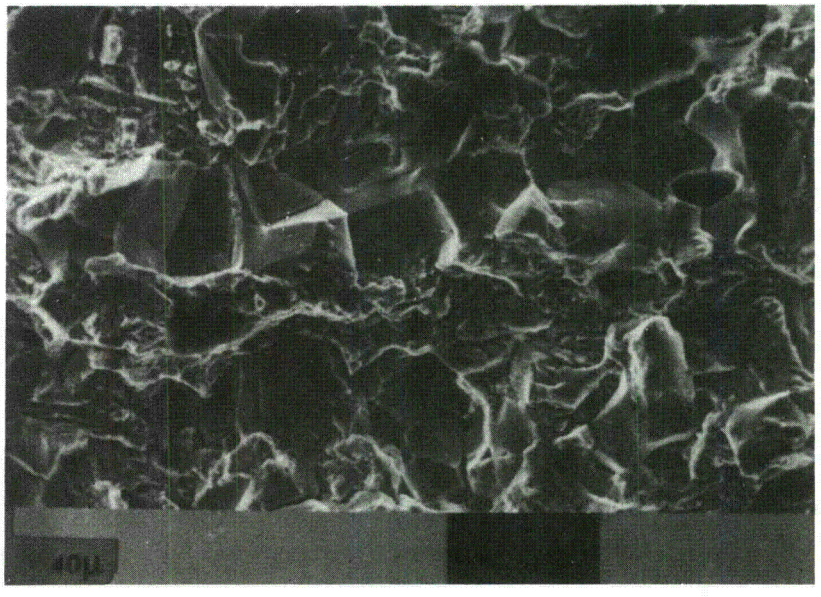

FIG. 4 INTERGRANULAR FRACTURE OBSERVED IN THE C-Mn STEEL TESTED IN AN AQUEOUS ENVIRONMENT (ΔK = 13 MN $m^{-3/2}$)

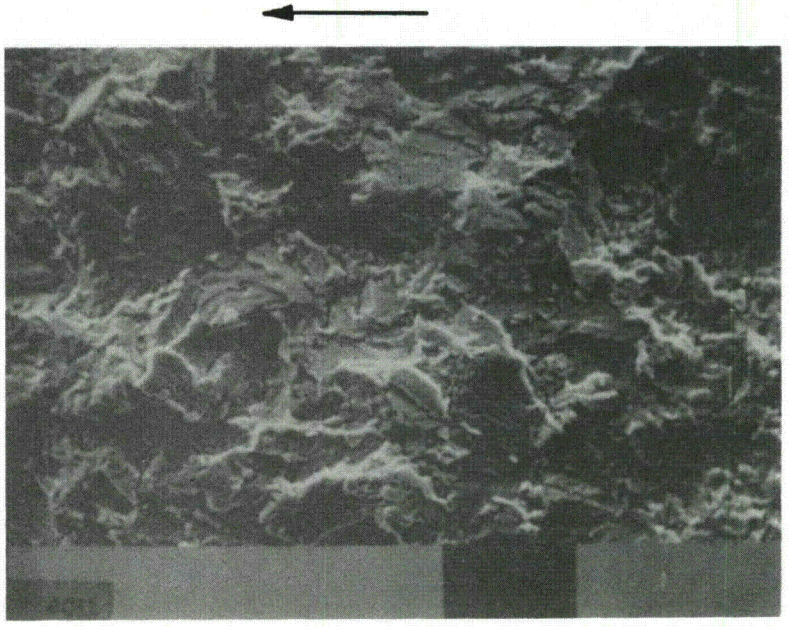

(quasi-cleavage)

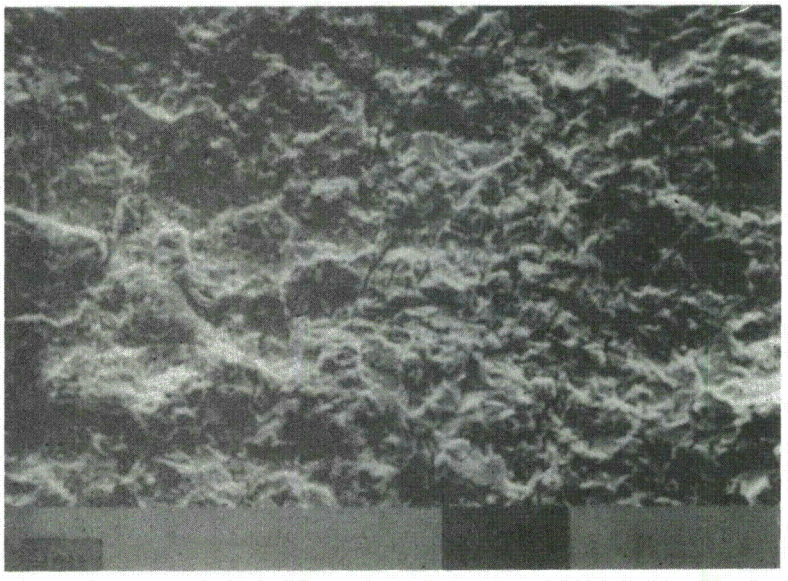

(ductile striations)

FIG. 8 OBSERVATION OF THE INDUCED QUASI-CLEAVAGE IN A533-B ON LOWERING THE CYCLIC FREQUENCY FROM 0.1 to 0.01 Hz IN A WATER ENVIRONMENT OF LOW pH

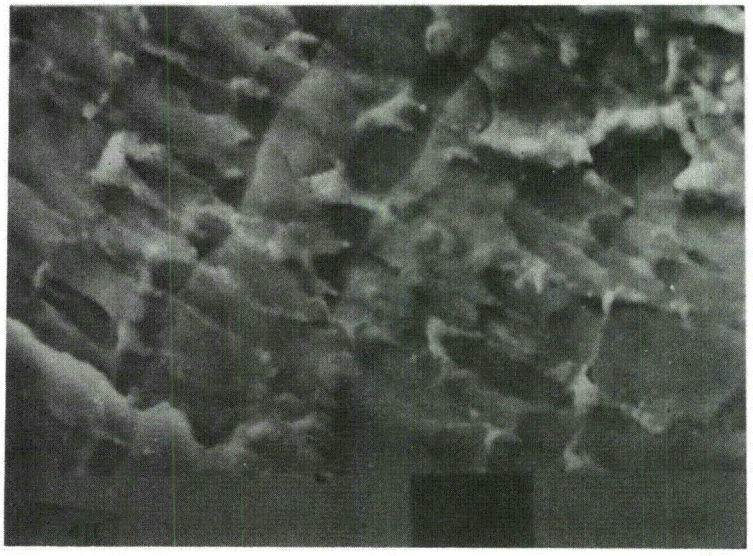

FIG. 6 BRITTLE STRIATIONS OBSERVED ON CLEAVAGE FACET IN THE C-Mn STEEL (ΔK = 45 MN $m^{-3/2}$, 0.01 Hz)

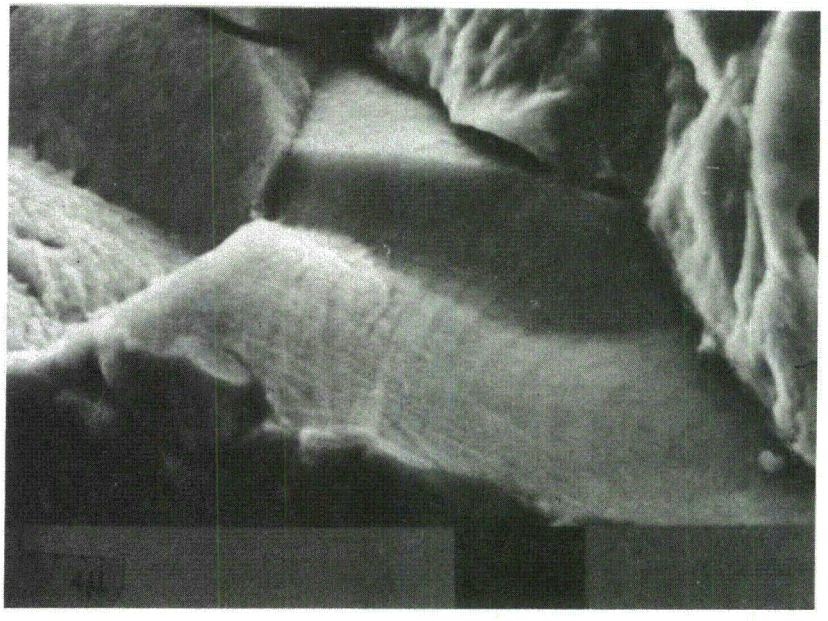

FIG. 7 BRITTLE STRIATIONS OBSERVED ON A GRAIN BOUNDARY IN THE C-Mn STEEL

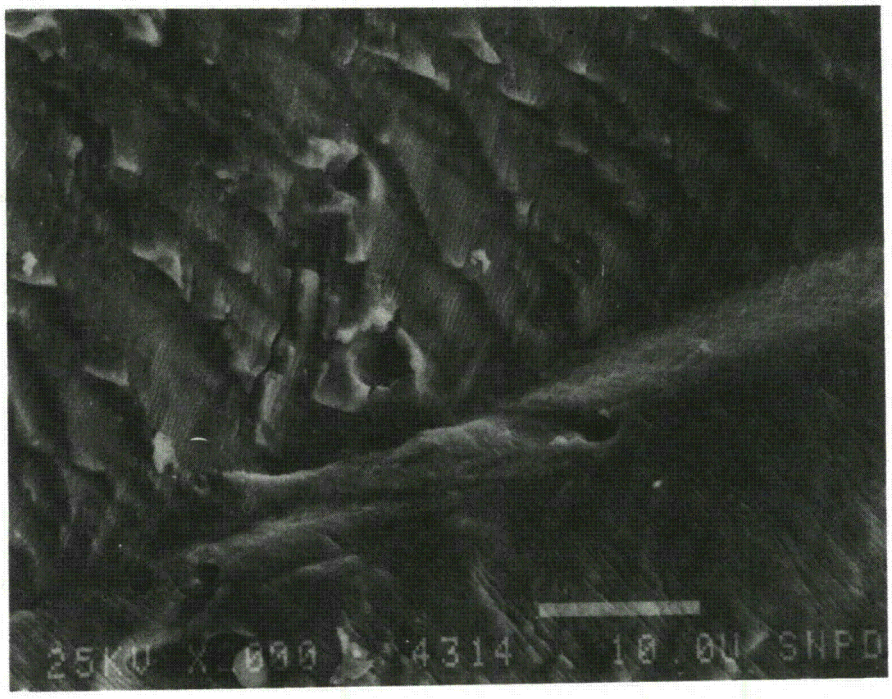

FIG. 10 DUCTILE STRIATIONS FORMED IN TYPE 304 STAINLESS STEEL TESTED IN AN AIR AT R=0 (ΔK = 40 MN $m^{-3/2}$)

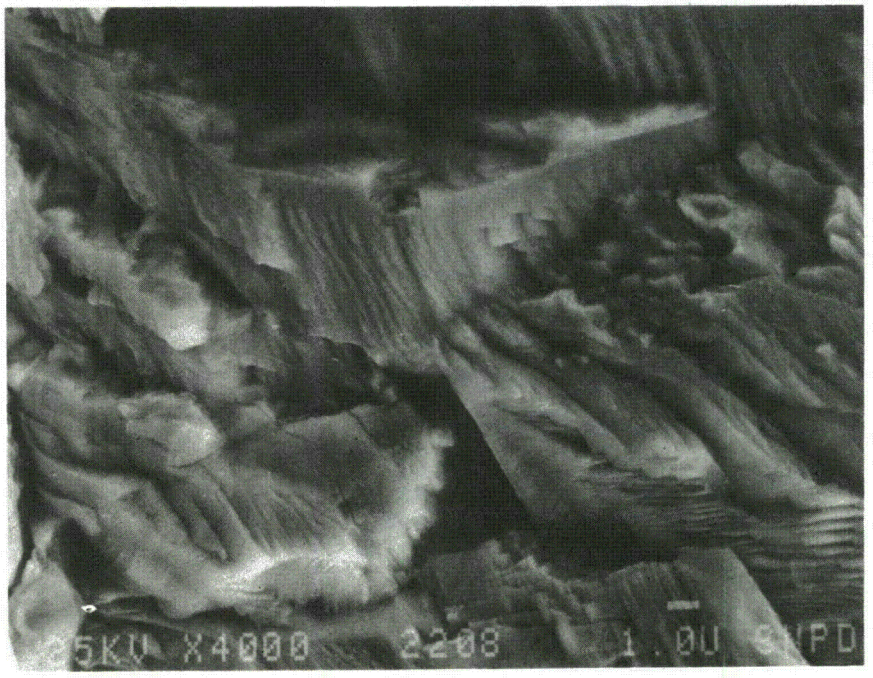

FIG. 11 FRACTURE SURFACE OF TYPE 304 STAINLESS STEEL TESTED IN AIR AT A HIGH R RATIO (0.7) SHOWING EVIDENCE OF SLIP ACTIVITY (ΔK = 10 MN $m^{-3/2}$)

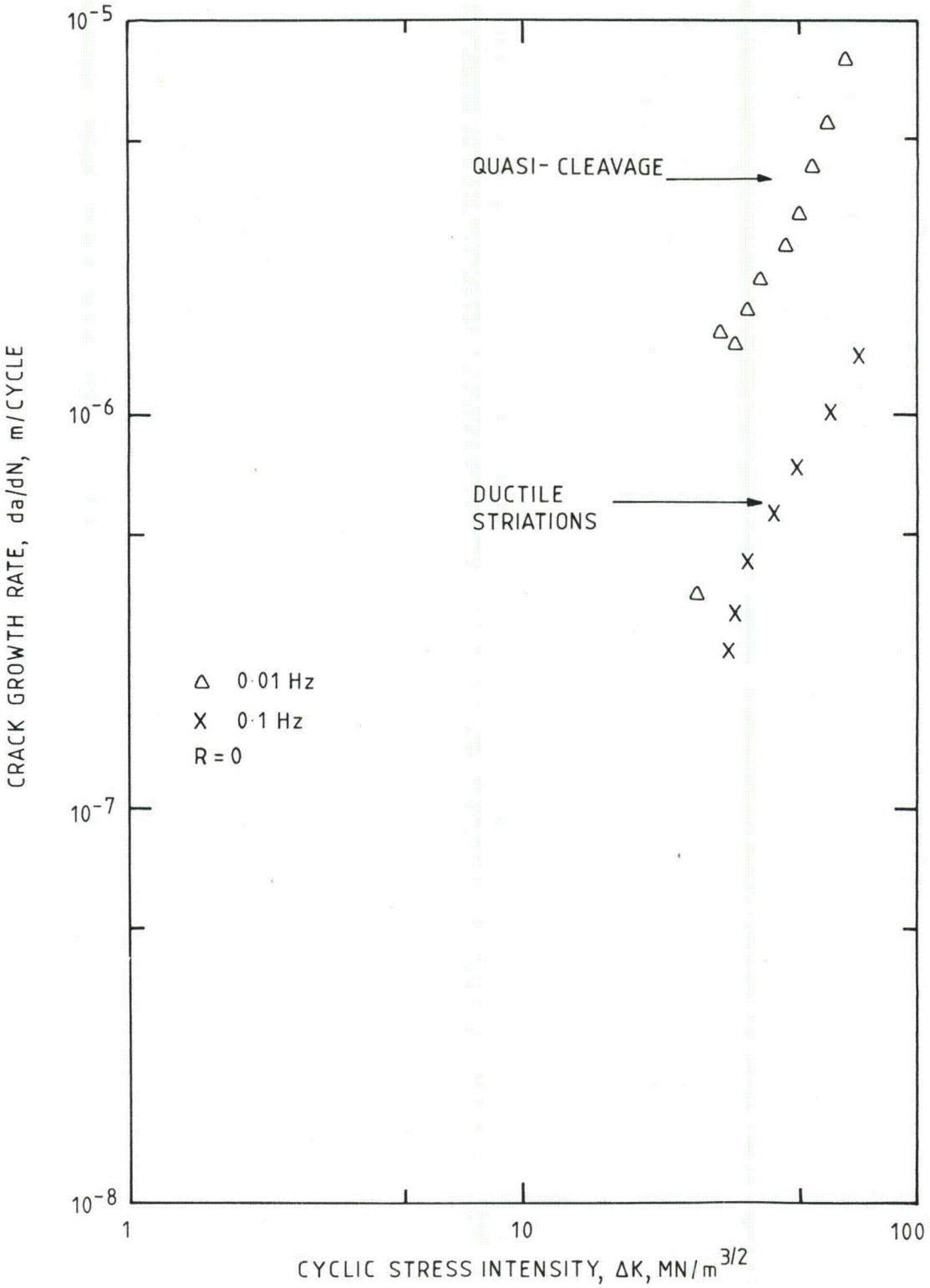

FIG.9. CRACK GROWTH PLOT SHOWING THE INCREASE IN CRACK GROWTH RATE IN A533-B WHEN QUASI-CLEAVAGE OCCURS AT 0·01 Hz IN A pH = 4 WATER ENVIRONMENT

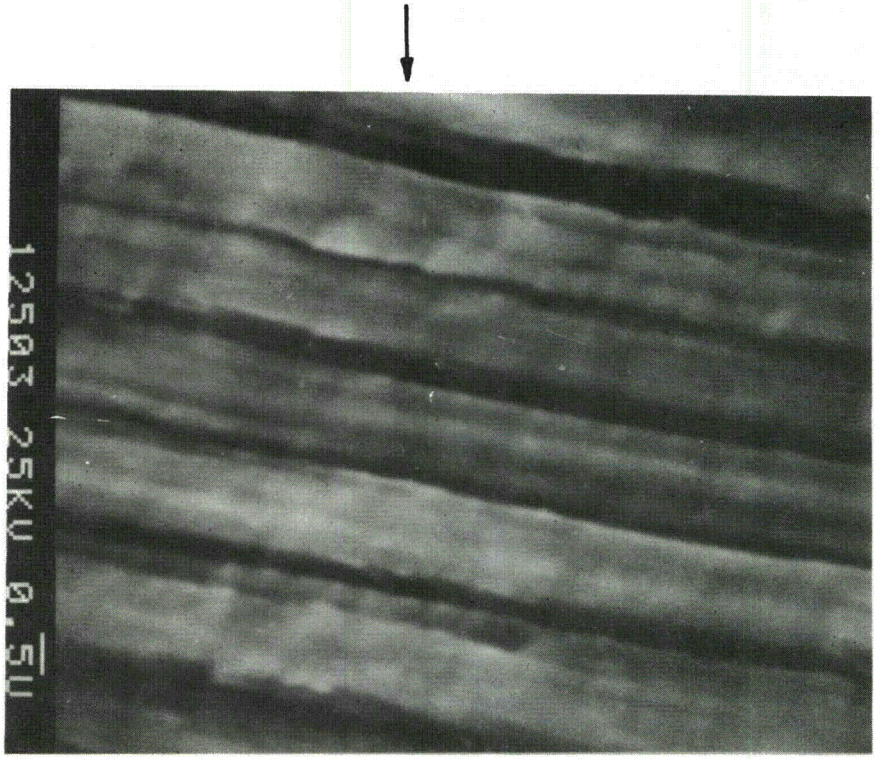

FIG. 13 MULTIPLE AND SINGLE STRIATIONS FORMED IN TYPE 304 STAINLESS STEEL TESTED IN AN AQUEOUS ENVIRONMENT (ΔK = 25 MN $m^{-3/2}$)

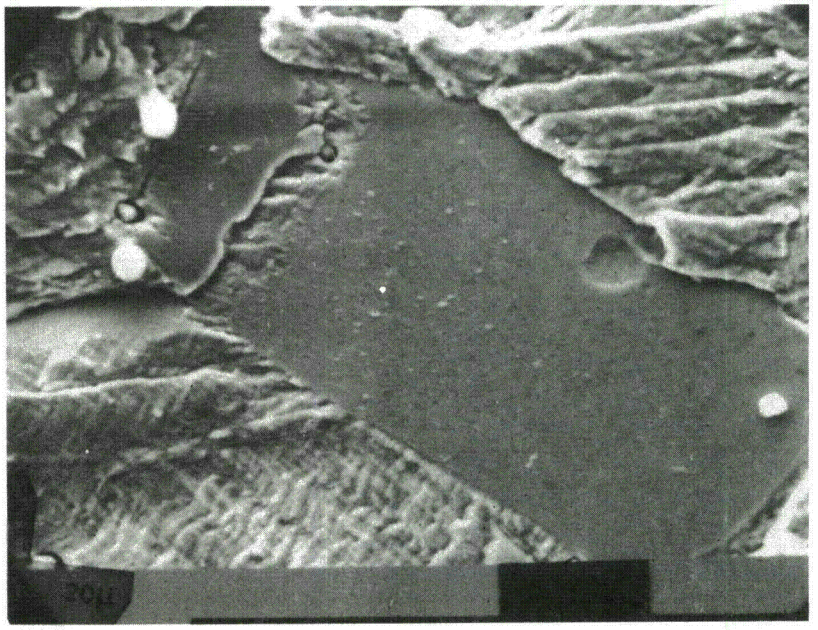

FIG. 14 TYPICAL FACET FORMED IN TYPE 304 STAINLESS STEEL TESTED IN AN AQUEOUS ENVIRONMENT (ΔK = 40 MN $m^{-3/2}$)

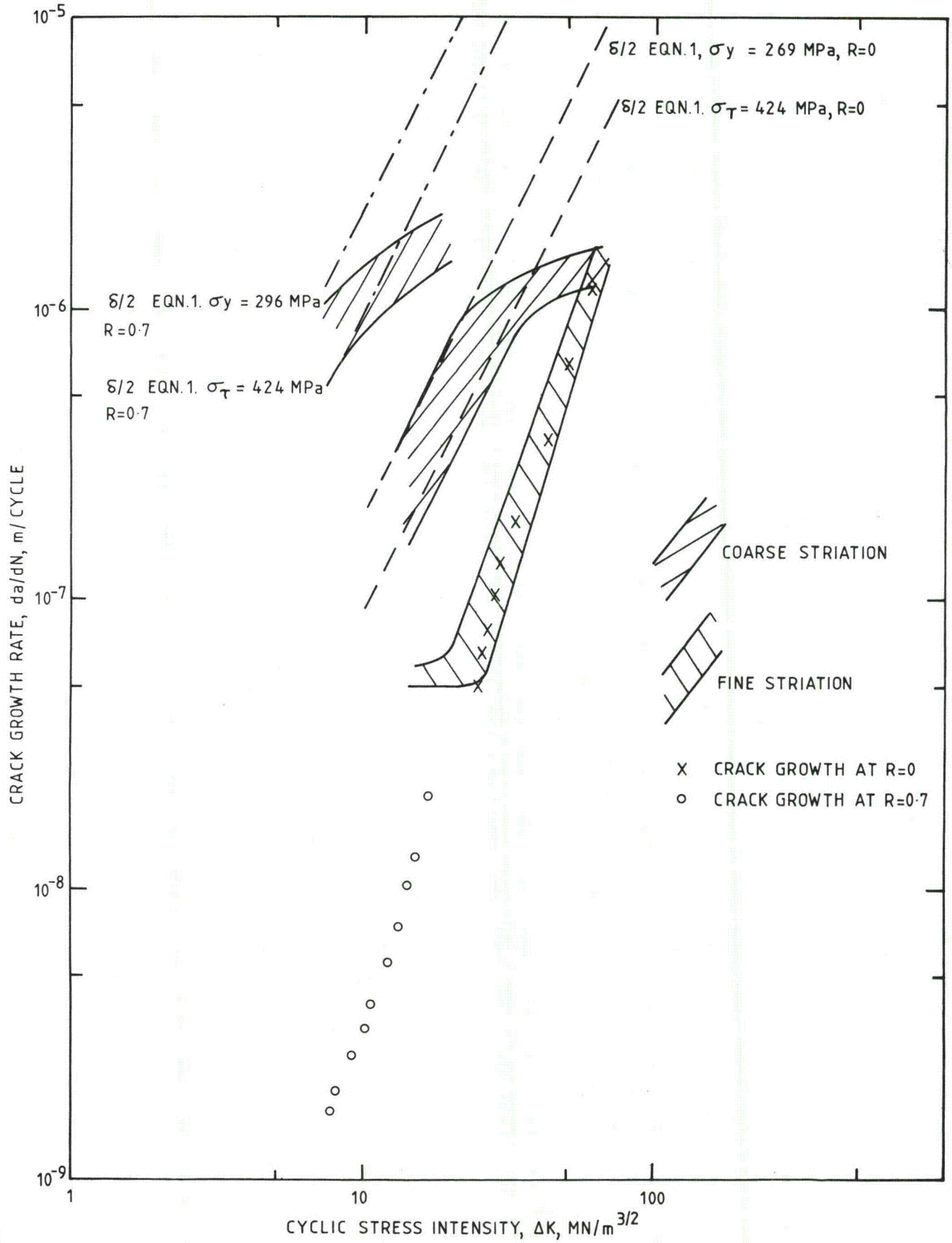

FIG.12. CORRELATION BETWEEN CRACK GROWTH RATES, STRIATION SPACINGS AND CRACK TIP OPENING DISPLACEMENTS FOR TYPE 304 STAINLESS STEEL TESTED IN AIR AT R=0 AND 0·7

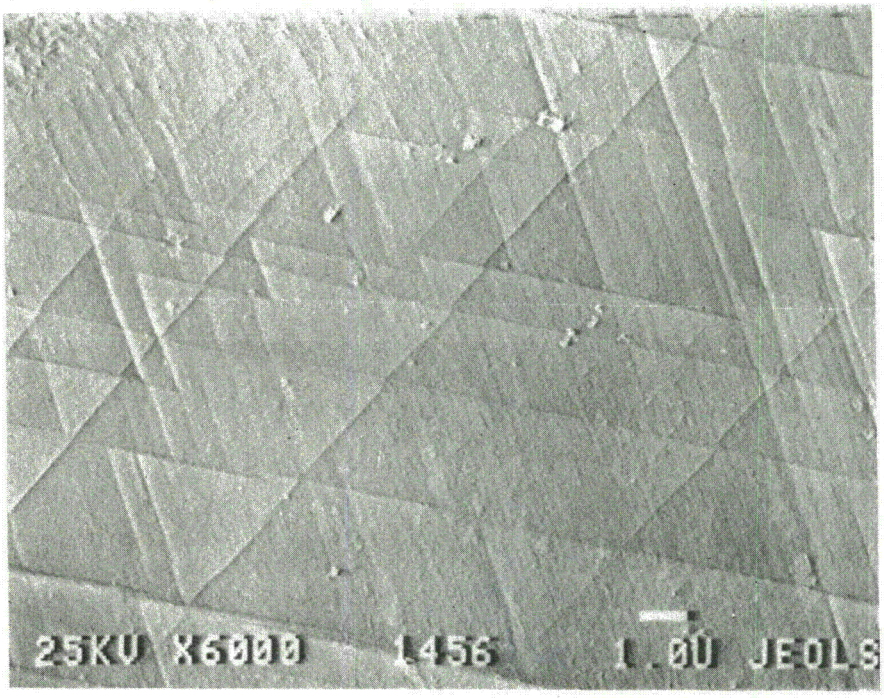

FIG. 15 SLIP LINE MARKINGS OBSERVED ON A FACET IN TYPE 304 STAINLESS STEEL.

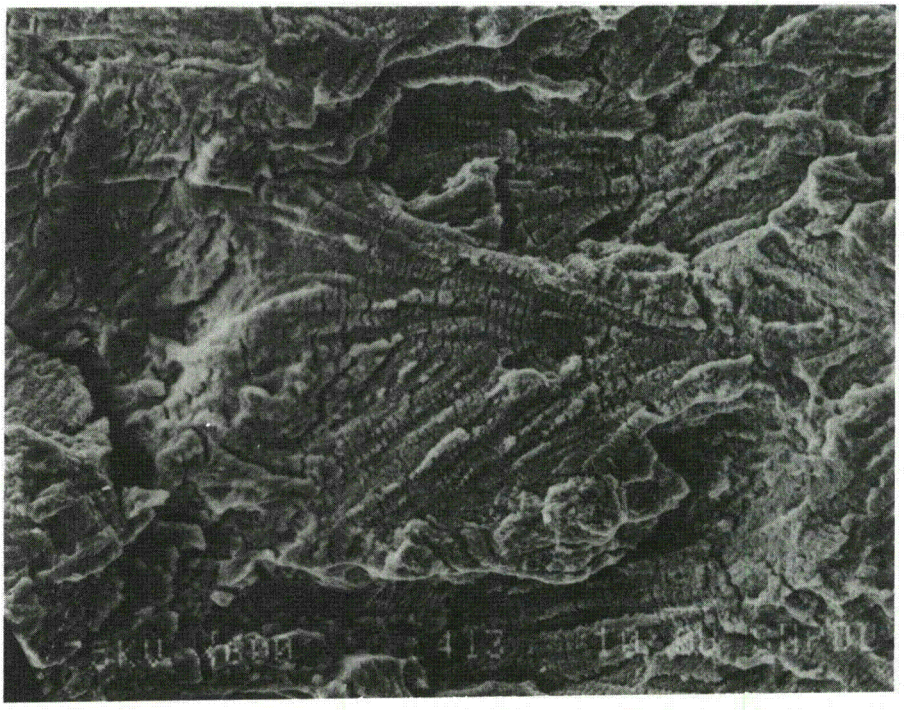

FIG. 16 TYPICAL DUCTILE STRIATIONS FORMED IN AN A508 FORGING SPECIMEN TESTED IN A HIGH TEMPERATURE PWR ENVIRONMENT (ΔK = 22 MN m$^{-3/2}$)

Paper to be presented at the IAEA Specialists' Meeting
on "Subcritical Crack Growth"
Freiburg, Federal Republic of Germany, May 13 to 15, 1981

K. Törrönen[1]
H. Hänninen[1]
W.H. Cullen, Jr.[2]

MECHANISMS OF ENVIRONMENT ASSISTED CYCLIC CRACK GROWTH OF NUCLEAR REACTOR PRESSURE VESSEL STEELS

[1]Technical Research Centre of Finland,
Metals laboratory, SF-02150 Espoo 15, Finland

[2]ENSA, Inc., Getzville, New York 14068, U.S.A.

ABSTRACT

An analysis of the cyclic crack growth rate data generated so far for pressure vessel materials in simulated light water reactor environments suggest a strong dependence on waveform, frequency, load ratio, temperature and material composition. To account for these observations a mechanistic crack growth model has been advanced based on hydrogen-induced cracking where anodic dissolution creates the conditions for hydrogen absorption at the crack tip. Hydrogen-induced cracking starts from the manganese sulfide inclusions, which act as strong hydrogen traps. The hydrogen-induced crack growth around the sulfides spans generally several prior austenite grains. At high hydrogen input rates brittle crack growth occurs also unconnected to inclusions. When crack growth uncovers manganese sulfide inclusions they dissolve and change the crack tip environment aggressive and condusive to hydrogen absorption. This hydrogen-induced cracking model explains why inclusions form a preferred crack path and the effect of sulfur on crack growth rate both in PWR and BWR conditions. Based on the model the observed crack growth rate dependence on different testing variables can be qualitatively explained.

INTRODUCTION

Recent years have witnessed a significant increase in the amount of research as well as published data on fatigue crack growth for pressure vessel and piping materials in simulated light water reactor environments. All the published data have been collected and reviewed in a recent report (1), and supplements for this report, in order to keep the collection up-to-date, will be published on a continuing basis. The collection and documentation of the available data are an important function by themselves to be used in the engineering design, or in inservice inspection analysis of nuclear power generation installations. However, recognition and understanding of the mechanical, material and environment related variables will better serve the longer range interests of design, safety and regulatory personnel associated with the nuclear power industry. Many of these influences have been rather carefully investigated on a macroscopic scale, but micromechanistic understanding has been far from complete, although many theories have been advanced (2 - 7). This paper describes some new attemts to gain further understanding of these micromechanisms and presents an interpretation of the experimental data based on a hydrogen assisted cracking model.

A foundation of the presentation and discussion of the various mechanistic theories which have been advanced is provided by the following synopsis of the major influences. In all cases, an aqueous environment similar to that in a light-water reactor was used in the research which provided these conclusions. In most of these results, this reactor-grade water was contained at reactor-typical operating pressures and temperatures.

a) Waveform Effects. As a general case, sinusoidal waveforms produce higher fatigue crack growth rates than ramp-hold, or ramp-reset type waveforms (5). The effects of mixed waveforms, and variable amplitude waveforms, have not been carefully investigated. Similarily, crack growth retardation due to proof-testing, or other overload transients have not been carefully investigated or documented.

b) Frequency Effects. For boiling water reactor environments, characterized by essentially pure water with about 200 ppb dissolved oxygen (during operation), fatigue crack growth rates increase monotonically with cyclic period (2, 8). For pressurized water reactor environments, characterized chiefly by lightly buffered water (1000 ppm boron as boric acid, 1 ppm lithium as lithium hydroxide) with less than 10 ppb dissolved oxygen, crack growth rates increase with increasing cyclic period, to periods of about sixty seconds duration, and then level off or decrease slightly for very long cyclic periods (5).

c) Load Ratio Effects. As with most environmentally susceptible materials, increasing load ratio produces a sizeable increase in crack growth rates, in terms of the applied cyclic stress intensity (ΔK) (9). There is a significant quantity of data which supports this overall effect, but the available data does not document the threshold, or near threshold values for crack growth rates, which are customarily strong functions of the load ratio and the environments.

d) Temperature Effects. Generally, waveforms with a rise time component which is large enough to

produce an environmental effect, will, in addition, produce higher crack growth rates at lower temperatures (5). There is some evidence that a peak in crack growth rates may occur at temperatures of about 200°C; that research was carried out in a BWR environment using a clad specimen (10).

e) Materials Related Effects.

1. Product Form. Product form by itself is not a predictable indicator of fatigue crack growth rates. Differences, where noted, are usually slight, and apparent trends usually have notable exceptions. Some work in a BWR environment indicated coarse-grained material may be slightly more susceptible than fine-grained materials (11).

2. Compositional Effects. Composition seems to have a strong effect, and recent evidence ties fatigue crack growth rates to sulfur content (12). While a definitive study has not been carried out, measurements of fatigue crack growth rates for several heats of A533B, and A508 Gr.2 show a clear trend of increasing crack growth rates with increasing sulfur content.

3. Irradiation. Recently, several tests have been conducted on irradiated pressure vessel steels in a simulated PWR environment (13, 14). The results, for 1 Hz and 17 mHz sinusoidal waveforms, indicate that irradiation results in little, if any, increase in

fatigue crack growth rates. There is, evidently, no degrading, synergistic effect of irradiation and environmentally sensitive waveform conditions. For the higher 1 Hz frequency, for which crack growth rates exhibit little environmental effect, the growth rates are often slightly lower, a fact which may be attributed to the increased yield strength.

The above five categories have been identified and singled out for their contribution to fatigue crack growth rates. The combined effects of two or more of these variables acting together has not been, in general, clearly identified. Individual micro-mechanistic processes have been suggested to account for each of the above influences, but again, the way in which these influences combine is, at the present, somewhat speculative, and supporting data is difficult to identify.

EXPERIMENTAL

Three heats of A533B-1 and two heats of A508 Cl.2 reactor pressure vessel steels were principally used in the experiments. The chemical compositions are listed in Table 1. The mechanical testing consisted of cyclic crack growth rate (CCGR) or corrosion fatigue (CF) studies in simulated light water reactor environments, slow strain rate (SSR) testing with simultaneous hydrogen charging, SSR testing with sign-changing polarization technique and tensile testing of hydrogen charged specimens. The main part of the experimental work, however, consisted of fractographical analysis of the fracture surfaces. In addition to the specimens tested at VTT in Finland, several CCGR specimens belonging to the International Cyclic Crack Growth Rate (ICCGR) Group round-robin testing as well as

Table 1 Chemical composition of reactor pressure vessel steels

Steel type	Chemical composition										Remarks
	C	Mn	P	S	Si	Ni	Cr	Mo	V	Cu	
A533B-1	0.19	1.28	0.009	0.013	0.25	0.61	0.04	0.55	0.004	0.10	Int. round robin (1HT-series)
A533B-1	0.18	1.42	0.005	0.006	0.22	0.63	0.18	0.50	0.01	0.04	SSR and hydrogen charging tests
A533B-1	0.21	1.60	0.008	0.012	0.21	0.70	0.10	0.47	0.01	0.17	Westinghouse spec. 02GB5
A508 cl. 2	0.24	0.77	0.006	0.010	0.18	0.85	0.50	0.62	0.00	0.08	Hydrogen charging tests
A508 cl. 2	0.22	0.64	0.006	0.010	0.27	0.77	0.35	0.60	0.01	0.06	Westinghouse spec. F-1

fractographic round-robin were studied by scanning electron microscopy.

The details of the ICCGR group round-robin testing are repoted elsewhere during this conference (15). In principal testing was performed in deionized water at 288°C using ITCT specimens. Sinusoidal waveform with constant load amplitude and load ratio of 0.2, and two frequences, 17 mHz and 1 Hz, were utilized. The dissolved oxygen content varied from essentially zero to 8 ppm in various tests due to different test facilities and practices. A few specimens tested at Westinghouse with load ratio of 0.7 were also available for fractography through the fractographic round-robin of the ICCGR Group.

In addition to cyclic crack growth rate investigations other techniques were used to obtain material for mechanistic studies. Round tensile specimens of A533B-1 steel were studied by using the slow strain rate (SSR) testing method with simultaneous hydrogen charging through cathodic polarization. The specimens had a gauge section diameter of 2.5 mm and length of 20 mm. The strain rate was 3.5×10^{-7} s^{-1}. The tensile specimens were cathodically charged during SSRT at 22°C in a 1 N H_2SO_4 solution containing 0.25 g/l of $NaAsO_2$. The current density was 10 mA/cm^2 and a platinum counter electrode was used.

Thin tensile specimens having a gauge section 0.5 mm thick, 5 mm wide and 20 mm long were cathodically charged at 22°C in same conditions as above with a current density of 50 mA/cm^2. The hydrogen charging time was 24 h. After charging, the specimens were tensile tested within 5 min at room temperature.

For round tensile specimens studied with SSR technique a sign-changing polarization technique (16) was used in H_3BO_3 - solution (12 g H_3BO_3/kg H_2O) at 80°C.

The sign-changing polarization technique comprised of short term anodic polarization (2 h at 0 mV_{SCE}) and following cathodic polarization (rest of the time during SSR test at - 1000 mV_{SCE}). The method was thought to take both stages of stress corrosion cracking into account, i.e. crack initiation and crack propagation.

Fracture surface of various test specimens were studied first without any attempt for oxide layer removal, and only in case a need for cleaning was evident, the ENDOX treatment (17) was utilized.

RESULTS

The observed cyclic crack growth rates in the international round-robin testing are summarized elsewhere during this meeting (15). In principal, a large variation of the 17 mHz test results is obvious; results showing no environmental influence at all as well as results above the old ASME Section XI water environment default line form the two extremes between which the data are scattered. The 1 Hz test results, on the contrary, are fairly consistent with the data laying along the ASME Section XI air line. The two Westinghouse specimens tested with load ratio of 0.7 at 17 or 8 mHz show much higher environmental influence compared to testing with load ratio of 0.2 (see Fig. 1).

Fractography of CCGR specimens

The CCGR specimens selected for detailed fractographic study are listed in Table 2. Important test variables, which have or might have an influence on the observed crack growth rate and consequently also on the micromechnism of cracking are also listed. These include waveform, frequency, load ratio, dissolved oxygen content and sulfur content of steel, the latter was measured spectroscopically close to the fracture

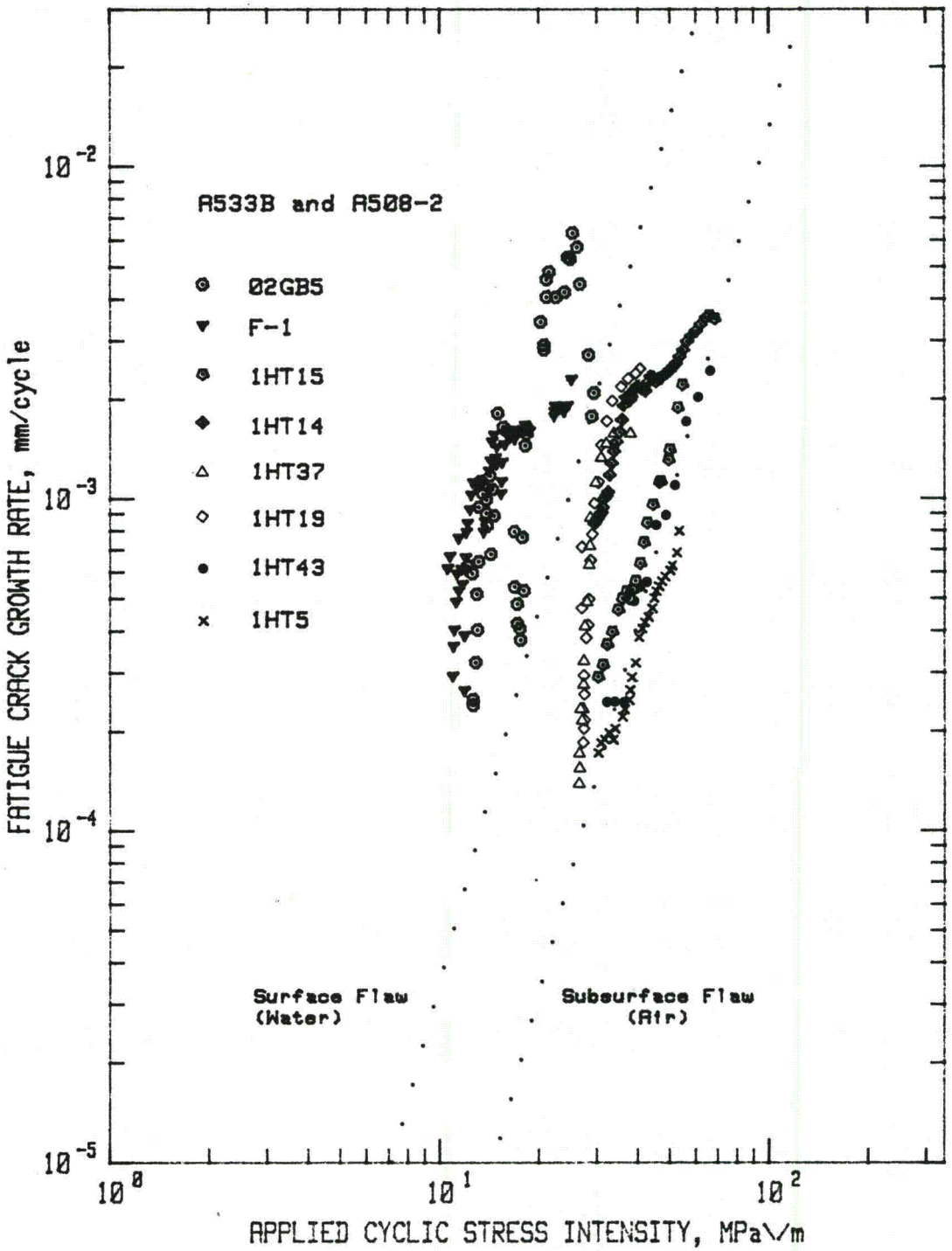

Fig. 1. The observed cyclic crack growth rates as a function of the applied cyclic stress intensity range for specimens used for detailed fractographic analysis. See Table 2 for test parameters.

surface. The observed cyclic crack growth rates as a function of the applied stress intensity range are given in Fig. 1.

The most thorough fractographic analysis was made for specimens 1HT37, -14 and -19, all showing roughly the same environmental acceleration of cyclic crack growth. However, the reported bulk dissolved oxygen contents in these tests varied from PWR to BWR conditions as indicated in Table 2. The fractographic analysis indicated only slight differences between these three specimens. The macroscopic features of the fracture surfaces are shown schematically in Fig. 2. A fairly dense distribution of elongated manganese sulfide inclusions are evident whenever the fracture mode has brittle features. The inclusion distribution is shown also in Fig. 3, which is a sulfur print of two specimens, taken from a polished surface parallel and close to the fracture surface. A typical feature was that a group of inclusions had generated brittle mode of crack growth, which spred over the remaining part of the fracture path. Especially in specimen 1HT37, this was evident. Three macroscopic brittle fracture mode areas were seen like fans; between these areas as well as on both sides typical ductile striations could be seen throughout the fracture path. Considerably smaller amount of inclusions was found in these ductile areas. However, some brittle features were also seen on the fracture surface connected to those inclusions (see Fig. 8).

The inclusions have been dissolved during the testing leaving only empty sites. A typical brittle fracture surface with inclusion sites can be seen in Fig. 4. A detail of the brittle fracture surface showing brittle striations is shown in Fig. 5 together with a typical ductile area. Brittle surfaces without any striations were also seen, although only occasionally, and mainly connected to the maximum environmental acceleration of

Table 2 Test parameters

Specimen code	wave form	frequency	load ratio	O_2	S
02GB5	sine	8 mHz	0.7	0-5 ppb	0.012%
F-1	sine	17 mHz	0.7	n.a.	0.010%
1HT37	sine	17 mHz	0.2	0 ppb	0.014%
1HT14	sine	17 mHz	0.2	8-100 ppb	0.012%
1HT19	sine	17 mHz	0.2	200 ppb	0.014%
1HT15	triangle	17 mHz	0.2	≤10 ppb	0.017%
1HT43	triangle	1 Hz	0.2	≤10 ppb	0.015%
1 HT5	sine	1 Hz	0.2	100-260 ppb	0.015%

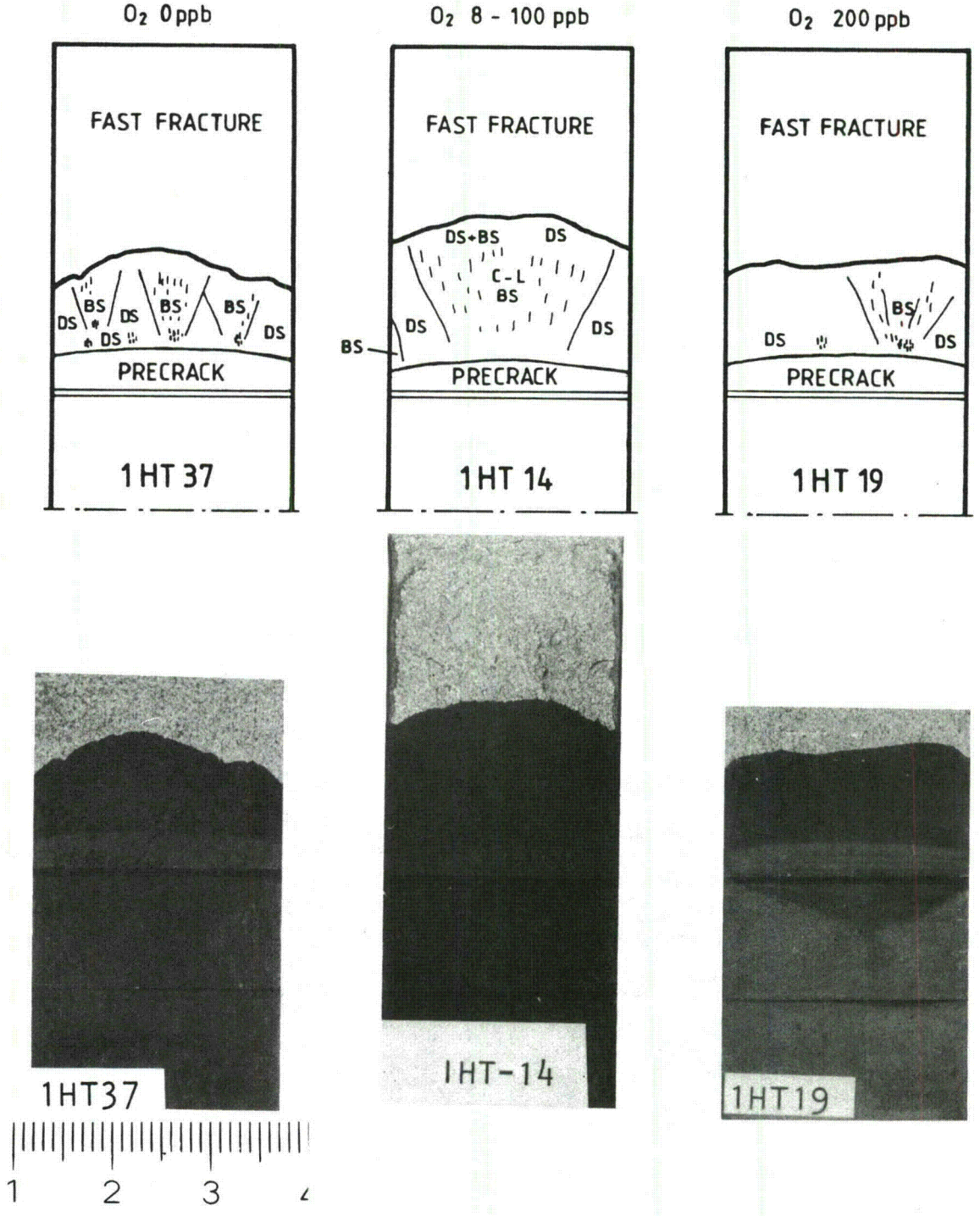

Fig. 2. Schematic illustration of the macroscopic features of the fracture surfaces of specimens 1HT37, 1HT14 and 1HT19 and corresponding macrophotographs. DS = ductile striation, BS = brittle striations, C-L = cleavage-like, elongated dots = inclusions.

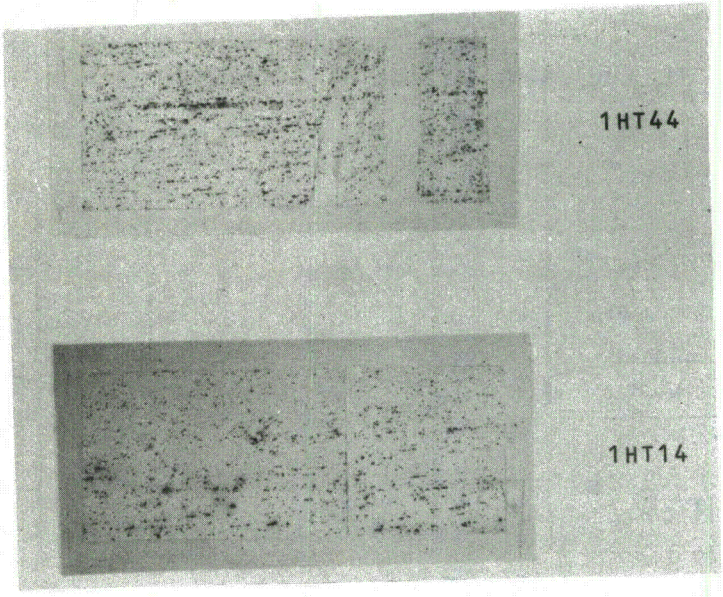

Fig. 3. Sulfur prints of specimens 1HT14 and 1HT44.

Fig.4. Brittle fracture surface with inclusion sites. Specimen 1HT14, ΔK = 34 MPa$\sqrt{m}$.

crack growth. An example is shown in Fig. 6. The clear correspondence between the brittle cyclic crack growth region and the true quasi-cleavage area can be seen in Fig. 7. Brittle striations are like superposed on the cleavage-planes.

The general sequence of fracture mode as a function of ΔK is indicated in Fig. 9. In the first part of the test the fracture propagation remains generally ductile. In the second part of the test when the environmentally assisted crack growth acceleration is seen, the striations become brittle and the amount of microcracks decreases. In the third part, which is not, however, always seen, the crack propagates along cleavage-like planes without any striations and microcracks. In the last part of the test a bend-over towards the ASME Section XI air default line occurs and features typical to the second region (i.e. brittle striations) reappear. Sometimes also ductile striations can be seen. Macrobranching is also often connected to the bend-over region.

The test may start also directly with brittle striations as was evident for specimen 1HT14 (see Fig. 10). Thus connection of the brittle fracture mode to inclusions is not always a necessity. Usually, however, a ductile fracture area preceeds the brittle fracture phase.

When the wave shape is changed from sinusoidal to triangle while keeping other test parameters the same, no or very slight environmental acceleration was seen (specimens 1HT15 and 1HT18). Consequently, the fracture surface in the studied specimen 1HT15 consisted ductile striations throughout (see Fig. 11), and only few inclusions could be seen.

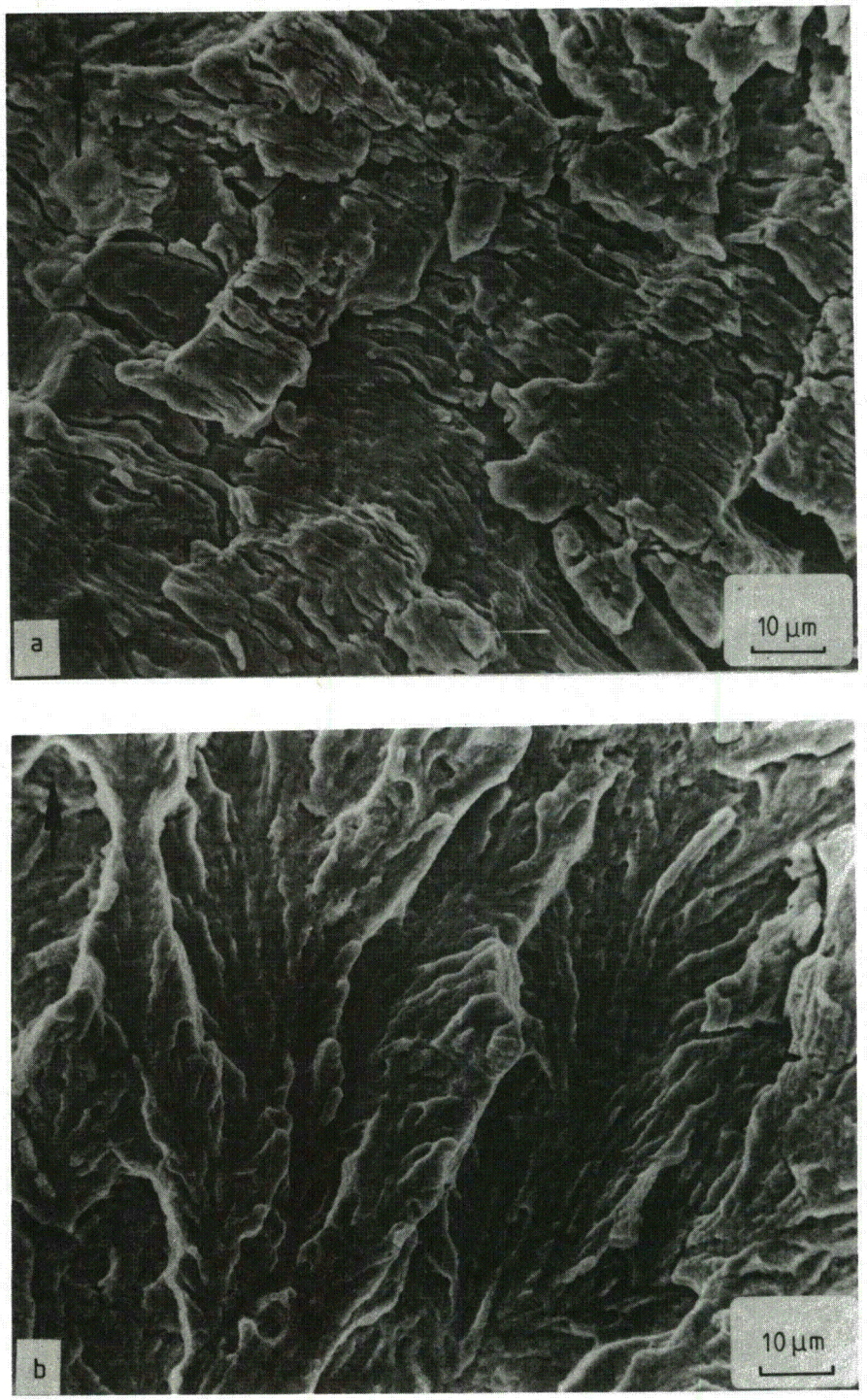

Fig. 5. Ductile (a) and brittle (b) striations in specimen 1HT14 at ΔK-level of 48 MPa$\sqrt{m}$.

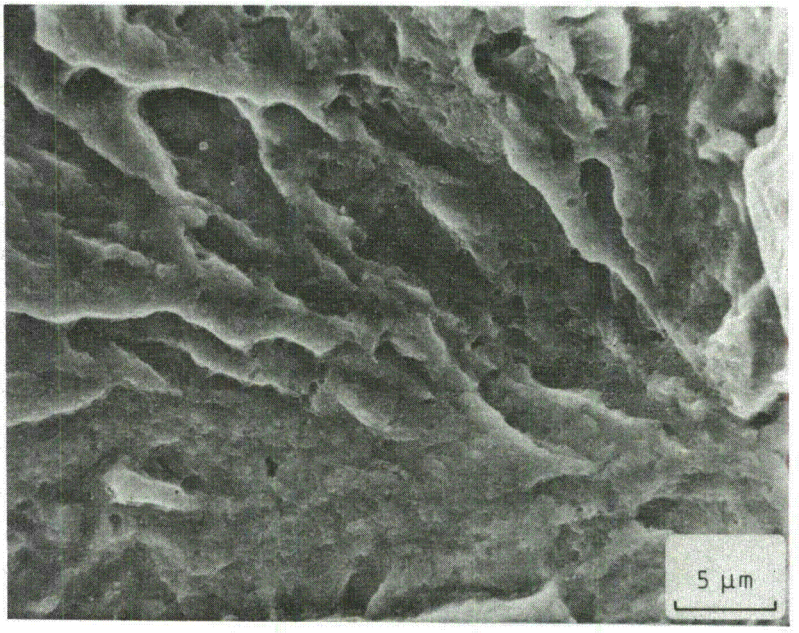

Fig. 6. Cleavage-like fracture surface; no striations can be seen. Specimen 1HT37, ΔK = 38 MPa$\sqrt{m}$.

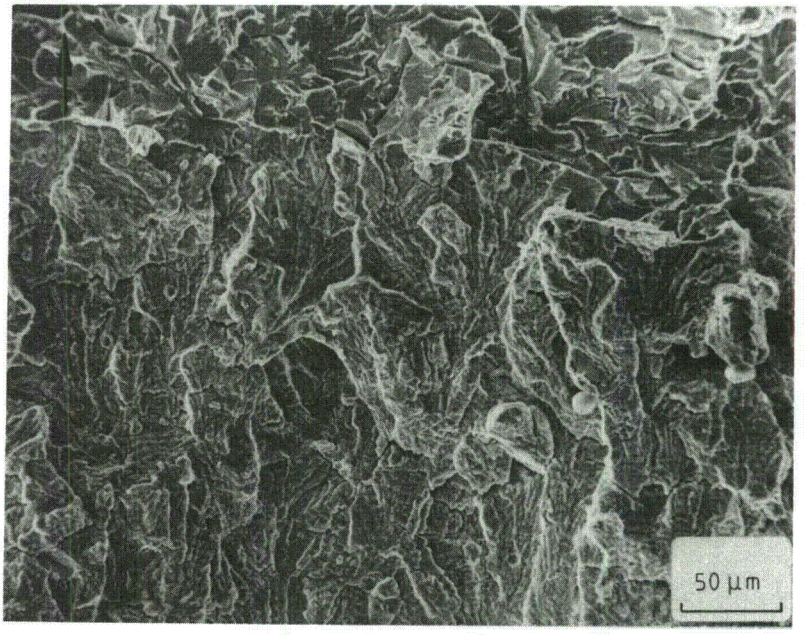

Fig. 7. Brittle striations and quasi-cleavage fracture, obtained after test termination at liquid nitrogen temperature. Specimen 1HT19, ΔK = 46 MPa$\sqrt{m}$.

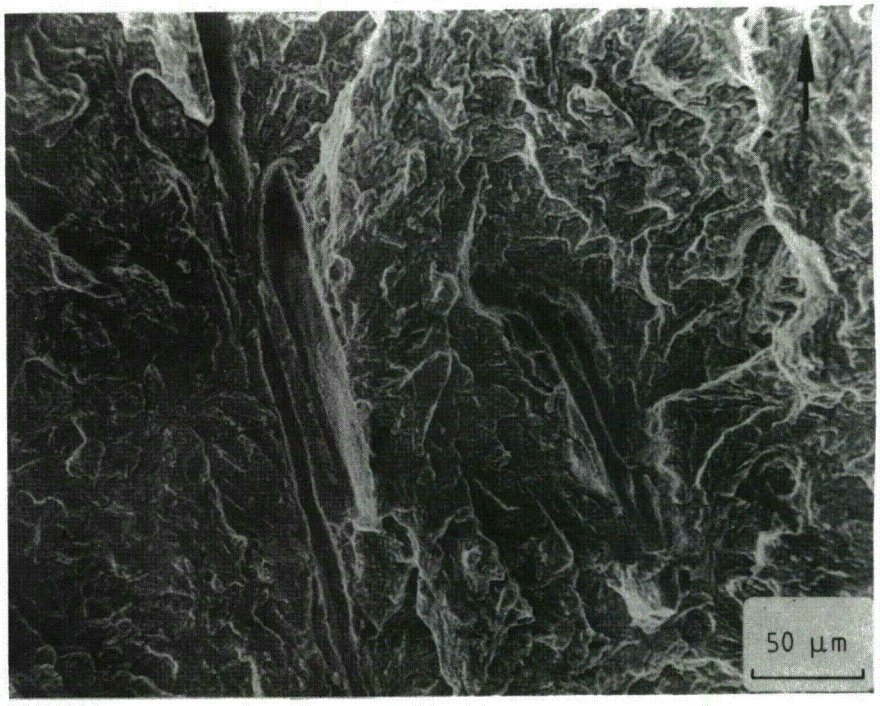

Fig. 8. Brittle features connected to the inclusions in otherwise ductile fracture area. Specimen 1HT14, ΔK = 37 MPa$\sqrt{m}$.

An increase of the frequency to 1 Hz had a similar effect than changing from sinewave to triangle wave shape. No environmental acceleration occurred and only ductile striations were seen. However, around the few inclusions on the fracture surface and independent of the bulk oxygen content, brittle areas could be seen (Fig. 12).

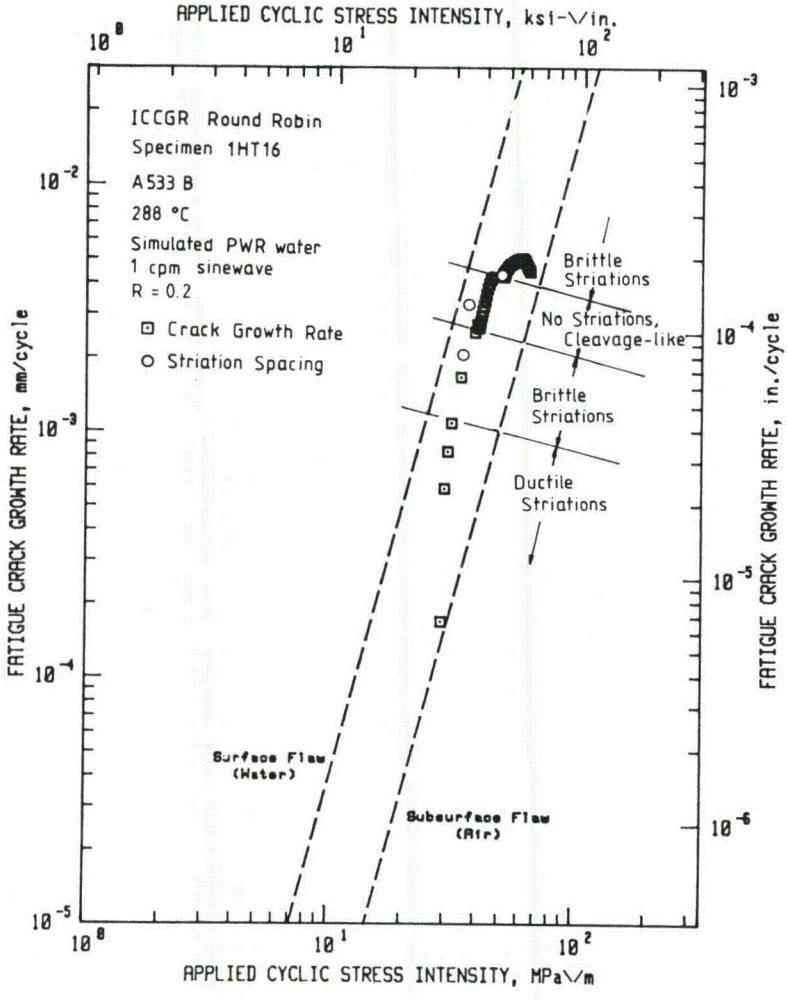

Fig. 9. Location of the four fractographically different crack growth areas as compared to the da/dN-ΔK curve. Specimen 1HT16.

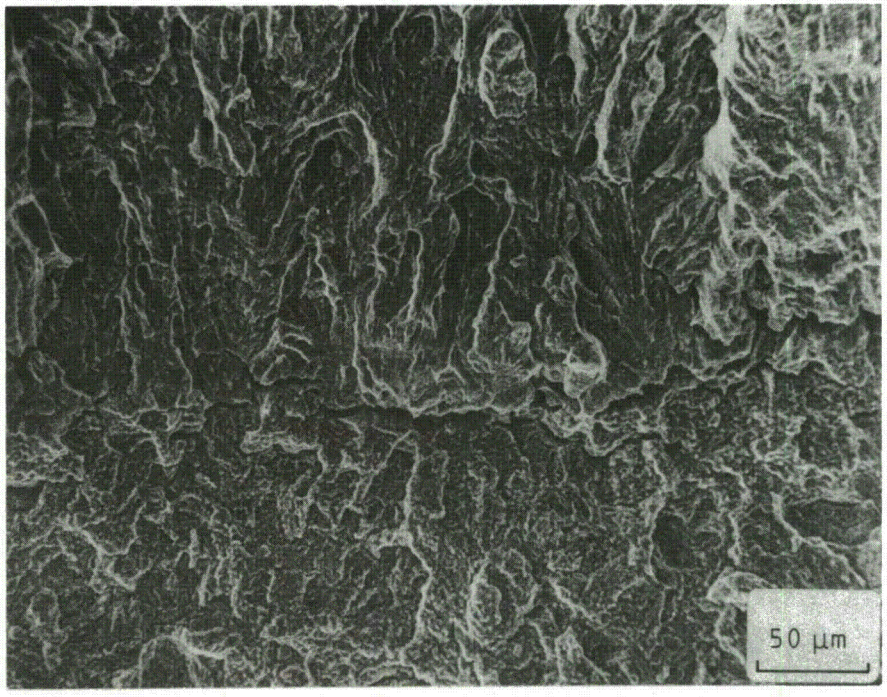

Fig. 10. Borderline between precrack area and actual testing. Note how the fracture mode is brittle from the beginning of the test.

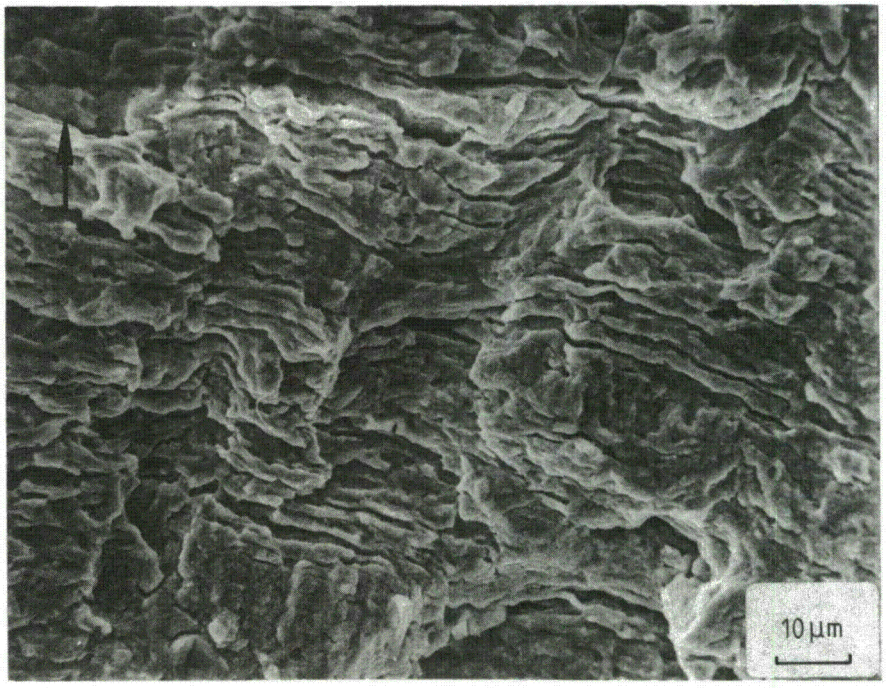

Fig. 11. Typical ductile striations in specimen 1HT15 (ΔK = 42 MPa$\sqrt{m}$).

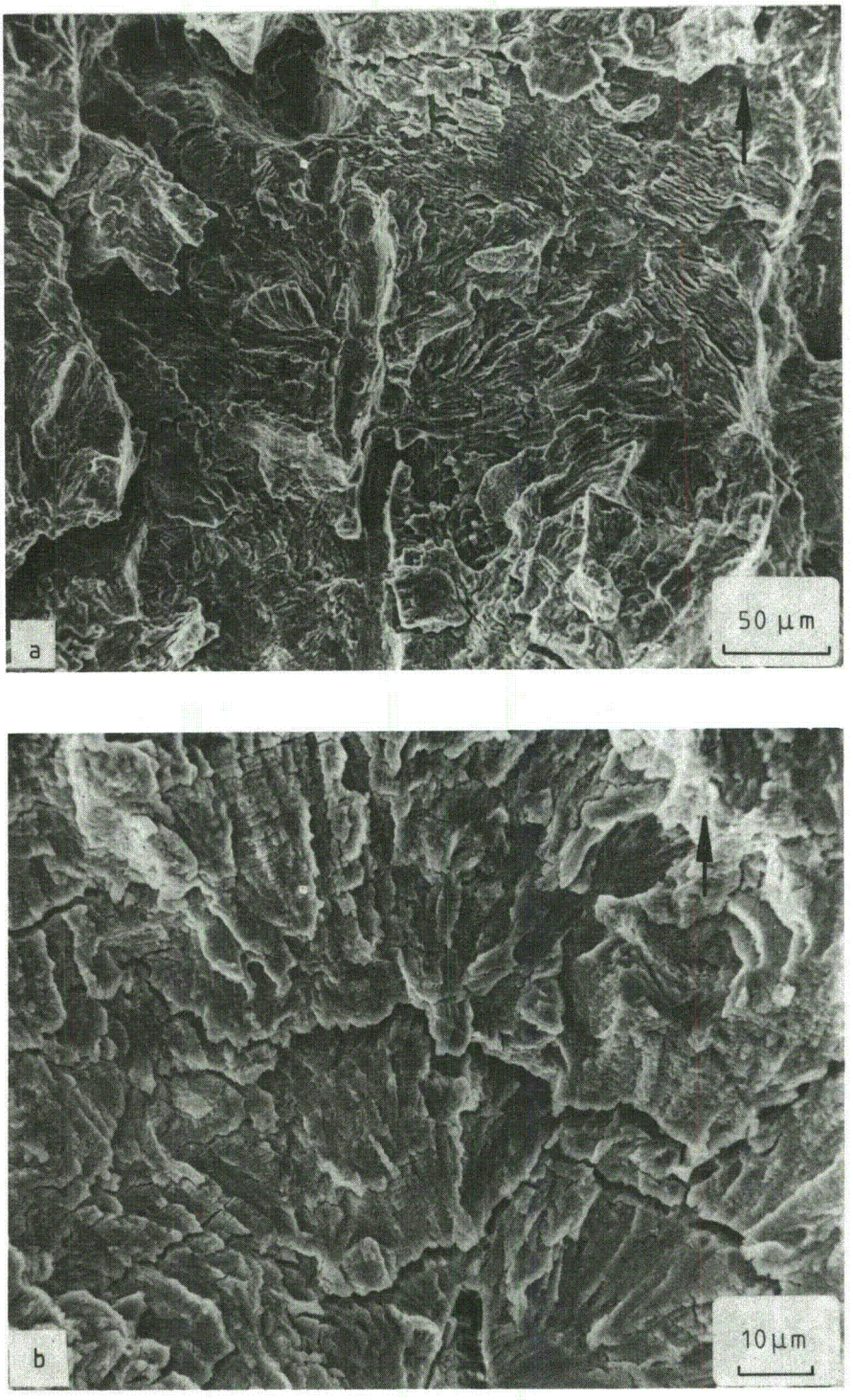

Fig. 12. Brittle fracture area around the inclusions in specimens 1HT5 (a) and 1HT43 (b). ΔK roughly 50 MPa$\sqrt{m}$ and 38 MPa$\sqrt{m}$, respectively.

To evaluate the load ratio effect two Westinghouse specimens tested with R = 0.7 were analysed fractographically. The specimens were, however, rather badly corroded, which made the analysis difficult. Often it was difficult the discern whether the striations were ductile or brittle. However, basing the analysis on the other features of the fracture surface, it was concluded, that in case of specimen F-1 the entire fracture surface was covered by brittle striations (only 1/3 of the fracture surface was available) (Fig. 13a). Specimen 02GB5 was little less corroded which facilitated the conclusion, that also in this case the fracture surface was mostly composed of brittle striations (Fig. 13b). However, cleavage-like areas without any striations were also seen, Fig. 14.

Fractography of hydrogen charged and SSRT specimens

In thin tensile specimens the cracking mode after hydrogen charging was generally ductile but the manganese sulfide inclusions where always surrounded by hydrogen-induced brittle fracture areas, Fig. 15. Also other inclusions were found to induce similar cracking but not to that extent as manganese sulfides.

In SSR-tested and simultaneously hydrogen charged specimens, the inclusions caused cracking throughout the specimen, Fig. 16(a). There were also cracks, which initiated directly from surface without any clear connection to inclusions.

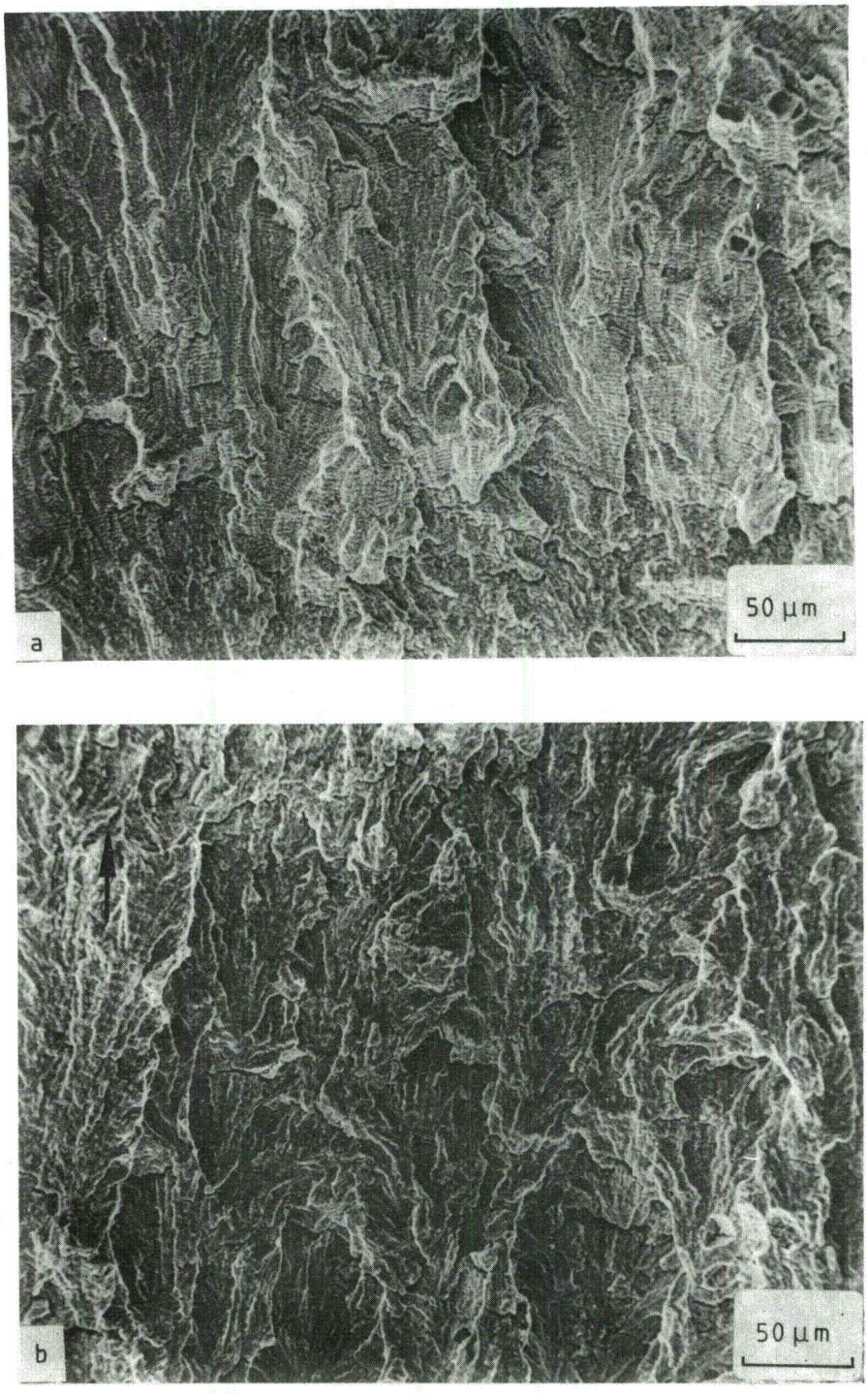

Fig. 13. Brittle striations in specimens F-1 (a) and 02GB5 (b).

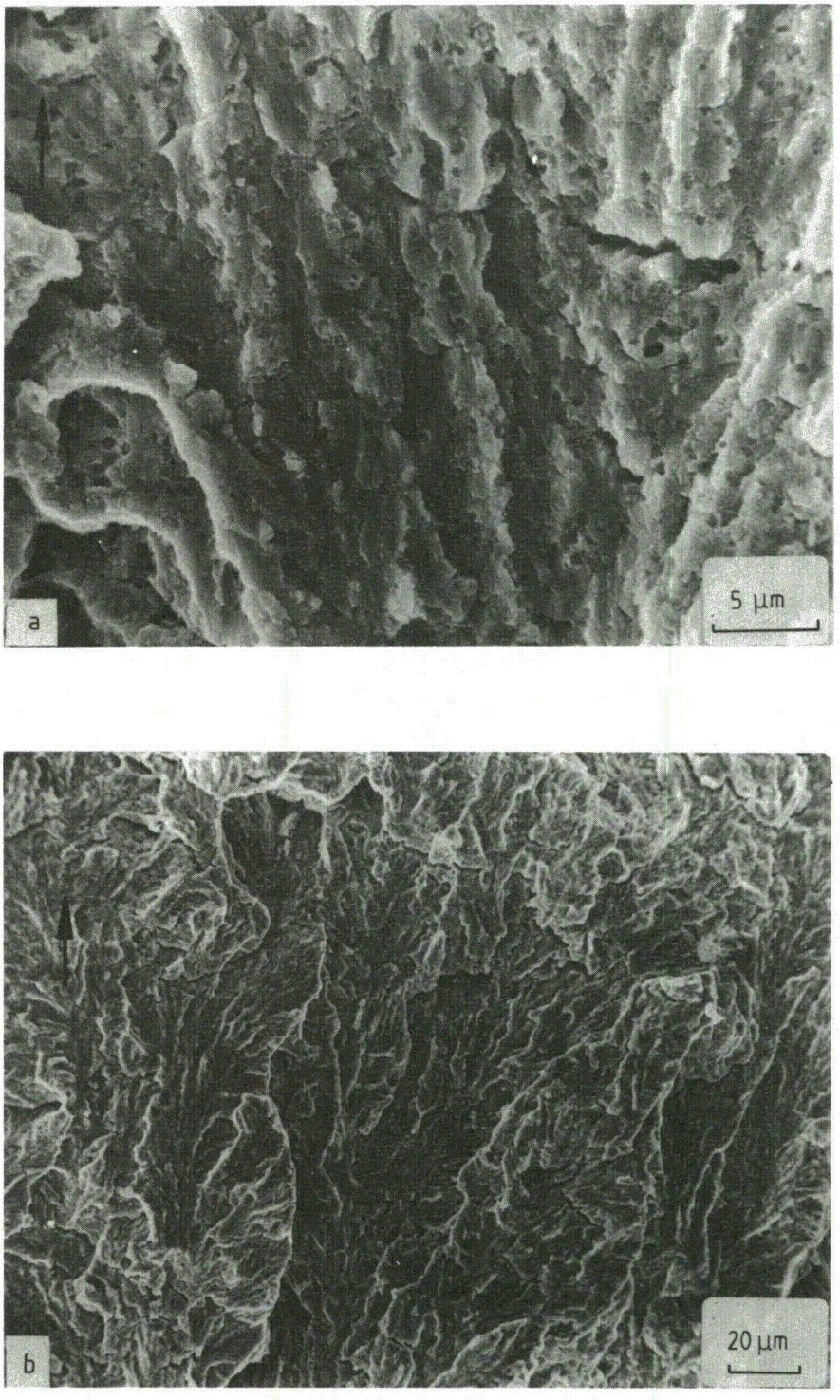

Fig. 14. Cleavage-like features without striations in specimen 02GB5.

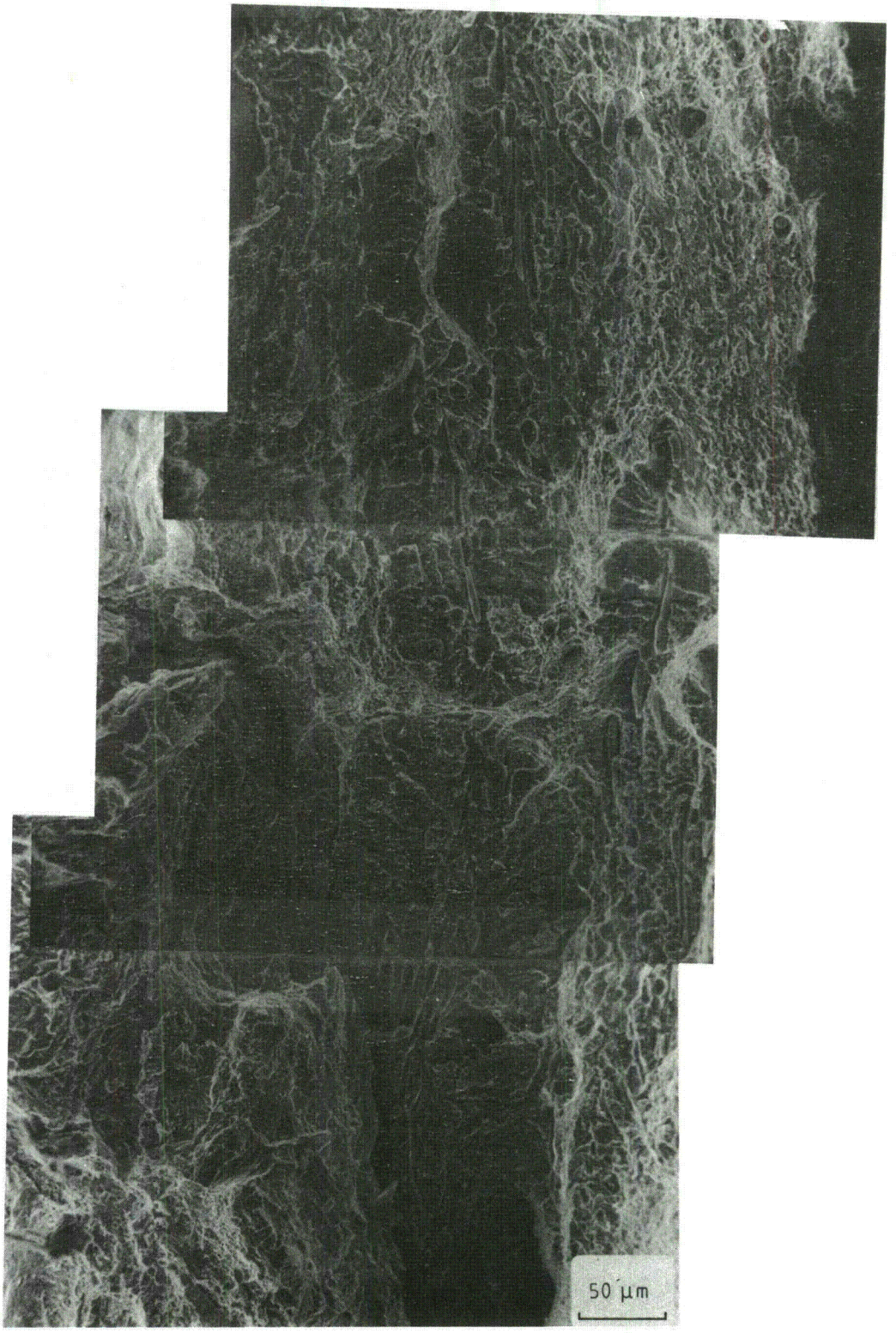

Fig. 15. Part of the fracture surface of hydrogen charged thin tensile specimen of A508 Gl.2 steel. Note the hydrogen-induced brittle cracking surrounding the manganese sulfide inclusions.

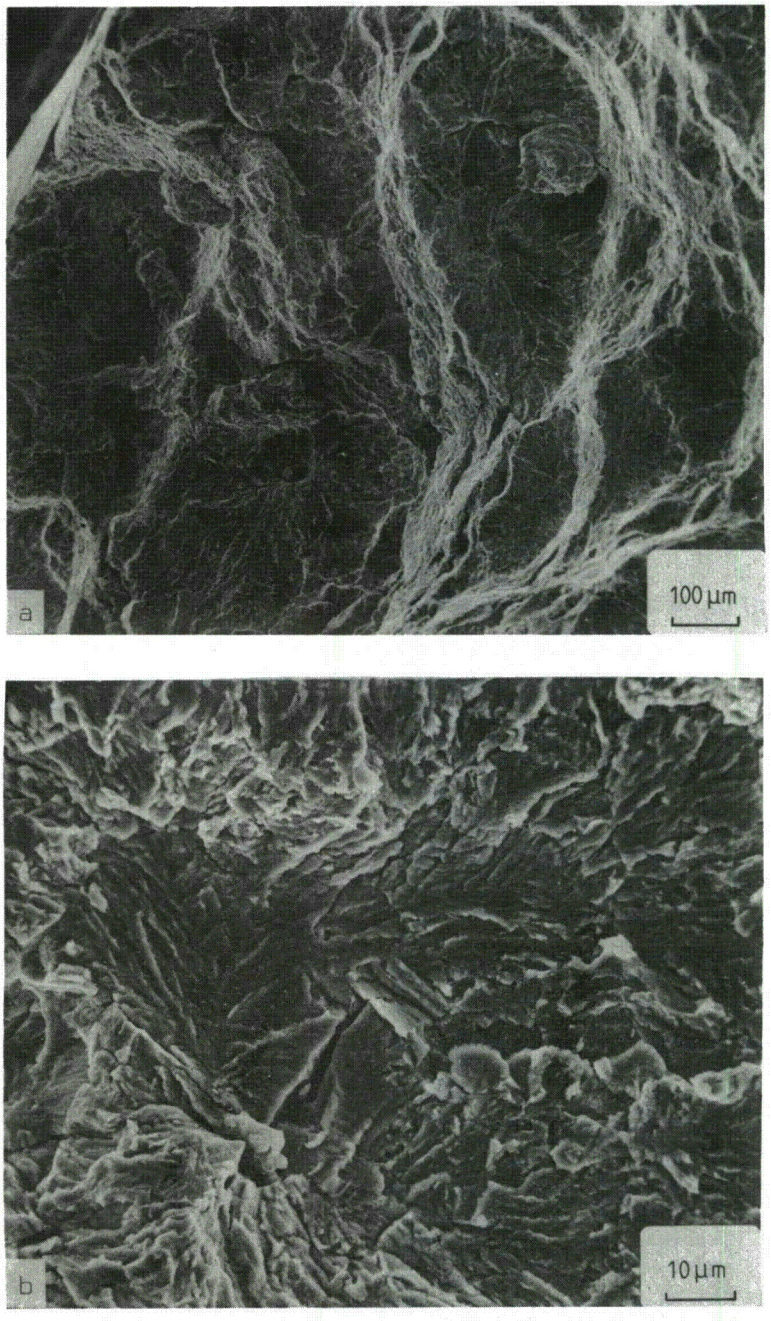

Fig. 16. Hydrogen-induced cracking in SSR-tested A533B-1 steel specimen. (a) a general view of the fracture surface. (b) a detail of the hydrogen-induced fracture surface around an inclusion.

A detail of the fracture surface near an inclusion is shown in Fig. 16(b). Hydrogen induced cracking produces a brittle fracture surface which resembles the mechanical cleavage cracking of this steel in liquid nitrogen temperature, Fig. 17.

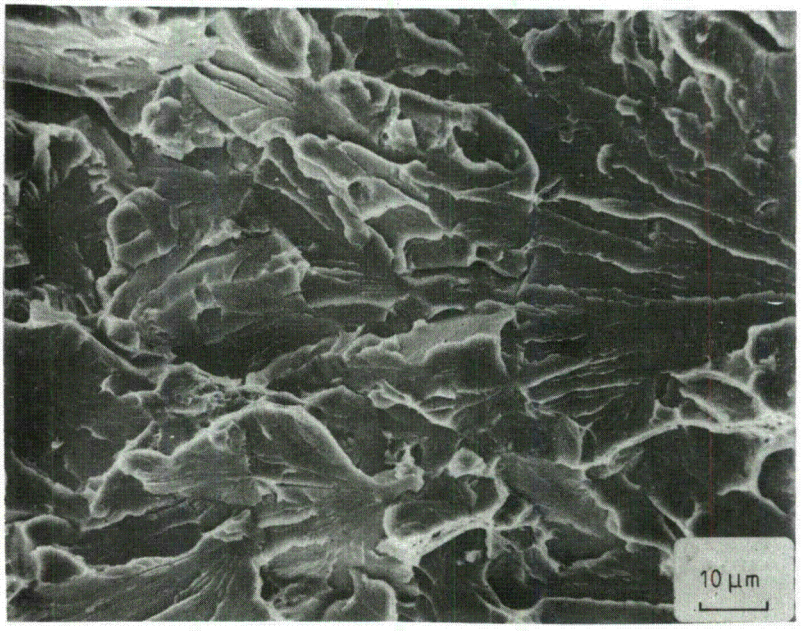

Fig. 17. Cleavage fracture of A533 B-1 steel at liquid nitrogen temperature.

The sign-changing polarization technique produced in SRR-test cracks initiating from the surface of the specimens. In Fig. 18 fracture morphology of A533 B-1 steel can be seen after this test. Fig. 18(a) shows a crack which has initiated from the surface. During propagation no connection to inclusions was observed. Fracture details (Fig. 18(b)) are similar to hydrogen charged specimens as was expected due to cathodic polarization. The fracture time was, however, markedly longer in this case. When the ductile fracture surface area was examined, the hydrogen induced cracks connected to inclusions were found even in the middle of the specimen, Fig. 18(c); small hydrogen induced crack is surrounding a small manganese sulfide inclusion.

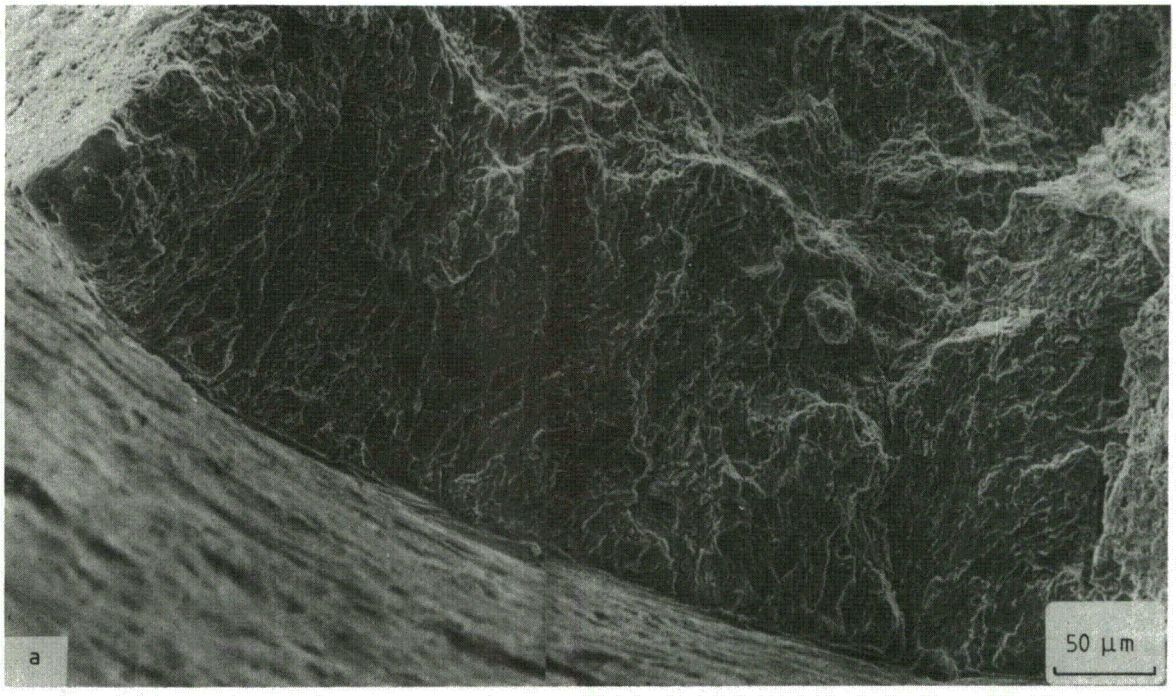

Fig. 18. Fracture morphology of A533 B-1 steel after SSR-test where sign-changing polarization technique was employed. (a) a crack started from the specimen surface. (b) detail of the fracture surface. (c) a small hydrogen induced crack in the middle of the specimen far in front of the surface cracks.

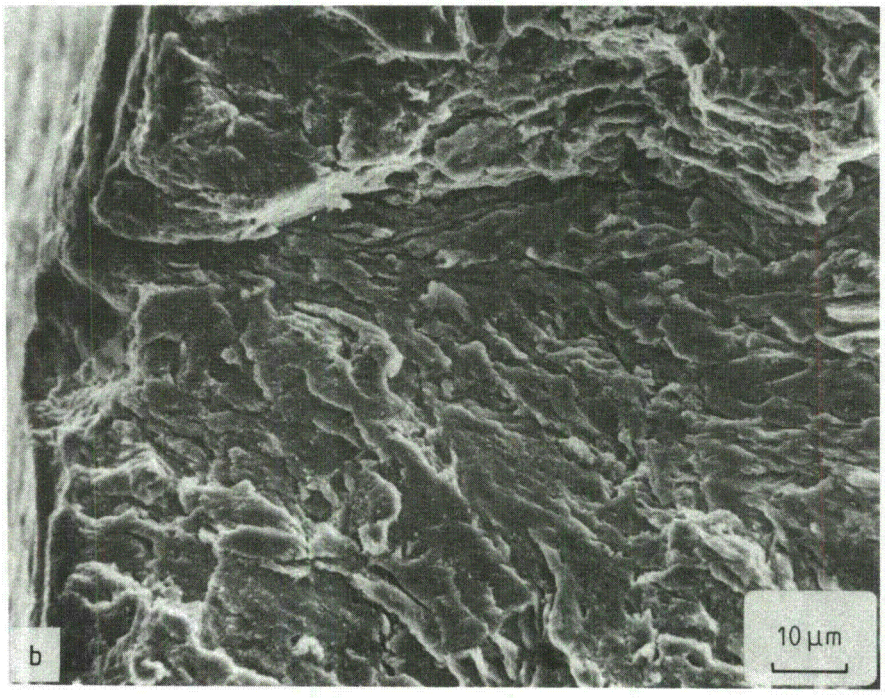

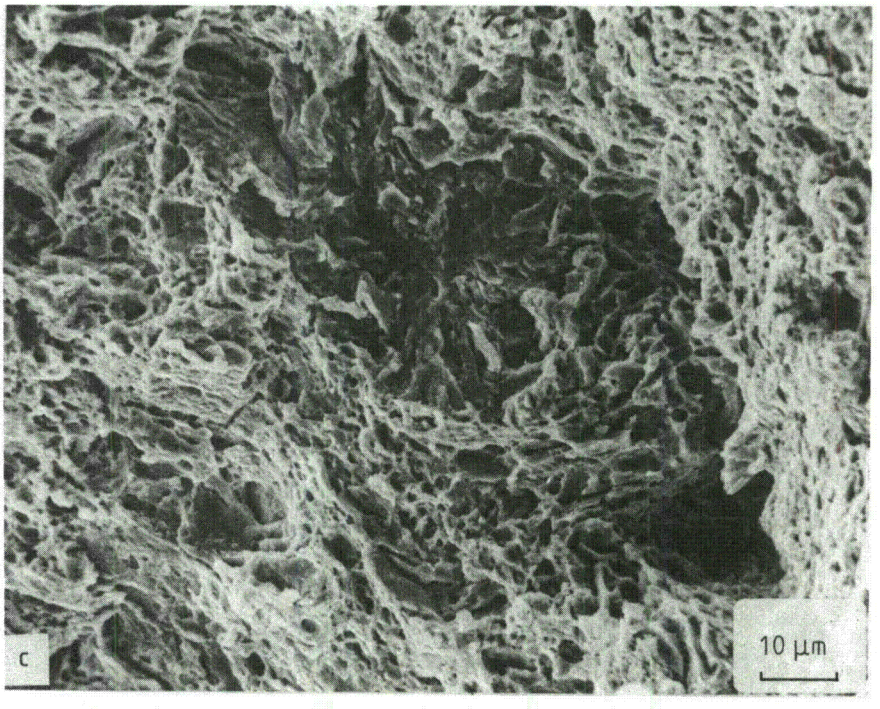

Fig. 18. Continued.

MECHANISM OF ENVIRONMENTALLY ACCELERATED CRACK GROWTH

Two basic mechanisms, dissolution-controlled and hydrogen-induced, have generally been proposed to explain environmentally enhanced crack growth in simulated PWR and BWR environments (2 - 7). In the former process the crack propagation is controlled by anodic dissolution of the metal at the crack tip, whereas in the latter process the mechanical separation at the crack tip is facilitated by hydrogen embrittlement. Both favoured mechanisms for crack propagation depend on the same rate-determining parameters, which makes it difficult to differentiate experimentally between these mechanisms (18). The authors favour the latter mechanism as the main crack propagation mechanism. Our opinion is based primarily on the fractographic evidence published earlier (6, 7, 19 - 23) and found during this work.

In this study further evidences have been presented of the similarities in fractography between hydrogen embrittlement (HE), corrosion fatigue (CF) as well as stress corrosion cracking (SCC) under cathodic polarization. The most important common factors supporting hydrogen-induced crack propagation mechanism in CF are brittle fracture surface morphology (brittle striations and cleavage-like fracture) and the role of manganese sulfide inclusions which as hydrogen traps seem to localize cracking to themselves and through subsequent dissolution to change crack tip electro-chemistry further conducive to hydrogen absorption.

In aqueous environments, the electrochemical conditions at the crack tip during both sustained and low frequency cyclic loading have been shown to differ from the bulk electrochemistry. Under a free corrosion potential, the pH-value established in the crack upon corrosion of steel is due to the hydrolysis of metallic ions (23, 24). For crack propagation from initial corrosion

crevices the maintenance of the acidified media at the crack tip is a necessary condition and occurs by continuous hydrolysis. Scully (25) has presented possible consequences of the relationship between crack tip strain rate and repassivation rate in order to have self-sustaining conditions at the crack tip. If the hydrolysis reaction cannot be maintained, the crack tip will repassivate completely and simultaneously the pH-value of the crack tip solution will start to rise towards that of the bulk solution and for the same reason the anion concentration at the crack tip will start to fall towards that of the bulk solution. The cathodic polarization is another process to cause deacidification. In CF of pressure vessel steels the dissolution of manganese sulfide inclusions likely have a marked effect on the crack tip electrochemistry. The drop of pH-value in O_2-containing pure high temperature water conditions would otherwise be limited by reduction of hydrogen ions inside the crack (26).

The crack propagation rate and CF fracture surface morphology do not markedly vary regardless of the bulk dissolved oxygen content. In O_2-containing high temperature water the anodic corrosion process inside the crevice is partly balanced by the reduction of oxygen outside the crevice, but the hydrogen ion reduction reaction is important inside the crevice in crack tip conditions. In O_2-containing water, the restricted access of oxygen into the crevice, displaces the potential inside the crevice to the negative side in deoxygenated small volume of water at the crack tip. In the absence of dissolved oxygen, the cathodic reaction is the reduction of hydrogen, which can then enter the metal. When dissolved oxygen is present in the bulk water, another cathodic reaction can occur on the external surface, i.e. the reduction of oxygen to hydroxyl ions. This reaction cannot occur, or occurs to a lesser degree, near the crack tip, where the solution is nearly, or totally deoxygenated. Because of similar

crack tip conditions no marked differences can be expected in CF mechanism in low or high O_2-containing water.

Hydrogen absorption occurs only during rise time of the fatigue cycles as bare metal surface at the advancing crack tip is exposed to the environment. This is evident as introduction of any length of hold time at peak load does not increase the environmental acceleration of crack growth rate. On the contrary, a retardation is sometimes seen. The oxide layers at the crack tip increase the hydrogen overvoltage and prevent penetration of hydrogen into the steel. Once the hydrogen has entered the metal, it diffuses along the stress gradient towards the region of high triaxial stress just ahead of the crack tip. The bulk diffusion rate at the elevated temperatures in question is high enough to allow, within seconds, an excess concentration of hydrogen in the plastic enclave (27). The presence of hydrogen in the plastic enclave introduces a microscopic embrittling effect and a subsequent increase in cyclic crack growth rate. So far up to nine different mechanisms have been proposed for hydrogen assisted cracking at the atomistic or lattice level (28). At the present time no preference for a particular one of the various models can be expressed. As stated in a recent review (28), it is possible that several of the proposed mechanisms may contribute to the overall cracking process.

The hydrogen induced cracking mechanism is outlined in Fig. 19, without taking into account the effect of inclusions. This study has clearly shown the importance of manganese sulfide inclusions in cracking process. In HE tests the inclusions were surrounded by brittle hydrogen-induced cracks spanning several prior austenite grains. In CF similar phenomenon was observed when the CF crack spred from group of inclusions like a fan. The exact mechanism of this hydrogen trapping, crack inition

form inclusion and propagation across several grains should be clarified.

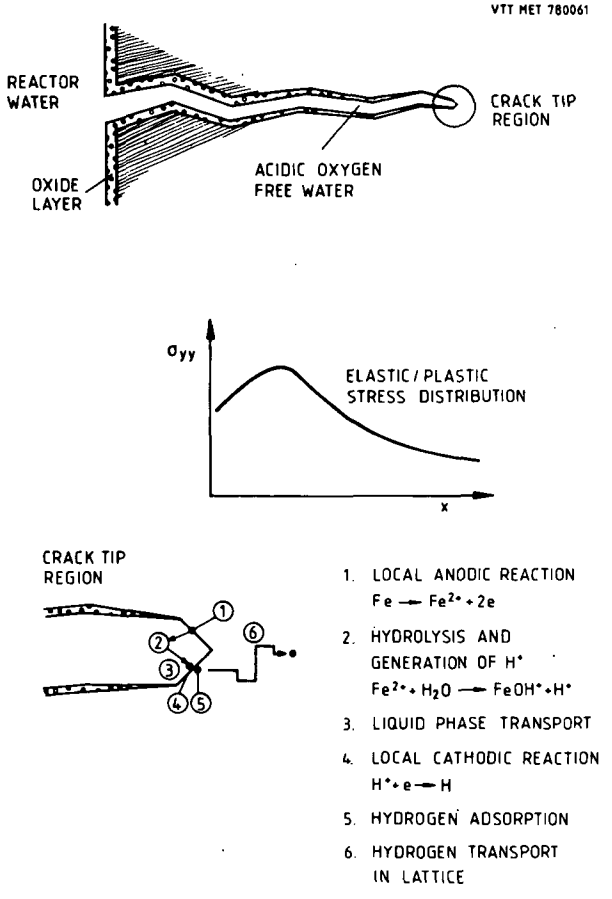

Fig. 19. Schematic illustration of hydrogen assistance during cyclic crack growth of reactor pressure vessel steels in high-temperature high-pressure reactor grade water.

Whether the environmental acceleration occurs is dependent on the frequency or loading rate, as discussed earlier. At high frequencies the interaction of the exposed metal with the environment is of no consequence, because the rate at which the metal fails by ductile fracture exceeds the rate at which the environment can affect fracture via hydrogen embrittlement. At lower frequencies, the formation of passivating film can

inhibit the entry of hydrogen at the crack tip. This film can be formed provided the rates of the anodic and cathodic reactions are sufficiently slow, as would be the case in completely deoxygenated water (PWR conditions) and provided that the crack tip straining rate is rather monotonic, as in trapezoidal load waveform testing. On the contrary, in the sinewave load testing, the continuous changes in the crack tip straining rate may prevent the passive film formation and hence facilitate the hydrogen entry and subsequent crack growth enhancement. If the frequency is lowered sufficiently, however, the film formation may occur, thus preventing the hydrogen entry. In the presence of dissolved oxygen (BWR conditions) the reaction rates may again be higher. This may facilitate pronounced hydrogen evolution even with longer ramp times, which in turn will result in the accelerated crack growth rates seen in BWR results at these frequencies.

It has been shown that in a water environment, the crack growth rate is limited by the oxidation rate of freshly exposed surface at the crack tip (29). Thus the resultant cyclic crack growth rate must be directly related to the area of the fresh surface generated during the crack advancement within one cycle. Furthermore, crack advancement is directly related to crack tip opening displacement CTOD (30), which for plain strain conditions is of the form

$$CTOD \cong 0.5 \frac{1}{\sigma_y E} (K_{max}^2 - K_{min}^2). \quad (1)$$

Inserting ΔK and load ratio R,

$$CTOD \cong 0.5 \frac{(\Delta K)^2}{\sigma_y E} \frac{1 - R^2}{(1 - R)^2} \quad (2)$$

where σ_y is the yield strength and E Young's modulus of elasticity.

Eq. 2 can be utilized for calculating the ΔK for a certain cyclic crack growth rate and R-ratio. Thus, the modified Paris equation for the accelerating part of the environmentally assisted cyclic crack growth is as follows:

$$\frac{da}{dN} = C\ (\Delta K)^m\ \left(\frac{\sqrt{1 - R^2}}{1 - R}\right)^m \qquad (3)$$

The expressions fit well with the observed data and thus explain the observed effect of load ratio.

A decrease in the environmental influence starts when a certain frequency- or loading rate-dependent cyclic crack growth rate is exceeded. The higher the test frequency, the lower the value of the crack growth rate at which the data bends over, which indicates a crack velocity dependence. As the growth rate accelerates due to hydrogen embrittlement, it eventually reaches a velocity where the rate-limiting surface reaction does not allow sufficient amount of hydrogen to be generated at the triaxial stress state region. The crack growth rate then slows down to a rate determined by the rate of hydrogen accumulation, becoming only weakly dependent on ΔK (6). Testing at a slower frequency allows more hydrogen to accumulate per cycle, and thus a faster crack growth rate.

CONCLUSIONS

1 Fractography of CF, HE and SCC under cathodic polarization shows similar features of cracking: brittle cleavage-like cracking morphology and connection of cracking into manganese sulfide inclusions.

2 Manganese sulfide inclusions localize hydrogen-induced cracking through hydrogen trapping around them. In high temperature water

conditions the dissolution of inclusions produces at crack tip electrochemical conditions conducive for enhanced hydrogen absorption. This is observed as brittle fan-shaped fracture surface areas originating from group of inclusions.

3 Hydrogen-induced cracking in CF may occur also in the absence of manganese sulfides.

4 Hydrogen-induced brittle cracking is mainly observed in the middle of the specimens where crevice chemistry conditions are established.

5 The O_2-content of the bulk-water does not have any marked effect on crack propagation rate or fractography under similar testing parameters which also supports the importance of crevice chemistry inside the crack.

6 The effect of such testing parameters like frequency, wave form, and load ratio on the observed cyclic crack growth rate can be explained by the hydrogen-induced cracking model.

ACKNOWLEDGEMENTS

This research was sponsored partly by the Ministry of Trade and Industry in Finland (K.T and H.H.) and the Reactor Safety Research Division of the U.S. Nuclear Regulatory Commission (W.H.C.). The continuous support of the agencies is appreciated. We like to express our sincere gratitude to Mr. Markku Kemppainen for conducting the fractographic work.

REFERENCES

|1| Cullen, W.H. and Törrönen, K., A Review of Fatigue Crack Growth of Pressure Vessel and Piping Steels in High-Temperature, Pressurized Reactor Grade Water,

NUREG/CR-1576, NRL Memorandum Report 4298, Naval Research Laboratory, Washington, D.C., March 1980.

|2| Atkinson, J.D. and Lindley, T.C., in The Influence of Environment on Fatigue, Institution of Mechanical Engineers, London, 1977, pp. 65-74.

|3| Atkinson, J.D. and Lindley, T.C., Metal Science, Vol. 13, No. 7, 1979, pp. 444-448.

|4| Tomkins, B., Metal Science, Vol. 13, No. 7, 1979, pp. 387-395.

|5| Cullen, W.H., Provenzano, V., Törrönen, K.J., Watson, H.E and Loss, F.J., Fatigue Crack Growth of A508 Steel in High-Temperature, Pressurized Reactor Grade Water, NUREG/CR-0969, NRL Memorandum Report 4063, Naval Research Laboratory, Washington, D.C., Sept. 1979.

|6| Bamford, W.H. and Moon, D.M., Corrosion, Vol. 36, No. 6, 1980, pp. 289-298.

|7| Johnson, R., McMinn, A. and Tomkins, B., in ICM3, Vol. 2, ed. K.J. Miller and R.F. Smith, Pergamon Press, Oxford, 1980, pp. 371-382.

|8| Hale, D.A., Kass, J.N. and Jewett, C., in BWR Environmental Cracking Margins for Carbon Steel Piping, First Semi-annual Progress Report, July 1978 to December 1978, NEDC-24625 (1979).

|9| Bamford, W.H., Trans. ASME, Series H, J. Engineering Materials and Technology, Vol. 101, No. 2, 1979, pp. 182-190.

|10| Kondo, T., Kikuyama, H., Nakajima, H., Shindo, M. and Nagasaki, R., in Corrosion Fatigue: Chemistry, Mechanics and Microstructure, NACE-2, eds. O.

Devereux et al., National Association of Corrosion Engineers, Houston, TX 77027, pp. 539-556 (1973).

|11| Suzuki, M., Takahashi, H., Shoji, T., Kondo, T. and Nakajima, H., in The Influence of Environment on Fatigue, Institution of Mechanical Engineers, London, pp. 161-169 (1977).

|12| Bamford, W.H. and Ceschini, L.J., in Structural Integrity of Water Reactor Pressure Boundary Components, Quarterly Progress Report, April-June, 1980, ed. F.J. Loss, NUREG/CR 1783, NRL Memorandum Report 4500, Naval Research Laboratory, Washington, D.C. 20375.

|13| Cullen, W.H., Watson, H.E., Taylor, R.E. and Törrönen, K. in Effects of Radiation on Materials, a forthcoming STP, American Society for Testing and Materials, Philadelphia, 1980.

|14| Cullen, W.H., Watson, H.E., Taylor, R.E. and Loss, F.J., J. Nuclear Materials, Vol. 96, 1981, pp. 261-268.

|15| Jones, R.L., Cyclic Crack Growth in High-Temperature Water: Results of a Testing Round Robin, This meeting.

|16| Rosenfeld, I.L. Krasnorutskaya, I.B., Konradi, M.V. and Spiridonov, V.V., 1978: Met. Prog. Vol. 14 No. 2, pp. 101-106.

|17| Yuzawich, P.M. and C.W. Hughes, Practical Metallography, Vol. 15, 1978, pp. 184-195.

|18| Ford, F.P., in ICM3, Vol. 2, ed. K.J. Miller and R.F. Smith. Pergamon Press, Oxford, 1980, pp. 431-444.

|19| Cullen, W.H. Watson, H.E, Törrönen, K.J., Provenzano, V., Loss, F.J. and Gabetta, G., in Structural Integrity of Water Reactor Pressure Boundary Components, ed., F.J. Loss, NUREG/CR-0943, NRL Memorandum Report 4064, Sept. 1979, pp. 43-54.

|20| Cullen W.H., Watson, H.E. and Provenzano, V., in Structural Integrity of Water Reactor Pressure Boundary Components, ed., F.J. Loss, NUREG/CR 1128, NRL Memorandum Report 4122, Dec. 1979, pp. 43-81.

|21| Cullen, W.H., Watson H.E., Törrönen, K. and Provenzano, V., in Structural Integrity of Water Reactor Pressure Boundary Components, ed., F.J. Loss, NUREG/CR 1268, NRL Memorandum Report 4174, Jan. 1980, pp. 27-36.

|22| Provenzano, V., Törrönen, K., Cullen, W.H. and Gabetta, G., in Proc. Int. Conf. on Analytical and Experimental Fracture Mechanics, Rome, 1980.

|23| Rosenfeld, I.L., in, Proc. of 5th Int. Congress on Metallic Corrosion, Tokyo, 1972, pp. 53-73.

|24| Brown, B.F., in Stress Corrosion Cracking and Hydrogen Embrittlement of Iron Base Alloys, ed. R.W. Steahle, J. Hochmann, R.D. McCright and J.E. Slater, NACE, Houston, 1977, pp. 747-750.

|25| Scully, J.C., Corrosion Science, Vol. 20, No. 8-9, 1980, pp. 997-1016.

|26| Taylor, D.F. and Silverman, M., in Corrosion/80, NACE, Houston, 1980, Paper 188.

|27| Louthan, M.R., Derrick, R.G., Donovan, J.A. and Caskey, G.R. in Effect of Hydrogen on Behavior of Materials, ed. A.W. Thompson and I.M. Bernstein, Metallurgical Society of AIME, New York, 1976, pp. 337-347.

|28| Hirth, J.P., Met. Trans., Vol. 11A, No. 6, 1980, pp. 861-890.

|29| Simmons, G.W., Pao, P.S. and Wei, R.P., Met. Trans., Vol. 9A, 1978, pp. 1147-1158.

|30| McClintock, F.A. in Fatigue Crack Propagation, ASTM STP 415, American Society for Testing and Materials, Philadelphia, 1967, pp. 170-174.

ELECTRON MICROGRAPHICAL INVESTIGATIONS OF A CORROSION FATIGUE FRACTURE SURFACE DEVELOPED UNDER PRESSURE WATER REACTOR CONDITIONS

Blind, D., Sturm, D. and Trunk, H. [1)]

1. Introduction

The present MPA-contribution is related to a test series performed in the Naval Research Laboratory (NRL) Washington DC (USA) with 2T-WOL-specimens /1/. The corrosion fatigue tests were carried out with ASTM A 508-2 material (similar 22 NiMoCr 3 7) in the as delivered as well as in the irradiated condition. The crack growth rates observed were found to be in accordance with the ASME-XI reference fatigue crack growth curves /2/. The crack growth mechanism is evidently hydrogen assisted /3,4/.

2. Material and Crack Growth Parameters of Corrosion Fatigue

For a metallographical and fractographical investigation in detail there was taken a specimen in the as delivered state (V 82-8). The 2T-WOL-specimen from /1/ to be examined in detail has been machined from a 15" thick forged ring in the longitudinal direction, Fig. 1, and was tested by corrosion fatigue under PWR-conditions. The chemical composition of the A 508-2 material, Table 1, as well as the mechanical properties, Table 2, are in accordance with the requirements. The specimen V 82 - 8 was precracked (roomtemperature, air) starting from the machined notch to a fatigue crack depth (fd) of 10 mm (several loading frequencies from 2 to 5 Hz), Fig. 2. Subsequently under PWR-conditions (288°C, 140 bar) the fatigue crack was enlarged to a depth of 19,5 mm (frequency 1 Hz), Fig. 3 The water chemistry was in accordance with the guidelines, Table 3. As for further crack growth from 19,5 mm up to 57 mm fatigue crack depth only the loading frequency was changed from 1 Hz to 17 mHz (1 cycle/minute), Figs. 3 and 4. The sinewave loading along the fatigue crack growth is characterized by constant load

[1)] Staatliche Materialprüfungsanstalt
Universität Stuttgart
Federal Republic of Germany

amplitude condition with a R-ratio of 0.2 .[2)]

At the beginning of the actual corrosion fatigue test from a crack depth of about 19,5 mm with a drastically reduced load frequency (1 Hz to 17 mHz) there was observed an acceleration of crack growth rate (da/dN = mm/cycle) by factor of about 7, Figs. 4 and 5. This accelerated crack growth rate was reduced by factor of about 6 within a further crack growth of 4,5 mm in contrast to the corresponding 10 % increase of ΔK. Subsequently, after a period of a very low crack growth rate there was firstly observed an overproportional acceleration of crack growth rate and secondly beginning from a crack depth (fd) of about 30 mm a monotonic correlation between da/dN and ΔK could be observed.

3. Metallographical Investigation

The polished metallographical cut I-I, Fig. 3, showed along the crack edge (fd = 0 - 57 mm) secondary cracks of different quantity and length. The angle between main crack and secondary cracks in average was about 45^{o}, Fig. 6. The grade of absence of (small) secondary cracks between crack depth 19,5 mm to 25 mm was striking. Between a crack depth of about 32 to 38 mm partially also an absence of secondary cracks could be observed. The length of secondary cracks was observed to be growing with increasing crack depth. The etched cut I-I showed a ferritic-perlitic/bainitic micro structure with normal grain size, Fig. 7. The crack path of the main crack as well as of the secondary cracks are transcrystalline. A selective corrosion attack against single components of the microstructure could not be observed. The magnetite layer - appearently independent of crack depth - had a thickness of 3 - 4 um[3)].

---

2) The fatigue crack growth rate from a depth of 57 to 86 mm was not evaluated due to the "limiting" length of the safety links which were used in the "daisy-chain"-arrangement in the autoclave.

3) The specimen remained in the autoclave under PWR-conditions for about 2 1/2 months after fatigue test has been finished.

The results of hardness tests (HV 0,015) in ferrite grains along the edge of the main crack did not show any particularities to be correlated to the crack growth "history" in a reproducible manner.

4. Microfractographical Investigation

For an investigation in detail the magnetite layer in several steps was carefully removed by the "Endox"-procedure /5/. Using this method the magnetite gets removed without altering the fracture surface in a relevant extent. The research was carried out with a 150 Å resolution SEM as follows.

Fatigue crack depth 0 - 19,5 mm

In accordance with the investigation of the metallographical cut here can be seen numerous secondary cracks in average oriented transverse to the main crack growth direction, Fig. 8 and 9. The fatigue crack surfaces generated in air (cf. Fig. 8) and in water (cf. Fig. 8) did not show significant dissimilarities.
Striations being in many cases the traces of ductile fatigue crack growth /6, 7,8/, could not be detected possibly because of the spacing in the 10^{-4} mm region and in accordance with the falsifying effect by magnetite growth on the surface. At a fatigue crack depth of 10 mm there could be seen a nearly continous secondary crack running across the whole specimen, Fig. 10. This secondary crack along the "crack stop mark" (CSM) was presumably caused by stopping the precracking in air atmosphere and restarting the fatigue loading procedure under changed conditions (1 Hz, PWR-conditions), cf. Fig. 3.

Fatigue crack depth 19,5 - 24 mm

Except some large secondary cracks there could be seen no small secondary cracks. The type of surface topography led to the assumption of predominate fatigue crack growth along of cleavage planes as "brittle" fatigue crack type /6, 7, 8/, Figs. 11 and 12. Only in a few cases there could be detected in limited areas slightly structured striations.

Fatigue crack depth 24 - 57 mm

At a fatigue crack depth between 24 and 30 mm a slightly increasing number of secondary cracks was revealed. In the crack depth region from 30 to 57 mm mainly secondary cracks in combination with a growing percentage of clear striations could be seen, Fig. 13. The striation spacings in this area which were measured from the fractographic pictures are in rather good accordance to the crack growth rates measured during fatigue corrosion test by compliance method, cf. Fig. 5. The amount of "brittle" parts of the fatigue crack surface from 24 to 57 mm fracture depth is clearly reduced (compared with the 19,5 to 24 mm region). In the areas of remaining "brittle" parts of the fatigue crack surface partly could be observed the absence of small secondary cracks (fd = 32 - 38 mm). Beginning from a fracture depth of 30 mm also the "brittle" parts of the fatigue crack surface are normally characterized by striations. The Figs. 14a and b show an example for "brittle" fatigue crack surface (centre) surrounded by more or less "tough" fatigue crack surface.

5. Summary

Metallographic and fractographic investigations have been carried out at a 2 T-W QL-specimen of A 508-2 material with which a corrosion fatigue test under PWR-conditions has been performed. There was observed a remarkable acceleration of crack growth rate after reducing frequency of fatigue load from 1 Hz to 17 mHz for a limited number of cycles referred to about 3 mm crack growth. In this region of accelerated crack growth the mechanism of "tough" fatigue crack propagation appears to change mainly to "brittle" fatigue crack growth along cleavage planes.
The reason for the acceleration of crack growth may be causally the hydrogen crack tip embrittlement which is promoted by a longer exposure time for hydrogen under stress. The crack tip embrittlement may also be assisted by 300°C tempering (ageing) effect /9, 10/.

More research work has to be done to get improved data concerning the acting fatigue corrosion crack growth mechanisms.

References

/1/ Cullen, W.H., Watson, R.E., Taylor, R.E. and Loss, R.J.:
Fatigue Crack Growth Rates of Irradiated Pressure Vessel Steels in Simulated Nuclear Coolant Environment
J. of Nuclear Materials 96 (1981) p. 261 - 268

/2/ ASME Boiler and Pressure Vessel Code
Section XI (1977)
Rules for Inservice Inspection of Nuclear Power Plant Components

/3/ Loss, F.J.:
Structural Integrity of Water Reactor Pressure Boundary Components.
Quarterly Progress Report, April-June 1980.
NUREG/IC 1783
NRL Memorandum Report 4400

/4/ Törrönen, K.:
Environmentally Enhanced Fatigue Crack Propagation in Nuclear Reactor Vessels
Paper presented at the IAEA Specialists Meeting on "Reliability Engineering and Lifetime Assessment of Primary Circuits"
Vienna, Austria, 1.- 3. December 1980

/5/ Goubau, B. and Werner, H.:
Microfractographic Investigation of Fracture Surfaces Coated with Magnetite
Practical Metallography 17 (1980) p. 209 - 219

/6/ Forsyth, P.J.E.:
Fatigue Damage and Crack Growth in Aluminium Alloys
ACTA METALLURGICA VOL. 11 (1963) p. 703 - 715

/7/ Beachem, C.D. and Pelloux, R.M.N.:

Electron Fractography - A Tool for the Study of Micromechanisms of Fracturing Process.
ASTM: Special Technical Publication No. 381,
Philadelphia, USA (1965), p. 210 - 245

/8/ Engel und Klingele:

Rasterelektronenmikroskopische Untersuchungen von Metallschäden.
Herausgeber: Gerling Institut für Schadensforschung und Schadensverhütung GmbH, Köln, 1974

/9/ Kußmaul, K. und Hänsel, G.:

Neue Beobachtungen über das Phänomen der Wechseldehnungs-Versprödung an einer Rißfront anhand von Sprödbruchversuchen.
Zeitschrift für Werkstofftechnik 2 (1971), S. 183 - 188.

/10/ Kußmaul, K., Schäfer, R., Blind, D.:

The Effect of Fatigue Embrittlement on Crack Growth and Fracture Behaviour. IAEA, International Working Group on Reliability of Reactor Pressure Components Technical Commitee on "Time and Load dependent Degradation of Pressure Boundary Materials".
Innsbruck, 20./21. November 1978

	chemical elements	C	Mn	P	S	Si	Ni [1]	Cr	Mo	Cu
Requirements	VdTÜV 365 4.72 22 NiMoCr 3 7	0,17-0,25	0,5-1	≤0,025	≤0,025	≤ 0,35	0,6-1,0	0,3 -0,5	0,5 -0,8	—
	ASTM A 508-2	<0,27	0,5-1	≤0,025	≤0,025	0,15-0,4	0,5-1,0	0,25-0,45	0,55-0,7	—
	specimen V 82 - 8 material A 508-2 according to /1/	0,2	0,6	0,013	0,012	0,20	0,73	0,35	0,56	0,05

[1] Q&T - Thickness ≥ 250 mm, Ni ≤ 1,20 and
Q&T - Thickness ≥ 500 mm, Ni ≤ 1,50 allowed

Table 1: Chemical Composition (weight percent)

			0,2 % non-proportional-elongation $R_{p0,2}$ (N/mm²)	tensile strength R_m (N/mm²)	reduction of area after fracture Z (%)	elongation after fracture A (%)
Requirement	VdTÜV 365 4.72 22 NiMoCr 3.7		≧430[1] bzw. 400[2]	long. ≧ 580 tang. ≧ 750	≧ 45	≧ 19
	ASTM A 508-2		≧ 345	550 - 725	≧ 38	≧ 18
specimen material according to /1/ A 508-2		20°C	464	630	66	24
		288°C	385	603	55	23,5

1) Q&T - Thickness ≦ 300 mm

2) Q&T - Thickness > 300 mm

Table 2: Mechanical properties of forged ring (Specimen V 82-8) in longitudinal direction

	chemical elements	B (ppm)	Li (ppm)	Cl (ppm)	F (ppm)	O_2 (ppm)	H_2 ($\frac{cm^3}{kg}$)
	as	$H_3 BO_3$	LiOH				
Guidelines	USA [1]	2000 - 2500	0,2 - 1	<0,15		<0,1	10 - 50
Guidelines	FRG [2]	<1000	0,2 - 2	<0,2		<0,05	20 - 40
	Test	1000	1	<0,15	< 0,1	~0,001	30 - 50

1) Pipe Crack Study Group
Investigation and Evaluation of Stress-Corrosion Cracking in Piping of Light Water Reactor Plants
NUREG - 0531

2) VGB Kraftwerkstechnik, Mitteilungen der VGB Technische Vereinigung der Großkraftwerksbetreiber
53. Jahrgang, Heft 4, April 1973 p. 207 - 209

3) cm^3 H_2 at ambient pressure

Table 3: Chemical composition of water

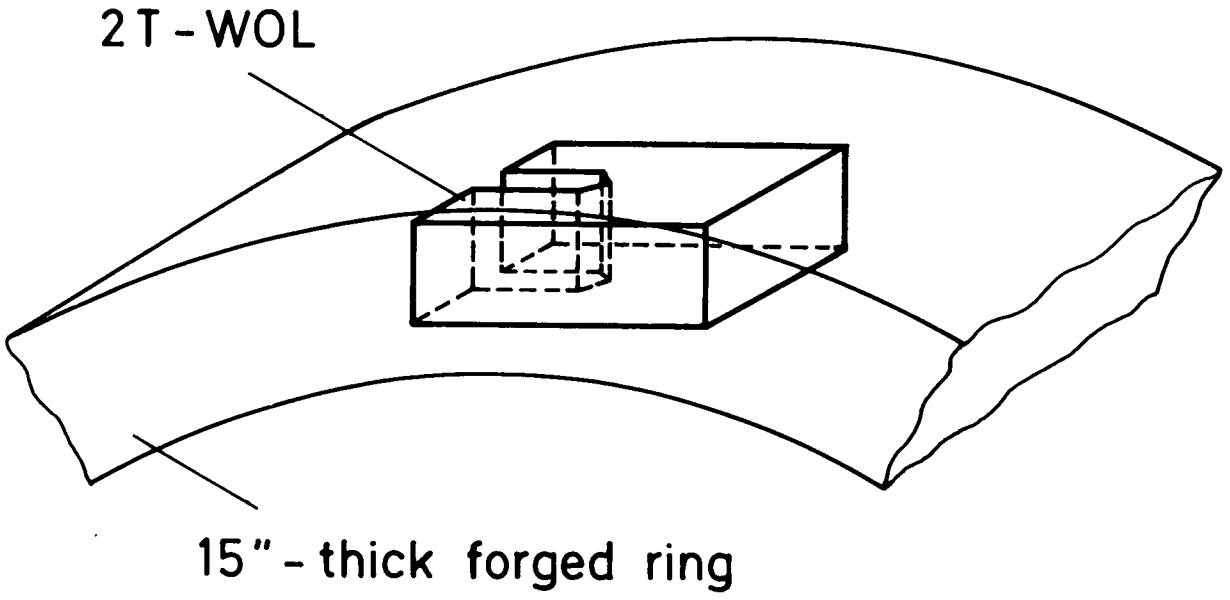

Figure 1: 2T-WOL-specimen from 15" thick forged ring

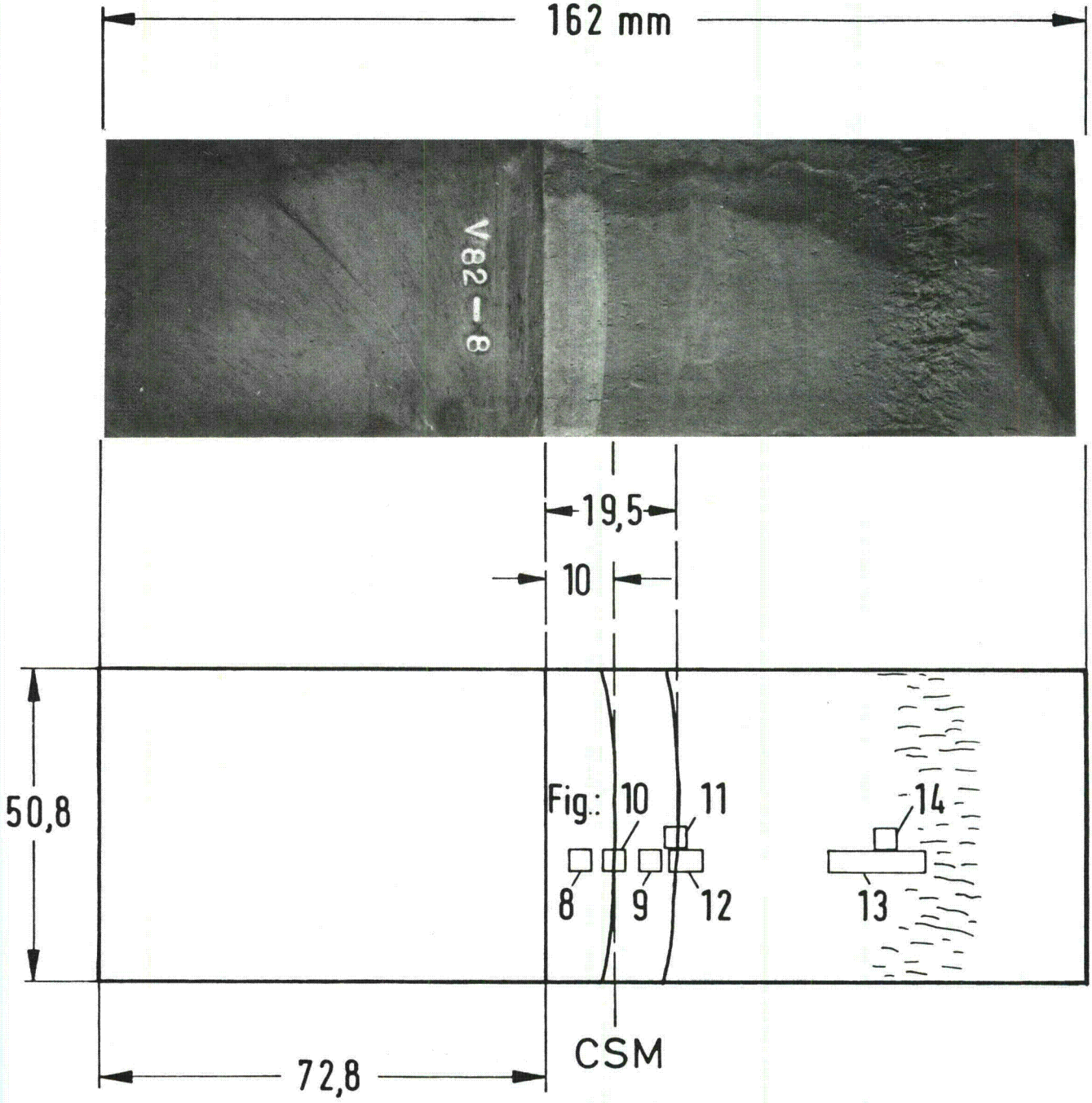

Figure 2: Macro fracture surface of specimen V 82-8 (top) and location of fractographic pictures (bottom)

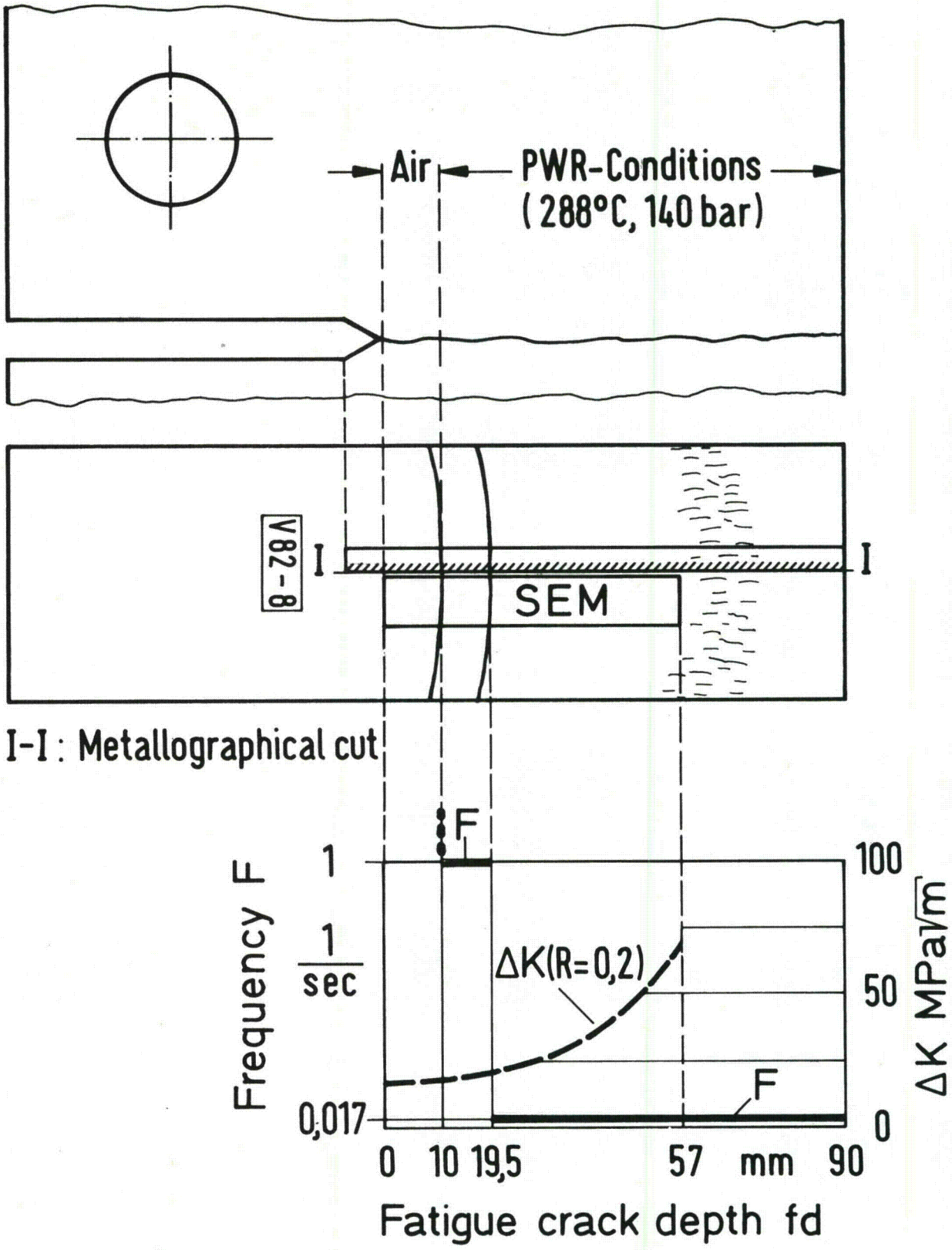

Figure 3: Configuration of 2T-WOL-specimen with metallographical and fractographical test sections. Corrosion fatigue parameters (Pressure, type of medium, temperature, frequency, stress intensi+--)

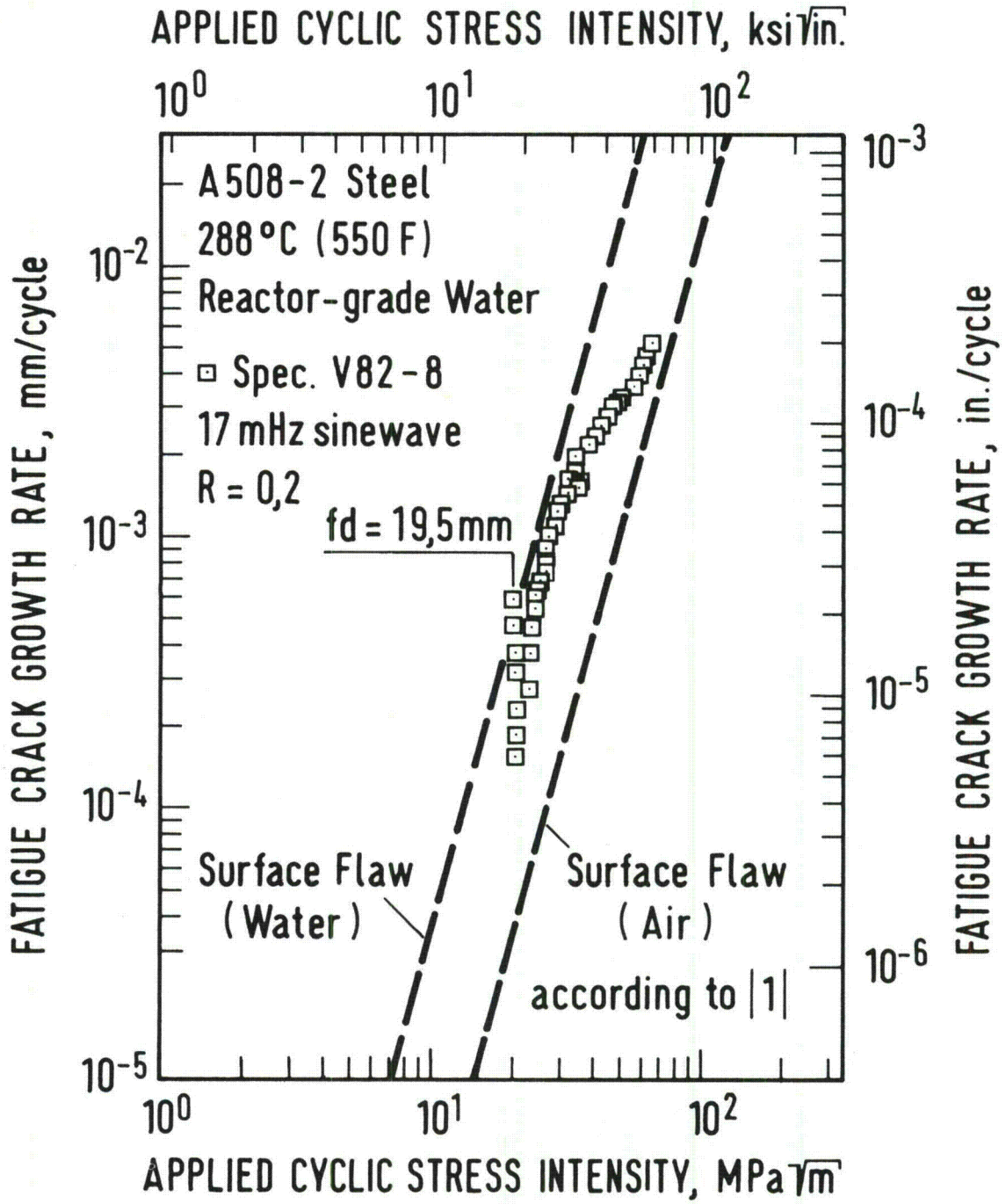

Figure 4: Fatigue crack growth rate versus applied cyclic stress intensity

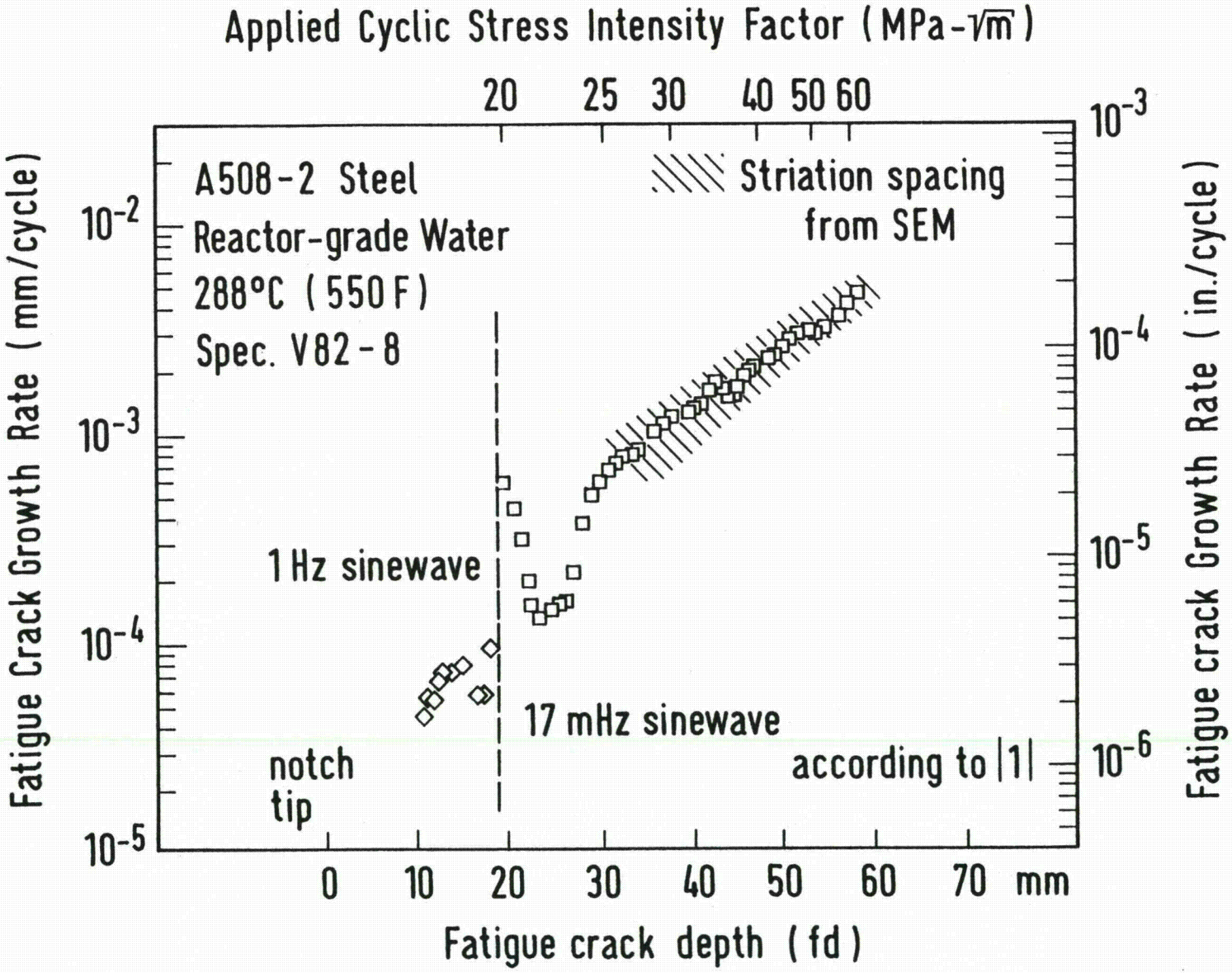

Figure 5: Fatigue crack growth rate versus crack depth

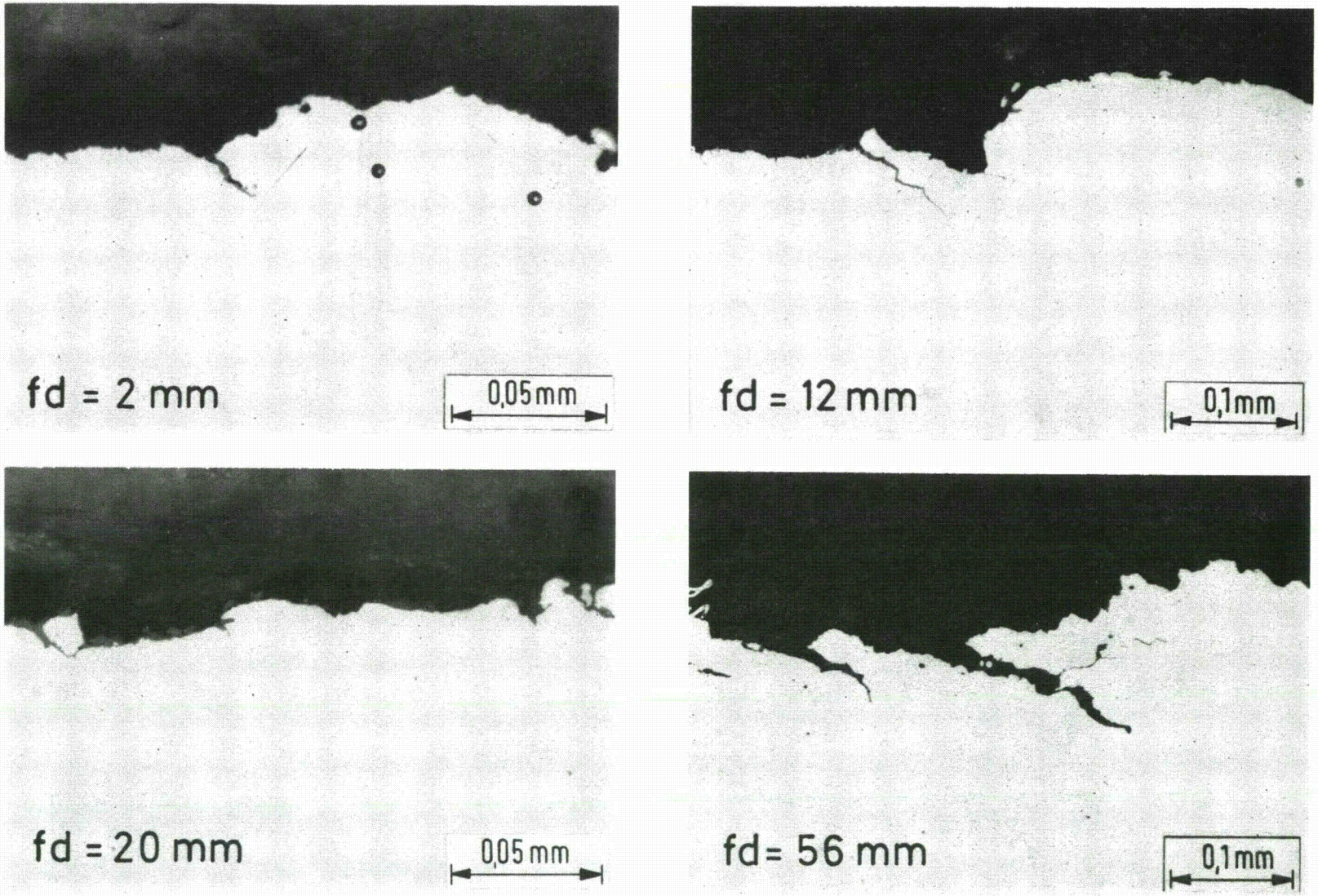

Figure 6: Polished metallographical cut I-I, details from fatigue crack path with secondary cracking according to different fatigue crack depths (fd) (cgd: crack growth direction)

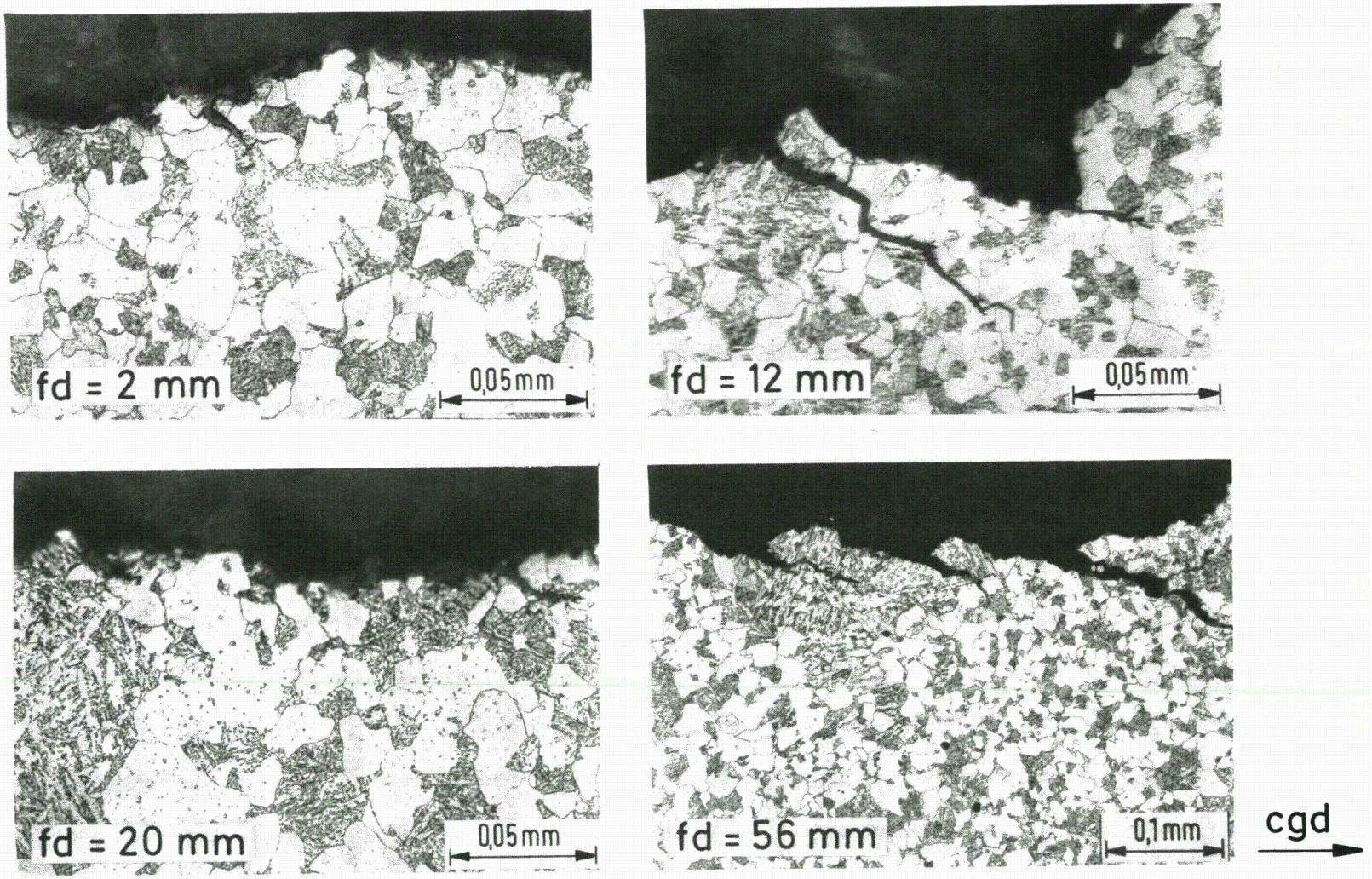

Figure 7: Etched metallographical cut I-I, details from fatigue crack path with secondary cracking
Location of pictures corresponding to Fig. 6

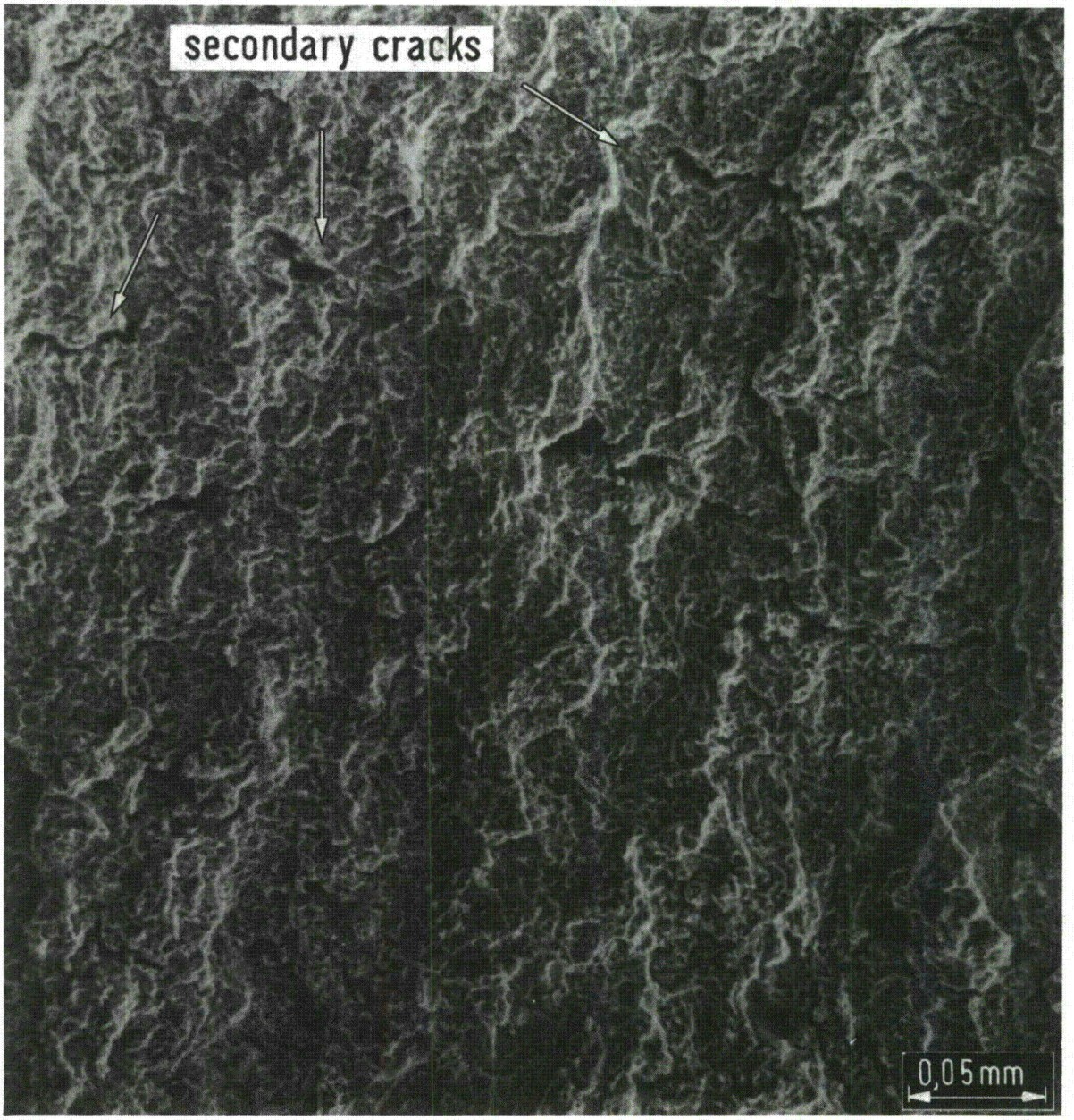

Figure 8: Fracture surface with secondary cracking transverse to main direction of crack growth

Parameters:

Crack depth (fd)	5 mm
Frequency	1 Hz
Medium	Air, Roomtemperature

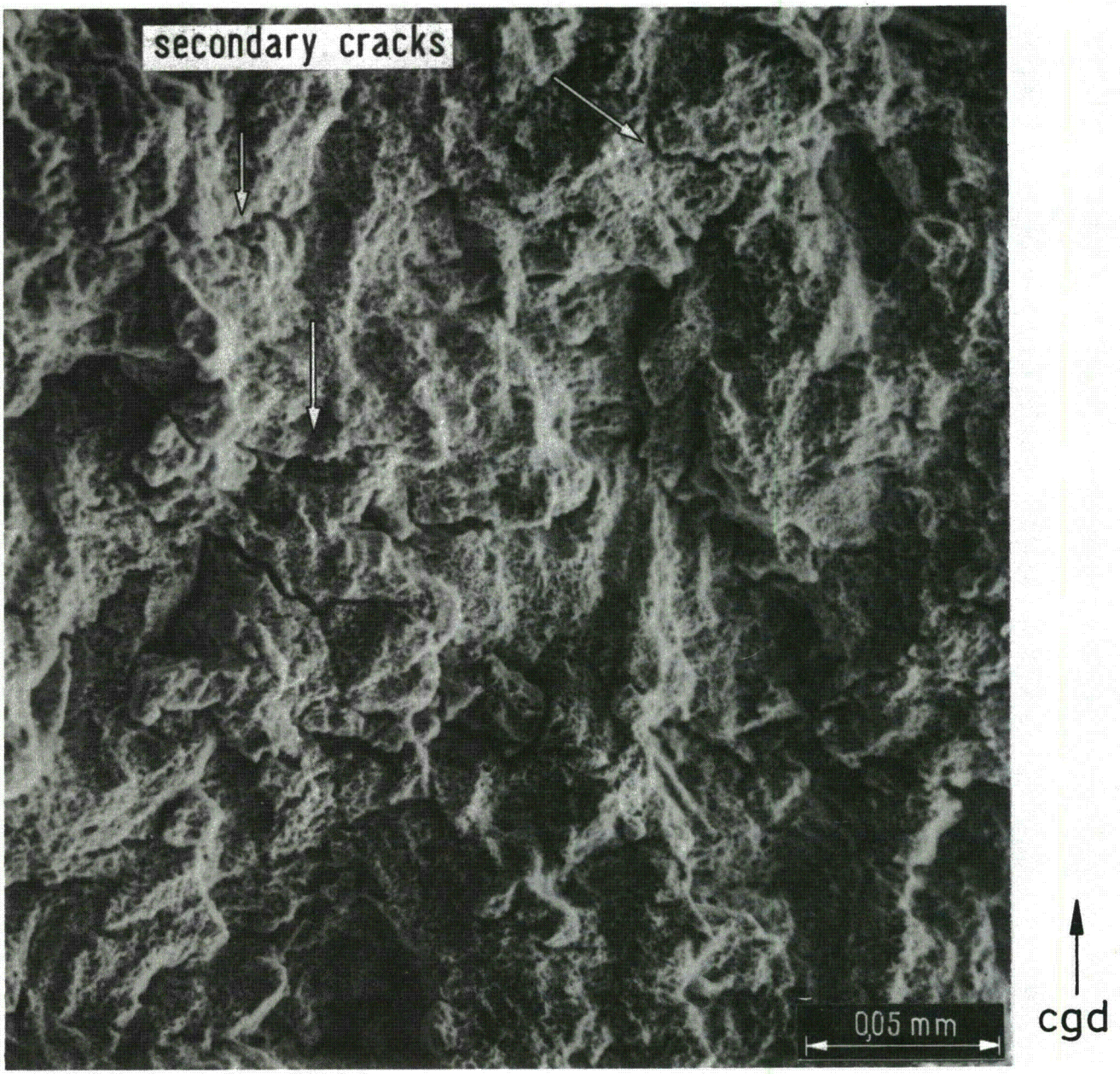

Figure 9: Fracture surface with secondary cracking transverse to main direction of crack growth

Parameters:	
Crack depth (fd)	17 mm
Frequency	1 Hz
Medium	PWR-Conditions (Water 288°C, 140 bar)

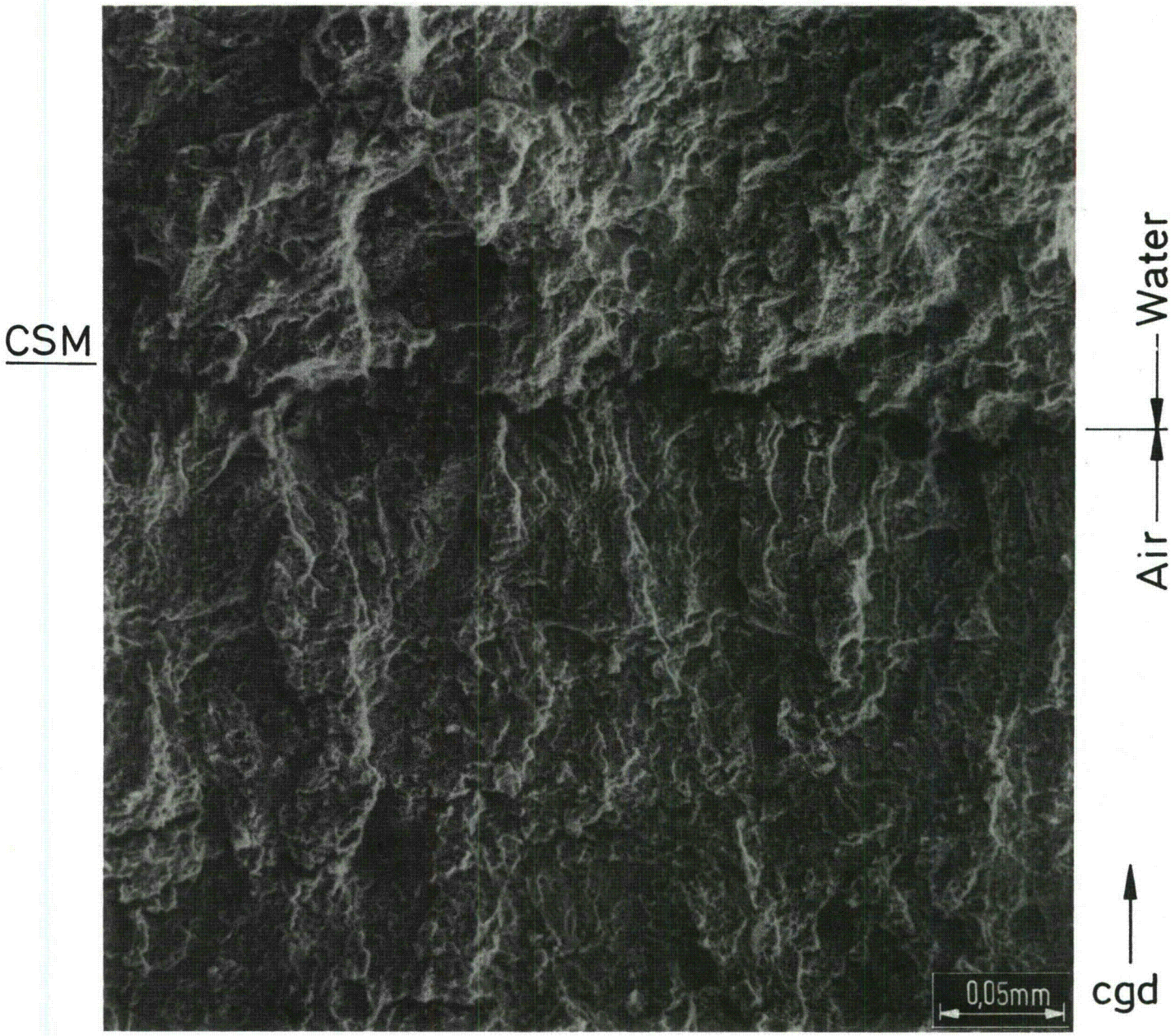

Figure 10: Nearly continuous secondary cracking (fd = 10 mm) along the "crack stop mark" CSM between precracking (Air, cf. Fig. 8) and corrosion fatigue (PWR-conditions, cf. Fig. 9)

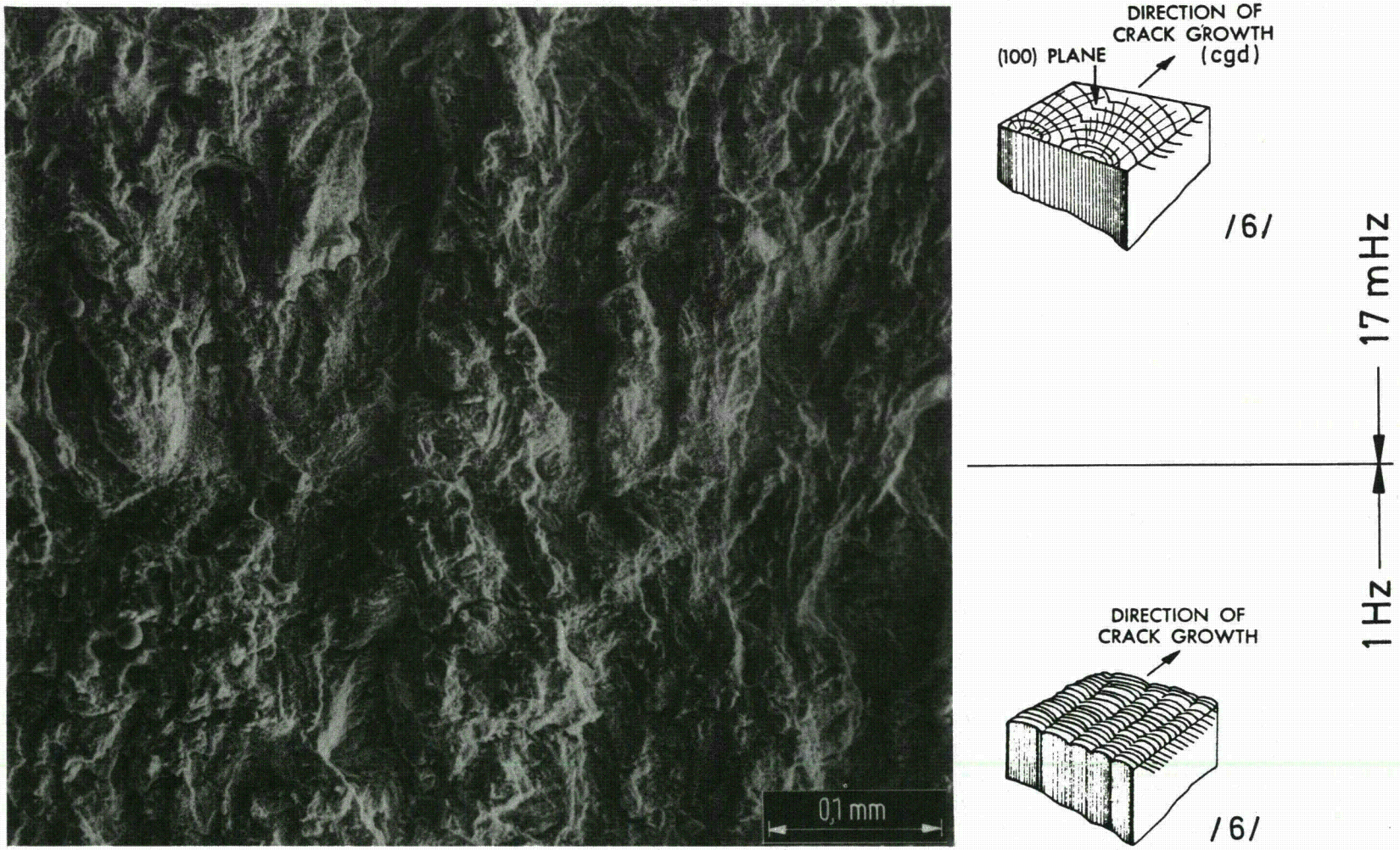

Figure 11: Fracture surface generated under PWR-conditions, region with change of frequency from 1 Hz to 17 mHz (fd = 19,5 mm)

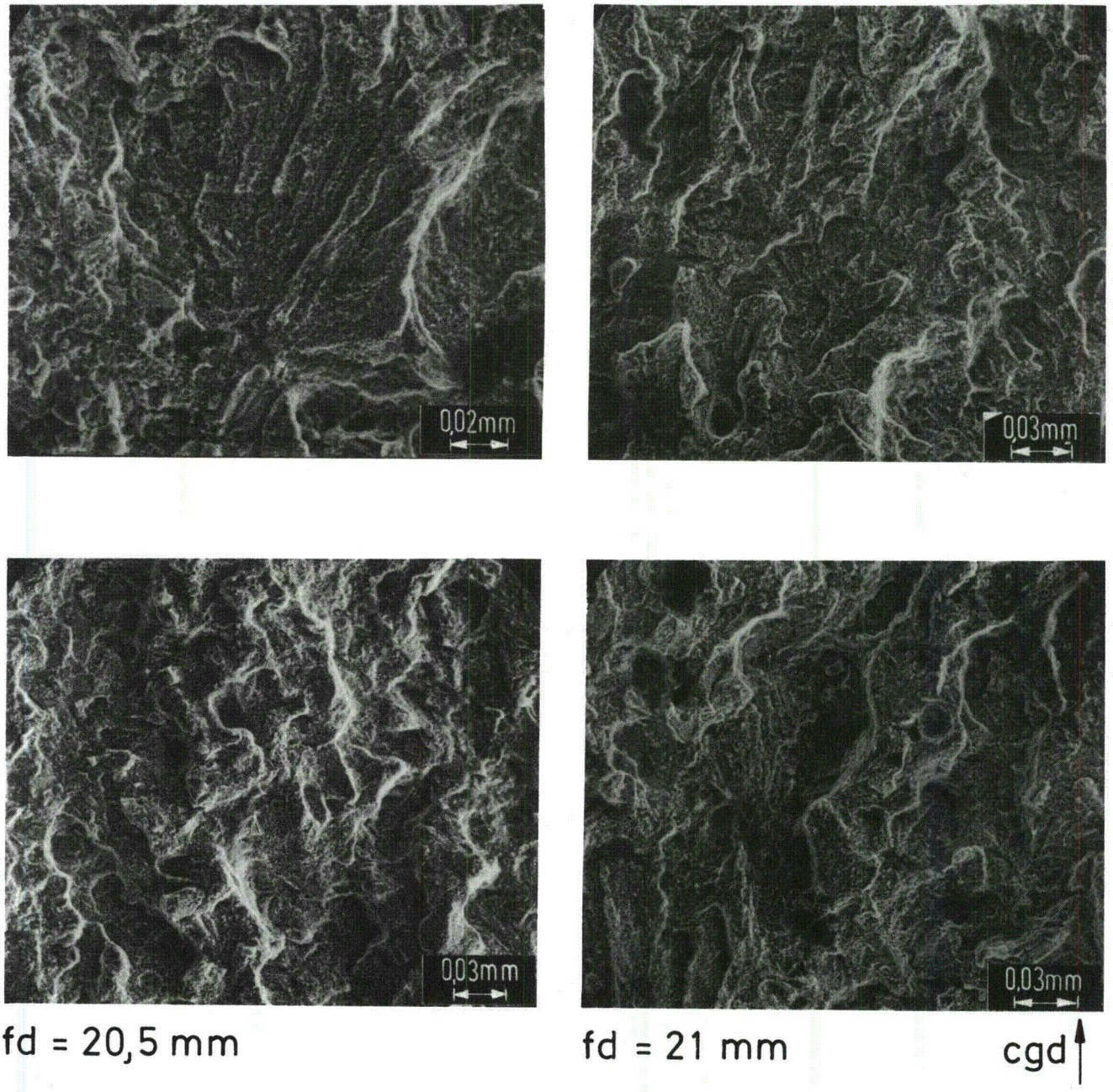

Figure 12: Examples for fracture surfaces in the "brittle" fatigue crack growth region (fd = 19,5 - 24,0 mm)

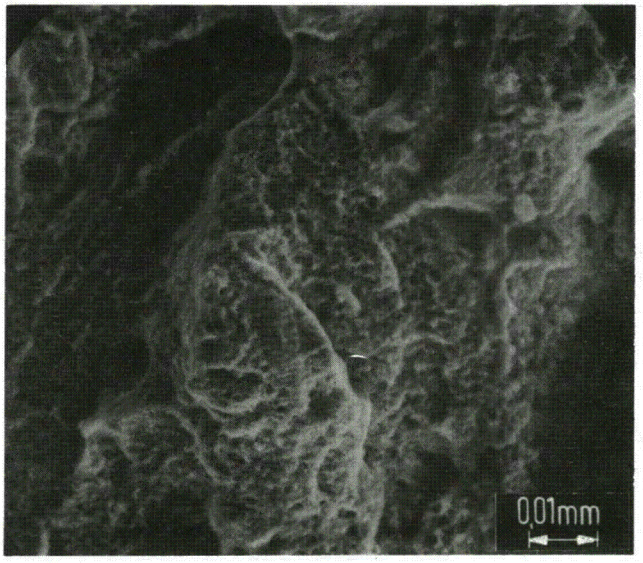

fd = 45 mm

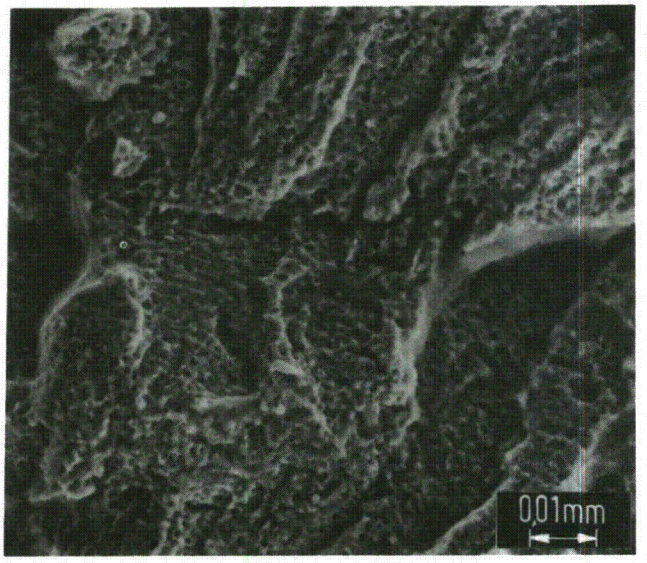

fd = 50 mm

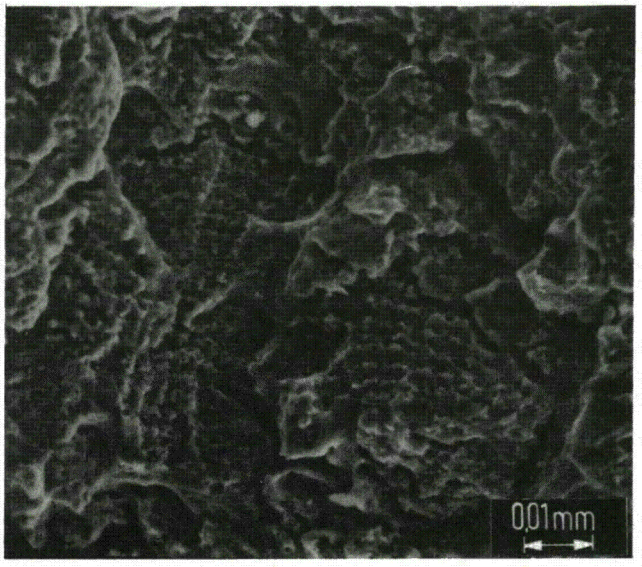

fd = 55 mm

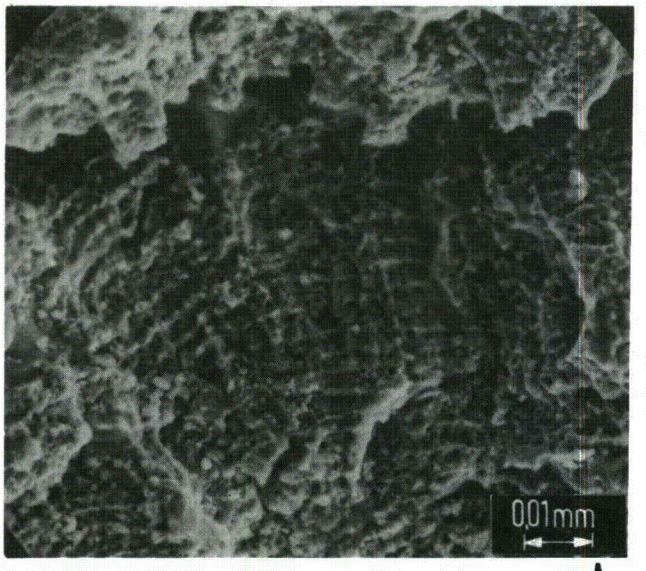

fd = 60 mm

cgd

Figure 13: Fatigue fracture surface (striations) along fatigue crack depth (fd) from 45 to 60 mm

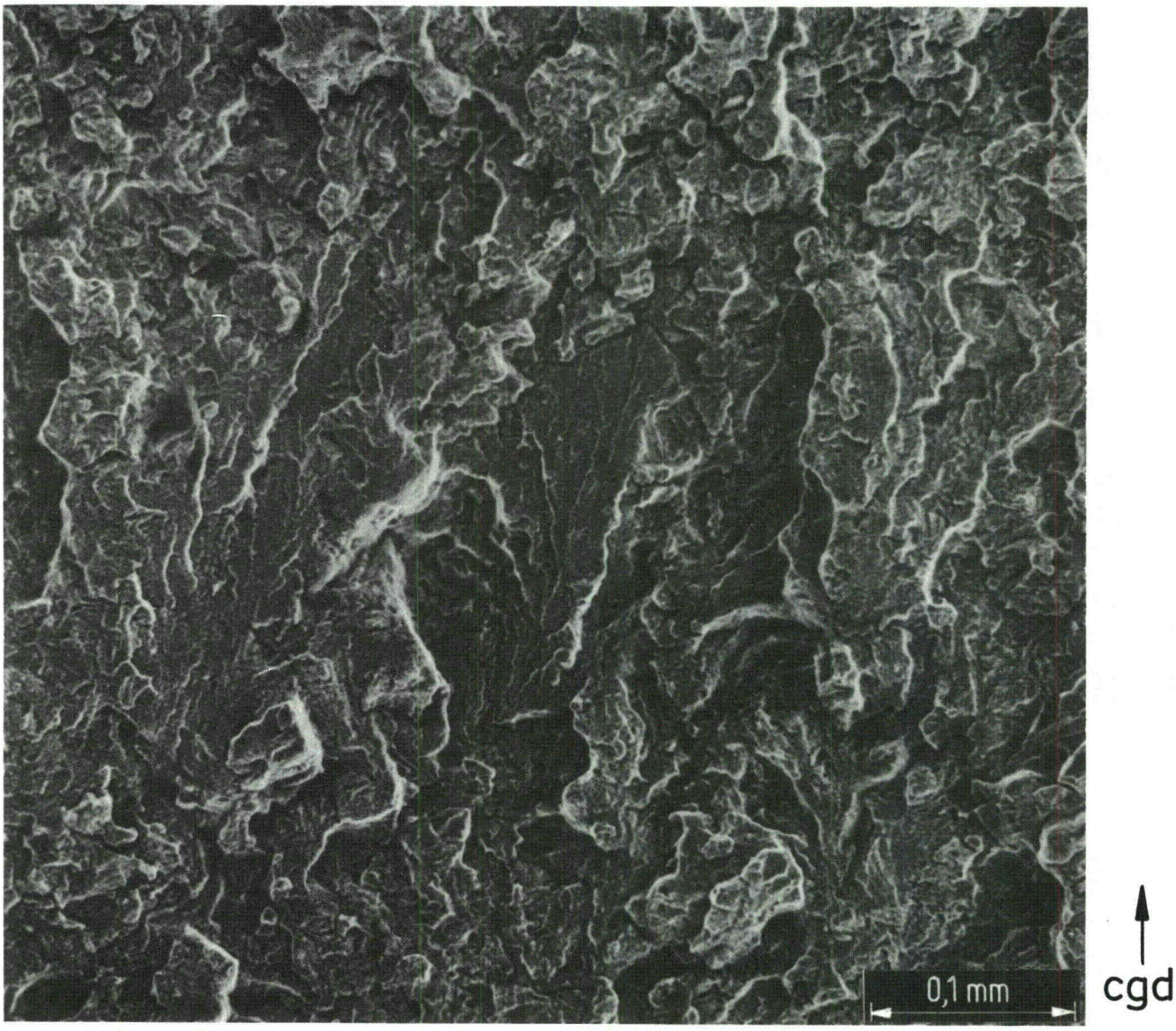

Figure 14a: "Brittle" fatigue crack (centre) under PWR-conditions (frequency 17 mHz) at a crack depth fd = 56 mm

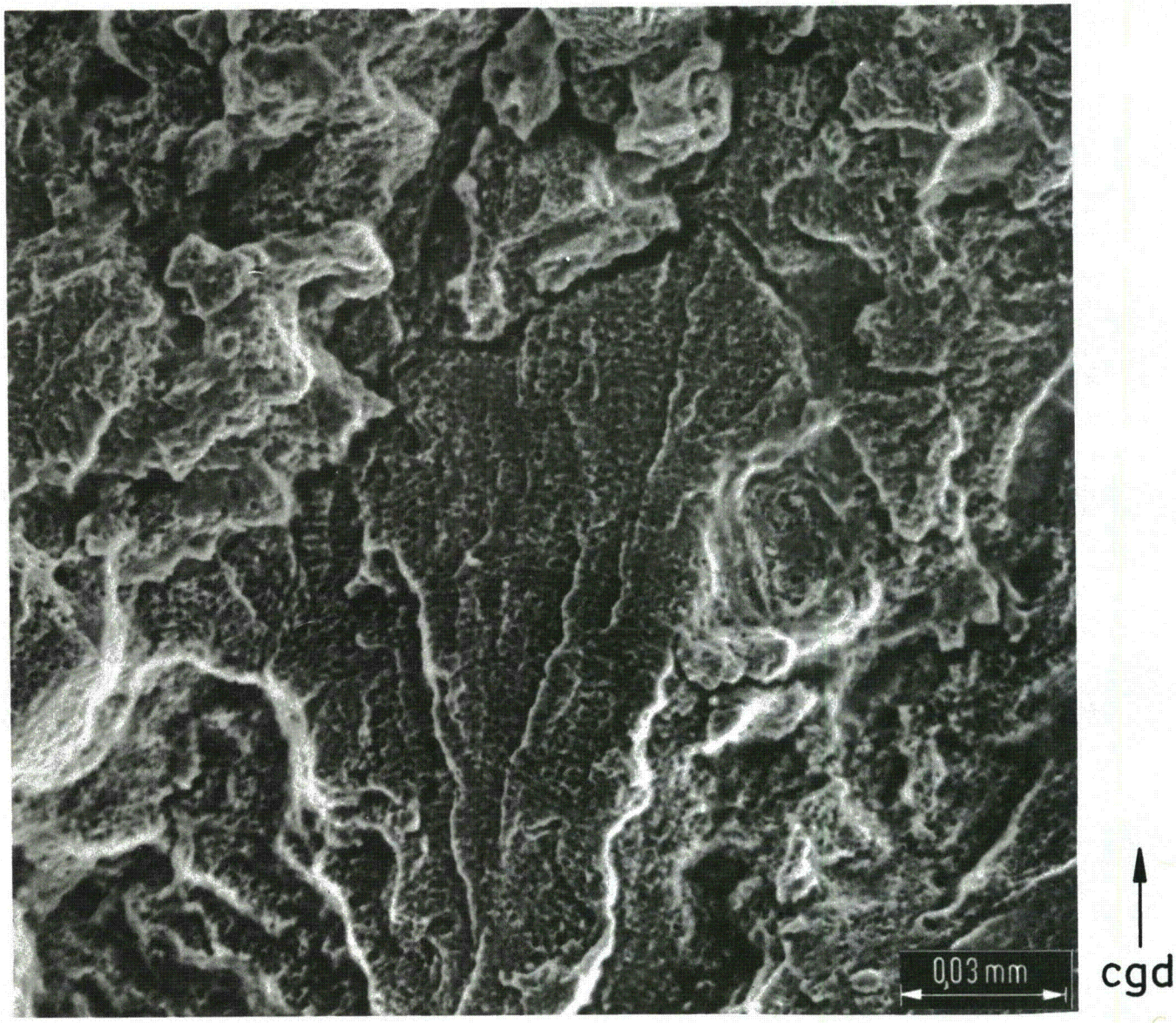

Figure 14b: Detail from Fig. 14a

Paper for:

IAEA Specialist Meeting on Corrosion Fatigue

"The Influence of Water Chemistry on Fatigue Crack Propagation in LWR Pressure Vessel Steels"

by

P M Scott & A E Truswell

Abstract

The results of an experimental programme designed to obtain corrosion fatigue crack growth data for pressure vessel steels are described. The work has concentrated on assessing the influence of various water chemistry variables possible in PWR or BWR primary coolants on fatigue crack propagation rates in A533-B steel.

At a low cyclic frequency, 0.0167 Hz, the only variable found to have a significant effect on crack growth rates when compared with an inert helium environment at the same temperature, 288^{o}C, is the dissolved oxygen concentration at levels in excess of 100 ppb. However, the effect of the oxygenated water on crack growth is observed to decay rapidly with time of exposure and this is attributed to passivation of surfaces previously created by high frequency cycling in a short period of time.

At higher cyclic frequencies of 1.0 Hz or greater, periods of constant crack growth rate independent of the applied cyclic stress intensity factor have been observed in all the aqeous environments examined. The reason for this behaviour is believed to be the occurrence of a form of strain rate sensitive stress corrosion cracking superimposed on normal fatigue behaviour. A mechanistic model based on this proposition is developed and is used to explain how the electrochemical conditions within the experimental rigs of different laboratories can influence the range of frequency and stress ratio over which the stress corrosion phenomenon can occur. It is suggested that this mechanism accounts for apparent laboratory to laboratory disagreements from nominally the same corrosion fatigue experiments.

Materials Development Division
Building 393
AERE, Harwell

March 1981

CONTENTS

1 Introduction

It is now over ten years since Kondo and his co-workers first reported that a typical (simulated) Boiling Water Reactor (BWR) environment could cause fatigue cracks to grow much faster in reactor pressure vessel steels than in the same steels exposed to an inert environment.[1] Subsequently, it was shown that a Pressurized Water Reactor (PWR) simulated primary circuit coolant could also cause very large increases in fatigue crack propagation rates.[2] Since then, a considerable international effort has been mounted to determine the influence of a large number of metallurgical and water chemistry variables which could possibly affect the rate of corrosion fatigue crack growth in reactor pressure vessel steels. Ultimately, a realistic and safe code of practice is required to enable the growth of any defect, which might be found as a result of in-service inspection and which might also be exposed to the primary coolant, to be quantitatively assessed.

The complexity of the necessary experimental equipment required to simulate LWR coolants, typically at 300°C and up to 17 MPa pressure, and the extremely time consuming nature of the experiments carried out at very low cyclic frequencies has dictated a comparatively slow rate of progress. Some confusing and apparent disagreements between the results from different laboratories have also been disclosed. In this paper, we describe the results of the UKAEA programme, which has, initially, concentrated on measuring the influence of various water chemistry variables while using comparatively few heats of A533-B plate pressure vessel steel. A mechanistic model based on the results, is described which, it is believed, goes a long way towards explaining the anomalies which have appeared between the results of different laboratories, and points the way to those electrochemical conditions it is necessary to avoid to prevent unusually fast corrosion fatigue crack propagation rates in reactor pressure vessel steels.

2 Experimental

The experimental rig consists of four independent high pressure, high temperature water loops, each connected to individual autoclaves which contain the fatigue specimens. A line drawing of the water recirculation loops and a cut-away drawing of the specimen assembly within the autoclaves is shown in Figure 1.

The feedwater to each of the recirculating loops can be varied over a wide specification of either PWR primary circuit water, BWR water or pure water; Table 1. The feedstock is de-ionised, de-oxygenated water with a

conductivity typically of 0.08 to 0.1 μS cm^{-1} and unmeasurable oxygen content, ie <10 ppb. For BWR water chemistry, a small portion of the feedstock is fully oxygenated at ~0.5 bar oxygen pressure (or by additions of hydrogen peroxide), and then mixed in the appropriate proportions with deoxygenated water to give the desired oxygen content. In this mode of operation the blowdown water from each high pressure loop is run to waste. For PWR primary water, the appropriate concentrations of boric acid and lithium hydroxide are added to a mixing tank which is pressurised to ~1.5 bar with either helium or hydrogen. The blowdown water from each loop in the PWR mode is returned to the mixing tank via a Potter column to provide continuous deoxygenation and lithiated and borated cation and anion resins to remove all ionic dissolved impurities other than lithium and borate ions.

The high pressure recirculating water loops can operate up to 300°C and 16 MPa pressure at a recirculation rate of ~40 litres/minute. The feedwater is metered in by a double diaphragm, positive displacement pump at typically 20 to 40 litres/hour and is matched by an equivalent blowdown rate through a back pressure regulator. Thus about 1% of the recirculating flow is blown down on each water circuit. Water sampling points on the feed and bleed water flows are available for wet chemistry analysis. Dissolved gases can also be removed from these sample flows by a gas stripper and are then analysed by gas chromatography.

The fatigue specimens for this work were 25 or 50 mm thick compact tension specimens cut from A533-B plate steel with one of the three orientations shown in Figure 2. The steel compositions and mechanical properties are shown in Table 2. The fatigue crack lengths in the specimens were determined in-situ from measurements of the crack mouth opening displacement using an encapsulated, linearly variable, displacement transducer. An on-line computer calculated the crack length from a calibration polynomial relating crack opening displacement divided by the applied load to crack length. This relation was determined in calibration experiments at 288°C in an inert helium environment.[3] Pre-cracking of the specimens was normally carried out in situ at the operating temperature and pressure over about eight hours. Step load reduction to the desired load range was followed by cyclic frequency reduction to the required frequency.

3 Results

A series of experiments were carried out initially to establish an inert environment (helium gas) fatigue crack propagation base-line against which the subsequent corrosion fatigue results could be compared. These results and those for each water chemistry examined are described under individual

sub-headings below.

3.1 Helium gas at 288°C

Compact tension specimens, 50 mm thick, all with L-S orientation manufactured from cast C8938 (Table 2) were used for these experiments. The results for sine and triangle waveshapes with cyclic frequencies in the range 10 Hz to 0.0167 Hz (1 cycle per minute) and stress ratios, R, (the minimum cyclic stress divided by the maximum cyclic stress) in the range 0.2 to 0.7 are shown in Figure 3. It can be seen that the mean slope of the results on the double logarithmic scales of Figure 3 is less than that given by the current ASME Section XI Appendix A code[4] such that the code line is non-conservative at values of ΔK less than 50 MPa$\sqrt{m}$. The practical significance of this is not very great[5] but for safe predictions of dry crack growth an adequate upper bound to these results is:

$$\frac{da}{dN} = 1 \times 10^{-11} \Delta K^3 \text{ metre/cycle } (\Delta K \text{ in MPa}\sqrt{m})$$

There is a small but perceptible frequency effect in the results shown in Figure 3 which appears to saturate with decreasing frequency, the highest propagation rates for any given value of ΔK being observed at 0.1 Hz. This could be due to a slight tendency to cyclic strain ageing although one specific study of this phenomenon in Sweden failed to find any evidence of strain ageing during fatigue crack growth.[6]

3.2 De-oxygenated aqueous environments at 288°C

In this series of experiments we have examined the effect of various chemical additives used in PWR primary circuit water on corrosion fatigue crack propagation in A533-B steel. The specimens all with L-S orientation, 25 or 50 mm thick, were manufactured from either cast C8938 or 63758.1 (Table 2). The results for one cyclic frequency of 0.0167 Hz (chosen to imitate the conditions under which considerably enhanced rates of crack growth had been observed elsewhere[2,7]) are shown in Figure 4.

The most important observation is that the chemical additives, boric acid, lithium hydroxide and molecular hydrogen in the concentration ranges encountered in PWR primary circuits have only relatively little influence on fatigue crack growth rates when compared with the inert helium environment for a frequency of 0.0167 Hz and R ratios in the range 0.2 to 0.7. Secondly, throughout this work, we have been unable to sustain crack propagation at 0.0167 Hz for values of ΔK less than 15 MPa$\sqrt{m}$, whereas at higher cyclic frequencies (1.0 Hz say) or in an inert environment, no such difficulty was

encountered. There is strong evidence from experiments where the crack has been extended and the crack tip sharpened by a burst of high frequency cycles followed by a return to 0.0167 Hz that this arrest phenomenon is due to oxide films forming on the crack flanks and at the tip; ie passivation. We also describe in the next section how raising the oxygen concentration can cause an arrested crack to start propagating again.

At relatively high values of ΔK, the evidence in Figure 4 shows that the slope of the crack growth curve decreases and approaches a value of two. Such behaviour is well known in tough, ductile steels in inert environments and considerable benefit would arise in crack propagation calculations on reactor pressure vessels by taking account of this fact.[5] Nevertheless, a safe, single, upper bound equation to these results is:

$$\frac{da}{dN} = 4 \times 10^{-11} \Delta K^3 \text{ metres/cycle } (\Delta K \text{ in MPa}\sqrt{m})$$

Clearly, the lack of an appreciable environmental effect on crack growth at a cyclic frequency of 0.0167 Hz is in apparent conflict with results from other laboratories (see Fig 9)[2,7] and the reasons for this are discussed in a later section.

Another series of tests using de-oxygenated aqueous environments were carried out in which the influence of specimen orientation was briefly examined. The specimens with either L-S or S-T orientation were manufactured from casts C8938 and C8982 respectively (see Table 2). Unfortunately this introduces some ambiguity into the significance of orientation to be drawn from the results, but the chemical compositions of the casts were very similar. The results are shown in Figure 5 for two frequencies of 1.0 Hz and 0.0167 Hz and a single R ratio of 0.7.

There is a uniform difference in the crack growth results at each test condition which is thought to be primarily due to orientation; the S-T orientation being particularly poor because the crack plane is in the plane of any non-metallic inclusions arising from the plate rolling process. The results in Figure 5 also show that temperature influences crack growth rates, those at 288°C being about double those measured at 20°C. Another interesting feature of the results is a small plateau-like feature in crack growth rates between 1.5 and 2.5 x 10^{-7} metres/cycles for a high frequency, 1.0 Hz, in pure water or water plus lithium hydroxide. This is particularly significant for the mechanistic model developed later.

A third series of tests in PWR primary water was initiated with specific intention of testing this mechanistic model of the origin of the very severe enhancement of crack growth rates observed in other laboratories at low clic frequencies and high R ratios. However, in this case, high cyclic

frequencies have been used in the range 1 to 5 Hz in combination with very high R ratios of 0.7 to 0.8. The results for 50 mm or 25 mm thick L-S orientation specimens manufactured from cast C8938 and 63758.1 respectively (Table 2) are given in Figure 6 and quite clearly show the plateau feature in crack growth rates; ie constant crack growth rate independent, over a specific range, of ΔK. Further experiments in this series are still in progress.

3.3 Oxygenated aqueous environments at 288°C

It is known that very small concentrations of oxygen in high temperature water can have a very profound influence on the electrochemical potential of ferritic steels[8] and by implication on corrosion and possibly corrosion fatigue kinetics. It could also be anticipated that under such conditions, contact with more noble materials (at 288°C) and the flowrate conditions would also be important; the latter because the width of a laminar flow boundary layer could result in diffusion controlled oxidation kinetics rather than by the bulk solution oxygen concentration. Thus, the effect of oxygen, whether present as an intentional additive as in BWR water simulations or unintentionally in other experiments, was an important parameter to investigate.

In our experience, controlling precise low levels of oxygen in solution has been difficult, requiring precise metering of the oxygenated water flow and a knowledge of the oxygen consumption characteristics of the water loop pipework. We conclude that inadvertent oxygen contamination other than as an initial experimental transient is unlikely except where there is a continuous uninterrupted supply, for example, through a leaking pump gland.

The experimental results for the influence of oxygen at various concentrations on corrosion fatigue crack propagation in 25 or 50 mm specimens with L-S orientation, manufactured from casts C8938 or 63758.1 respectively (Table 2), are shown in Figure 7. The sine wave cyclic frequency was 0.0167 Hz and the R ratio was varied between 0.2 and 0.7. No effect of steel cast was observed but an influence of oxygen concentration on crack propagation rates is evident in Figure 7 for concentrations in excess of 100 ppb up to 500 ppb. In these cases, high rates of crack growth were observed initially in each experiment comparable with the worst observed by others in either simulated normal BWR water (200 ppb oxygen[9,10]) or simulated PWR primary water (<10 ppb oxygen)[2,7] However, these high rates of growth were only measured for the first few millimetres of crack growth following in situ pre-cracking at a relatively high frequency of 1.0 Hz. The rate of crack growth decelerated over the first few days of each experiment, after which the cracks grew as though the oxygenated

water were not present. An experiment was also carried out in which the crack growth rate was allowed to decay in the manner just described, followed by a burst of high frequency cycles (1.0 Hz) at the same cyclic stress in order to push the fatigue crack on a few millimetres over a period of a few hours. After this procedure the cyclic frequency was reduced to 0.0167 Hz and the high initial rate of crack growth was restored, which then decayed away as before. In another experiment a fatigue crack propagating at 1.0 Hz at ΔK ~15 MPa$\sqrt{m}$ in deoxygenated pure water was allowed to arrest by reducing the frequency to 0.0167 Hz at the same cyclic stress, and then oxygen was injected at a concentration of 1200 ppb. The outlet oxygen concentration (probably most representative of the bulk loop concentration) rose steadily over a period of a few days and when it reached 1100 ppb, the crack suddenly started propagating again, but not at an unusually fast rate.

All these observations, and particularly the last one mentioned above, are not consistent with a crack blunting mechanism as either the reason for the decay in crack growth rate observed in oxygenated water or the arrest of cracks at low cyclic frequencies for ΔK <15 MPa$\sqrt{m}$ in de-oxygenated water. Only a passivation mechanism is capable of explaining all the features of these observations. Thus oxide filming of the specimen and particularly the crack flanks reduces the dissolution rate which can be sustained at the crack tip and, apparently, can block fatigue slip step emergence at the crack tip at low values of ΔK. Oxygen, at the concentrations used, enhances dissolution but is also eventually negated by the passivation process. The quantitative implications of this description are addressed in the Discussion section.

The influence of the applied cyclic frequency has also been examined in a short series of experiments using simulated BWR water (ie 100-200 ppb) and a single stress ratio, R = 0.7. The results are shown in Figure 8. At cyclic frequencies between 0.1 and 1.0 Hz a small plateau feature around 1 to 2 x 10^{-7} metres/cycle was observed unlike the results for the low frequency of 0.0167 Hz, where the initial high crack growth rates decayed to the normal inert environment rate as described above. These plateaux in crack growth are considered to be significant, particularly as it is now known that at very high oxygen concentrations of >1200 ppb the high crack growth rates, which we observed only in the initial stages of our experiments with lower oxygen concentrations, can be sustained at very low cyclic frequencies (see Fig 10).[11,12]

4 Discussion

It is clear from the results described above that there is a major discrepancy between the experimental data reported here for PWR primary water environments and those described by Bamford et al[2,7] reproduced here in Figure 9. It has been suggested that the sulphur content of the steel may be a factor[13], in that all the results described in this paper refer to modern, relatively clean steels, while those in Figure 9 refer mainly to older, dirtier steels. We believe that steel sulphur content may indeed play an important role but that this can only be clearly understood if metallurgical factors such as this one and water chemistry variables are considered together. Both sets of variables will combine under some circumstances to produce adverse electrochemical conditions while other combinations are benign. Measurements of electrochemical potential are therefore seen as an important requirement to improve our understanding of the basic processes in any future work.

The importance of passivation kinetics in accounting for the influence of oxygen has been cited earlier. An independent examination of the oxide films on the steel specimens in this programme exposed to water or water + LiOH at 288°C has revealed important differences in morphology and oxide tenacity from those produced by Bamford et al under nominally the same conditions.[14] This is important prima facie evidence that the electrochemical conditions within the two experimental rigs are different. One obvious physical difference is the flowrate regime each experimental rig operates in; the one described here having a much faster flowrate and almost certainly turbulent flow over the specimen. Moreover, in an international 'round robin' series of tests described in another paper at this conference[15] the plateaux features in the crack propagation curve were seen in static or low flow autoclaves but not in the high flowrate conditions used in this work. It is these plateaux rates of crack growth which appear to be the main difference between those results which show very large enhancements in crack growth rates compared to an inert environment and those which do not. It is suggested that this plateaux phenomenon is in reality due to stress corrosion cracking, where chemical reaction rates rather than the applied ΔK control the rate of crack advance, and that the electrochemical conditions which allow this to occur or not is the crucial difference between individual laboratories.

Stress corrosion cracking tests of the classical type, where pre-cracked, bolt loaded, compact tension specimens of A533-B, A508-II and weldments thereof have been used, have been in progress in simulated (low flowrate) PWR water for several years.[13] In all tests on plate steel, forging steel or weld metal, no crack extension has occurred even after 40,000 hours. However, in the case

of the weld HAZ specimens, crack growth has occurred in every case within 2000 hours at stress intensities as low as 48 MPa$\sqrt{m}$. This evidence, as it stands, does not immediately suggest that stress corrosion cracking would be a problem in corrosion fatigue tests on any materials other than weld HAZs.

It is, however, well known that applied cyclic stresses of relatively small amplitude can depress the apparent static load threshold for stress corrosion by about a factor of two in several ductile metal/environment combinations known to exhibit stress corrosion cracking.[16] It has been established that in such circumstances the crack initiates at some specific strain, well below the nominal static threshold, usually by rupture of a passive film, but that if the dynamic strain is also not above a certain threshold value, then repassivation dominates and crack growth arrests. The sensitivity of many stress corrosion systems which depend on passive film breakdown to the applied strain rate is very well established and casts a great deal of doubt on the value of a single static stress or stress intensity threshold parameter such as K_{Iscc}. For dynamic strain conditions, the apparent K_{Iscc} is just one necessary, but not sufficient, condition which must be satisfied for crack growth to occur, even when the electrochemical conditions for stress corrosion cracking are favourable. Application of a monotonic or cyclic stress allows a low creep rate to persist, and increases the rate of slip step emergence at the crack tip so that dissolution rates remain high and crack propagation proceeds. The work hardening properties of the metal would also be expected to be important here. Therefore, the necessary and sufficient conditions for stress corrosion cracking to start and then continue propagating are: (i) a critical crack tip strain must be exceeded (characterised by K_{Iscc} but determined dynamically), (ii) a critical crack tip strain rate, $\dot{\varepsilon}$, must also be exceeded and (iii) the electrochemical conditions must be favourable.

For a quantitative interpretation of the corrosion fatigue crack propagation kinetics, it is necessary first to estimate the crack tip strain rate during the tensile part of the fatigue cycle. In the case of small scale yielding, the crack tip opening displacement, δ, as a function of the crack tip stress intensity, K, is given by:

$$\delta = \frac{K^2}{E\sigma_y}$$

where E is the elastic modulus and σ_y the yield stress. The crack tip strain rate, $\dot{\varepsilon}$, is defined by:

$$\dot{\varepsilon} = \frac{1}{\delta} \frac{d\delta}{dt}$$

For sine wave cycles, where the increasing tensile strain takes place over T seconds, the stress intensity as a function of time is:

$$K = \frac{\Delta K}{2}\left[\frac{1+R}{1-R} + \cos \pi \left(1 + \frac{x}{T}\right)\right]$$

where x/T is the fraction of T seconds elapsed in the tensile half cycle. Thus, the instantaneous strain rate at any point in the cycle is:

$$\dot{\varepsilon} = \frac{1}{\delta}\frac{d\delta}{dx} = \frac{-2\pi}{T}\left[\sin \pi\left(1 + \frac{x}{T}\right)\right] \Big/ \left[\frac{1+R}{1-R} + \cos \pi \left(1 + \frac{x}{T}\right)\right]$$

Similarly for linear ramps, where the increasing strain takes place over T seconds:

$$K = \frac{\Delta K}{2}\left[\frac{1+R}{1-R} + \left(\frac{2x}{T} - 1\right)\right]$$

and $$\dot{\varepsilon} = \frac{1}{\delta}\frac{d\delta}{dx} = \frac{2}{T} \cdot \frac{1}{\frac{R}{1-R} + \frac{x}{T}}$$

These functions for $\dot{\varepsilon}$ are plotted in Figure 11 as a function of x/T, from which it can be seen that $\dot{\varepsilon}$ varies in a complex way during a fatigue stress cycle. However, high R ratio cycles with ramp loading produce the most uniform crack tip strain rate during the cycle. An average measure of the tensile crack tip strain rate in a fatigue cycle is given by

$$\dot{\varepsilon}_{av} = \frac{1}{T}\int_{\delta min}^{\delta max} \frac{1}{\delta}\, d\delta = \frac{2}{T} \ln \frac{1}{R}$$

This function together with the maximum and minimum excursions in $\dot{\varepsilon}$ during a fatigue cycle are shown as a function of R ratio in Figure 12. It can be seen that to establish a correlation between the rates of crack growth and the crack tip strain rate involves a compromise if $\dot{\varepsilon}_{av}$ is used, but this is a better approximation the higher the R ratio.

In Table 3 the plateaux rates of crack growth derived from Figures 6, 9 and 10 are given as a function of $\dot{\varepsilon}_{av}$ and are plotted in graphical form in Figure 13. Data for cycles with hold times at constant stress have been excluded. These rates of crack growth have been converted to a time base and corrected, where necessary, for the component of fatigue crack growth which would occur anyway in an inert environment and, particularly in the case of relatively low R ratios, for the portion of the cycle spent with K above the stress corrosion threshold, ie the apparent dynamic K_{Iscc}. A value of 28 MPa$\sqrt{m}$

appears to fit the threshold data quite well. Table 4 shows values of ΔK as a function of R for which K_{max} or K_{min} exceed 28 MPa$\sqrt{m}$. It can be seen from Figure 13 that a correlation exists between $(da/dt)_{plateau}$ and $\dot{\varepsilon}_{av}$.

Independent measurements of dissolution transients have been made for two different stainless steels following sudden increases in strain in water (plus sodium sulphate to confer electrical conductivity) at 97°C.[17] These transients, i, decay over periods of tens of seconds as:

$$i = i_o (t - t_o)^{-\frac{1}{2}}$$

although for the first few milliseconds the decay rate is exponential. On the basis of these observations and a low measured activation energy of ~4 Kcal/mole, a kinetic model was derived based on crack tip cation solvation and transport as the rate determining processes.[17] Thus if the same rate determining processes were relevant to the plateaux rates of crack growth, during corrosion fatigue at low frequencies, then da/dt should be a function of $\dot{\varepsilon}^{\frac{1}{2}}$ as indeed appears to be the case in Figure 13. The upper bound drawn on the graph obeys the equation:

$$\frac{da}{dt} = 5 \times 10^{-4} \dot{\varepsilon}_{av}^{\frac{1}{2}} \quad \text{mm/sec}$$

It seems likely that cycles with hold times at constant stress will give, effectively, rather lower plateau rates than cycles without such periods.

Another deduction can be made from the electrochemical dissolution transient measurements[17], concerning the maximum possible bare surface dissolution rates and hence the maximum possible rate of electrochemical crack penetration. The maximum current densities measured at 97°C were 2 and 0.25 amps/cm^2 for potentials of +100 and -400 mv (wrt S.C.E.) respectively. From Faraday's law of electrochemical equivalents:

$$\left(\frac{da}{dt}\right)_{max} = \frac{i_{max} M}{ZF\rho}$$

where Z is the number of electrons involved in the reaction, ρ is the density, M is the molecular weight and F = 96,500 coulombs/equivalent is the Faraday. These maximum possible penetration rates are plotted on Figure 13 and agree within an order of magnitude with the plateaux rates observed in the corrosion fatigue experimental results deduced from Figure 6. The activation energy to convert these calculated maximum penetration rate from 97°C to 288°C is at present not known. It is apparent that in these fairly high frequency experiments, the oxide rupture rate exceeded the rehealing or repassivation

From Figure 13 it is possible to deduce that in our experiments with A533-B steel in PWR water, strain rate sensitive stress corrosion is possible for strain rates greater than 1 sec^{-1}. For the low oxygen concentration, BWR environment data in Figure 8, the plateau rates of crack growth are observed at values of $\dot{\varepsilon}$ as low as 0.14 sec^{-1}. It is probable that a lower strain rate threshold is appropriate to that environment. In water at 288°C containing 8000 ppm oxygen, there is enough evidence to suggest that the threshold strain rate is in the region of 10^{-8} sec^{-1}.[17,18] This is consistent with well established notions for other stress corrosion systems that the threshold strain rate depends on the electrochemical potential.[16] Figure 13 can therefore be divided into three zones; a zone where bare surface dissolution rates are controlling, a zone where diffusion processes within the fluid are rate controlling and a threshold value of $\dot{\varepsilon}$ which depends on the water chemistry, and, very probably, on the steel metallurgy; in other words, the electrochemical potential. It is clear that the threshold for the electrochemical conditions with PWR water in our experimental rig is between 0.1 and 1 sec^{-1} and in fact probably close to the larger of these two values. From the results of Bamford et al, it is suggested that the threshold for the stress corrosion phenomenon is around 0.01 sec^{-1} since high corrosion fatigue crack propagation rates were not observed in experiments at 0.1 cpm and R=0.2. In fact the rates of crack propagation in these particular tests were equivalent to the inert environment fatigue crack growth rates, despite the fact that the value of K exceeded the threshold of 28 MPa$\sqrt{m}$.

It is possible from the above treatment of the corrosion fatigue results in terms of a fatigue plus strain rate sensitive stress corrosion mechanism to derive a map of combinations of R ratios and cyclic frequencies where the resulting strain rate will give resolvable plateau features in corrosion fatigue experiments. Such a map is shown in Figure 14 which divides into four basic areas; (i) where the fatigue crack growth rate is always faster with respect to time than the bare surface dissolution penetration rate, (ii) where the bare surface dissolution kinetics controls the plateau rate, (iii) where diffusion kinetics control the plateau rate and (iv) where passivation prevents stress corrosion cracking and either the crack arrests completely or only grows at the appropriate fatigue crack growth rate. Such a diagram was used in combination with Figure 13 to plan the experiments which led to the experimental results shown here in Figure 6.

Finally a calculation scheme for predictive purposes can be derived on the basis of the model using the principle of superposition of fatigue crack growth and stress corrosion cracking. The equation is:

$$\frac{da}{dN} = C_1 \Delta K^n + TC_2 \left(\frac{2}{T} \ln \frac{1}{R}\right)^{\frac{1}{2}} \left(1 - \frac{x}{T}\right)$$

where C_1, C_2 and n are constants, T is the tensile going period of any fatigue stress and $(1-\frac{x}{T})$ takes values between zero and one for Kmin < K_{ISCC} < K_{max}. Some examples are shown on a standard fatigue crack growth graph in Figure 15.

5 Conclusions

(i) Fatigue crack propagation rates have been determined for A533- B steel in an inert helium environment at 288°C, the upper bound being

$$\frac{da}{dN} = 1 \times 10^{-11} \Delta K^3 \text{ metres/cycle } (\Delta K \text{ in MPa}\sqrt{m})$$

This crack growth equation predicts faster crack propagation rates than the current ASME XI Appendix A code for dry cracks when $\Delta K < 50$ MPa $\sqrt{m}$, but slower rates for $\Delta K > 50$ MPa $\sqrt{m}$.

(ii) Corrosion fatigue crack growth data for a modern heat of A533-B steel in a PWR primary water environment have been determined at 0.0167 Hz (1 cycle/minute) for R ratios of 0.2, 0.5 and 0.7. The upper bound to these data is:

$$\frac{da}{dN} = 4 \times 10^{-11} \Delta K^3 \text{ metres/cycle } (\Delta K \text{ in MPa}\sqrt{m})$$

The high crack growth rates observed in nominally the same experiments in the USA have not been reproduced.

(iii) Corrosion fatigue crack growth data for A533-B steel in simulated BWR environments containing 100 to 500 ppb oxygen have shown a marked but transitory effect of oxygen on crack growth rates. Passivation causes these transient high growth rates to decay and eventually rates of growth appropriate to deoxygenated environments are observed.

(iv) A mechanistic model to explain these observations and those of other investigators who have observed much higher sustained crack propagation rates in either low flowrate simulated PWR

water or air saturated BWR water has been described. It is suggested that the observation of unusually high corrosion fatigue crack growth rates is dependent on the coincident operation of a strain rate sensitive stress corrosion process. Whether this phenomenon is observed or not depends primarily on the electrochemical potential, itself a result of a combination of metallurgical and water chemistry factors and, conceivably, electrical coupling with dissimilar materials.

(v) A quantitative calculation scheme based on conclusion (iv) has also been developed and has been used to define the experimental conditions required to observe chemical reaction rate dominated crack growth processes during corrosion fatigue tests. Experiments defined with the help of the model have been carried out and the evidence obtained supports the quantitative predictions within the range of variables tested so far.

References

1 T Kondo, T Kikuyama, H Nakajima, M Shindo and R Nagasaki, Proceedings of a Conference on "Corrosion fatigue: Chemistry, Mechanics and Microstructure" p539-556, University of Connecticut, USA, 14-16 June 1971

2 T R Major, D M Moon and J D Landes, Transactions of the ASME, J of Pressure Vessel Technology 99 (1977), 238-247

3 P M Scott and A E Truswell in "The measurement of crack length and shape during fracture and fatigue" p 69-84, Engineering Materials Advisory Services Ltd, 1980

4 ASME Section XI (1980)

5 P M Scott and B Tomkins - this conference

6 J Wiberg, Int J Press Ves & Piping, 8 (1980) 79-90

7 W H Bamford, Transactions of the ASME, J of Engineering Materials and Technology 101 (1979) p 182-190

8 M E Indig, Report NEDC 24625 (1979)

9 D A Hale, C W Jewett and J N Kass, Transactions of the ASME, J of Engineering Materials and Technology 101 (1979) p 191-198

10 D A Hale, J Yuen and T Gerber, Report GEAP-24098 (1979) and D A Hale, Report NEDC 25322 (July 1980)

11 T A Prater and L F Coffin, Report NEDC 25322 (July 1980)

12 T Williams, Private communication

13 W H Cullen, F J Loss, H E Watson, W H Bamford and L J Ceschini "Influence of critical variables on environmentally-assisted crack growth rates of RPV materials in PWR coolant environments", 8th Water Reactor Safety Information Meeting, Gaithersburg, Maryland, USA, October 1980

14 A McMinn, Private communication

15 R Jones, this conference

16 R N Parkins, Conference on "Defects and crack initiation in environment sensitive fracture" Newcastle University, 12-14 Jan 1981

17 F P Ford and M Silverman, Report HTGE 451-8-12 (1979)

18 F P Ford and M J Povich, G E Report No 79 CRD 007 (1979)

Table 1

PWR and BWR Water Chemistry Specifications

	BWR		PWR	
	Specification	Typical in this work	Specification	Typical in this work
Pressure, MPa	6.9	8.0 ± 0.2	17.2	15.0 ± 0.5
Temperature, ^{o}C	288	288 ± 0.5	288-315	288 ± 0.5
Conductivity (inlet), $\mu S\ cm^{-1}$	<0.1	<0.08	1-40	25 ± 2
Conductivity (outlet), $\mu S\ cm^{-1}$		<1.0		25 ± 2
Oxygen, ppb	50-200	<10-1100 as required. For >200 ±100	<100	<10
Hydrogen, ml/kg at STP	-	-	0-50	40
LiOH, ppm	-	-	0.6 - 6.2	3.4 - 6.2
H_3BO_3, ppm	-	-	0-13,000	10,000-13,000
Cl^-, ppm	<0.1	0.06	<0.15	0.06
F^-, ppm	<0.1	<0.02	<0.15	<0.02
pH (room temperature)	6.5-7.0	6.5 - 7.0	4.0 - 10.5	5.6 ± 0.1

Table 2

Composition (%) and mechanical properties at 20°C of SA 533 Grade B Class 1 Steel

	ASME specification	S-T orientation specimens	L-S orientation specimens	T-L orientation specimens	L-S orientation specimens
Cast		C8982	C8938	1 HH	63758.1
Country of Origin		UK	UK	USA	France
Carbon	0.25 (max)	0.19	0.21	0.19	0.185
Manganese	1.01-1.66	1.25	1.24	1.28	1.395
Phosphorus	0.035 (max)	0.017	0.016	0.009	0.010
Sulphur	0.040 (max)	0.013	0.012	0.013	0.006
Silicon	0.13-0.32	0.025	0.20	0.25	0.195
Molybdenum	0.41-0.64	0.49	0.49	0.55	0.485
Nickel	0.37-0.73	0.68	0.66	0.61	0.655
Chromium	-	0.13	0.08	0.04	0.130
Vanadium	-	-	-	0.004	-
Copper	-	0.07	0.09	0.10	0.095
Aluminium	-	-	-	-	0.022
Cobalt	-	0.009	0.013	-	-
Tin	-	0.011	0.012	-	-
Tantalum	-	0.002	0.002	-	-
Tensile Strength MPa	552-689	579-585	571-601		607-612
Yield Strength (0.2% offset) MPa	344	395-435	398-408	386	468-472
Elongation in 50 mm %	18	29	23-35		28-29
Reduction of area %	-	66	62		-

Table 3

'Plateau' Rates of Corrosion Fatigue Crack Growth

Reference	$(\frac{da}{dN})_{obs}$ mm/cycle	ΔK MPa $\sqrt{m}$	R	f Hz	T secs	$1-\frac{x}{T}$ for K>28MPa$\sqrt{m}$	$(\frac{da}{dN})_{scc}$ mm/cycle	$(\frac{da}{dt})_{scc}$ mm/sec	$\dot{\varepsilon}$ sec^{-1}
Water + 8.0 ppm oxygen at 288°C A333-6 steel Reference 11	2.9×10^{-2}	20 to 24	0.5	0.00021	4320	0.6 to 0.8	2.9×10^{-2}	9.6×10^{-6}	3.2×10^{-4}
	7.3×10^{-3}	22 to 30	0.5	0.0021	432	0.7 to 1.0	7.3×10^{-3}	2.0×10^{-5}	3.2×10^{-3}
	1.8×10^{-2}	25 to 28	0.5	0.021	43.2	0.9 to 1.0	1.8×10^{-2}	4.6×10^{-5}	3.2×10^{-2}
	1.0×10^{-2}	44 to 50	0.2	0.0021	432	0.6 to 0.7	1.0×10^{-2}	3.6×10^{-5}	7.5×10^{-3}
	1.5×10^{-3}	7 to 9	0.8	0.0021	432	1.0	1.5×10^{-3}	3.5×10^{-6}	1.03×10^{-3}
PWR water at 288°C A533-B A508-II and welds References 2,7	6×10^{-3}	45 to 80	0.25	0.0083	60	1.0	6×10^{-3}	1.0×10^{-4}	4.6×10^{-2}
	3×10^{-3}	35 to 100	0.16	0.0167	30	0.4 to 0.8	3×10^{-3}	1.7×10^{-4}	1.2×10^{-1}
	6×10^{-3}	20	0.70	0.0083	60				
			0.70	0.0167	30				
	1.1×10^{-3}	15 to 25	0.67	0.0167	30	1.0	1.1×10^{-3}	3.5×10^{-5}	2.7×10^{-2}
	2.3×10^{-3}	22	0.22	0.0167	30	0.7	2.3×10^{-3}	1.4×10^{-4}	1.0×10^{-1}
	3.2×10^{-3}	40 to 60	0.21	0.0167	60	0.6 to 0.8	3.2×10^{-3}	7.6×10^{-5}	5.2×10^{-2}
	2.5×10^{-3}	20 to 25	0.70	0.0167	60	1.0	2.5×10^{-3}	4.2×10^{-5}	1.2×10^{-2}
'Round Robin' Pure water at 288°C A533-B Reference 15	2.7×10^{-3}	45 to 60	0.2	0.0167	30	0.6 to 0.7	2.1×10^{-3}	1.1×10^{-4}	1.1×10^{-1}
This work PWR water at 288°C A533-B	1.5×10^{-4}	23 to 30	0.7	1.0	0.5	1.0	1.5×10^{-4}	3.0×10^{-4}	1.43
	2.1×10^{-5}	12 to 16	0.7	5.0	0.1	0.8 to 1.0	1.7×10^{-5}	1.7×10^{-4}	7.1
	2.5×10^{-5}	7 to 11	0.8	5.0	0.1	1.0	2.1×10^{-5}	2.1×10^{-4}	4.5

Note: f = cyclic frequency, T = that part of the cyclic period with the tensile strain increasing

$1-\frac{x}{T}$ = fraction of tensile period spent with K>28MPa$\sqrt{m}$

$$(\frac{da}{dN})_{scc} = (\frac{da}{dN})_{obs} - (\frac{da}{dN})_{fatigue}$$

$$(\frac{da}{dt})_{scc} = (\frac{da}{dN})_{scc} \cdot \frac{1}{T(1-\frac{x}{T})}$$

$$\dot{\varepsilon} = \frac{2}{T} \ln \frac{1}{R}$$

Table 4

Values of ΔK required for K_{min} or K_{max} in a fatigue cycle to exceed a value of K_{Iscc} = 28 MPa $\sqrt{m}$ as a function of R ratio

$R = \frac{K_{min}}{K_{max}}$	K_{max} = 28		K_{min} = 28	
	ΔK	K_{min}	ΔK	K_{max}
0	28	0		
0.1	25.2	2.8	252	280
0.2	22.4	5.6	112	140
0.3	19.6	8.4	65.3	93.3
0.4	16.8	11.2	42	70
0.5	14	14	28	56
0.6	11.2	16.8	18.7	46.7
0.7	8.4	19.6	12	40
0.8	5.6	22.4	7	35
0.9	2.8	25.2	3.1	31.1
0.95	1.4	26.6	1.5	29.5

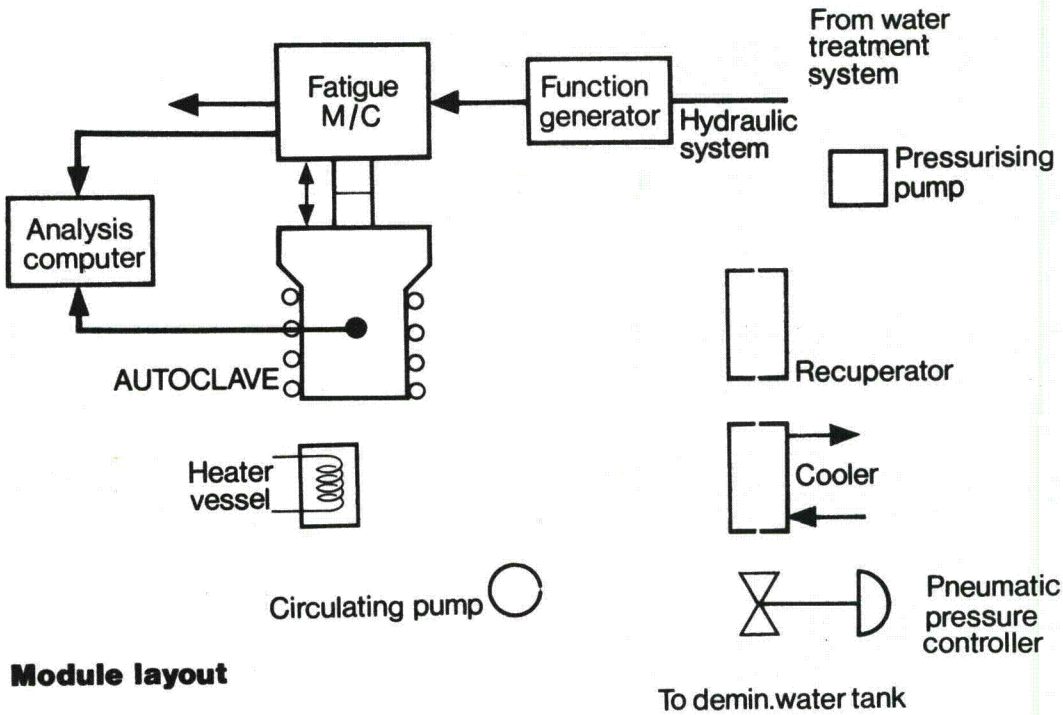

Module layout

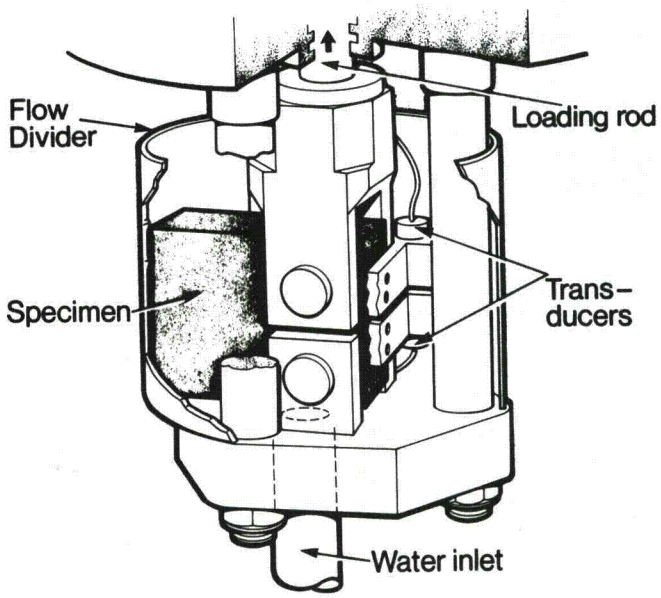

Specimen mounted in autoclave

Fig 1 Schematic Diagrams of the Corrosion Fatigue Test Rig

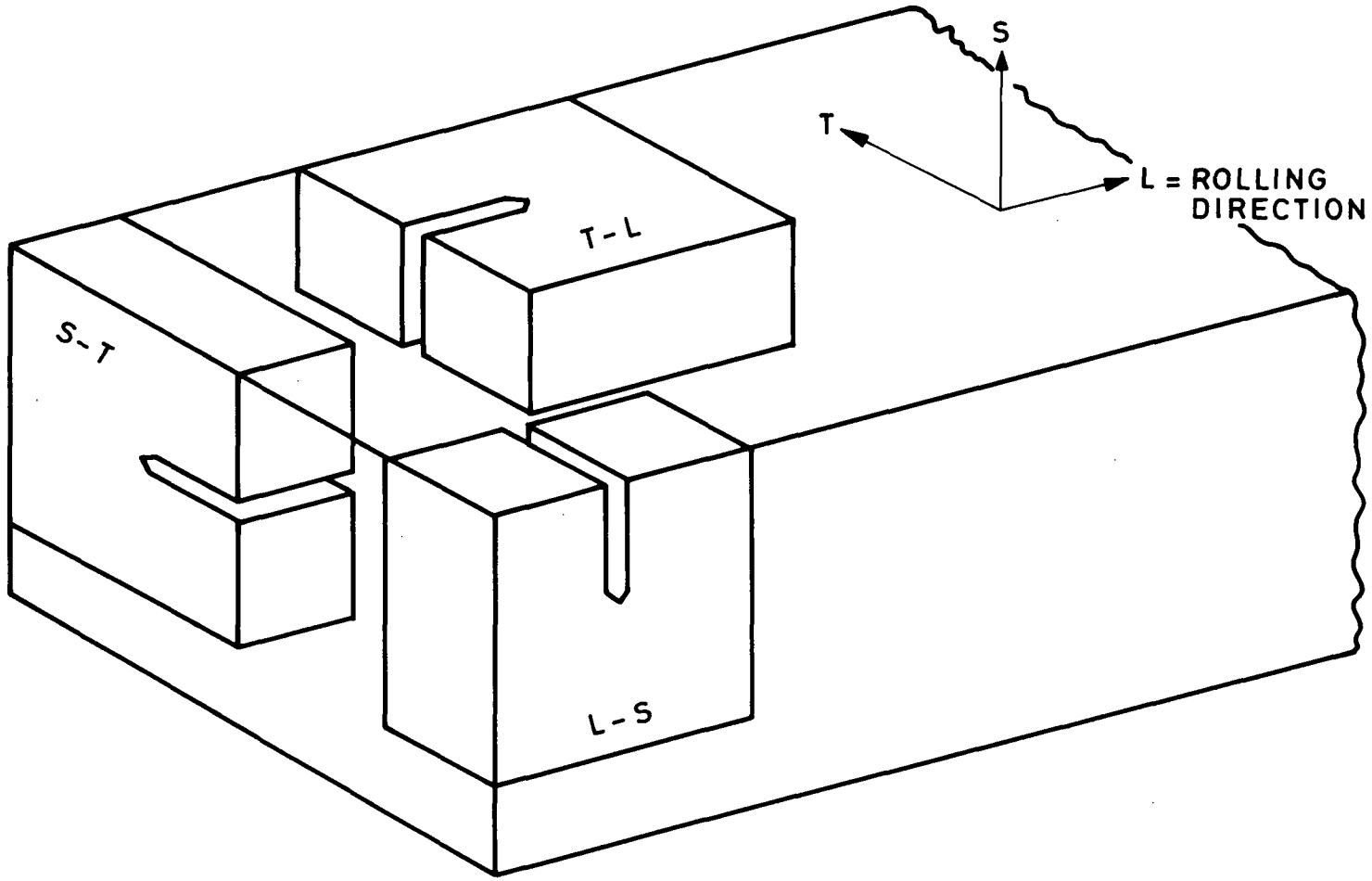

FIG. 2. SPECIMEN ORIENTATIONS.

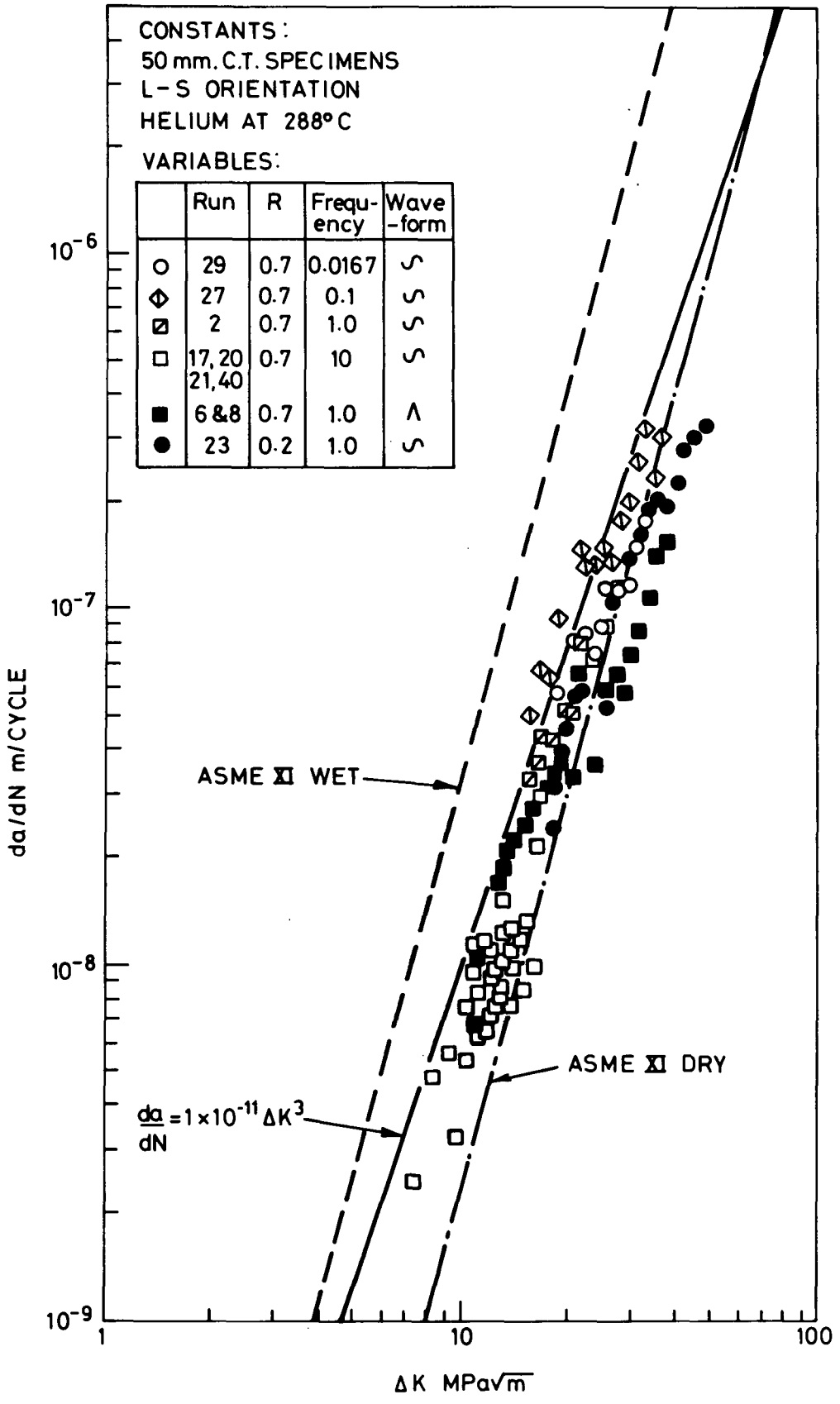

FIG. 3. CRACK PROPAGATION DATA FOR A533-B STEEL IN HELIUM AT 288°C.

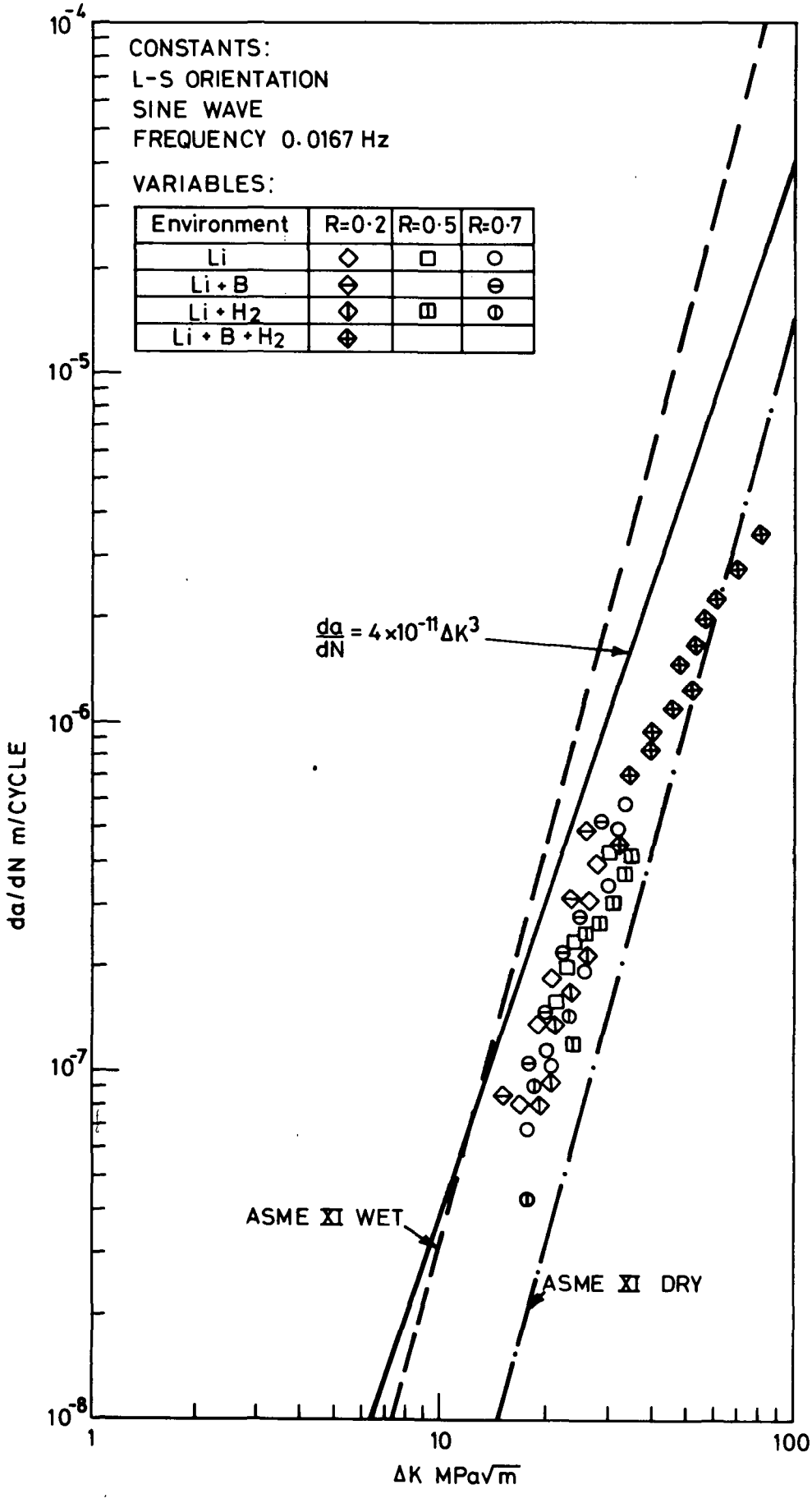

FIG. 4. INFLUENCE OF PWR WATER CONDITIONS ON CRACK PROPAGATION RATES IN A533B STEEL AT 288°C.

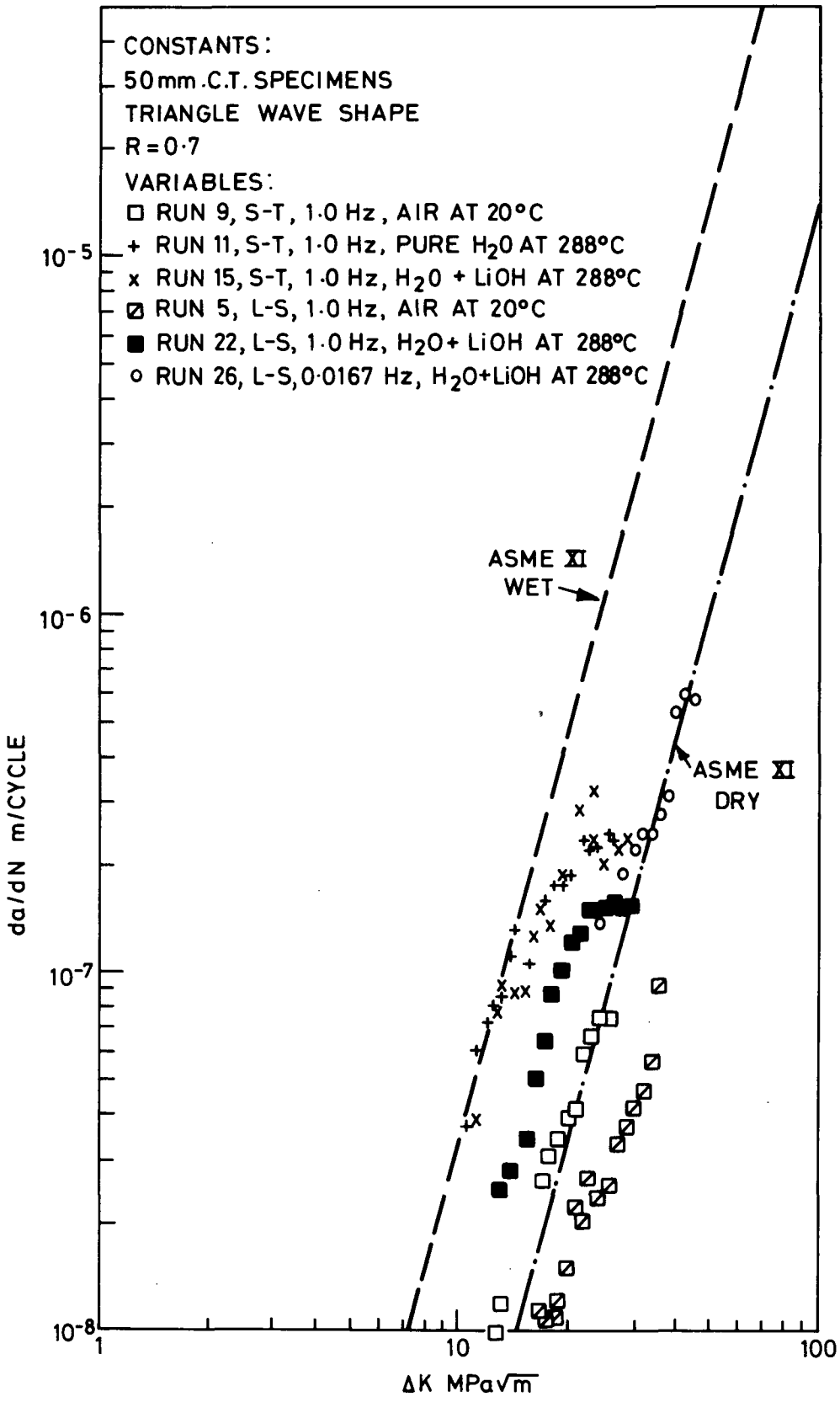

FIG.5. RESULTS FOR S-T ORIENTATION SPECIMENS OF A533-B STEEL & COMPARISON WITH L-S ORIENTATION SPECIMENS.

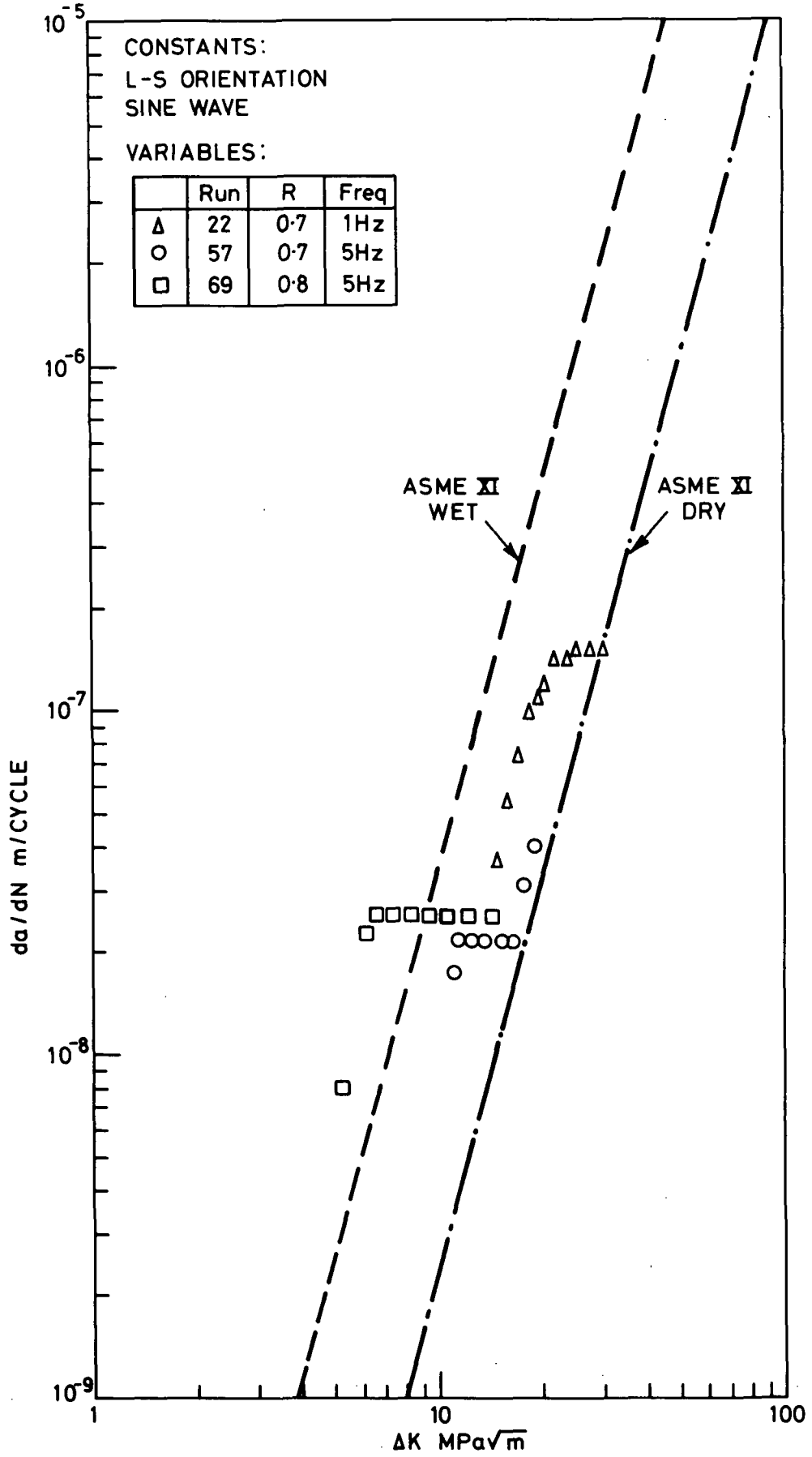

FIG.6. INFLUENCE OF R RATIO & FREQUENCY ON CRACK PROPAGATION RATES IN A533-B STEEL IN PWR WATER AT 288°C.

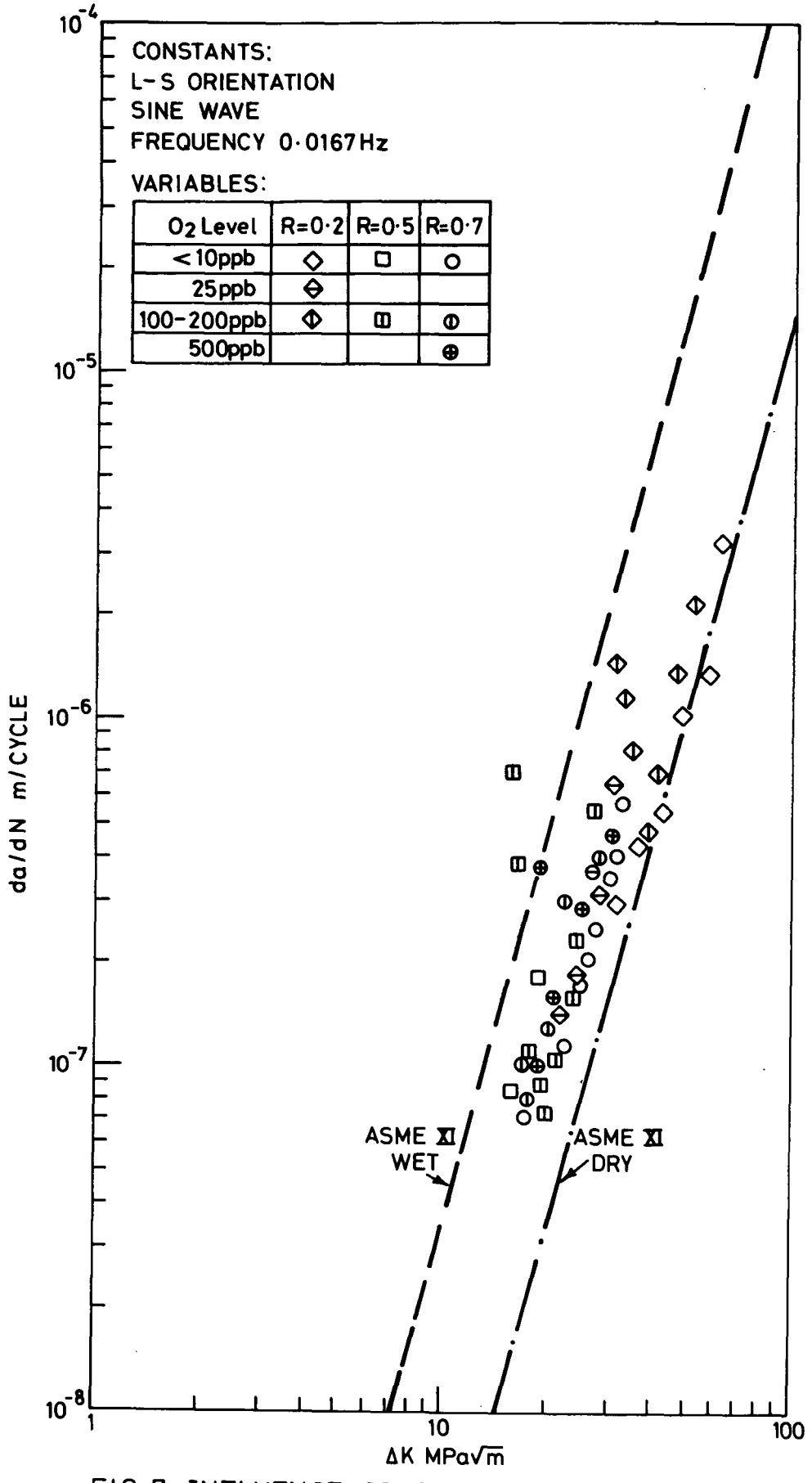

FIG. 7. INFLUENCE OF OXYGEN LEVEL ON CRACK PROPAGATION RATES IN A533B STEEL AT 288°C

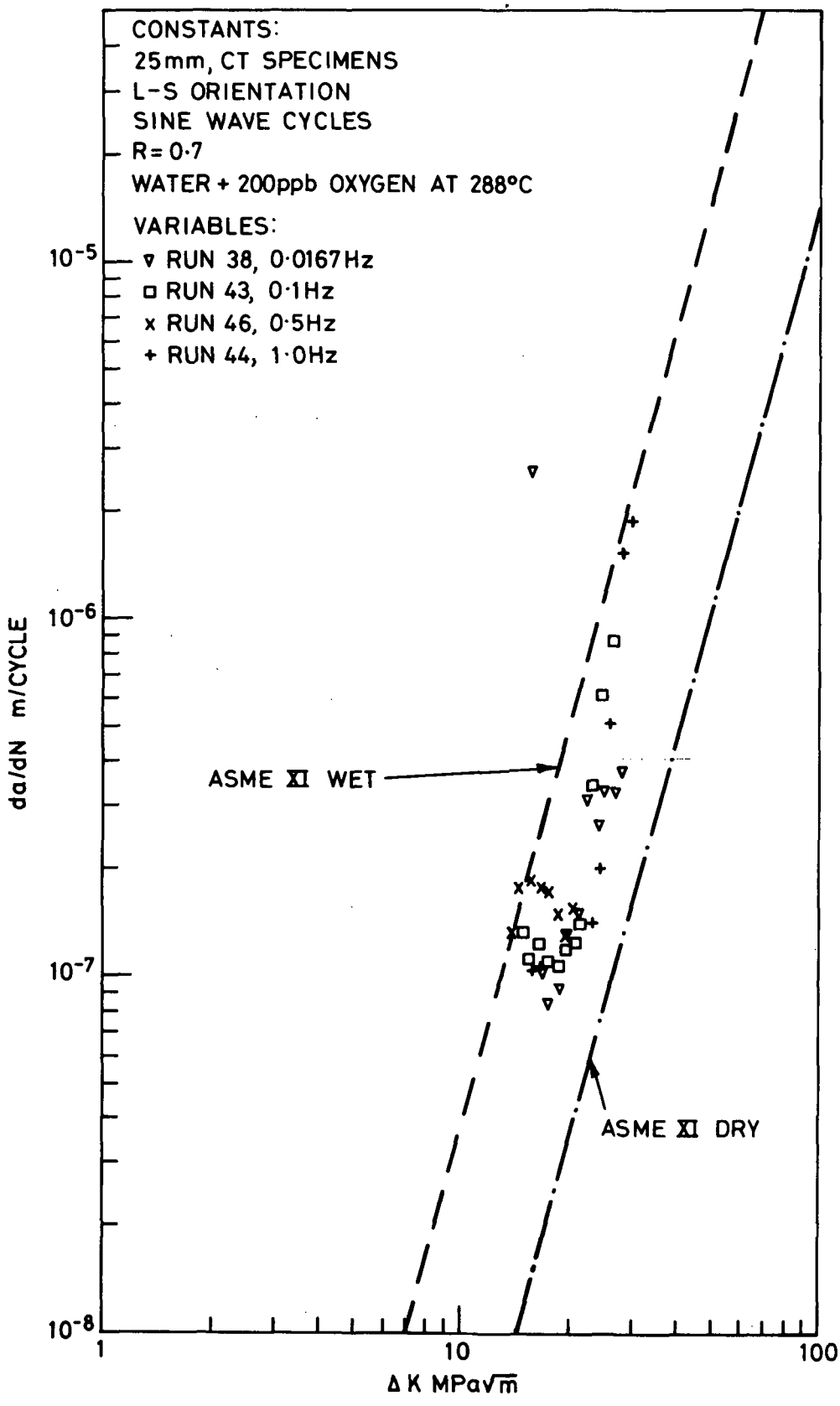

FIG. 8. INFLUENCE OF FREQUENCY ON CRACK PROPAGATION RATES IN A533-B STEEL IMMERSED IN WATER PLUS 200ppb OXYGEN AT 288°C.

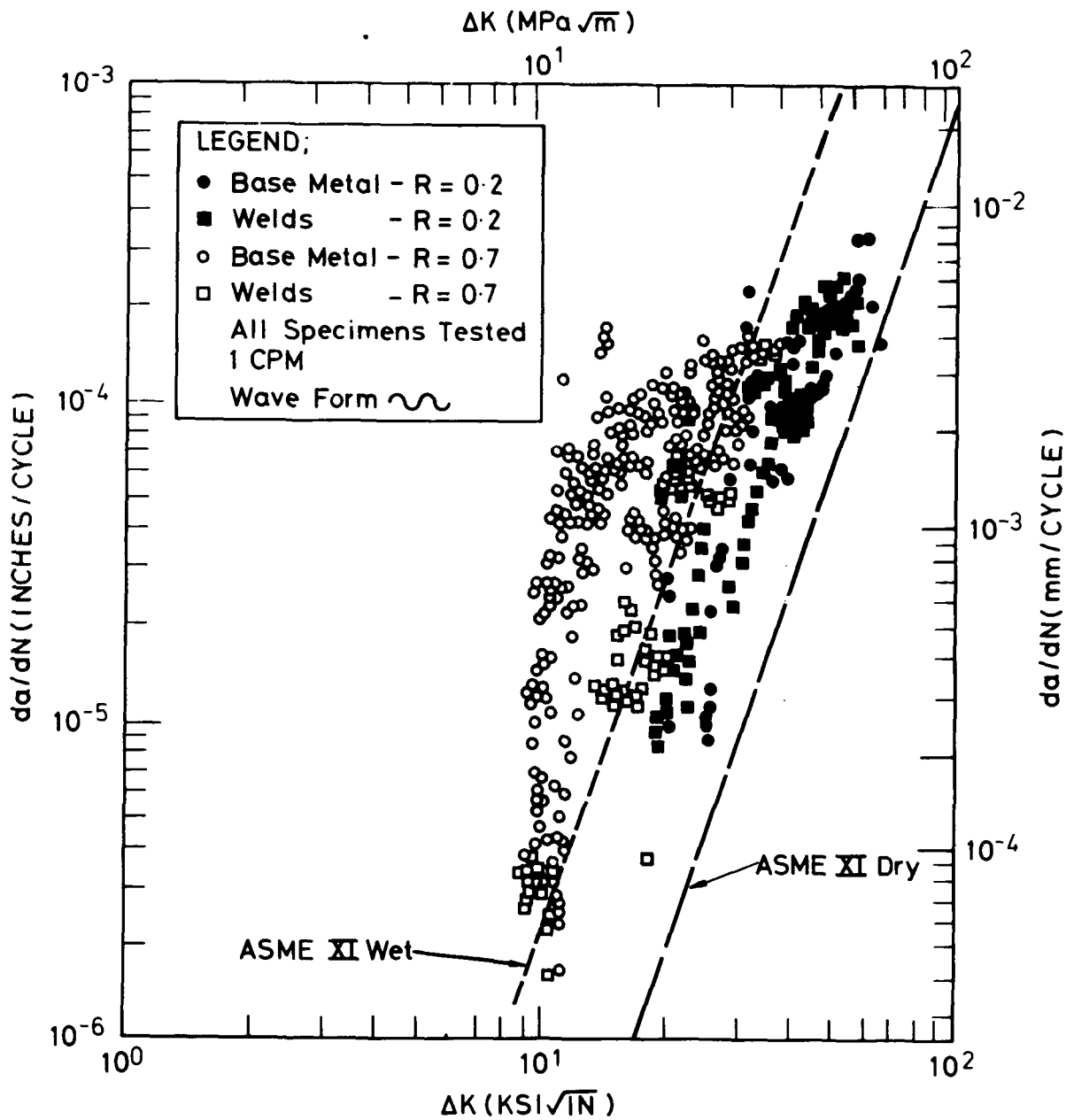

FIG.9. CORROSION FATIGUE DATA FOR A533-B-1 AND A508-2 BASE METALS AND WELDMENTS IN PWR PRIMARY WATER [7]

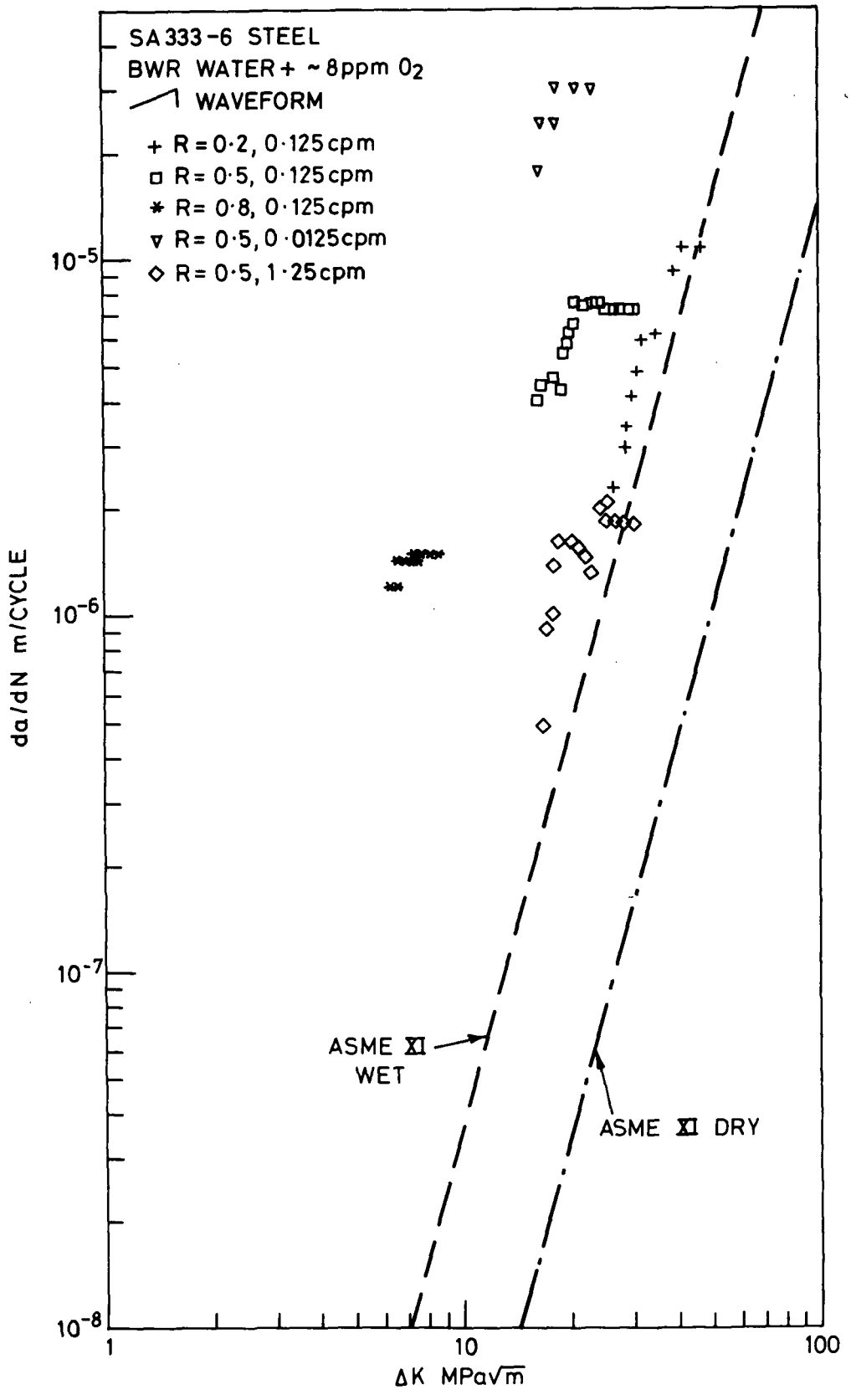

FIG. 10. CORROSION FATIGUE DATA FOR SA 333-6 STEEL IN AIR SATURATED WATER AT 288°C [11]

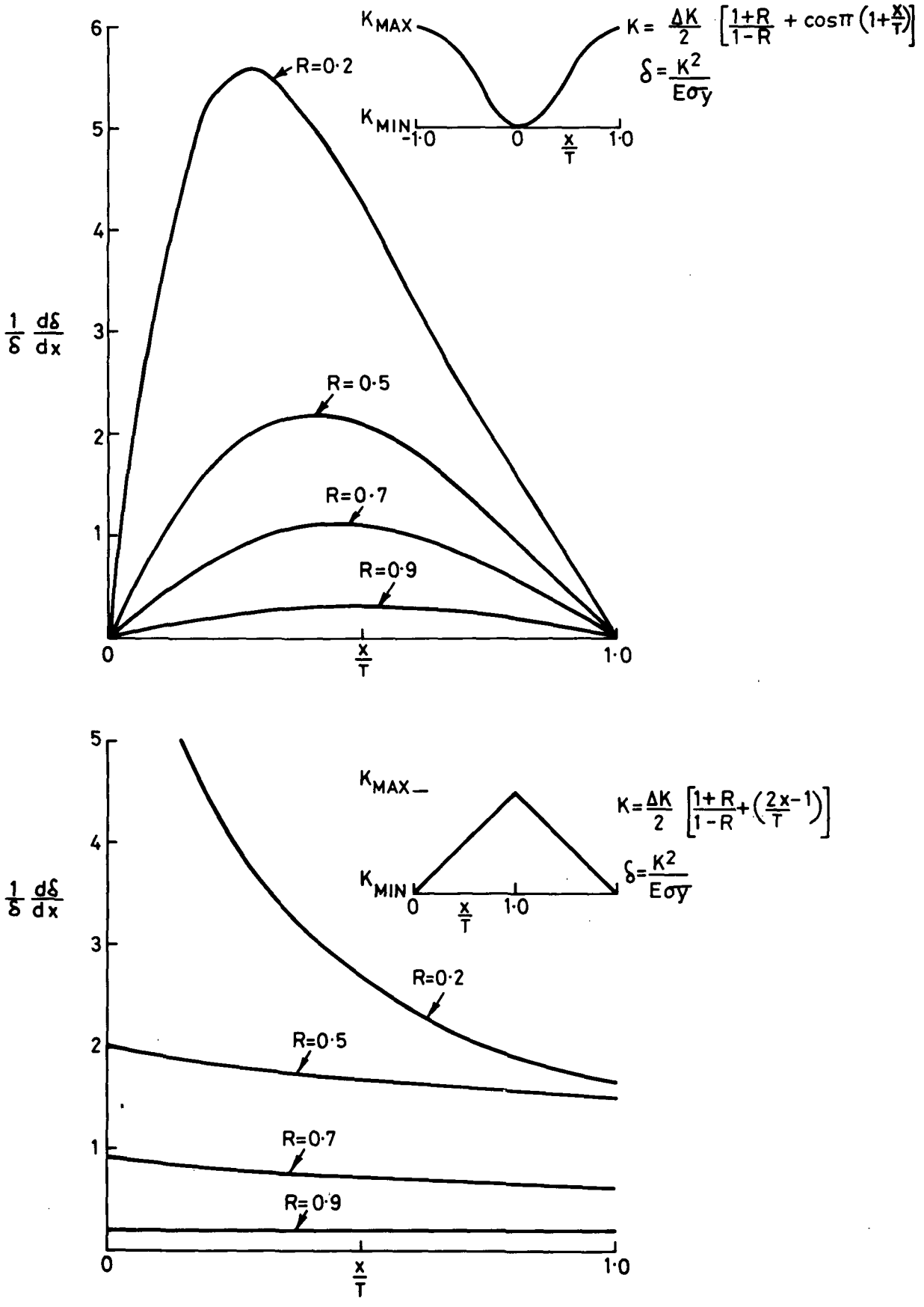

FIG. 11. CRACK TIP STRAIN RATES DURING SINE & TRIANGLE FATIGUE CYCLES.

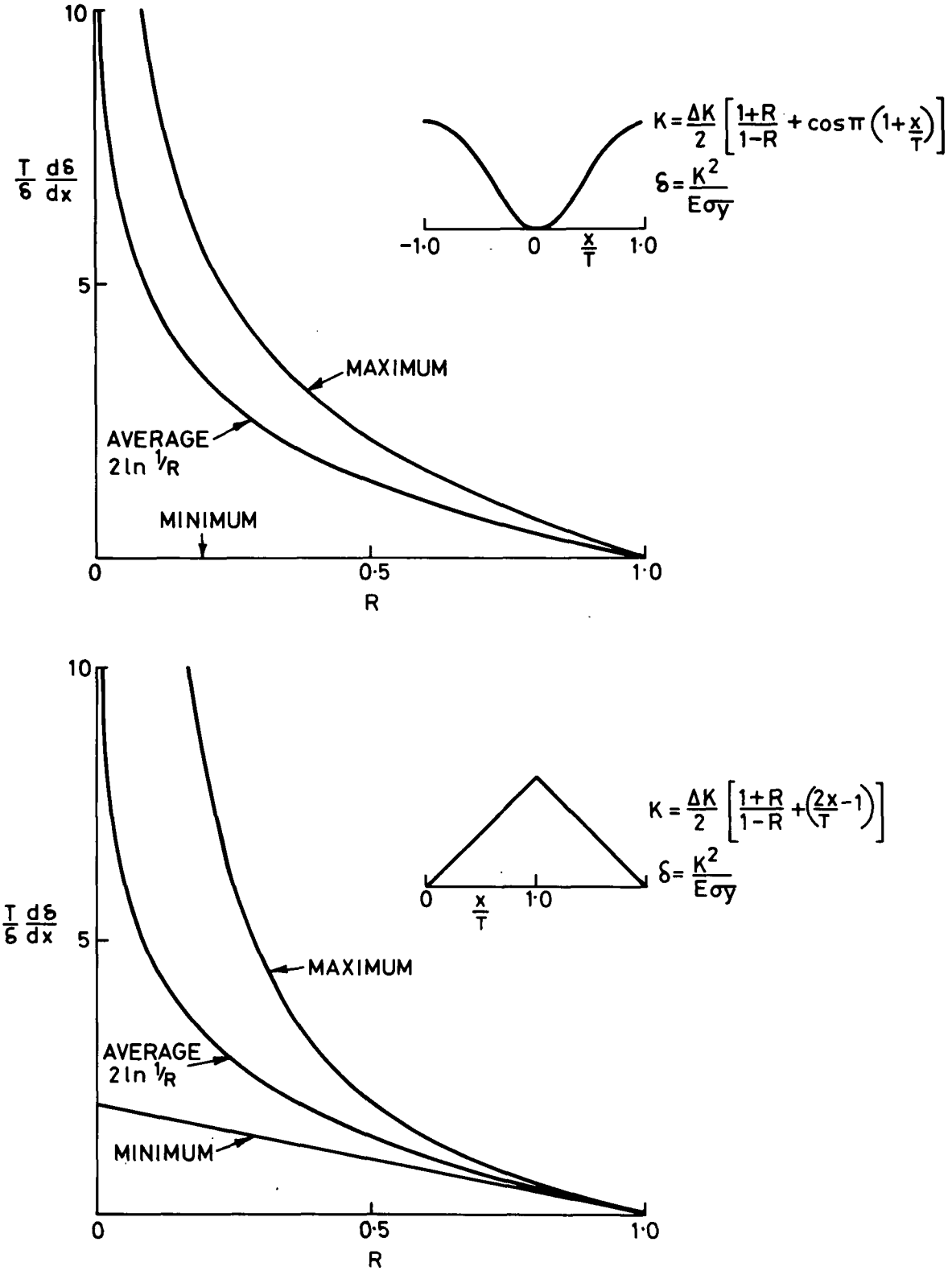

FIG. 12. AVERAGE & MAXIMUM & MINIMUM CRACK TIP STRAIN RATES DURING SINE & TRIANGLE FATIGUE CYCLES AS A FUNCTION OF STRESS RATIO.

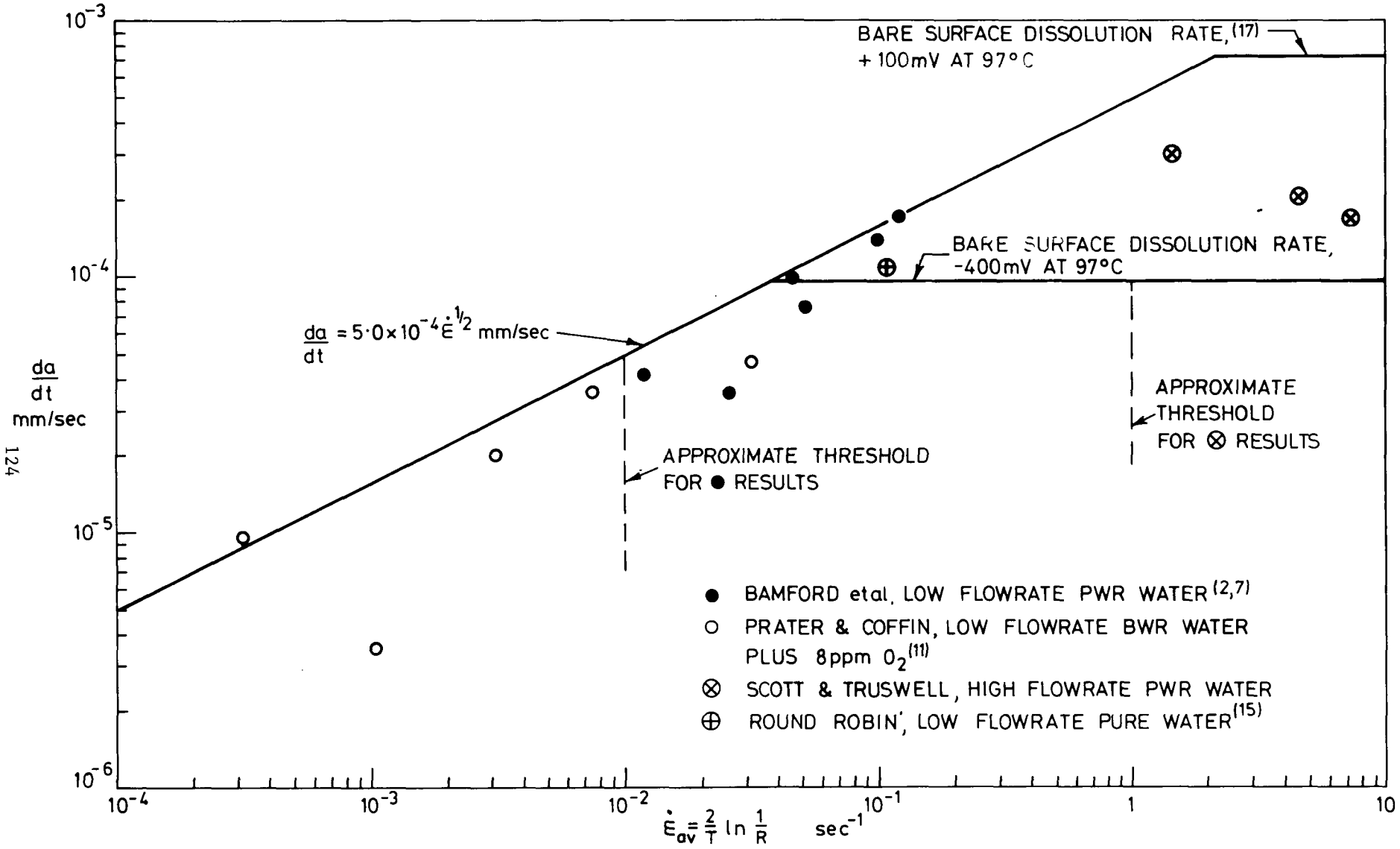

FIG.13. PLATEAU RATES OF CRACK GROWTH AS A FUNCTION OF CRACK TIP STRAIN RATE

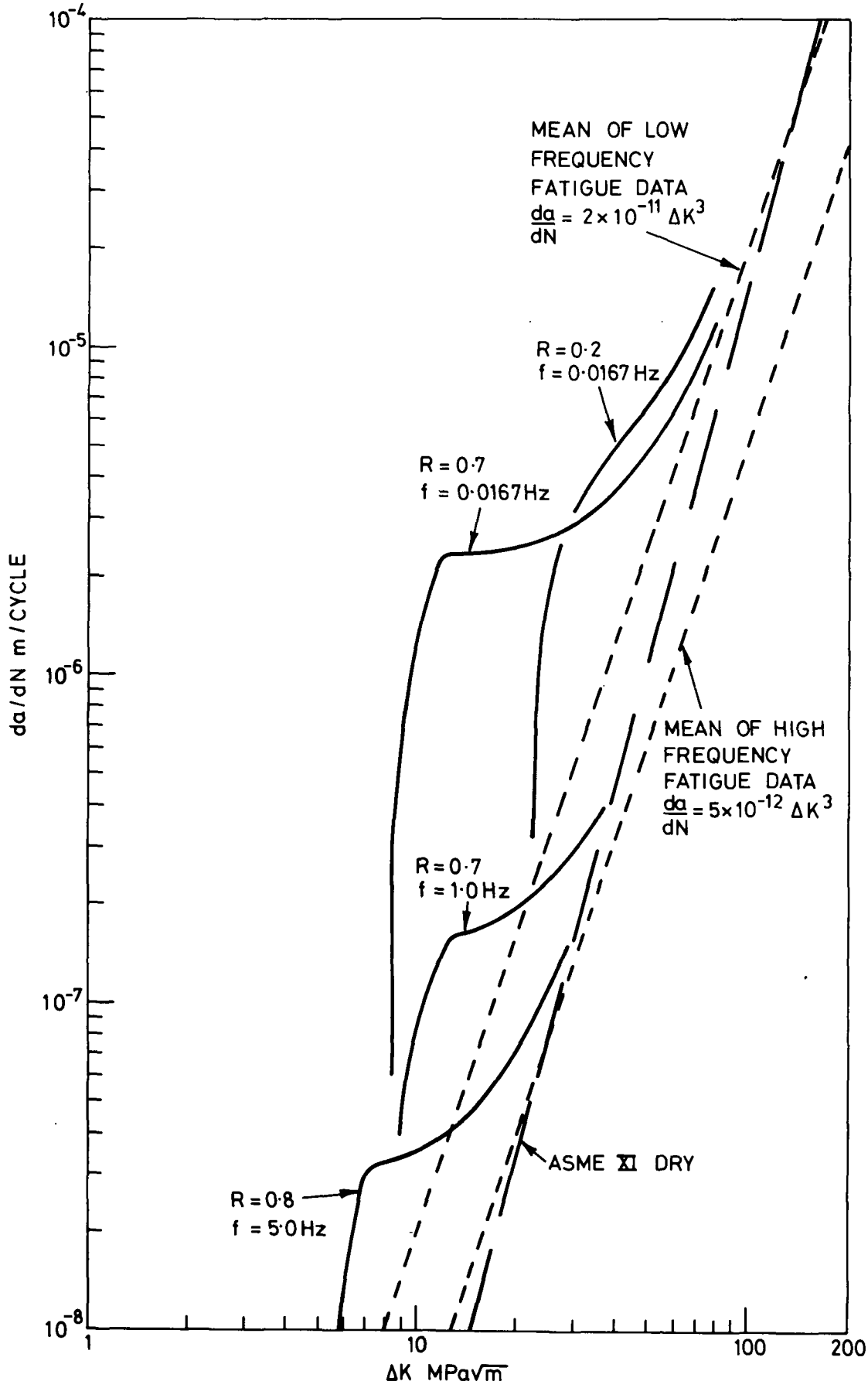

FIG. 14. CALCULATED CORROSION FATIGUE CRACK PROPAGATION CURVES INCLUDING STRAIN RATE SENSITIVE STRESS CORROSION CRACKING.

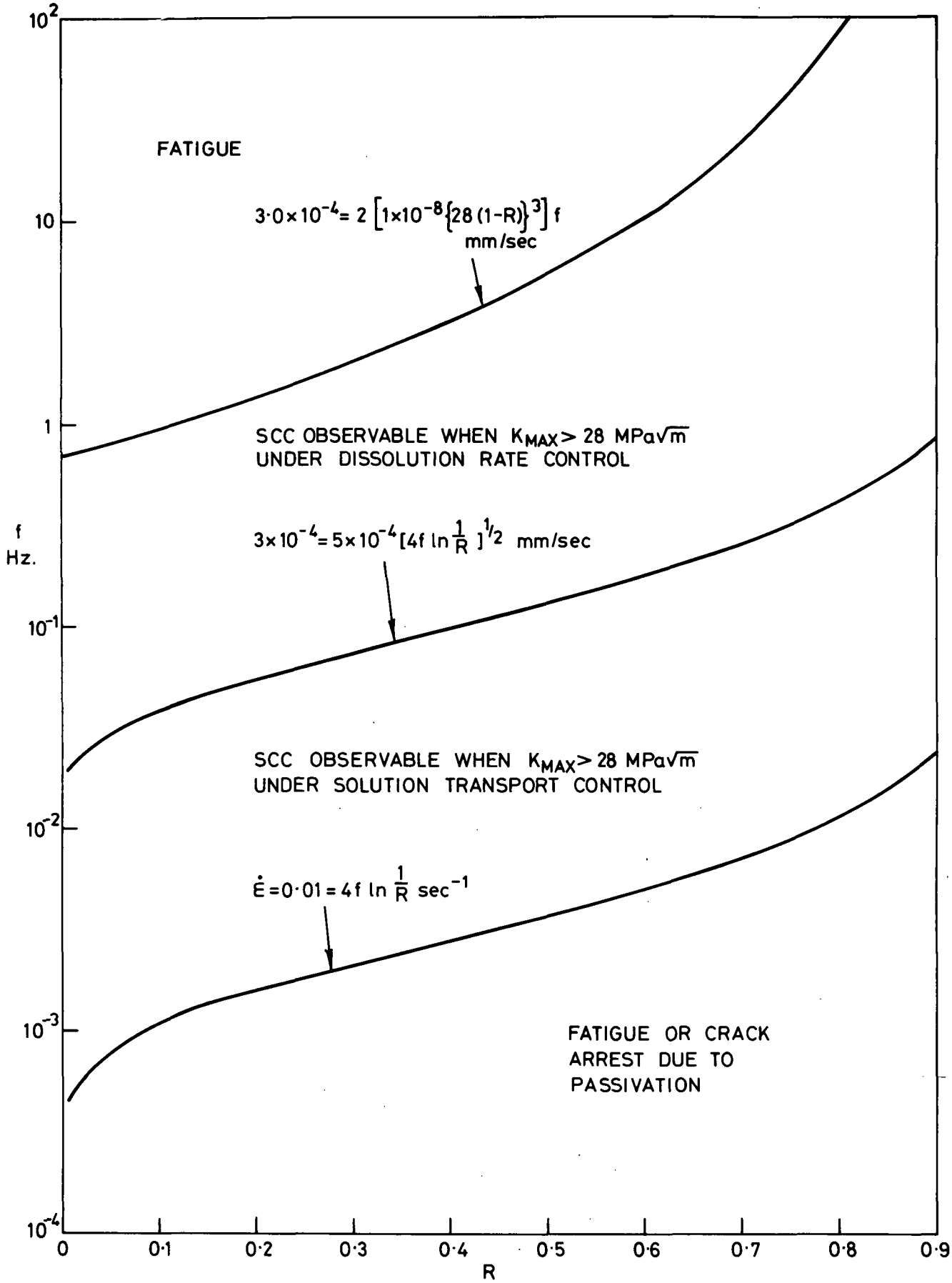

FIG.15. COMBINATIONS OF FREQUENCY AND STRESS RATIO FOR WHICH STRAIN RATE CONTROLLED STRESS CORROSION CRACKING CAN BE OBSERVED.

• IAEA - SPECIALISTS MEETING ON SUBCRITICAL CRACK GROWTH
FREIBURG - FEDERAL REPUBLIC OF GERMANY
13-15 MAY 1981

FATIGUE CRACK GROWTH OF LOW ALLOY STEELS IN PWR ENVIRONMENT

C. AMZALLAG* - J.L. BERNARD**

Abstract :

The paper presents different features of the fatigue crack growth rates of low alloys steels, in pressurized hot water environment.

The materials studied are a forged steel A 508 Cl 3 and a rolled steel A 533 B1. The parameters investigated were : frequency - sulfur content. waveform, stress ratio R.

The results are compared with published data, and suggestions on the mechanisms involved are made.

* Creusot-Loire - Centre de Recherches - 42701 FIRMINY - FRANCE

** Framatome - Tour Fiat - Cedex 16 - 92084 PARIS LA DEFENSE - FRANCE.

1. INTRODUCTION

The pressurized hot water environment is known to enhance the fatigue crack growth rates of low alloy steels.

Creusot-Loire, with Framatome and with also other organisations, are conducting, for several years, experimental programs aimed to the study of fatigue crack propagation in this environment.

This paper presents the results obtained on pressure vesel and the remarks which emerge.

The materials investigated are : a forged steel A 508 Cl 3, used in the French plants, and a rolled steel A 533 B1, used in other plants.

Attention was paid to the effects of frequency, waveform, R ratio and metallurgical variables, such as sulfur content.

2. EXPERIMENTAL PROCEDURE

2.1. Materials

The chemical and mechanical properties of the materials are given respectively in tables I and II - Two heats of A 533 B1 steel have been studied.

2.2. Specimens

The specimens tested are Compact-Tension Specimens, with T.L. orientation for the A508 steel, and both T.L. and L.T orientation for the A 533 Steel.

2.3. Testing device.

Tests are performed in autoclaves mounted in servo hydraulic testing machines. The crack growth is monitored continuously through the measure of compliance by a LVDT attached to the lips of the specimen, inside the autoclave. In order to get a calibration curve relating the crack opening to the crack length, beach marks are produced during the test, by cycling at high frequency with the maximum load constant and increased minimum load.

A view of one of the autoclave device is given in Figure 1. Two water chemistries have been used (C1 and C2). They are listed in table III.

2.4. Test matrix.

The test matrix is given in table IV, which indicates, for each test, the parameters investigated : frequency waveform, R ratio, sulfur content.

3. RESULTS AND DICUSSION

3.1. Reference tests.

Reference tests were conducted on A 533 and A 508 steels at low R ratio (R=0.2), with a triangular waveform and frequencies of 60 cpm and 1 cpm.

Sulfur levels were less than 0.014% (see table IV).

Results are given in figure 2 and compared to those obtained on A508 steel in air, at 290°C. It was shown elsewhere [1] that there was no significant difference between A 508 and A 533 steds in air environment.

It can be observed that :

(i) The FCGR results of A 533 steel at 60 cpm in pressurized hot water environment are in the upper part or slightly higher than the scatterhand in air, indicating a slight effect of environment at this frequency.

(ii) The FCGR results of A 533 and A 508 steels at 1 cpm fall out the scatterband of the results in air, indicating a significant effect of the frequency in the environment. Such effect is now well established [2.3.4].

(iii) The results of A 533 and A 508 steels at 1 cpm are very similar.

3.2. Influence of sulfur content.

Tests have been conducted on A 508 steel having 0.009% S and A 533 steel having 0.018% S. Results are given in figure 3 which shows very different behaviours for the two materials :

- The FCGR of A 508 steel (lowest sulfur content) in hot water environment is slightly above the scatterband of results in air.

- The FCGR of A 533 steel (highest sulfur content) in hot water environment exhibits the shape of plateau already reported by BAMFORD AND MOON [5] in PWR environment and VOSIKOVSKY [6] in other aqueous environments..

It is higher than the FCGR of the material having the lowest sulfur content for $\Delta K < 50$ MPa $\sqrt{m}$. For $\Delta K > 50$ MPa$\sqrt{m}$, the FCGR become equivalent.

For the material having the highest sulfur content, a second test has been performed with a 0.8T - CT specimen taken from the 2T - CT specimen of the first test. The results obtained are fully in accordance (figure 3) with the previons results.

To explain the sulfur effect, two hypotheses can be advanced. On one hand, it is known that the MnS inclusions act as traps for hydrogen. It can be thought that, in the present case, some embrittlement occured at the crack tip due to the S level. On the other hand, dissolution of sulfide inclusions can produce a more agressive environment at the crack tip which increases metal dissolution. At the present time, it is difficult to establish wether one of the two processes dominates or both are acting.

Examination of the results reported by CULLEN et al [7] tends also to show that the highest FCGR correspond to materials having high sulfur contents.

3.3. Influence of the waveform of the cycle.

Tests were performed on A 533 steel with a sinusoïdal wave shape. The results obtained are compared in figure 4 with the results obtained on the same material tested with a triangular wave shape.

It appears that, at the same frequency, the sinusoïdal wave shape enhances the FCGR. This could be explained by means of the local crack tip strain rate. Asssuming for the purpose of a simple explanation of the phenomenon, that $\varepsilon_{CT} \sim COD$ (e.g. [8]) and $COD \sim K^2$ [10], it implies that $\dot{\varepsilon}_{CT} \sim K \frac{dK}{dt}$.

Consequently, $\dot{\varepsilon}_{CT}$ diminishes when K increases up to K max in the sinusoïdal cycle while $\dot{\varepsilon}_{CT}$ increases in the triangular cycle.

In these conditions, it is possible that (i) critical deformations leading to deterioration of the oxyde film and (ii) critical strain rates for hydrogen diffusion or dissolution of metal occur more easily with the sinusoïdal cycle.

3.4. Influence of R ratio

Tests at high R ratio (R = 0.6) have been performed on A 508 steel with a low sulfur content. The results obtained are compared in figure 5 with results obtained with low R ratio(R = 0.2), on the same material. We can see that the crack growth rate curves follow roughly the same line for low and high R ratios. It appears that R ratio does not affect markedly the FCGR in the range investigated.

The examination of results reported in reference[7] , on a weld having an equivalent sulfur content and obtained with a sine wave form (f = 1 cpm) leads to a similar observation (i.e. a slight effect of R ratio).

However, tests performed on the same weld at the same frequency but with a positive sawtooth did show a significant effect of the R ratio. Such controversial effects of R ratio, on low sulfur containing materials, need more investigation.

4. CONCLUSIONS

The data generated in this study have shown several features of the fatigue crack growth rates of low alloy steels in hot water environment. They can be summarized as follow :

- a definite effect of frequency was observed,
- high sulfur content enhance corrosion-fatigue
- for a given frequency, sinusoïdal waveform is more detrimental than a triangular one
- in the range of rates investigated, the effect of R ratio on the FCGR of low sulfur containing materials does not appear as firmly established.

The reported results are in accordance with published data.

It has been suggested that the phenomena observed could be related to mechanisms involving dissolution and/or hydrogen embrittlement associated with manganese sulfides, and crack tip strain rate effects. The suggestions which have been advanced need more investigations.

TABLE I - Chemical composition

Material	C	S	P	Si	Mn	Ni	Cr	Mo	Cu	Co
A 533 B.1 Heat A	0.19	0.013	0.009	0.25	1.28	0.61	0.04	0.55	0.100	
A 533 B.1 Heat B	0.22	0.018	0.012	0.25	1.48	0.68		0.52	0.13	
A 508 Cl 3	0.16	0.009	0.008	0.18	1.27	0.68	0.23	0.48	0.05	0.01

TABLE II - Tensile characteristics at room temperature

Material	σy N/mm^2	σuts N/mm^2	E %	R.A. %
A 533 B.1 Heat A	452	597	27	66
A 533 B.1 Heat B	471	617	20	
A 508 Cl 3	462	594	15	74

TABLE III - Water chemistries

C1	pH at R.T. : 7	
	Chloride	< 0.1 ppm
	Fluoride	< 0.1 ppm
	Electrical conductivity	< μ mho/cm
C2	pH at R.T. : 5.1	
	Oxygen	< 0.10 ppm
	Chloride	< 0.15 ppm
	Fluoride	< 0.15 ppm
	Hydrogen	25-35 cm^3 (STR)/kg of water
	Total suspended solids	≤ 1.0 ppm
	Boron	2500 ppm
	LiOH	as require to adjust pH to value of 5.1
	Electrical conductivity	2,40 μ mho/cm

TABLE IV - Test matrix

Material	Spec.	Frequency cpm	Wareform	Stress ratio R	Sulfur content
A 533 B.1 Heat A	1HT.15	1	Triangle	0.2	0.013
	1HT.43	60	Triangle	0.2	
	1HT.50	1	Sinus	0.2	
A 533 B1 Heat B	IG1	1	Triangle	0.2	0.018
	IG1.1	1	Triangle	0.2	
A508 C13	H4.46002	1	Triangle	0.2	0.009
	H4.46005	1	Triangle	0.6	

REFERENCES

[1] BERNARD J.L, HOUSSIN B, SLAMA G, "Validation des caractéristiques de calcul des matériaux constituant le circuit primaire des réacteurs à eau sous pression" Reliability Problems of Reactor Pressure Water Components", Vol. 1, IAEA, Vienna, 10 - 13 oct. 1977, pp 251 - 287.

[2] KONDO T, et al, "Fatigue crack propagation behaviour of A 533 B and A 302 B Steels in high temperature aquaeous environments", HSST Program 6th Annual Information Meeting, April 25 - 26, 1972.

[3] SCOTT P.M., "Corrosion fatigue in pressure vessel steels for light water reactors", Metal Science, Volume 13, No7, July 1979, pp 396 - 401.

[4] BAMFORD W.H, "Application of corrosion fatigue crack growth rate data to integrity analyses of nuclear reactor vessels", Journal of Engineering Materials and Technology", Vol. 101, July 1979 pp 182 - 190.

[5] BAMFORD W.H, MOON D.M, "Some Mechanistic observations on the crack growth charachteristics of pressure vessel and piping steels in PWR environment", Corrosion Nace, Vol. 36, No 6, June, 1980, pp 289 - 298.

[6] VOSIKOVSKY O, "Fatigue crack grouth in on X-65 line-pipe steel at low cyclic frequencies in aquaeous environments", Journal of Engineering Materials and Technology", october 1975, pp 298 - 304.

[7] CULLEN W.H, LOSS F.J., WATSON H.E, BAMFORD W.H, CESCHINI L.J", Influence of critical variables on environmentally assisted crack growth rates of PVP materials in PWR coolant environments", Presented to, 8th Water Reactor Safety Information Meeting, National Bureau of standards, Gaithersburg, Maryland, 30 october 1980

[8] ATKINSON J.D, LINDLEX T.C, "The effect of frequency and temperature on environmentally assisted fatigue crack growth below K_{1SCC} in steels", Proc. conf. on the Influence of Environment on Fatigue, INST. of mechanical Engineers, London, 18-19 May, 1977.

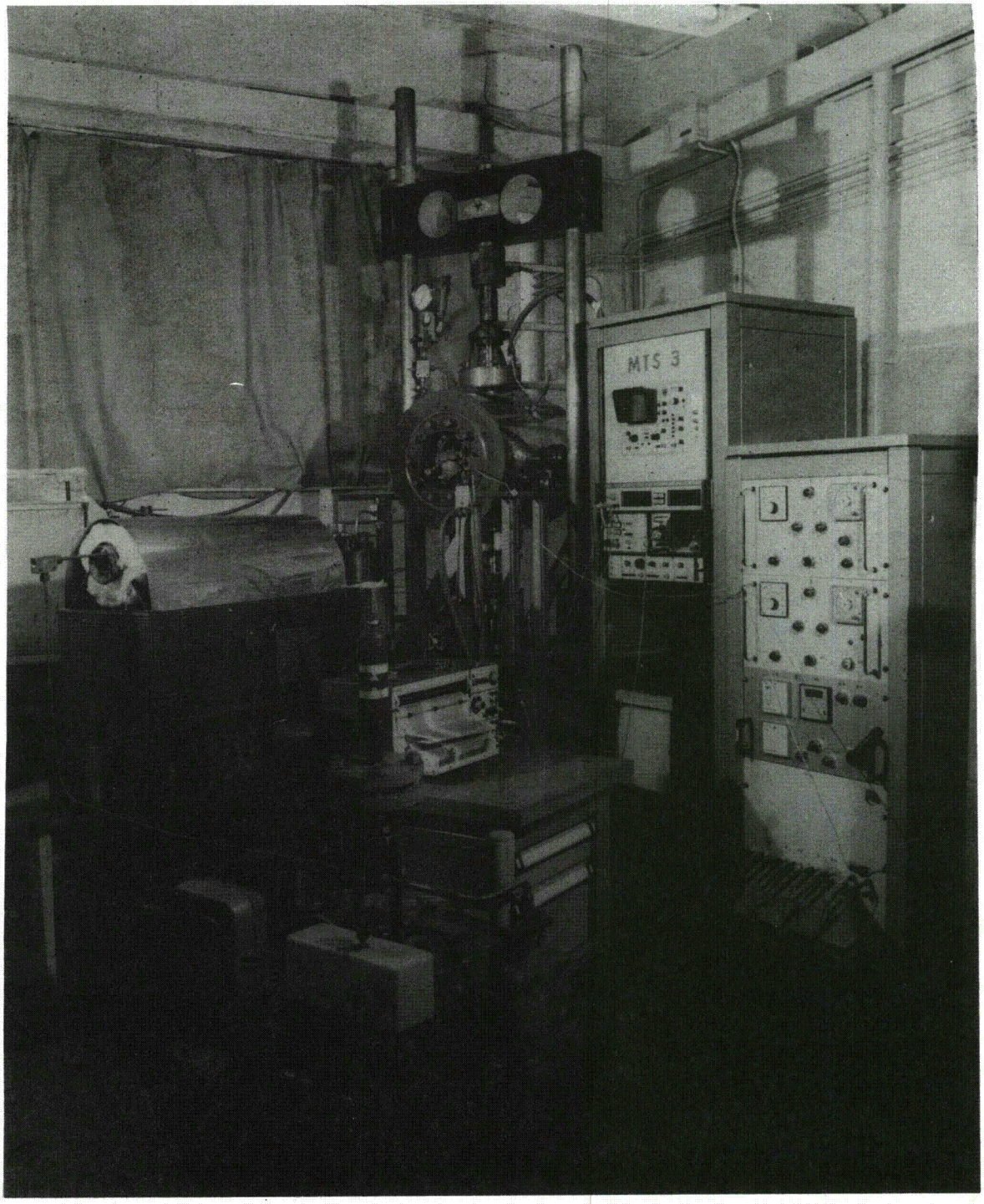

FIGURE 1 - VIEW OF A TESTING DEVICE

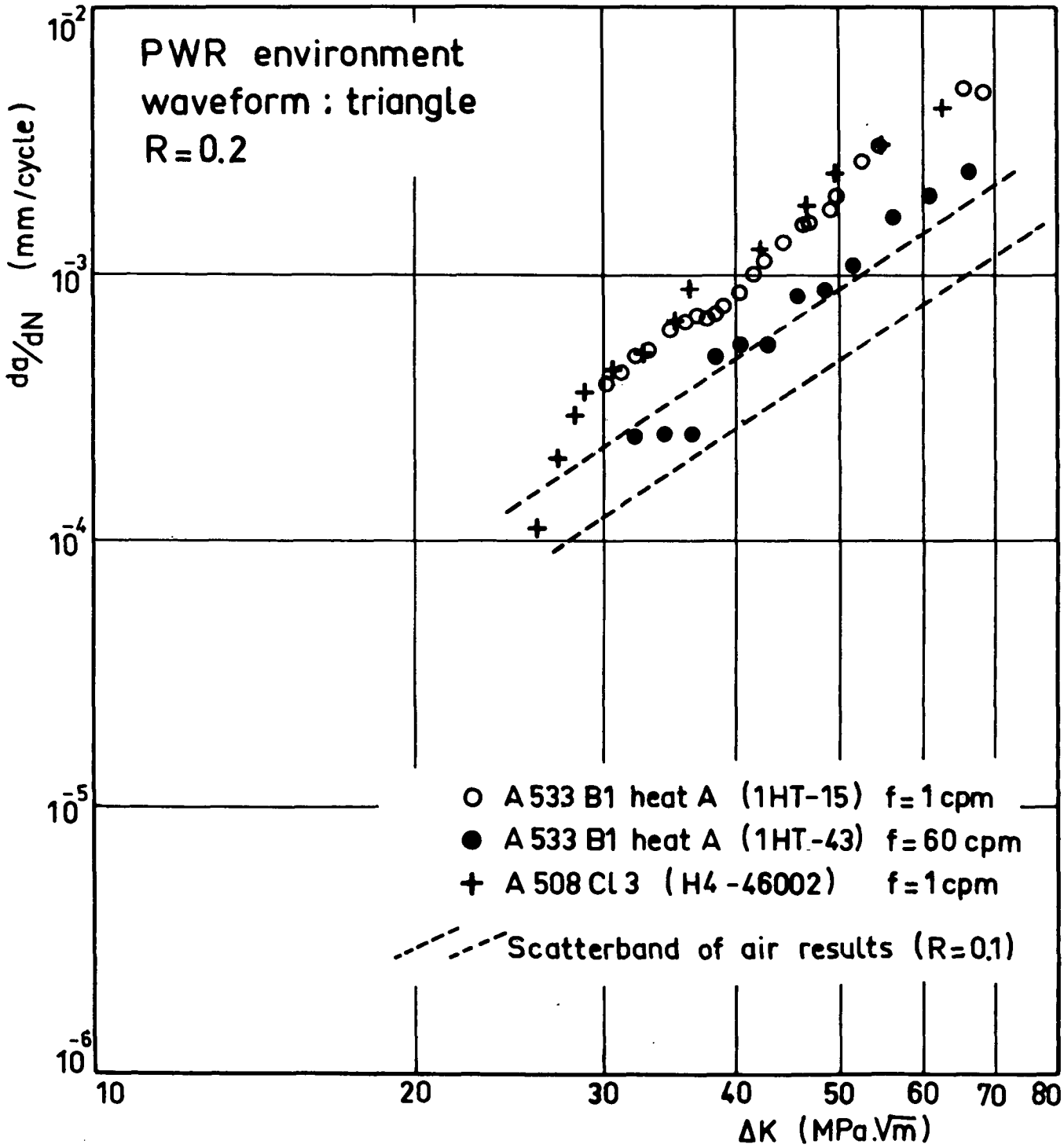

FIG. 2 - REFERENCE FCGR RESULTS AT R = 0.2

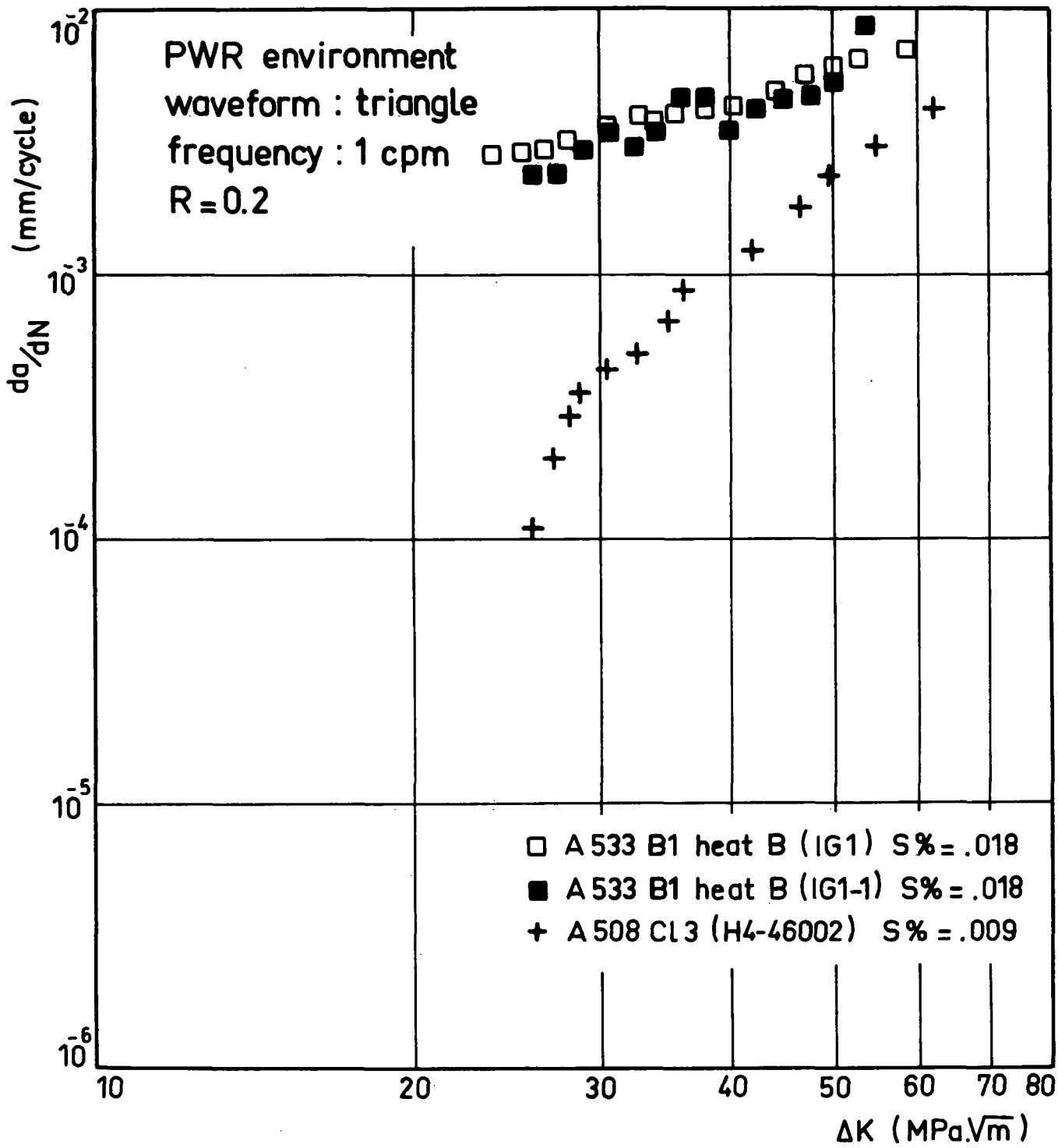

FIG. 3 - INFLUENCE OF SULFUR CONTENT ON THE FCGR OF LOW ALLOY STEELS IN PWR ENVIRONMENT

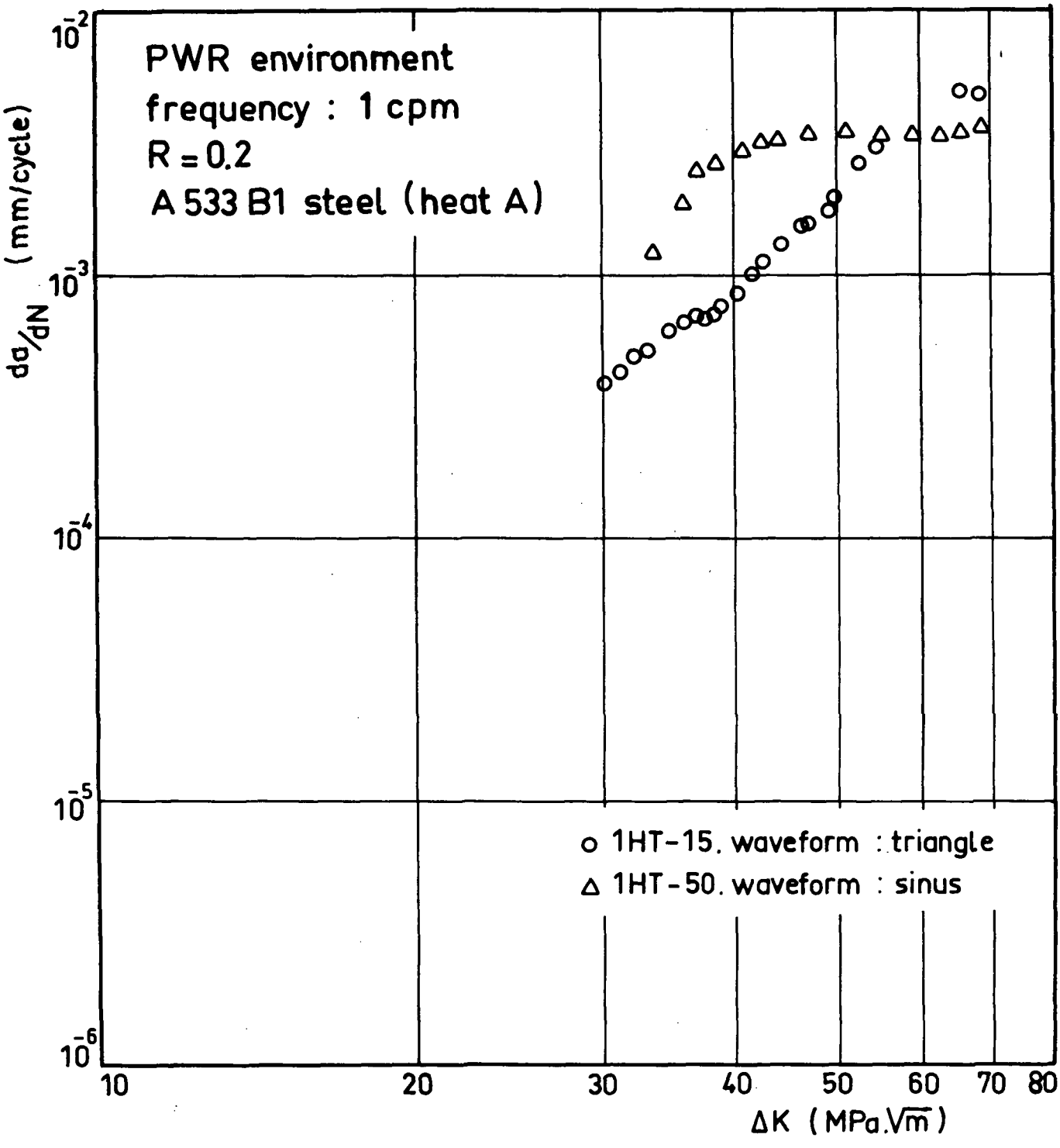

FIG. 4 - INFLUENCE OF THE WAVEFORM ON THE FCGR OF THE A533 B1 STEEL (HEAT A)

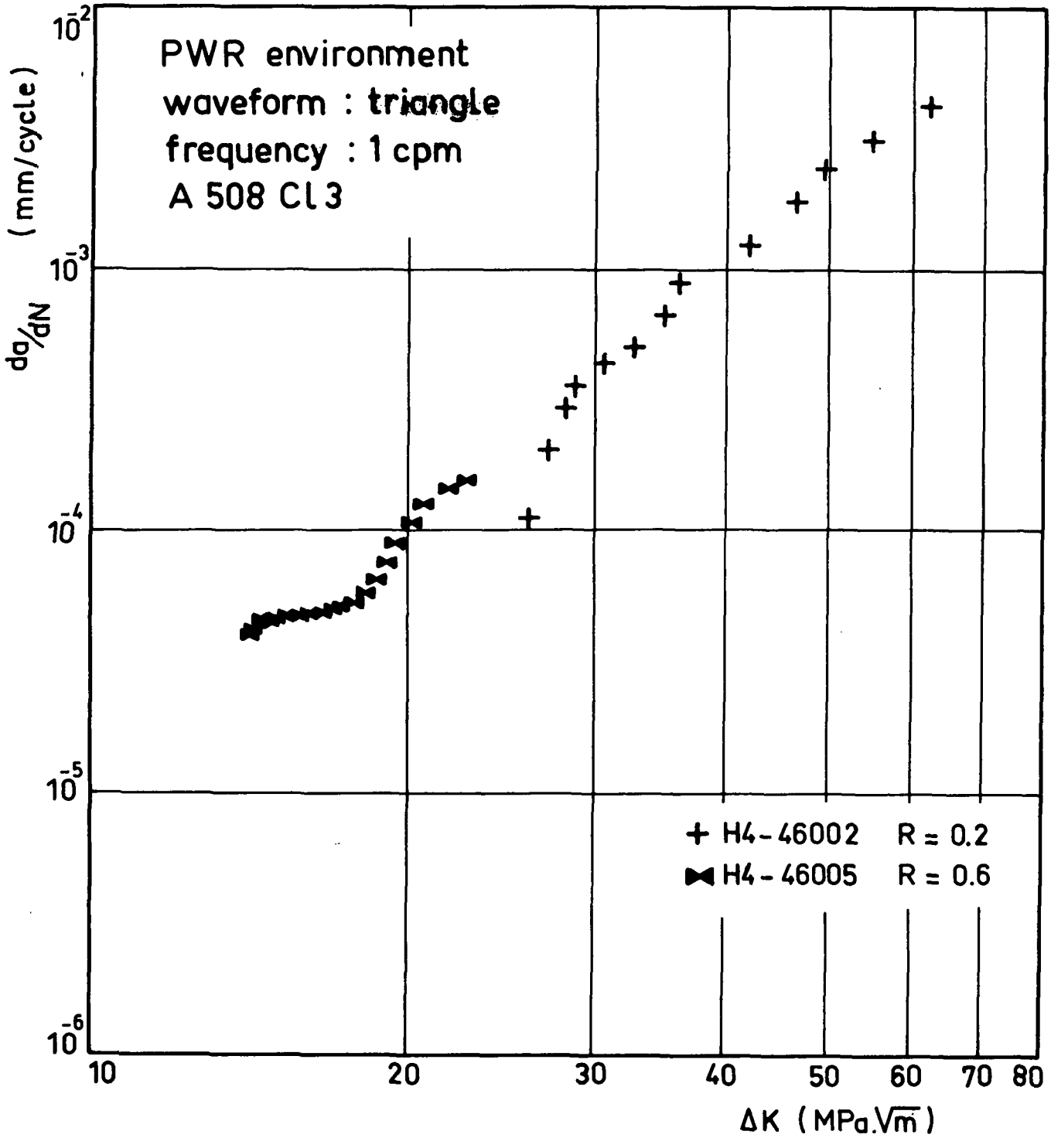

FIG. 5 - INFLUENCE OF THE STRESS RATIO R ON THE FCGR OF A508 CL3 STEEL.

Role of Loading Variables in Environment Enhanced Crack Growth for Water Cooled Nuclear Reactor Pressure Vessel Steels

T. Shoji and H. Takahashi

Dapartment of Engineering Science
Faculty of Engineering
Tohoku University
Sendai,Japan

H. Nakajima and T. Kondo

Japan Atomic Energy Research Institute
Tokai, Japan

1. Introduction

The expected total service life may be subjected to the estimation of the growth rate of flaws from some subcritical to a critical size under the influence of various factors that may contribute to the rate processes of the crack growth, eg. cyclic or sustained loads, chemical environment, temperature, and metallurgical state of the materials. It is now known that the aqueous environment within nuclear reactor pressure vessels, typically at 280°C-300°C and 7-17MPa, can cause fatigue cracks in pressure vessel steels to grow considerably faster than they would in air at the same temperature. ASME Design Code/Section XI provides the references fatigue crack growth curves for carbon and low alloy ferritic steels both in air and light water reactor environment including the R ratio effect. The range of R covered experimentally in recentlly available data [1][2] is 0.1 to 0.78 but many of the actual loadings experienced are for even higher R ratios. The recent experimental data [1][2] have now transgressed these lines and the possibility exists that the most adverse condition may not have been attained or quantified, and this means that the ASME design lines are constantly under review and fresh upper bounds may have to be drawn. It is also evident that no materials testing programme can simulate every conceivable operating condition in power stations, so that it is very important that the mechanisms of crack growth be understood to give confidence in long-term predictions of defect growth in pressure vessel.

The objective of this paper is to lay the groundwork for Design Code development by discussing from a mechanistic standpoint of the role of loading variables (mechanical factors) in corrosion fatigue crack growth acceleration.

2. Background

The significance of the strain rate effects in environment sensitive cracking has been widely recognized [3][4][5] with a rapidly increasing volume of experimental evidence indicating that the function of stress in a number of makedly different systems that display environment sensitive fracture is related to the strain rate that the stress produces. As have been pointed out by Ford [6], the interaction of fundamental parameters involved in the cracking process in ductile metals/aqueous environment system is tabulated as shown

in Fig. 1 where crack advancement from a preexisting flaw is assumed to be governed by an electrode reaction rate at the crack tip where a protective film is being rupture by the mechanical straining. In the case of slip dissolution model for crack advancement, the crack growth is faradically equivalent to the dissolution rate at the crack tip. On the other hand, in the case of hydrogen embrittlement, the reduction of water molecules or protons at the crack tip, absorption of the resulting hydrogen adatoms and their subsequent matrix diffusion to a favorable area (for instance, those with high triaxiality or high dislocation density) where cracking may take place. In both cases, the fundamental rate-determining parameters are oxide rupture rate, passivation rate and solution renewal rate.

Crack tip strain rate has direct influence upon oxide film rupture rate (bare surface nucleation rate). Hence it is of most importance to evaluate the crack tip strain rate for various loading conditions experienced in pressure boundary components during service operation. In other words, the role of loading variables have to be examined from this point of view, ie. crack tip strain rate. When the accurate evaluation of crack tip strain rate becomes possible for constant loads, cyclic load and dynamic slow straining, the reasonable correlation among the data obtained from SCC, CF and SSRT may be derived, and making the most of obvious advantage of SSRT that the results can be obtained relatively speedily in many systems as compared to constant load or strain or cyclic load experiments, SCC and/or CF behavior of the system of interest may be evaluated from SSRT behavior readily and relevantly.

Regardless of types of loading, ie. constant, cyclic and monotonically increasing load, the rapid dissolution reaction at the mechanically created bare surface and the subsequent repassivation plays a predominant role in environment enhanced crack growth. An example of the current transient under potentiostatic condition obtained from rapid extension test for A533B-1/ 0.1M-Na_2SO_4 combination is demonstrated in Fig. 2. The decay of the current at the early stage follows a simple relationship that is

$$i = i_{max} \exp(-\beta t)$$

where i is the current after time t, i_{max} is the initial current peak at time zero, and β is the repassivation constant. The difference of polarization behavior between fresh surface and polished surface of A533B-1 steel in 0.1M-Na_2SO_4 (25°C) is shown in Fig. 3, where the very high activity of bare surface is clearly demonstrated. Strain rate at the crack tip controlls

the crack advancement.

3. Mechanism and Mechanics of Environment Enhanced Crack Growth

3-1. Evaluation of Crack Tip Strain Rate and Crack Opening Rate.

Linear Elastic Fracture Mechanics and Elastic-Plastic Fracture Mechanics provide a useful tool for quantitative evaluation of the crack tip strain rate or crack opening rate. In LEFM approach for stationary crack, the crack opening displacement can be given by

$$\delta = \frac{K^2}{\sigma_y E} \tag{1}$$

where δ: crack opening displacement
K: stress intensity rate
σ_y: yield stress
E: Young's modulus

Hence, the crack opening rate is

$$\dot{\delta} = \frac{2K\dot{K}}{\sigma_y E} \tag{2}$$

where $\dot{K}$ is time variation of K $(=\frac{dK}{dt})$

Basing on the above expression, $K\dot{K}$ seems to be of importance for crack tip deformation rate and the relationship between the stress intensity rate and the crack tip opening rate is non-linear, but the effect should not be extreme when rates are measured after initial loading has result in a relatively large stress intensity factor. The significance of $\dot{K}$ in corrosion fatigue crack growth enhancement has been demonstrated experimentally for Cr-Mo steel/ 0.1N-H_2SO_4 systems [7] as shown in Fig. 4 and have a form

$$da/dN]_{E.} \propto \dot{K}^{0.45} \tag{3}$$

Basing on the BCS model, Parkins et al [8] correlate the crack opening rate with beam deflection rate $\dot{\ell}$, under constant load P.

$$\dot{\delta} = \frac{6P\dot{\ell}}{\delta G \pi^3} \tag{4}$$

On the other hand, Johnson and Radon [9] obtained the relationship between near tip strain rate and crack speed for growing crack in steady state. According to their analysis, strain rate at elastic/plastic interface, which may be important in hydrogen assisted cracking or hydrogen induced cracking, under constant loading condition can be obtained

$$\dot{\varepsilon}_y \simeq \pi K_I \dot{a}/[E\sqrt{(2\pi r_p)^3}] \tag{5}$$

where r_p: plastic zone radius

In this expression, the direct correspondence of near crack tip strain rate with crack growth rate is clear.

Recent development of Elastic-Plastic Fracture Mechanics made it possible to analyse the stress and strain field around growing crack in terms of J and δ where the ductile crack growth analysis is of interest [10].

For stationary crack, crack opening displacement can be related to J-integral as

$$\delta = \alpha \frac{J}{\sigma_o} \tag{6}$$

where α: numerical constant depending on work hardening exponent and Young's modulus and σ_o flow stress

Hence, crack opening rate is

$$\dot{\delta} = \alpha \frac{\dot{J}}{\sigma_o} \tag{7}$$

For a growing crack, Rice and Sorensen [11] and Rice, Drugan and Sham [12] obtained the near tip expression for the rate of opening displacement at distance r from the growing tip,

$$\dot{\delta} = \alpha \frac{\dot{J}}{\sigma_o} + \beta \frac{\sigma_o}{E} \dot{a} \ell n(R/r) \quad \text{as } r \longrightarrow 0 \tag{8}$$

where $\alpha/\beta \simeq 0.1$, $R \simeq 0.2E \frac{J}{\sigma_o^2}$ for simplicity.

Taking a tearing modulus T_{mat} as a material property, $\dot{J}$ can be related to crack growth rate,

$$\dot{J} = \left(\frac{\sigma_o^2}{E}\right) T_{mat} \cdot \dot{a} \tag{9}$$

Hence,

$$\dot{\delta} = \varepsilon_o \dot{a} \ (\alpha T_{mat} + \beta \ell n(\frac{R}{r})) \tag{10}$$

Taking typical values T_{mat}=300, the first term is predominant except the region very close to crack tip and the representative expression becomes

$$\dot{\delta} = \varepsilon_o \dot{a} \times \alpha T_{mat}$$

$$\doteqdot 0.5\dot{a} \tag{11}$$

In this case, the crack opening rate is proportional to crack growth rate. Basically similar relationship can also be obtained for fatigue crack growth. Based on the model for fatigue crack growth without environment assist proposed by Yokobori et al. [13], crack growth per cycle, $da/dN|_{inert}$, can be written as

$$da/dN = nb \tag{12}$$

where n is the number of dislocation emitted from crack tip until the time concerned, and depends on ΔK and K_{max}, and b Burgers vector. This expression can be rewritten in the time base crack growth rate,

$$da/dt = da/dN \times f = nbf \tag{13}$$

which means that the time base crack growth rate is proportional to the dislocation emission rate at the crack tip, that is, strain rate at the crack tip. Essentially the same result can be drawn by modifying the experimental result obtained by Davidson and Lankford [14], where the plastic strain range $\Delta\varepsilon_p$ has the form

$$\Delta\varepsilon_p = C/(A + Br) \tag{14}$$

where A and B depend on ΔK but C is constant, r distance from the crack tip. The plastic strain increment with fatigue crack growth is

$$d(\Delta\varepsilon_p)/da = -d(\Delta\varepsilon_p)/dr = BC/(A + Br)^2 \tag{15}$$

Here time base expression is

$$(d(\Delta\varepsilon_p)/dt)/(da/dt) = BC/(A + Br)^2 \tag{16}$$

Therefore the averaged strain rate near tip region is

$$\dot{\varepsilon}_p = [BC/(A + Br)^2]\,\dot{a} \qquad (17)$$

which yields a proportionality between the averaged strain rate near tip region and time base fatigue crack growth rate although the slight effect of ΔK is yet involved in A and B.

As a consequence of above discussion, it may be possible to take the crack growth rate $da/dt|_{inert}$ produced mechanically as a potential representative parameter for description of crack tip strain rate or crack opening rate which is controlling parameter for environment enhanced subcritical crack growth. A laboratory air generally can be regarded as an inert environment for high toughness pressure vessel steels and piping materials such as SA533B-1 and SUS304 or 316 stainless steel respectively.

Fig. 5 shows a modified illustration for explaining an interplay of mechanical, metallurgical and environmental factors, paying attention to the conjoint reaction at the crack tip. The mechanical factors such as ΔK, K_{max}, $\dot{K}$ or frequency, wave form and hold time, have a significant influence upon the local environmental condition and the rate of formation of fresh metal surface at the crack tip. The latter rate can be directly evaluated in terms of crack tip strain rate, in other words, crack growth rate mechanically induced, $da/dt|_{inert}$ or $da/dt|_{air}$. The resultant crack growth rate in aggresive environment $da/dt|_E$ is expected to be strongly influenced by the quantity of $da/dt|_{air}$.

3-2. Corrosion Fatigue Data Evaluation by Use of $da/dt|_E$-$da/dt|_{inert}$ Diagram

The feasibility of this new approach to interpret the environmental effects on fatigue crack growth in examined in many material/environment systems including data appeared in cited references. The results are shown in Fig. 6 to 12 where the time base crack growth rate in environment $da/dt|_E$ are plotted against the time base crack growth rate in inert or air environment (hereafter $da/dt|_E$-$da/dt|_{air}$ diagram is denoted as growth rate diagram). In Fig. 6, $da/dt|_E$ data are uniquely related to $da/dt|_{air}$ regardless stress intensity range ΔK, stress ratio R and frequency. Fig. 7 shows growth rate diagram for several low alloy steels in 85°C pure water environment with four dissolved oxygen content conditions, condition 1, 2, 3 and 4 are in wet condition in N_2 gas, in pure water with D. O. 0.5 ppm, in pure water with

5 ppm and in wet condition in O_2 gas.

No systematic effects of O_2 on crack growth enhancement are observed because of relatively high content of oxygen. Fig. 8 also shows a growth rate diagram for A533B-1 steel in 85°C pure water including the extreme mechanical conditions, extreme high frequency, 30 Hz and stress ratio 0.9~0.95. In spite of these extreme conditions, a single relationship between $da/dt|_E$ and $da/dt|_{air}$ can be obtained. These results support the validity of present concept for crack growth enhancement that $da/dt|_{air}$ as a representative parameter for crack tip strain rate controls the degree of crack growth enhancement. Fig. 9, 10 and 11 show the effect of high temperature water on cyclic crack growth for the ferritic vessel steel and the austenitic stainless steel peculiar to BWR or PWR use. Fig. 9 involve the data at different stress ratio and the single relationship can be drawn. These data were plotted from maximum growth rate data in the references which involve great scatter. At the small $da/dt|_{air}$, the environment accelerations factor $(da/dt|_E/da/dt|_{air})$ reaches to a thousand. It is important to note here that the cracking behavior of austenitic stainless steel is different with others and the diagram shown in Fig. 10 suggests the existence of a simple time dependent cracking SCC at lower $da/dt|_{air}$.

Fig. 11 shows the crack growth data of SA533B-1 steel with three different microstructures in simulated BWR environment including the stress ratio effects. Three microstructures involve base metal, oil quenched and oil quenched+tempered microstructure. The quenched material with martensite microstructure shows the highest sensitivity to stress ratio R and crack growth rate have higher values than other two microstructure. This tendency essentially agrees with the data on weld HAZ of the same material that the coarse martensitic-bainitic microstructure possess the higher growth data than other weld HAZ microstructure, for example, sorbitic microstructure and base metal, tempered bainitic structure when the effects of local residual stress on growth data in actual weld HAZ is considered in relation to particular responce of each microstructure to stress ratio R.

3-3. Slow Strain Rate Test Using Fracture Mechanics Specimens and its Correlation with SCC and CF Data

Slow strain rate tests of A533B-1 base metal were performed in the simulated BWR environment. The reference growth data are also obtained in air at R. T.. 1T CT specimens with side groove depth of 25% were used for both tests in reference environment and simulated BWR environemnt. Experimental results are evaluated by Elastic Plastic Fracture Mechanics in terms of J-resustance curve. Fig. 12 shows the load-loadline displacement curve obtained in air and water environment. The displacement was measured by LVDT attached to the grips. The early deviation from the linear portion on the initial P-Δ curve is clear in test in water environment. Furthermore, the large amount of crack extension in SSRT is quite apparent when compared with in-air test at the same J level. The J-resistance curve in both environment is shown in Fig. 13. The significant reduction of J_i and dJ/da in water environment than in air is observed and these values are tabulated in Table 1. Crack opening angle is one of the promising parameter in Elastic-Plastic Fracture Mechanics to evaluate the material resistance against ductile fracture. Fig. 14 indicate the opening profiles near tips of growing cracks with various values of $T \equiv (E/\sigma_0^2)\, dJ/da$, and near a stationary crack tip: base on $\alpha=0.65$, $\beta=5$, $R=0.2EJ/\sigma_0^2$ ($\approx$plastic zone size)[12]. The decrease of crack opening angle at smaller tearing modulus is clearly shown. As expected from this figure, the COA value in water environment is smaller than that in air. The environmental effects on crack growth reduce the mechanical work for crack extension and consequently keep the crack tip sharp. Crack growth rate can also be evaluated in SSRT test. The growth rate can be obtained as a function of applied load if the crack growth continuously monitored. However, in present study, average crack growth rate is evaluated as follows,

$$da/dt|_E = \frac{\Delta a}{|t_{total} - t_i|_E}$$

where t_{total} and t_i are total testing time and time for initiation and Δa crack growth length. The $da/dt|_{air}$ value in SSRT are evaluated using J-resistance curve in air. Namely, Δa in air corresponding J_{final} was devided by $|t_{total} - t_i|_{air}$ where t_i is time at which applied J is equal to $J_{i_{air}}$. The growth rate diagram obtained in SSRT are also plotted with corrosion fatigue data in Fig. 15.

Both growth data obtained from SSRT and CF shows good agreement on $da/dt|_E$-$da/dt|_{air}$ diagram. The SCC data can be plotted on the same diagram through

appropriate evaluation of $da/dt|_{air}$ in SCC tests and direct comparison of SCC data, CF data and SSRT data will become possible and the importance of SSRT using fracture mechanics specimen should be emphasized as a rapid predictive testing for SCC and CF. Furthermore the quite low loading rate effect on crack growth which may realize at the start-up operation has to be taken into consideration.

4. Concluding Remarks

Basing upon the previous discussion, environmental enhanced crack growth occurs at wide $da/dt|_{air}$ range. $da/dt|_{air}$ can be obtained by

$$da/dt|_{air} = da/dN|_{air} \times f$$

$da/dN|_{air}$ is a function of stress intensity range, stress ratio and other mechanical variables. Hence the $da/dt|_{air}$ is obtained by many conbinations of $da/dN|_{air}$ and frequency, ie. small da/dN and high frequency or large $da/dN|_{air}$ and low frequency.

When the maximum acceleration appeared at a $da/dt|_{air}$, the possible ΔK range where the maximum acceleration occurs depends on the frequency. Therefore, the maximum acceleration in crack growth is possible at any ΔK condition and possible maximum growth data is expected to be pararel to growth data in air as shown in Fig. 16. At lower ΔK level, the consideration for the threshhold is needed and, on the other hand, at higher ΔK level, the crack blunting or branching effects have to be considered.

From a practical standpoint, the significance of two dynamic stressing situation should be emphasized. First one is monotonic loading at extremely low strain rate simulating the start-up operation. The other is extremely high R fatigue at rather high frequency simulating the stress oscillations on a high mean stress. The crack growth characteristics under these stressing situation has not been widely subjected to examination. Based on the enhancement mechanism proposed here, considerable crack growth accelerations are predicted in ferritic vessel steel/high temperature water environment systems at the wide range of ΔK corresponding to the each cyclic frequencies.

In order to develop the mechanistically-based design rule for environmentally enhanced crack growth including corrosion fatigue, stress corrosion cracking and slow strain rate tests on pressure boundary materials in high temperature aqueous environment, the growth rate diagram provides a physical basis to understand the acceleration mechanism and also a useful tool to predict the maximum acceleration under conceibable operating conditions. Especially, the collection of crack growth data under very low frequency (or SSRT tests) and high R and high frequency condition is urgently desired to develop the design rule more reliable.

Furthermore the usefullness of SSRT using Fracture Mechanics specimen are emphasized from its validily as a predictive testing and also from a toughness evaluation in terms of J_{IC} or tearing modulus T_{mat} in BWR environment.

Acknowledgements

The authors wish to express their gratitude to Prof. M. Suzuki of TOYOTA Institute of Technology for his continuous encouragement and interests in this work. Thanks are also extended to the staffs of Department of Engineering Science of Tohoku University and of material engineering laboratories of JAERI for their stimulating discussions.

References

[1] W. H. Bamford and D. M. Moon and L. J. Ceschini, NUREG/CR-1268, NRL-Memorandum Report 4174, March 1980.

[2] D. A. Hale, C. W. Jewett and J. N. Kass, ASME J. Engineering Materials and Technology, Vol. 101, 1979, pp. 191.

[3] R. N. Parkins, Br. Corrosion J., Vol. 7, No. 1, 1972, pp. 15.

[4] J. C. Scully, Metal Science, Vol. 12, No. 6, 1978, pp. 290.

[5] F. P. Ford, Metal Science, Vol. 12, No. 7, 1978, pp. 326.

[6] F. P. Ford, ICM 3, August 1979, Combfidge, U. K..

[7] T. Shoji et al., Corrosion-NACE, Vol. 34, No. 8, 1978, pp. 276.

[8] R. N. Parkins et al., First US-Japan Joint Symposium on Corrosion Problem in LWR, 1978, Fuje, Japan.

[9] Johnson and Radon, Int. J. Fracture, Vol. 10, No. 1, 1974, pp. 125.

[10] ASTM STP 668, 1979, American Society for Testing and Materials, Philadelphia U. S. A..

[11] J. R. Rice and E. P. Sorensen, J. Mechanics and Physics of Solids, Vol. 26, 1978, pp. 163.

[12] J. R. Rice et al., Fracture Mechanics: Twelfth Conference, ASTM STP 700, ASTM, 1980, pp. 189.

[13] T. Yokobori et al., in Fracture 77, Vol. 1, ICF-4, Waterloo, Canada, 1977, pp. 665.

[14] D. L. Davidson and J. Lankford, "Fatigue Crack Tip Stress and Strain Range Distribution, The Energy for Crack Propagation and The Effect of Water Vapor on These Factor", private communication.

[15] J. P. Atkinson and T. C. Lindley, The Influence of Environment on Fatigue, IMechE Conference Publications 1977-4, 1977, p. 65.

Table 1 Summary of J-resistance data in ambient air and BWR environment: SA533B-1 1TCT

Environment	J_i(kJ/m^2)	T_{mat} *)	COA(°)	Remarks
Ambient Air	360	277	24.3	room temperature
288°C Water	210	162	16.7	$\dot{\Delta}$ =3.8-8.3x10^{-3}mm/min D.O. ~0.1ppm

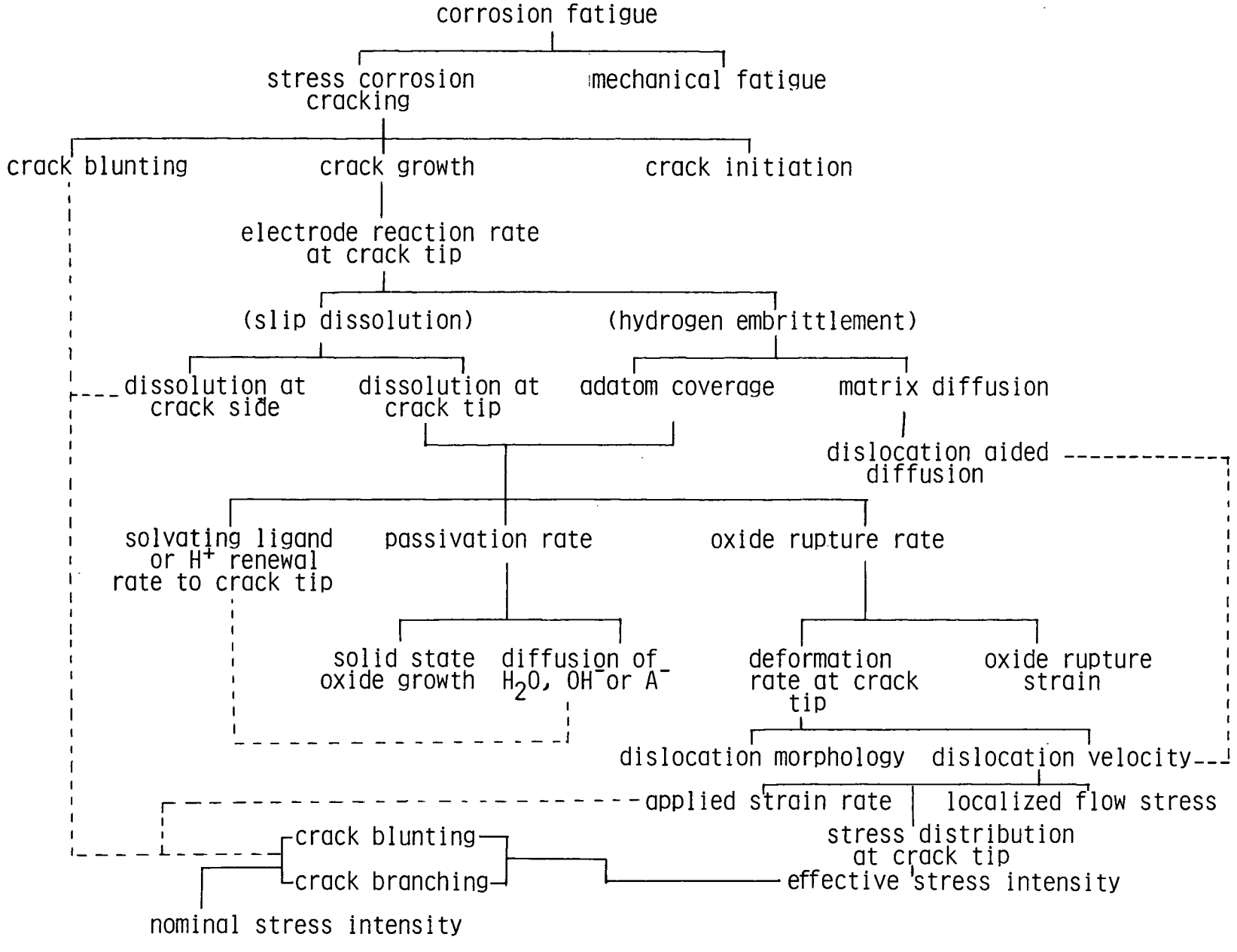

Fig. 1 Tabulation and interrelationship of fundamental paremeters involved in the mechanism of environmental cracking in ductile alloy/aqueous environment systems [6]

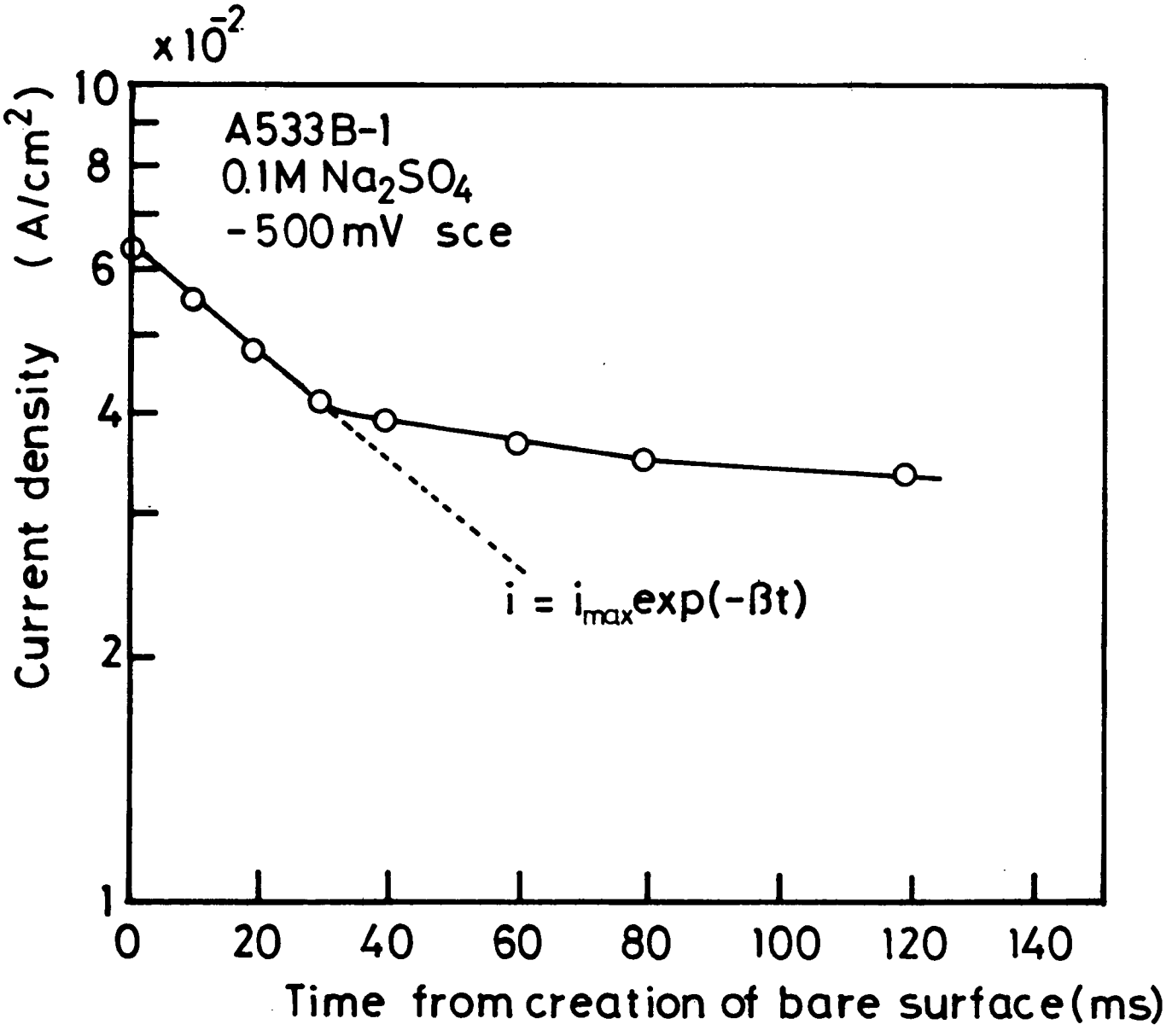

Fig. 2 Observed current/time transient of A533B-1 in 0.1N-Na_2SO_4 at 25°C

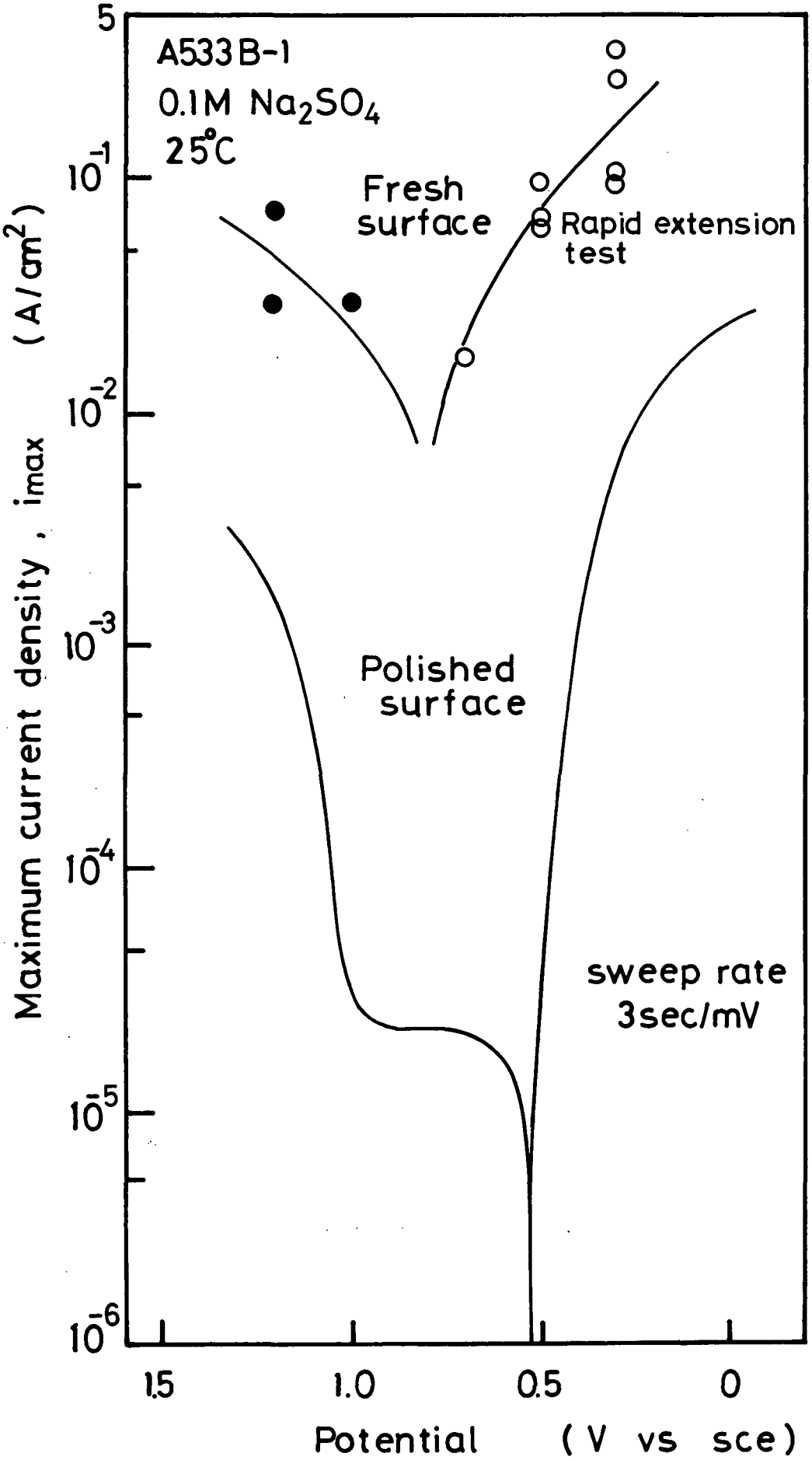

Fig. 3 Difference of polarization behavior of bare surface and polished surface of SA533B-1 in 0.1N-Na_2SO_4

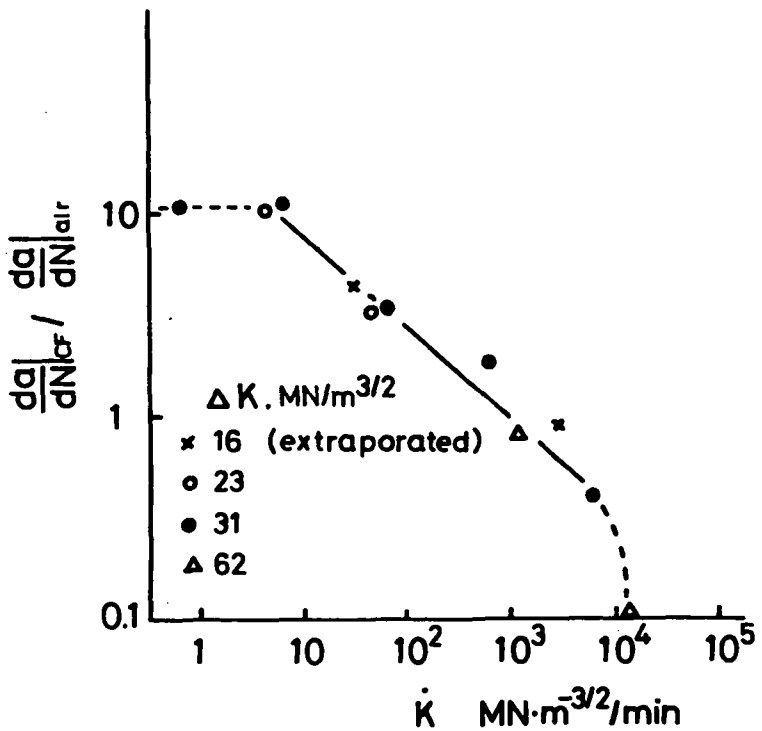

Fig. 4 Significant of stress intensity rate K on fatigue crack growth acceleration [7] (Cr-Mo steel/0.1N H_2SO_4)

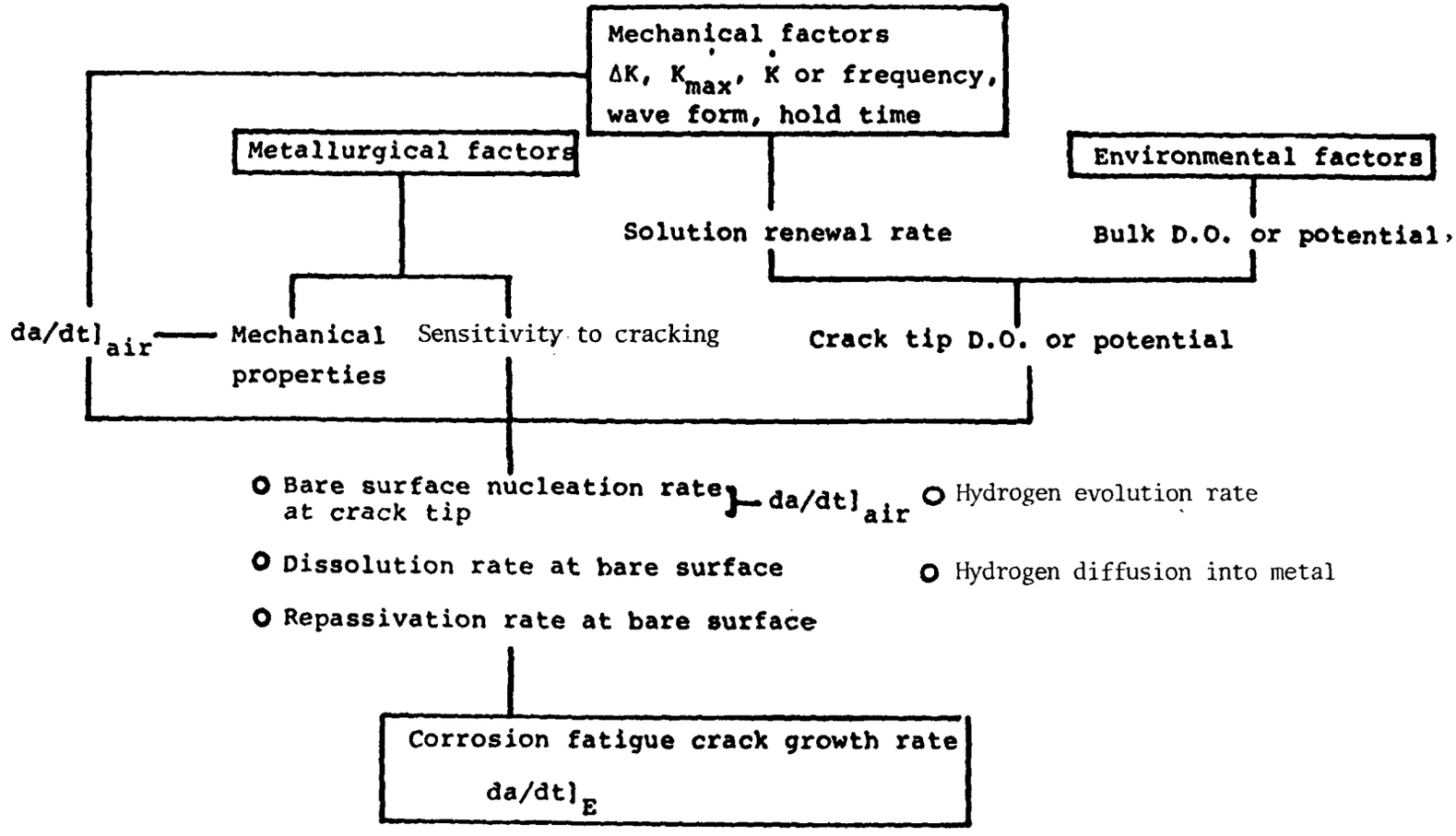

Fig. 5 A modified illustration of interplay of mechanical, metallurgical and environmental factors

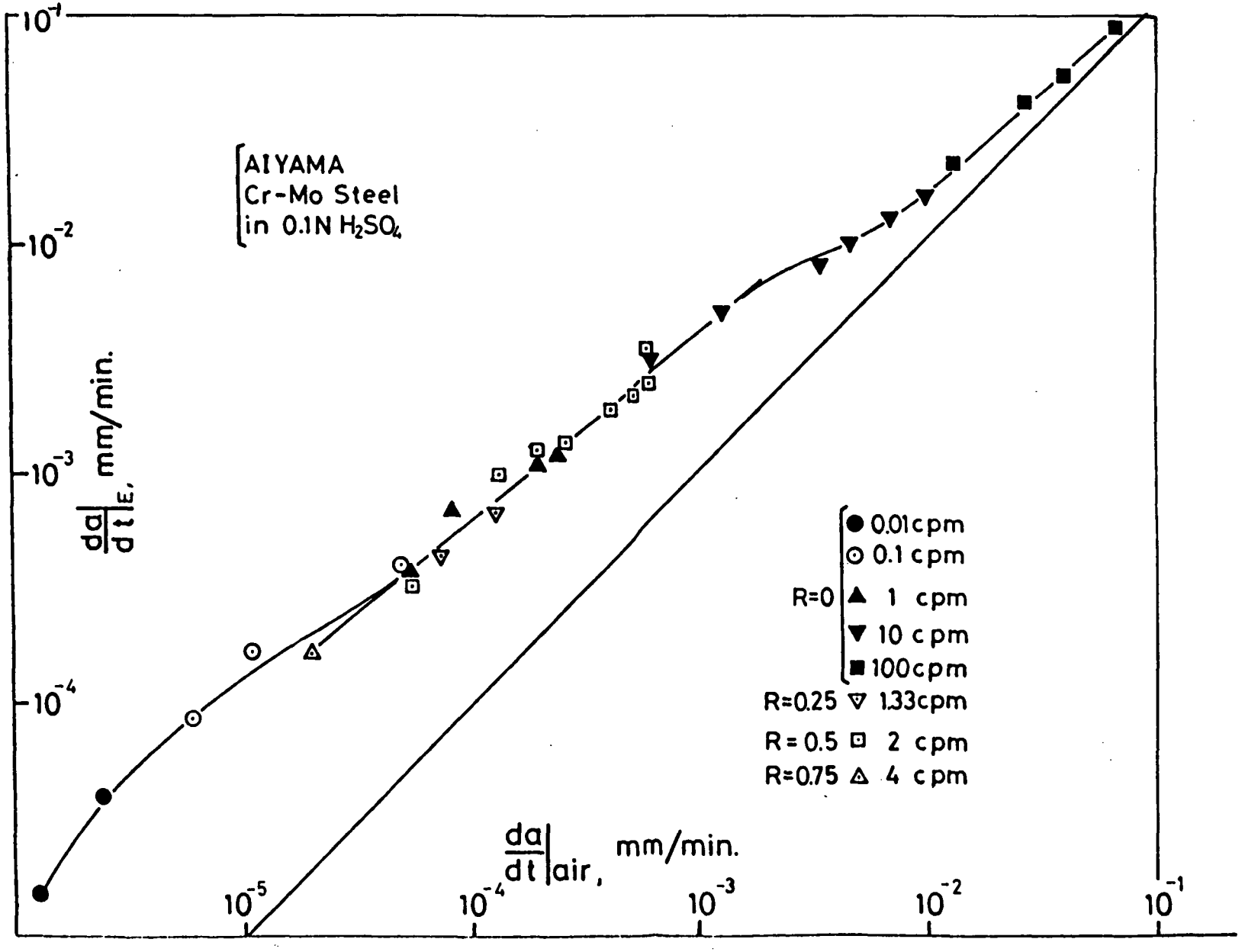

Fig. 6 Growth rate diagram for 4145 steel/H_2SO_4 environment

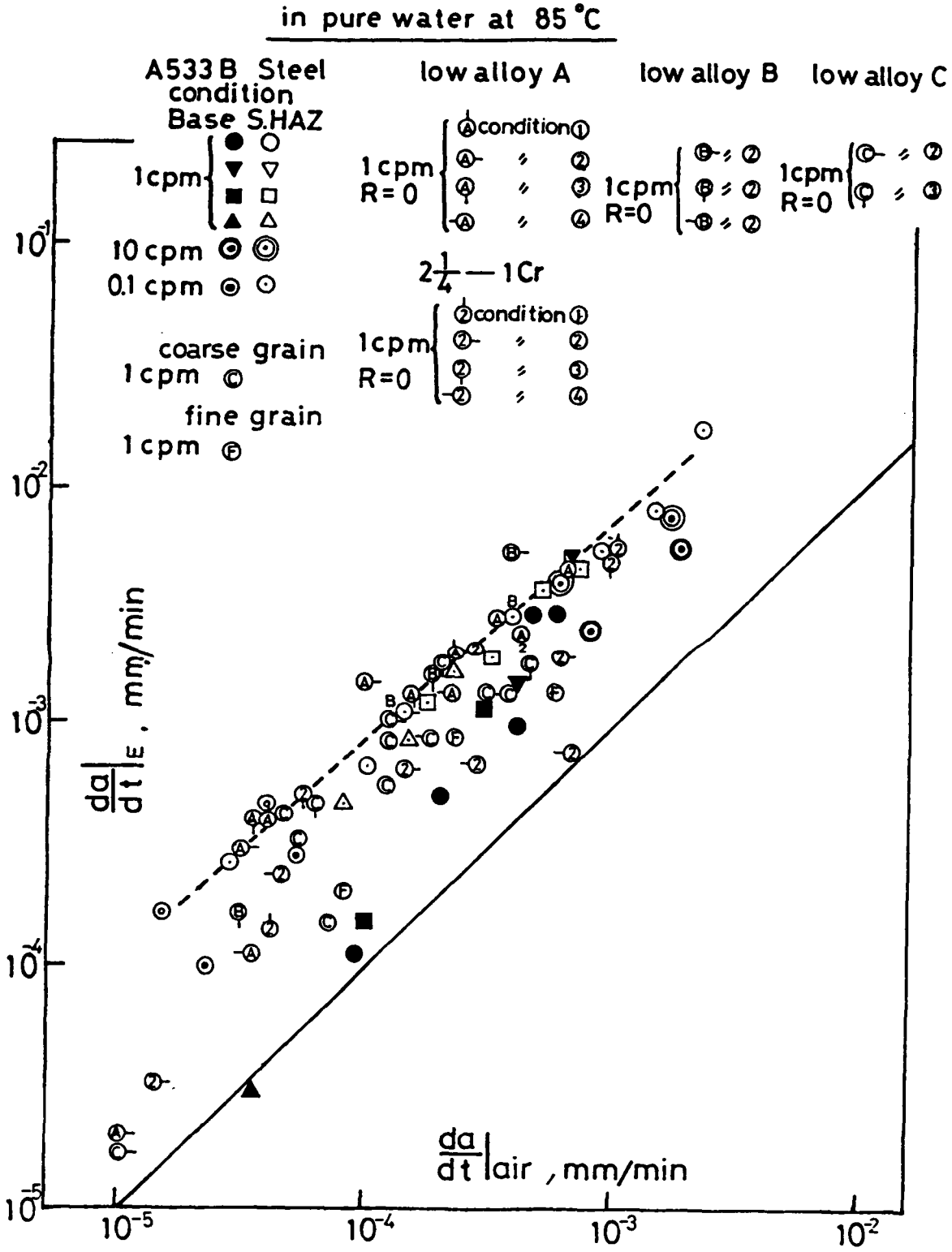

Fig. 7 Growth rate diagram for low alloy steels/85°C water system with different O_2 condition

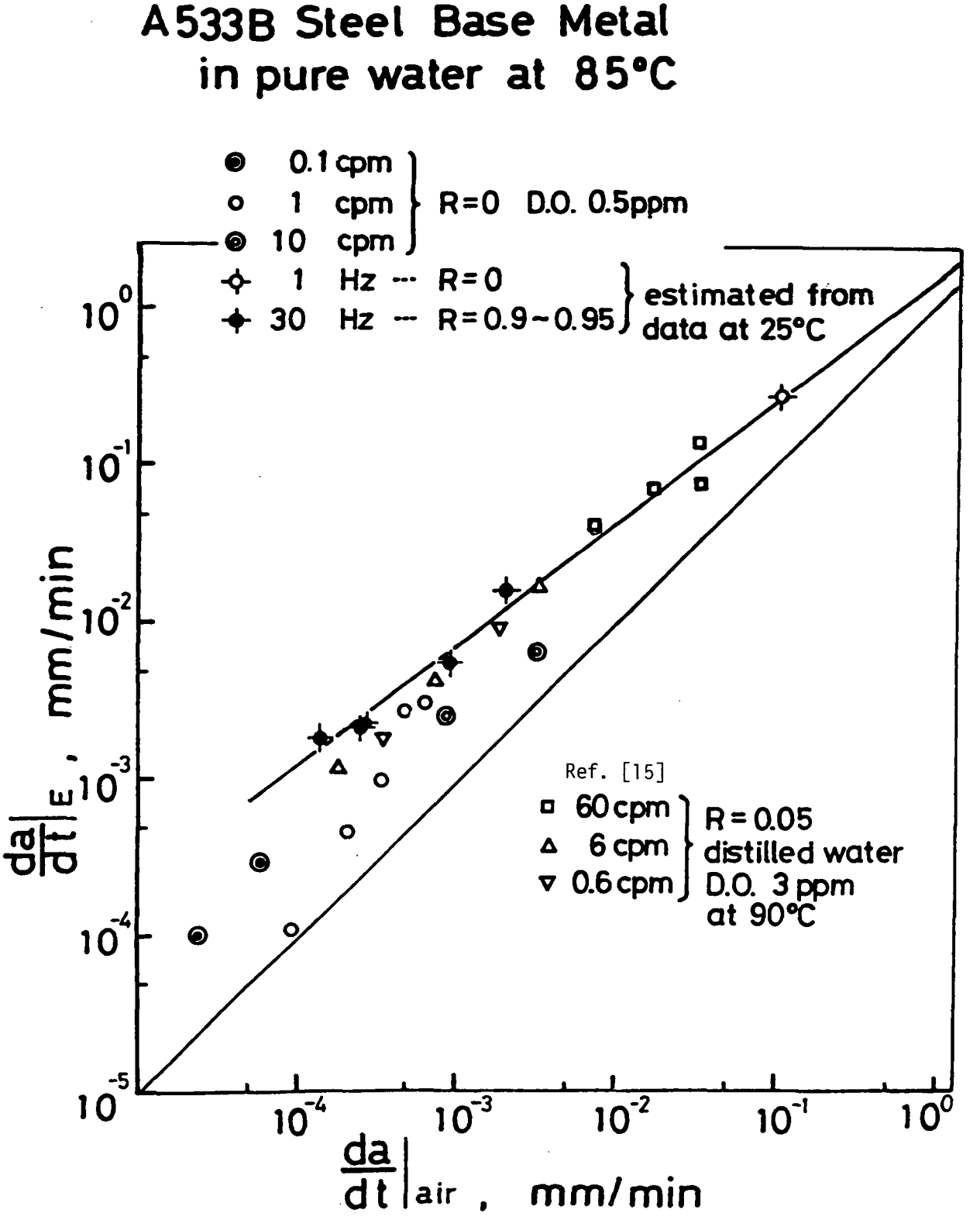

Fig. 8 Growth rate diagram for A533B-1 steel/85°C water with extreme high R high frequency condition

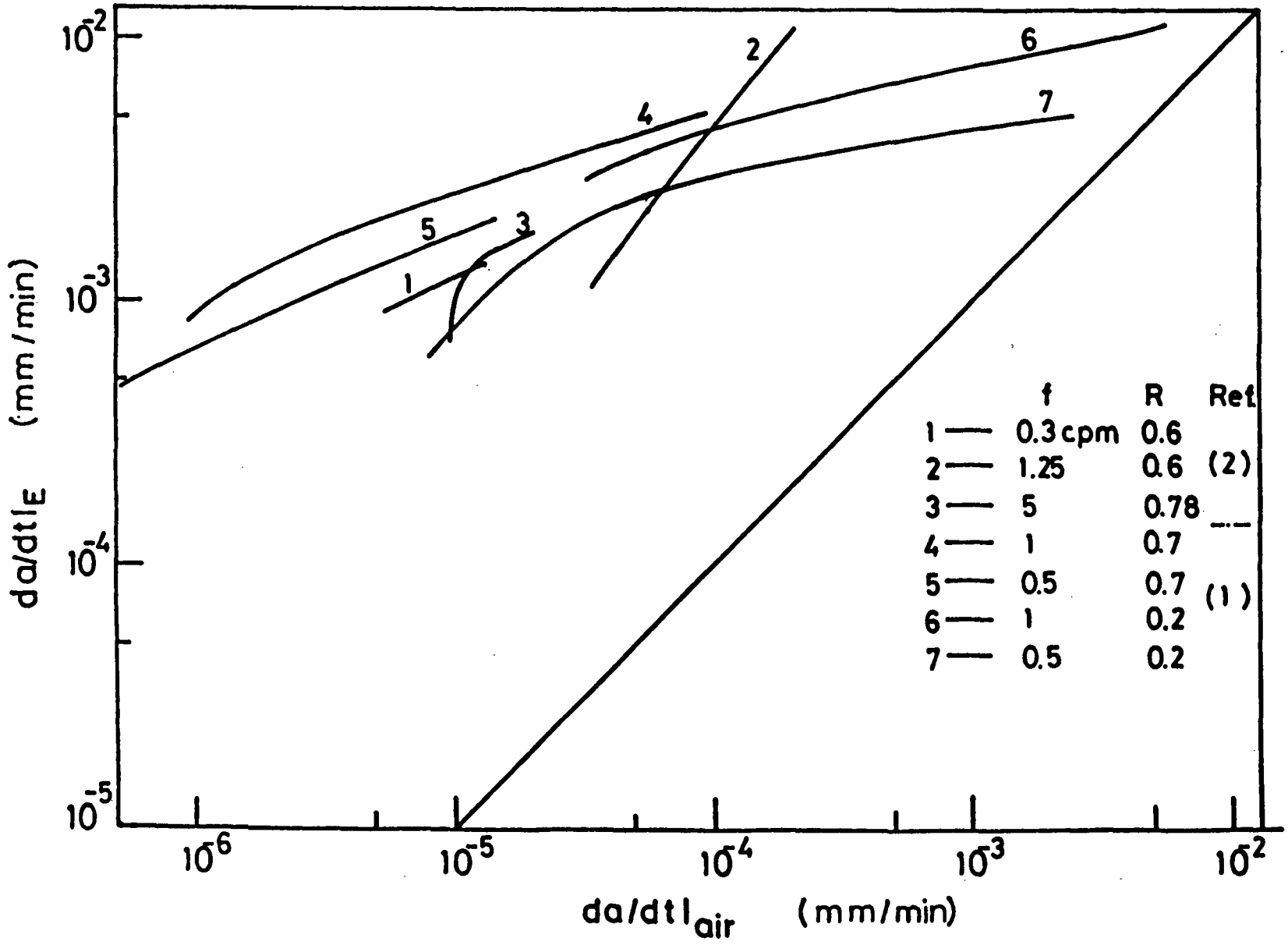

Fig. 9 Growth rate diagram for the ferritic vessel steels/aqueous environment systems peculiar to BWR and PWR

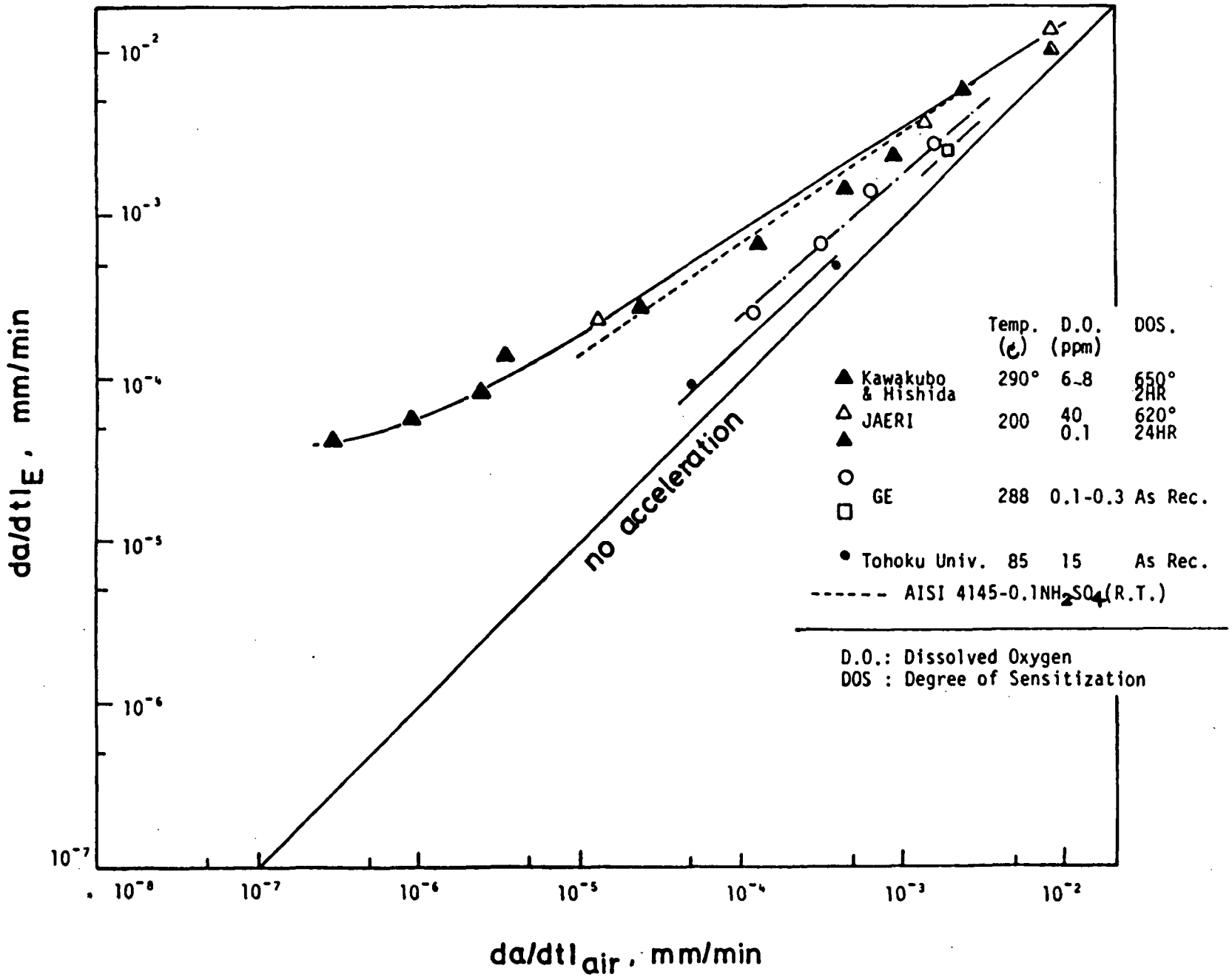

Fig. 10 Growth rate diagram for the austenitic stainless steels/aqueous environment systems peculiar to BWR

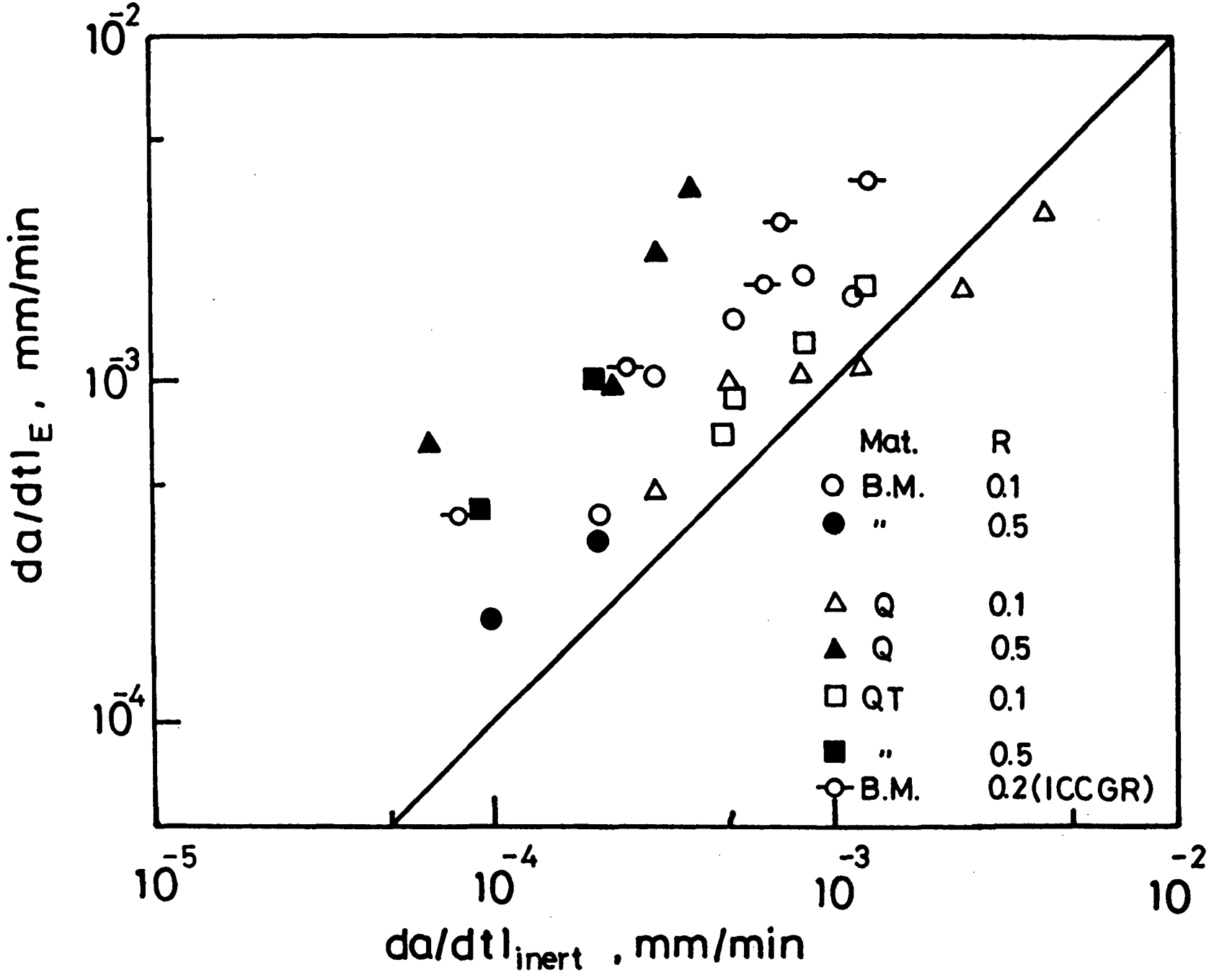

Fig.11 Growth rate diagram for SA533B-1/aqueous environmetn(BWR)

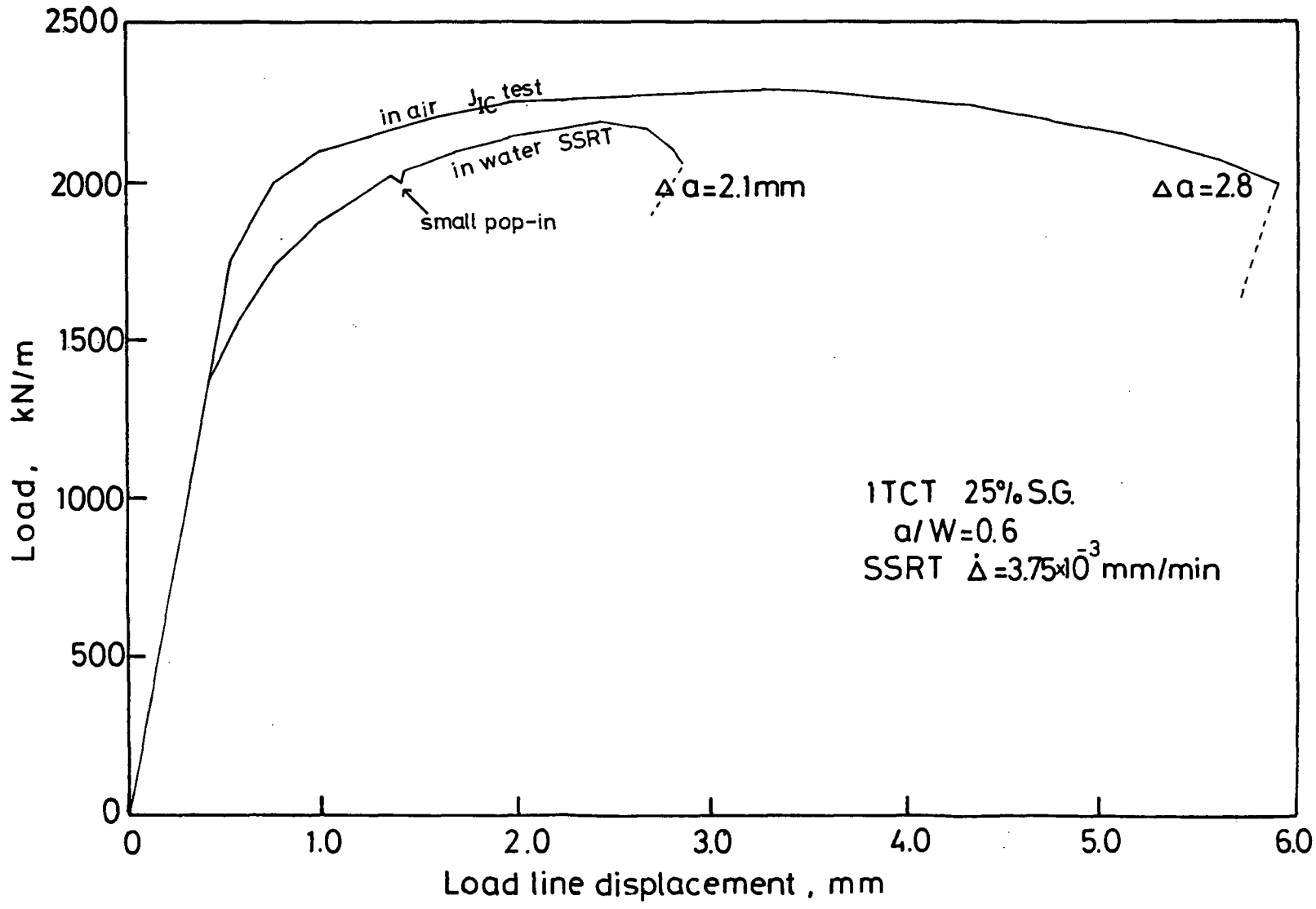

Fig.12 Load-displacement curves in ambient air and BWR environment

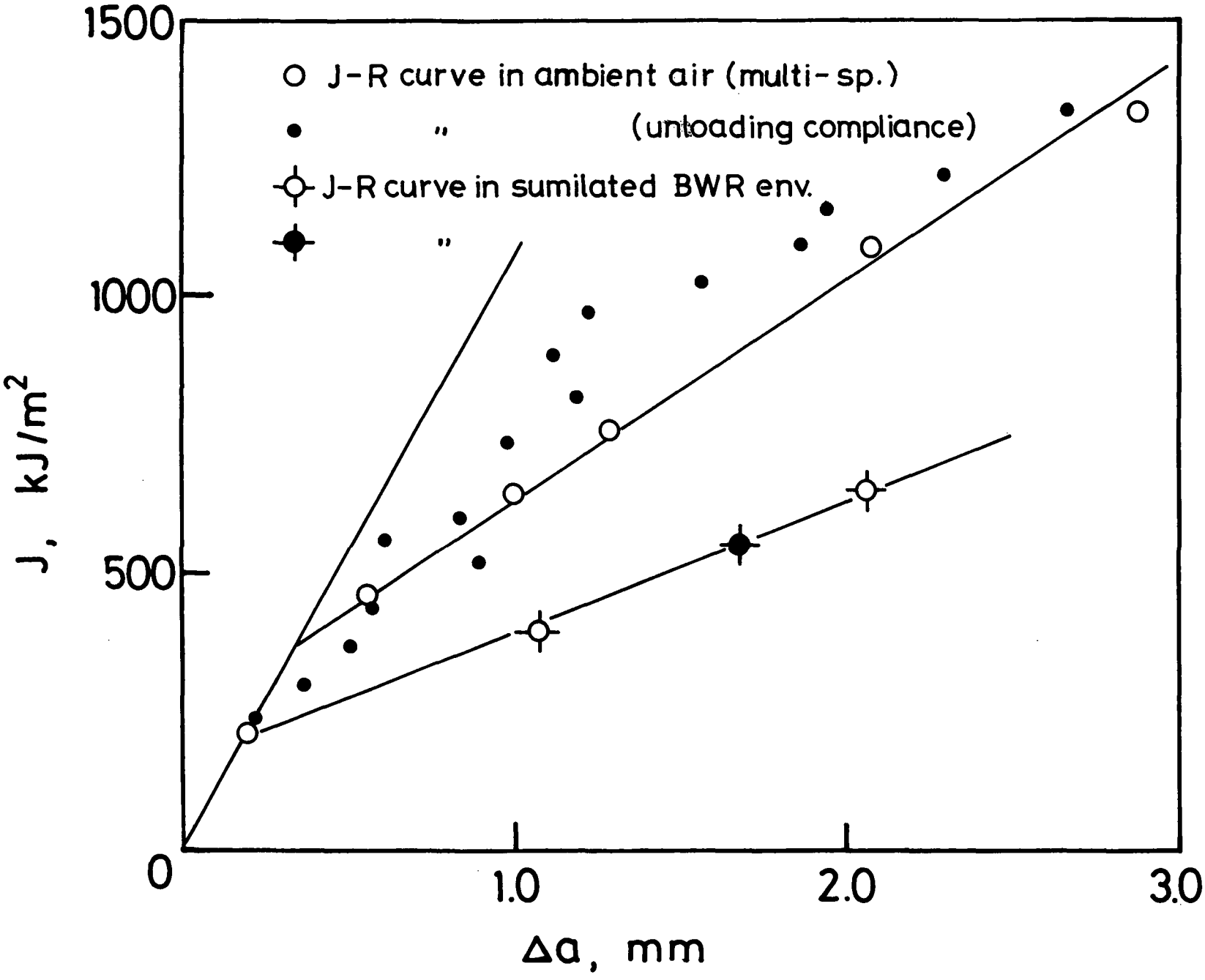

Fig. 13 J-resistance curves in ambient air and BWR environment

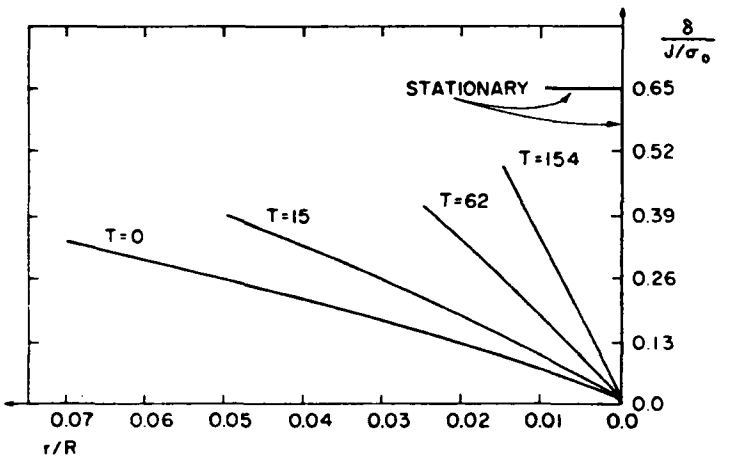

Opening profiles near the tips of growing cracks with various values of $T = (E/\sigma_0^2)dJ/da$, *and near a stationary cruck tip: based on* $\alpha = 0.65$, $\beta = 5$, $R = 0.2\ EJ/\sigma_0^2$ ($\approx$ *plastic zone size*).

Fig. 14

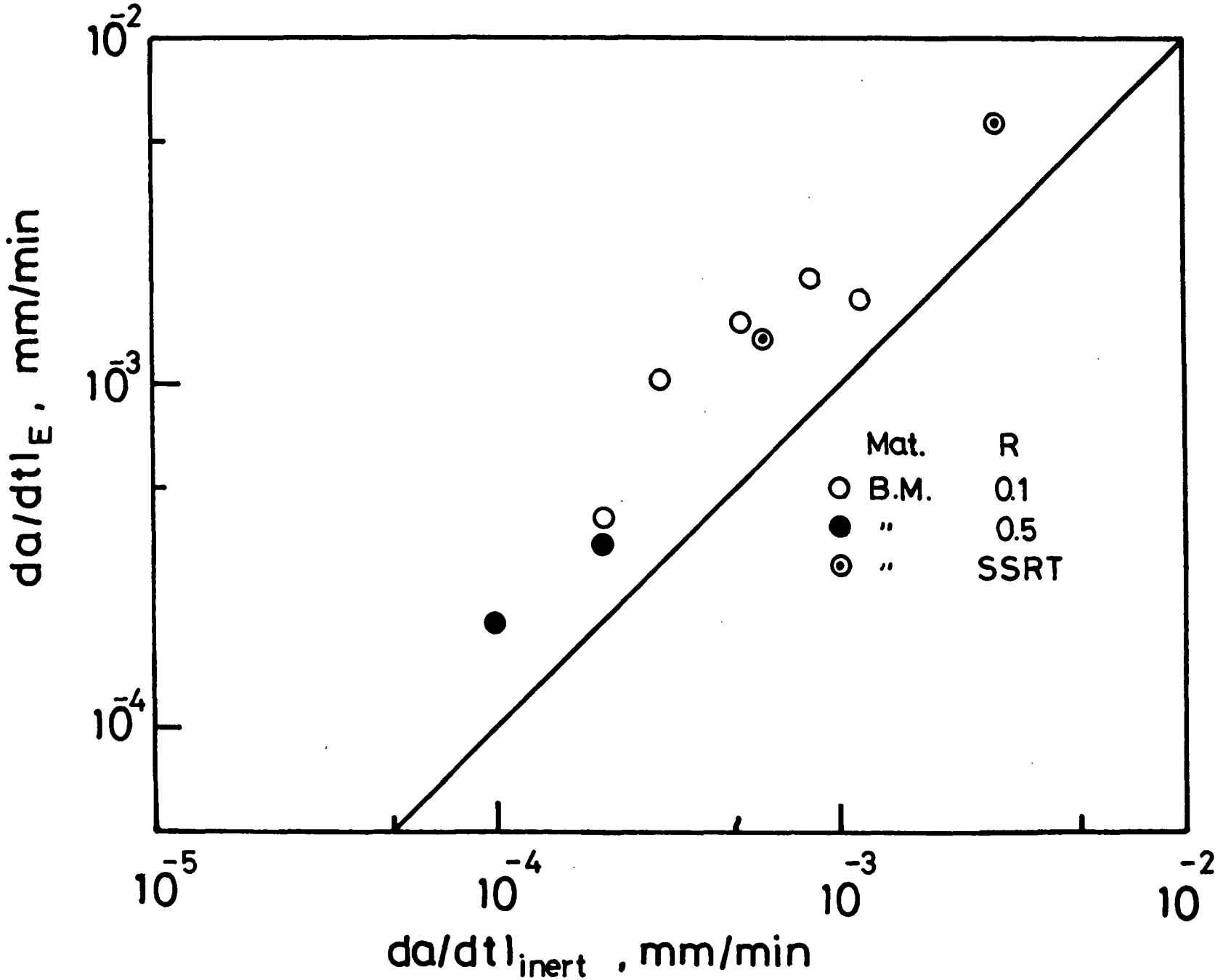

Fig.15 Growth rate diagram for SA533B-1/aqueous environmetn(BWR)

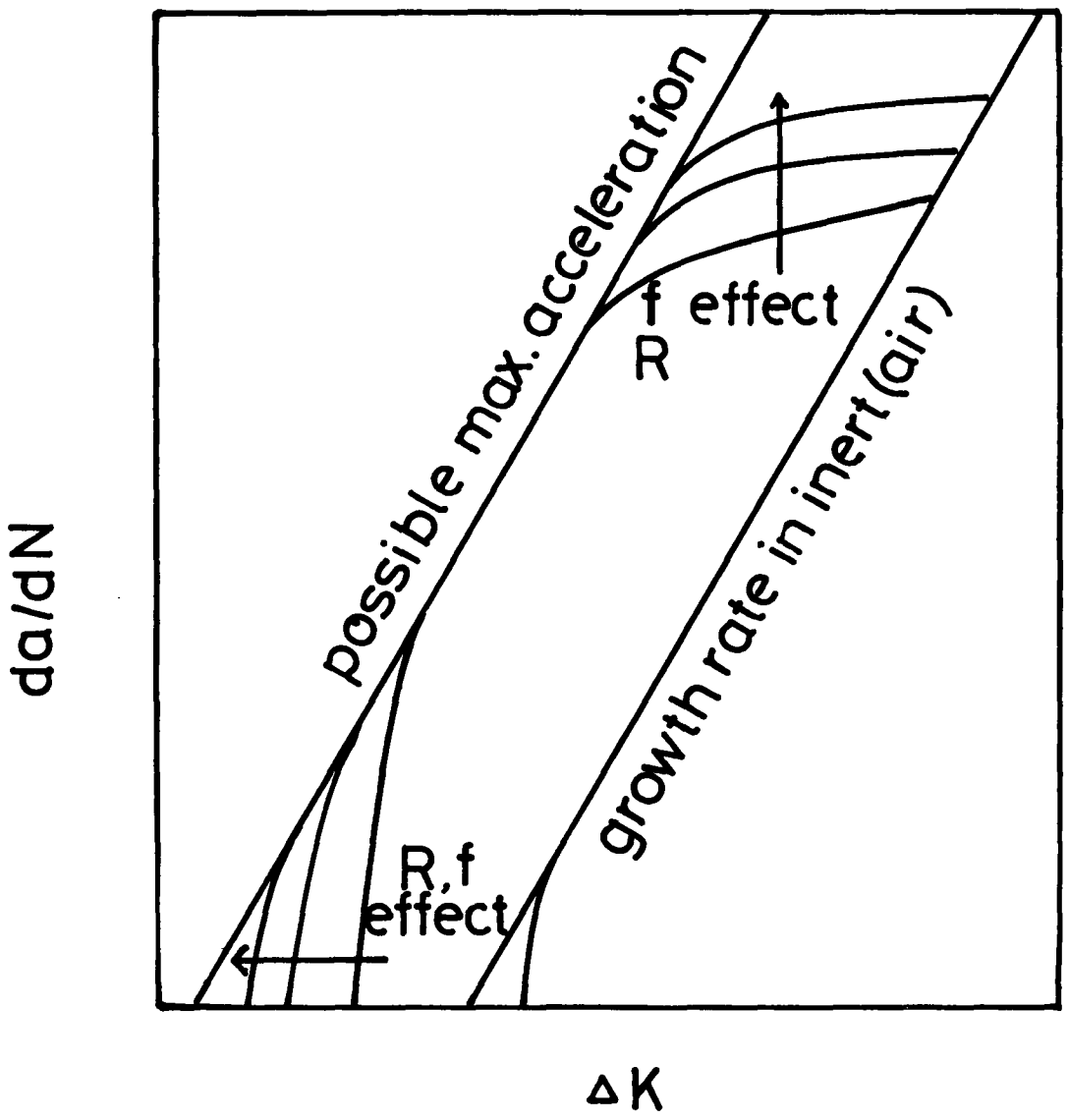

Fig. 16 Schematic illustration of corrosion fatigue crack growth behavior of pressure vessel steel/high temperature water environment combination

Central Electricity Research Laboratories

CORROSION FATIGUE MECHANISMS IN FERRITIC PRESSURE VESSEL STEELS EXPOSED TO SIMULATED PWR ENVIRONMENTS

by

J.D. Atkinson, S.T. Cole and J.E. Forrest
Materials Division
Central Electricity Research Laboratories
Kelvin Avenue
Leatherhead
Surrey KT22 7SE

To be presented at an I.A.E.A. Meeting
"Sub-critical Crack Growth",
Freiburg, Germany, 13-15 May 1981.

SUMMARY

Fatigue crack propagation rates have been measured in A533B pressure vessel steel exposed to simulated PWR environments over the temperature range 25-290°C. At low R ratios with sine wave loading at 1cpm an environmental enhancement over equivalent air data of up to X7 was observed at 290°C in static low oxygen water (< 10ppb) at a measured specimen potential of -840mV (SHE). A minimum fatigue crack growth rate was observed at 200°C with different apparent activation energies above 175°C and below 175°C.

A model of the cracking process is presented in which the environmental enhancement is related to crack opening rate during the ascending stress part of the fatigue cycle. The model is discussed in relation to PWR corrosion fatigue data on the effects of waveshape, frequency and R-ratio.

INTRODUCTION

It is now well established that under certain conditions of stress and environment, the pressure vessel steels used in Light Water Reactors (LWR's), are susceptible to environmentally-assisted subcritical crack growth [1-4] in simulated reactor environments, over the temperature range 25-290°C. To ensure safe reactor operation, attempts have been made to quantify the defect growth occurring during a 40 year design life using fracture mechanics to characterise crack growth and fracture[5-7]. A key input into such calculations is a realistic time or cycle based crack growth law.

Experiments are in progress at many centres worldwide trying to assess the maximum crack growth rates likely in simulated Pressurised Water Reactor (PWR) and Boiling Water Reactor (BWR), service conditions (288°C, 1200 psi). The main difference in the two water chemistry specifications is dissolved oxygen, 10-100ppb in a PWR and ≈ 200 ppb in a BWR, with additions of boric acid and lithium hydroxide to primary PWR water to reduce reactivity and control pH and a hydrogen overpressure of 30cc/Kgm water. Co-operative round robin experiments[8] have resulted in very scattered data in simulated PWR environments and recent detailed experiments in Europe[9] have not been able to reproduce the very rapid crack growth rates previously determined under simulated PWR conditions in the USA[10]. These discrepancies may be due to material, stress, environmental or rig differences but they highlight the need for a mechanistic understanding of the mechanical and electrochemical processes involved in environmentally-assisted cracking.

The aim of the present programme was to measure crack propagation rates in A533B steel and corresponding corrosion potentials using an Ag/AgCl reference electrode, during fatigue tests in simulated PWR environments.

2. EXPERIMENTAL PROCEDURE

2.1 Specimen Preparation

Standard compact tension specimens of 25mm thickness were tested. Specimens A and B were supplied by EPRI as part of a round robin series of experiments on A533B (1HT6 and 1HT51). Specimen C (MF5) was made from Ex-Marrel Freres A533B plate. Details of the chemical compositions and mechanical properties are given in Tables 1 and 2.

2.2 Autoclave/loading System

The 25mm ASTM compact tension specimens were tested in the loading frame of a 250kN servo-hydraulic fatigue machine and enclosed in a Type 316 stainless steel autoclave. The load bar of the machine passes into the autoclave through a Grafoil sliding seal which imposes a measured friction loss of about 1kN and this and the differential pressure stress across the seal were allowed for in calculating the specimen load.

The autoclave was filled with 10ℓ of water and heated by means of external heaters yielding temperature control of ± 2°C at 160°C. The system was vented repeatedly to remove gas (mainly N_2) from the space above the water.

After reaching the test temperature the system was allowed to equilibrate overnight prior to starting the test. During this period a small tensile load (≃ 5kN) was maintained on the specimen to avoid compressive loading of the pre-cracked specimen. A similar procedure was adopted for each temperature change carried out, and fatigue cycling was only recommenced when the specimen temperature was stable.

2.3 Fatigue Testing

Fatigue tests were conducted at 1 cycle per minute with a sinusoidal waveform. An external load cell was used to monitor applied load with appropriate corrections for autoclave pressure and sliding seal friction. Tests B (specimen 1HT51) and C (specimen MF5) were run at constant K_{max} and ΔK with a load ratio ($R = K_{min}/K_{max}$) of 0.2 by load shedding every 0.5mm of crack extension. Test A (specimen 1HT6) was carried out with fixed applied loads throughout so the ΔK increased as the crack propagated at R = 0.2.

Crack length monitoring was achieved with the d.c. electrical resistance method.

2.4 Water Chemistry

PWR primary water consists of demineralized low conductive water to which is added boric acid for reactor activity control (reduced during core life), LiOH for pH control, and hydrogen to reduce oxygen levels.

The autoclave was filled with doubly deionised water having a conductivity <0.1μS and dosed with a 2000ppm boric acid and 1ppm liOH. De-oxygenation was achieved by nitrogen bubbling to a level of <8ppb O_2. Oxygen was analysed using a colorimetric technique capable of measuring to 0.4ppb[11] although it was not possible to analyse for oxygen after the test because of interference due to Fe^{2+} ions from specimen and autoclave corrosion. However the presence of Fe^{2+} together with H_2 indicates that the oxygen level was reduced to zero during the test and this was confirmed by measurements of the specimen potential (see Section 2.5). The pH changed during test C from 6.9 to 7.2 measured at 20°C.

2.5 Potential Measurement

The measurement of specimen corrosion potential is considered of great importance for these corrosion fatigue tests in view of the work of Vermilyea and Indig[12] which showed a transition from a high potential to a low one with decreasing oxygen content of the water.

Two electrodes were inserted for the constant ΔK, variable temperature test, with the tips of the asbestos wicks on either side of the crack tip. The construction of the electrode is shown in Fig. 1 and is essentially that described by Underwood and McKay[13]. The potential between this and the specimen was measured with a high impedance voltmeter and the corrosion potential of the specimen (SHE) was calculated from the half cell values for the chloride electrode using the calibration shown in Fig. 2. The two cells gave readings within 20mV of one another and showed consistent behaviour when parameters such as temperature were varied.

Concern that the use of the potential drop method for crack length monitoring could substantially change the corrosion potential proved unfounded as at the test temperatures (150-290°C) the change was only a few mV and the corrosion potential reverted to the original value on switching off the direct current (40 amps).

2.6 Crack Length Monitoring

The direct current potential drop method of crack monitoring was chosen by virtue of its proven reliability and accuracy. A current of 40 amps was passed through the specimen via silver wires and the potential difference across the crack measured on a milli-voltmeter via pure iron wires. Both sets of wires were covered with PTFE tubing to insulate them from one another and to minimise water contamination.

The potential difference across a steel reference placed in series with the specimen was measured to eliminate artefacts due to current or temperature variations. Calibration curves of crack length versus potential drop were obtained from a saw cut specimen and from test specimens with deliberate beach marks. The crack length measured by this potential drop technique was accurate to approximately $\pm$0.2mm.

The ASTM E-24 seven point polynomial method was used to convert crack length (a) versus number of cycles (N) into crack growth per cycle versus cyclic stress intensity (ΔK).

The possibility that the continuous current could influence crack growth rate was investigated, but no measurable change was found when the current was switched off.

3. EXPERIMENTAL RESULTS

Fatigue crack propagation rates have been measured for A533B plate in PWR quality water, at both constant load range (Test A) and constant stress intensity range (Test B) over a range of temperatures. The chemical analyses of the steels are given in Table 1.

3.1 Test A at Constant Load and 290°C

A plot of average crack growth rate ($^{da}/_{dN}$) versus stress intensity range (ΔK) is given in Fig. 3. The test A on specimen 1HT6 was conducted with a 1cpm sinewave, R = 0.2 loading at a starting ΔK of 27.5MPa$\sqrt{m}$. This test exhibited a large enhancement (up to $\sim$X7 over air data) and showed 3 stage growth behaviour. In Region I at low ΔK the crack growth rate increased rapidly with increasing ΔK up to about 35MPa$\sqrt{m}$ when in Region II a quasi-plateau region with da/dN only slightly dependent on ΔK occurred. Towards the end of the test in Region III ($\sim\Delta K$ = 50-75MPa$\sqrt{m}$) the crack growth rate again became ΔK dependent and followed published air data quite closely. Microexamination of the fracture surface with the magnetite film removed revealed a complex fracture mechanism, which although of ductile appearance did not show clear striation formations, as shown in Fig. 7 at ΔK of 30MPa$\sqrt{m}$.

3.2 Tests B and C at Constant ΔK over the temperature range 150-290°C

The effect of temperature on crack growth rate for specimen 1HT51 (test B) fatigued at a ΔK of 45MPa$\sqrt{m}$,R = 0.2 with a 1cpm sinewave are included in Fig. 4. This shows a slow growth rate at 200°C, which is close to equivalent air data, and enhanced growth at 290°C.

In a second test on specimen MF5 (Test C) the corrosion potential of the specimen was monitored continuously. This is shown with a plot of crack length in Fig. 5. The specimen was held at a small positive static load during each temperature change for periods up to 15 hours. During this period for each increase in specimen temperature the corrosion potential was found to move to a more negative value. Once the temperature had stabilised the corrosion potential remained stable during each step of fatigue. At 290°C the corrosion potential was found to be -840mV (SHE), and the reference electrodes remained stable in the autoclave for up to 30 days.

On specimen MF5 at a ΔK of 35MPa$\sqrt{m}$ a minimum crack growth rate was also observed at 200°C. At 290°C the potential drop measurement began to cycle with the applied fatigue load, which probably indicated that some crack closure was occurring. The crack growth rate at 290°C in this test was slightly slower than that measured at 250°C, and further tests are in hand to examine the dependence on temperature, and to eliminate crack length or closure effects, by examining a range of R ratios.

The observed effects of temperature are summarised in Fig. 4 with the BWR experiments on SA333 steel by Kondo et al [1] as a comparison. The fracture surfaces of specimen MF5 (Test C) shown in Fig. 6, illustrate the banding caused by differences in oxide formed at each temperature.

4. DISCUSSION OF RESULTS

It is clear from the results described, that the present fatigue experiments in non-refreshed autoclaves, with simulated PWR water, demonstrate an enhanced fatigue crack propagation rate under certain temperature and corrosion potential conditions. The evidence that A533B steel is not susceptible to stress corrosion cracking in its parent plate form [3], under static loads suggests that it is the dynamic crack tip strain which produces the environmental crack growth component. The corrosion potential measurements are consistent with Indig's work [12], which demonstrated that as the cathodic reaction changed from oxygen reduction at positive potentials ≈ -200mV SHE, to hydrogen ion reduction at oxygen levels ≤10ppb (≈-840mV at 275°C).

The possible mechanisms of crack advancement in water reactor environment have been discussed in depth by a number of authors [14,15,16,22] but as yet there is no general agreement. In BWR environments Ford and Silverman [14] suggests that the slip dissolution model of cracking can explain the observed constant extension rate test (CERT) and corrosion fatigue data at 290°C. They proposed that the rate controlling step is the diffusion of solvating ligands down the crack. In PWR environments the situation is less clear. Scott and Truswell have recently suggested [4] that the dynamic stress corrosion cracking observed in BWR environments can also occur in a low O_2 PWR environment, but other workers [19] have suggested that there is evidence of hydrogen assisted cracking. Tomkins has argued convincingly on crack tip mechanics grounds [16] that for a dissolution assisted model of corrosion fatigue

crack propagation, half the crack tip opening displacement (CTOD) at maximum load (ϕ_{max}) represents an upper bound for crack growth per cycle with a $(\Delta K)^2$ growth rate dependence. The crack growth results for A533B steel tested at 90°C in distilled water [20] showed a maximum environmental enhancement close to that predicted on this model. For a hydrogen assisted mechanism Tomkins[16] suggests that an upper bound crack growth rate of the order of the plastic zone size may be appropriate.

However for high temperature aqueous environments which form passive oxide films it seems likely that both dissolution and hydrogen embrittlement must be preceded by slip step emergence and oxide rupture. Therefore the fine balance between the rates of bare metal production (i.e. active sites) and repassivation will have a direct influence on the fatigue crack propagation rate in both models.

4.1 Crack Tip Model

Consider the deforming crack tip shown in Fig. 8, where rupture of oxide at the crack tip due to plastic flow leads to metal dissolution at the newly created slip step, and on the cathodic sites either oxygen reduction or hydrogen ion reduction takes place. In a fatigue test at $K_{max} < 0.7\ K_{1c}$ with a ductile steel in Stage II and mode I deformation the slip step emergence rate (d_γ/dt) will be related to the crack opening rate. For a pure fatigue situation with crack advance by ductile striation growth, Tomkins [16] has demonstrated that the striation spacings are related to maximum opening of the crack (ϕ_{max}) rather than the cyclic component ($\Delta\phi$) as expected, but in air the crack growth rate in Stage II is much less than the striation measurements. However Tomkins [16] suggests that during a corrosion fatigue test the dissolution occurring at the crack tip enables the crack profile to change so that $\phi_{max}/2$ is attained at much lower ΔK levels than the Stage II - III transition in air. This suggests that the relevant crack opening rate with respect to oxide rupture in a corrosion fatigue test is $d\Delta\phi/dt$, which is superimposed on the R-dependent static crack opening.

$$\text{since } \phi = 0.50\,\frac{K^2}{E\sigma_y} \qquad \ldots \quad (1)$$

where σ_y is the yield stress and E is Young's modulus [16].

$$\frac{d\gamma}{dt} \propto 2\,(K_{inst} - K_{min})\,\frac{dK}{dt} \qquad \ldots \quad (2)$$

where K_{inst} is the instantaneous stress intensity value and varies throughout a fatigue cycle, from K_{min} to $K_{max}(\Delta K)$.

If t_c is the time between oxide rupture events

$$\text{Then assuming } \frac{1}{t_c} \propto \frac{\delta\gamma}{\delta t} \qquad \ldots \quad (3)$$

$$t_c \propto \frac{1}{(K_{inst} - K_{min})}\,dK/dt$$

A similar relation has been developed by Newman [15] based on the stress distribution ahead of the crack.

If parabolic oxidation are operating at the crack tip and L is the depth of metal removed by corrosion in time, t.

$$L \propto t^{\frac{1}{2}} \qquad \ldots \quad (4)$$

The average velocity of corrosion, V, at a constant value of $\Delta K \; dK/dt$, is given by

$$V = \frac{L_c}{t_c} \propto t_c^{-\frac{1}{2}} \qquad \ldots \quad (5)$$

The maximum increment of crack growth during one fatigue cycle due to the dissolution process is

$$\left.\frac{da}{dN}\right|_{env} = \int_o^{T_r} V \, dt \qquad \ldots \quad (6)$$

where

$$\int_o^{T_r} V \, dt = b \int_o^{T_r} \left((K_{inst} - K_{min}) \frac{dK}{dt} \right)^{\frac{1}{2}} dt \qquad \ldots \quad (7)$$

where b is a constant dependent on the corrosion mechanism, integration limits are over the ascending part of the fatigue cycle (so T_r is the rise time) the role of the descending part is assumed to be merely crack resharpening.

To use equation (7), explicit K(t) waveforms must be substituted using K(t). For a haversine waveform

$$\left(\frac{da}{dN}\right)_{env} = \frac{B \; \Delta K \; T_r^{\frac{1}{2}}}{1-R}$$

for $R < 0.7$ $\qquad \ldots \quad (8)$

where B is a constant for a material/environment system and R is the load ratio (K_{min}/K_{max})

Solution of equation (7) for a number of standard fatigue waveforms demonstrates [22] that a sinewave should be more damaging than a trapezoidal waveform as observed by the U.S. Naval Research Laboratory. Equation (8) also demonstrates that a simultaneous stress ramp and stress are necessary to rupture oxide. Hence hold periods during a fatigue cycle are not expected to enhance fatigue crack growth and if blunting or complete repassivation of the crack tip occurs, retardation effects are likely to result [16,20]. Also this model of environmentally assisted cracking would predict an absence of cracking in constant load stress corrosion specimens as reported by Westinghouse [3].

The dependence of the environmental crack growth rate on $(1-R)^{-1}$ is in accord with published data on LWR pressure vessel steels [7,18]. Ford [14] and Silverman have suggested a model where

$$\frac{1}{t_c} \propto {}^{d\phi}/_{dt} \; / \; \phi \qquad \ldots \quad (9)$$

Using equations (4), (5) (7) and (9) leads to

$$\left(\frac{da}{dN}\right)_{env} \propto (1-R) \qquad \ldots \quad (10)$$

Scott, using a similar model finds a dependance on $\ln\left(\frac{1}{R}\right)$.

The difference is a result of our choice of crack opening rate as the important crack tip parameter rather than a gauge length determined strain rate as used by Ford[14] and Scott[4].

According to equation (8) $(da/_{dn})_{env}$ depends on $T_r^{\frac{1}{2}}$. Experimental data supporting this has been reported [20] and is shown in Fig. 9. As pointed out by Tomkins [16] the crack is unable to resharpen if the environmental component of growth is of the same order as the crack width and this imposes a limit on the crack growth rate.

The analysis given above, using equation (4), applies specifically to situations where anodic dissolution controlled by oxide rupture/passivation is occurring. However it could equally be applied to the case where atomic hydrogen produced by the cathodic reaction is absorbed on to the clean exposed slip steps, and equation (4) could be adapted to calculate the amount of hydrogen available. The fractographic observations of Cullen et al [19] on A533B exposed to PWR water at NRL of quasi-cleavage are consistent with such a process. There have been no reported observations of microcrack formation ahead of the crack tip at 290°C in PWR water. This suggests that any hydrogen embrittlement effects if present must be very local to the crack tip surface and involve local changes in the cohesive strength of the lattice or changes in plasticity. Further support for this view is that all the published PWR data lie below the $\phi_{max}/2\text{-}R$ dependent upper bound developed by Tomkins[16].

The region of fatigue crack growth observed in Fig. 3 and other published data with a low ΔK dependence [3] is also consistent with equation (7). The temperature dependence of crack growth rates illustrated in Fig. 4 are difficult to interpret without detailed polarisation curves for each temperature studied. The apparent activation energy of 4 Kcal/gm mole from 25-175°C was discussed in detail by Atkinson and Lindley [20]. It would be consistent with diffusion of solvating ligands to the crack tip as a rate controlling step. The abrupt change in behaviour between 150 and 200°C for low dissolved oxygen concentration with a reduction in crack growth rate down to the level observed in air is quite different from the published data in BWR coolant which actually showed a maximum around 200°C [1]. The differences in PWR and BWR environments lead to the formation of quite different oxides. At high oxygen levels haematite is stable whereas in low oxygen water as shown in Fig. 10 on a Pourbaix diagram magnetite is stable at 300°C, with hydrogen evolution as the cathodic reaction. The apparent activation energy above 200°C is higher than in

the low temperature region with a value of 20Kcal/gm mole. Such a high value of apparent activation enthalpy is consistent with a rate controlling step involving micro slip at the crack tip. The abrupt change in behaviour between 150-200°C demonstrates that a deeper understanding of the processes operating at the crack tip is required.

The Pourbaix diagram for the Fe-H_2O system at 300°C (Fig. 10 10^{-6}M Fe^{2+}) is very similar to that at ambient temperatures Fe_3O_4 and Fe_2O_3 are formed as the oxide phases the latter at high oxygen levels. The potential of the CERL specimens is consistent with the diagram in that Fe_3O_4 is the observed corrosion product. The 2000ppm boric acid/1ppm LiOH solution used is calculated to yield a pH $\simeq 7 \pm 1$ at 290°C.

Data on high temperature polarisation characteristics are sparse but a schematic representation of a polarisation curve for pure iron in de-oxygenated acidic sulphate solution [24] is shown in Fig. 11. The classical active-passive transition is observed with the higher potentials being characterised by the formation of Fe_2O_3.

The role of dissolved oxygen as a cathodic reaction has been investigated by Indig [12]. A sudden transition in the corrosion potential of carbon steel as a function of oxygen concentration is observed with an upper shelf where oxygen reduction is thought to be the main cathodic reaction to a lower shelf where hydrogen evolution occurs (Fig. 12). The CERL result is consistent with the presence of a very low dissolved oxygen content and the temperature variation of the corrosion potential agrees well with the trend observed by McDonald [25] for A508 steel.

Thus the importance of measuring corrosion potential and oxygen content in corrosion fatigue studies is apparent. It is probable that some or all the scatter in interlaboratory round robins and the lack of reproducibility of early U.S.A. experiments in Europe is due to differences in corrosion potential between rigs and to changes during tests. There appears to be a trend for high oxygen BWR water to give large environmental enhancements, low oxygen PWR water in low flow or static rigs to give medium to large environmental enhancement [8] whereas the high flow rate rig at Harwell has not shown significant environmental enhancement under PWR conditions [4]. The oxides grown in these rigs are fundamentally different with Fe_2O_3 forming in high oxygen BWR environment, easily stripped Fe_3O_4 in low flow rate PWR water, and adherent Fe_3O_4 in the Harwell rig [26]. Introduction of large amounts of dissolved oxygen into the latter rig led to transient high crack growth rates followed by a transition back to a slower regime. Fe_2O_3 was formed as the oxide. It thus seems possible to correlate the occurrence of environmental enhancement with the type of oxide formed and hence with the corrosion potential.

The rate of repassivation of bare metal at the crack tip will be determined by the electrochemical properties of the passivating oxide e.g. solubility, conductivity, and hence parameters such as water chemistry, temperature and flow rate which determine the corrosion potential and hence oxide morphology and composition will affect crack growth rate. There is clearly a need for a detailed electrochemical study of these parameters.

Until measurements are made it is only possible to speculate as to the effect of flow rate on corrosion potential. Two counteracting effects would be expected and these are shown in Fig. 11. Firstly the increased rate of supply of oxygen to the corroding surface would cause the transition from upper to lower shelf potential to shift to a lower oxygen level and hence for a given oxygen level an increase in potential. Secondly a decrease in potential at the lower shelf level might occur as has been determined in erosion-corrosion studies on ferritic steel at lower temperatures (165°C) by Bignold et al [27]. The corrosion potential in a rapidly flowing system will therefore show a sensitive dependence on oxygen level and flow rate.

At potentials > -200mV(SHE) crack advance is likely to be by slip-dissolution type processes. At potentials $\lesssim$-800mV(SHE) some form of hydrogen assisted is possible so crack advance could be by either dissolution or hydrogen embrittlement. Until measurements of corrosion potential are made in all simulated PWR rigs it is not possible to distinguish between these alternative models and define accurate limits to possible crack growth rates.

CONCLUSIONS

1. The corrosion potential of an A533B steel fatigue specimen has been measured at various temperatures under corrosion fatigue conditions. At 290°C in a non-refreshed simulated PWR environment the potential was -840mV SHE corresponding to a very low oxygen environment.

2. An enhanced crack growth rate (up to 7x air data) was observed in PWR quality water with a very low (<10ppb) dissolved oxygen concentration.

3. A minimum crack growth rate was observed at 200°C for R = 0.2, ΔK = 35MPa$\sqrt{m}$ and 1c.p.m. sinewave.

4. An oxide rupture model of cracking has been suggested which predicts that the environmental component is related to the stress intensity value and the rate of change of stress intensity with time.

5. The measurement of corrosion potential and the identification of oxides on specimens provides important information on the mechanism of cracking, and should be routinely carried out with every corrosion fatigue test.

ACKNOWLEDGEMENTS

The authors acknowledge useful discussions with Drs. G.G. Chell, G.J. Bignold, P. McIntyre, P. McKay and T. Underwood at CERL and A. McMinn of UKAEA, SNL.

The work was carried out at the Central Electricity Research Laboratories and is published with permission of the Central Electricity Generating Board.

REFERENCES

1. Kondo, T., Kikuyama, T., Nakajima, H., Shindo, M. and Nagasaki, R., 1971, International Conference on Corrosion Fatigue, Storr Connecticut
2. Gerber, T.L., Heald, J.D. and Kiss, E., 1974, Trans. ASME (H), J. Eng. Mat. Tech. 96, 255-261
3. Mager, T.R., Moon, D.M., Landes, J.D. and McLoughlin, J.M., (1973). HSST Progress Report ORNL-4971
4. Scott, P.M. and Trustwell, A.E., 1981, this meeting
5. Riccardella, P. and Mager, T.R., 1971, ASTM STP 513
6. Marshall, W., 1976, HMSO London, "Integrity of Nuclear Pressure Vessels".
7. Bamford, W., 1979, Trans. ASME, 101, 182-190
8. Jones, R.L., 1981, this meeting
9. Scott, P.M., 1979, Metal Sci. Journal, 13, 396-401
10. Bamford, W., 1977, in The Influence of Environment on Fatigue, I. Mech. E., 51-56
11. Goodfellow, G.I. and Webber, H.M., 1979, The Analyst, 104, 1245
12. Indig, M.E., 1979, EPRI CAC Workshop, Palo Alto
13. Underwood, T. and McKay, P., 1981, CERL Report in Preparation
14. Ford, F.P. and Silverman, M., 1979, First Semi-annual Report, EPRI Project RP1332-1
15. Newman, J.F., 1978, CEGB Laboratory Note RD/L/N 120/78
16. Tomkins, B., 1979, Met. Sci. Journal, 13, 396-401
17. Shoji, T., Takahashi, H., Nakajima, H. and Kondo, T., This meeting
18. Shoji, T., Aiyama, S., Takahashi, H. and Suzuki, M., 1978, Corrosion, 34, 8, pp. 276-282
19. Cullen, W.H., Provensano, V., Torronen, K.J., Watson, H.E. and Loss, F.J., NRL Memorandum 4063

20. Atkinson, J.D., and Lindley, T.C., 1977, in the Influence of Environment on Fatigue, I. Mech. E., London, 65-74

21. Loss, F.J., 1981, NRL Memo. 4400

22. Barsom, J.M., 1972, Trans. ASME, Paper 71-PVP-12

22. Atkinson, J.D., Cole, S.T. and Forrest, J.E., 1981, to be published

23. Mann, G.M.W., 1977, CEGB Laboratory Note RD/L/N 77/76

24. McKay, P. and Underwood, T., private communication

25. McDonald, D.D., Szklarska-Smialowska Z. Pednekar S.P. Mizuno 1., and Choi H.J., 1980, EPRI Progress Report, Project T 115-5

26. Scott, P.M., 1980 Private communication

27. Bignold, G.J., Garbett, K., Garnsey, R. and Woolsey, I.S., 1980 Paper 1, Water Chemistry II BNES Conference, Bournemouth

Table 1

Chemical Composition

Specimens	C	Si	Mn	Ni	Cr	Mo	Cu	S	P	Co	Sn	Ta
1HT6, 1HT51	0.19	0.205	1.25	0.68	0.13	0.49	0.07	0.013	0.017	0.009	0.011	<.002
MF5	0.16	0.22	1.39	0.63	0.10	0.51	0.11	0.005	0.006	0.006	0.02	-

Table 2

Mechanical Properties

Specimen	$\sigma_{Y\ 20^oC}$ MPa	$\sigma_{Y\ 290}$ MPa	$\sigma_{UTS\ 20}$ MPa	$\sigma_{UTS\ 290}$ MPa
1HT6, 1HT51	399	359	555	478
MF5	450	410	600	530

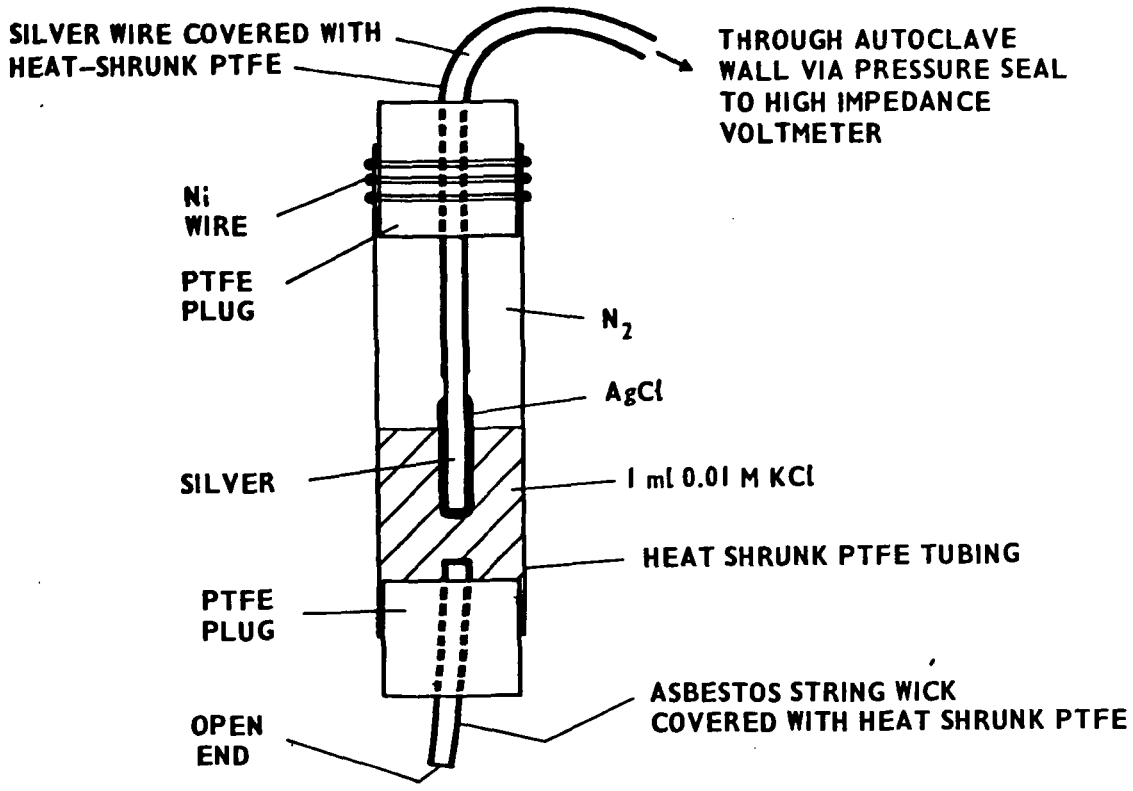

FIG. 1 CONSTRUCTION OF HIGH TEMPERATURE AND PRESSURE Ag/AgCl ELECTRODE

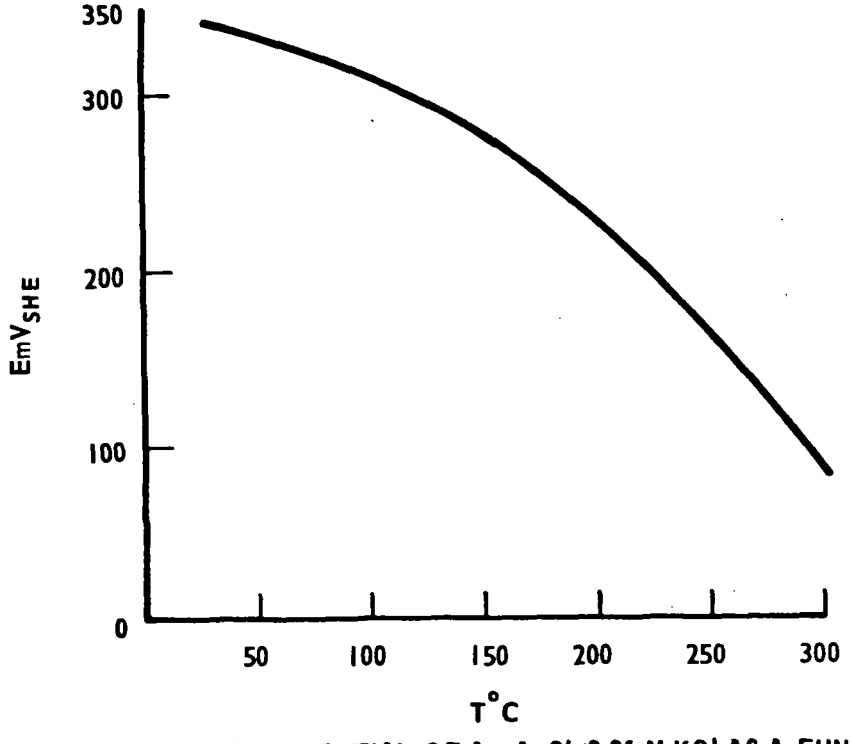

FIG. 2 HALF CELL POTENTIAL OF Ag/AgCl/0.01 M KCl AS A FUNCTION OF TEMPERATURE

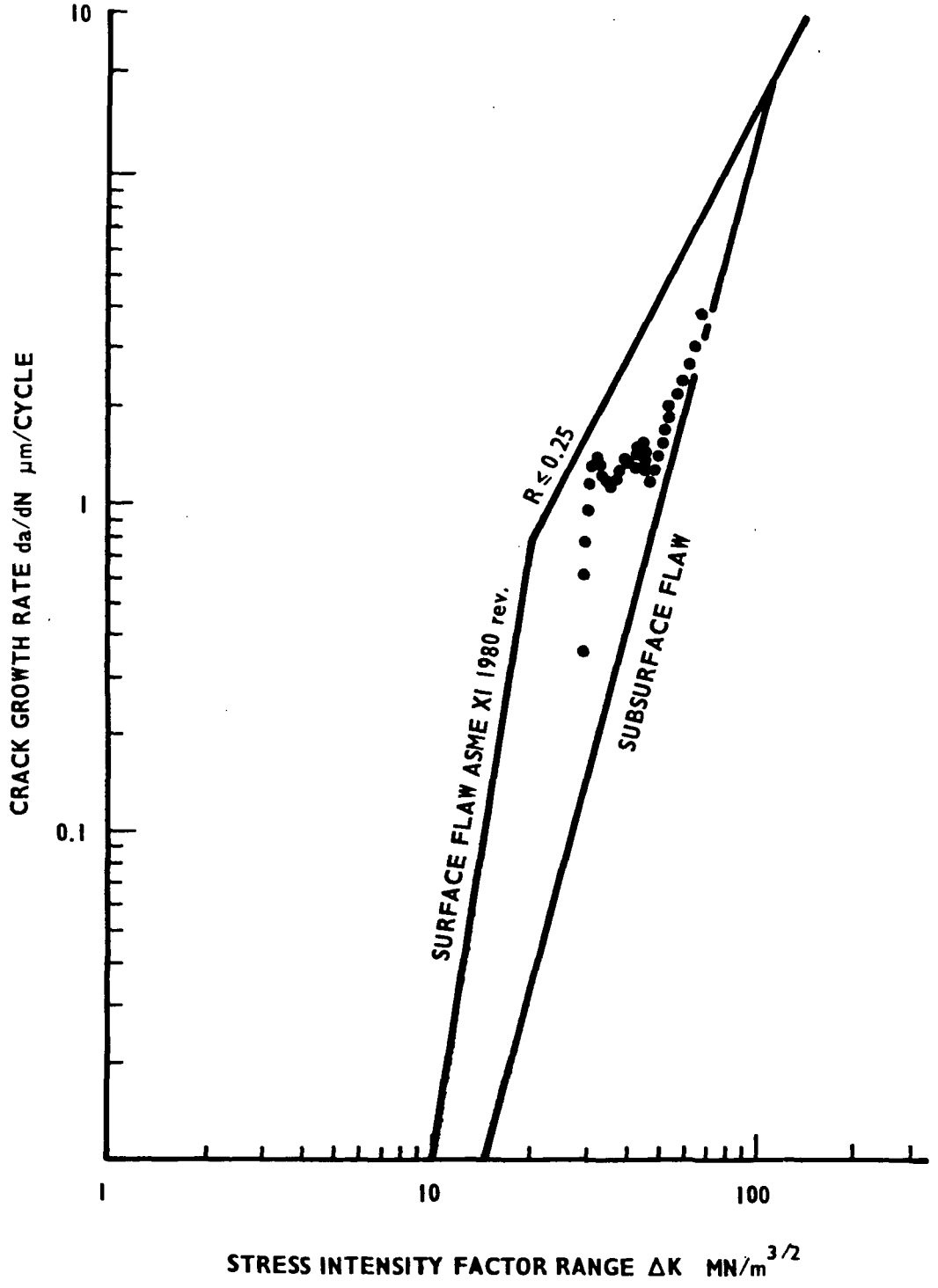

FIG. 3 FATIGUE CRACK GROWTH OF A533B IN 290°C SIMULATED PWR WATER WITH R = 0.2 1CYCLE/MINUTE SINEWAVE.SPECIMEN 1 HTG

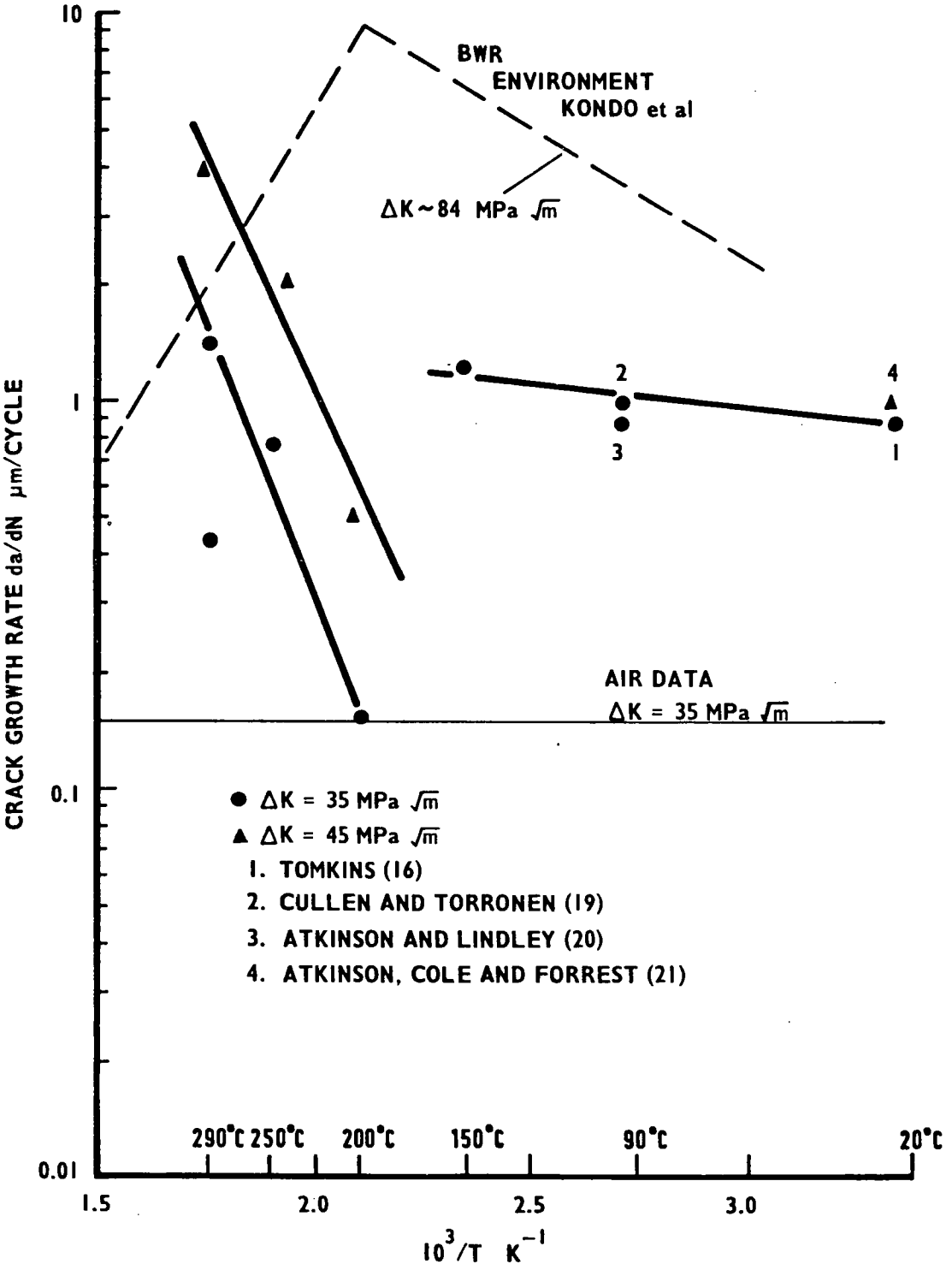

FIG. 4 CRACK GROWTH RATE AS A FUNCTION OF TEMPERATURE

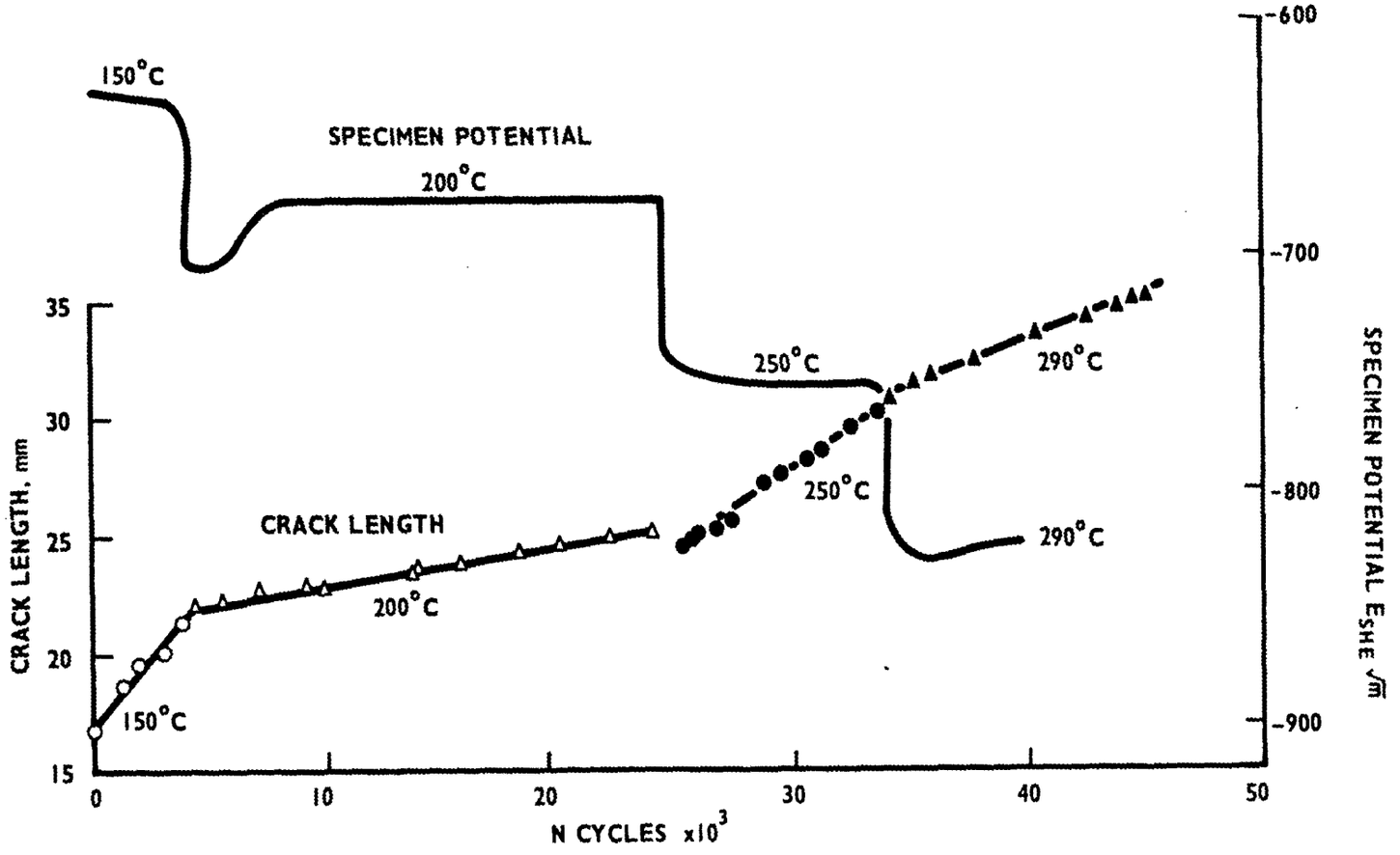

FIG. 5 CRACK LENGTH AND SPECIMEN POTENTIAL DURING CORROSION FATIGUE TEST C. MARREL FRERES A533B, SIMULATED PWR WATER, ΔK = 35 MPa $\sqrt{m}$, 1 CYCLE/MIN SINEWAVE, R = 0.2 SPECIMEN MF5

JDA/JDH(24.8)RL 5.3.369

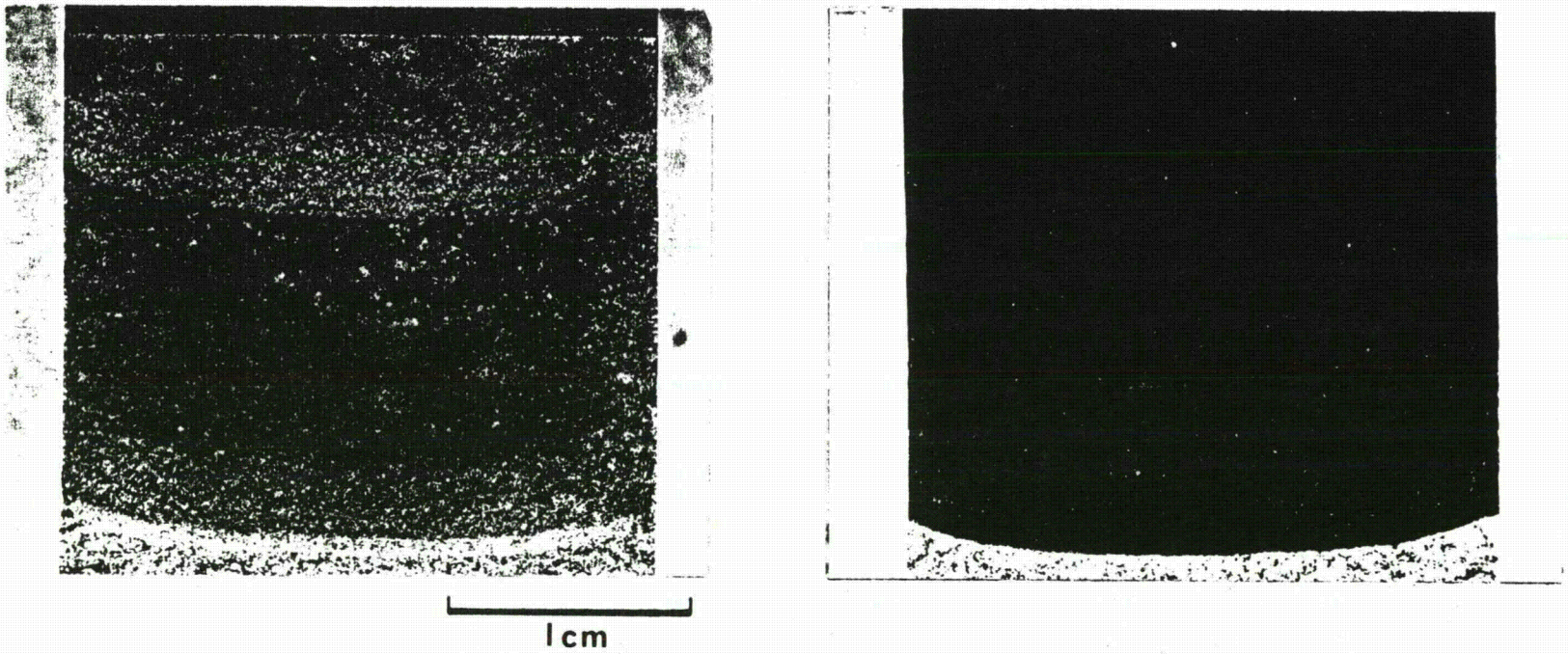

FIG.6 FRACTURE SURFACE OF MARREL FRERES A533B CLASS 1 AFTER TEST AT $\Delta K = 35 MPa\sqrt{m}$, R = 0.2, 1 c.p.m. SINE IN SIMULATED PWR WATER.

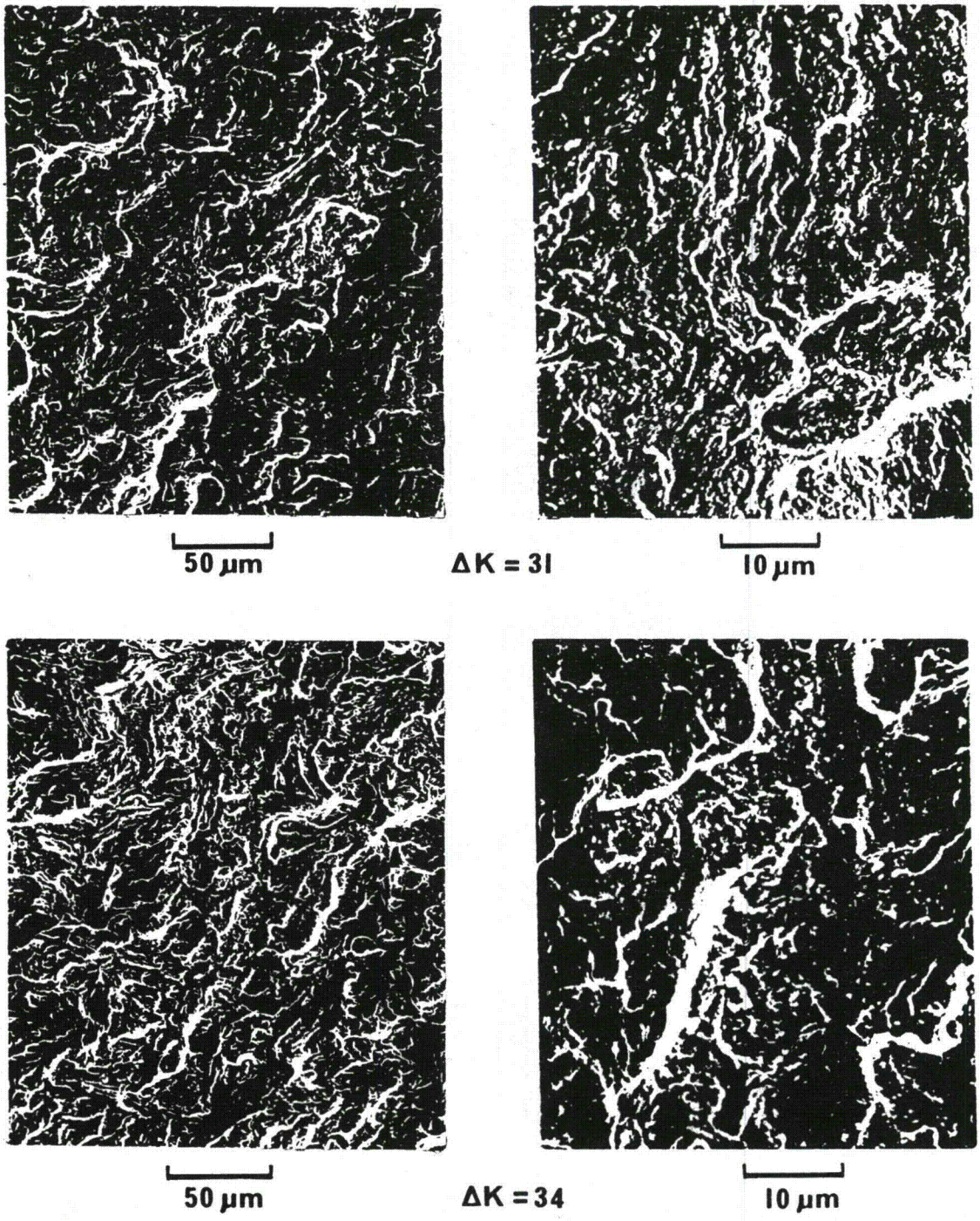

FIG.7 DETAIL OF FRACTURE SURFACE (OXIDE STRIPPED) FOR CONSTANT LOAD SPECIMEN, R.=0.2, 1c.p.m.

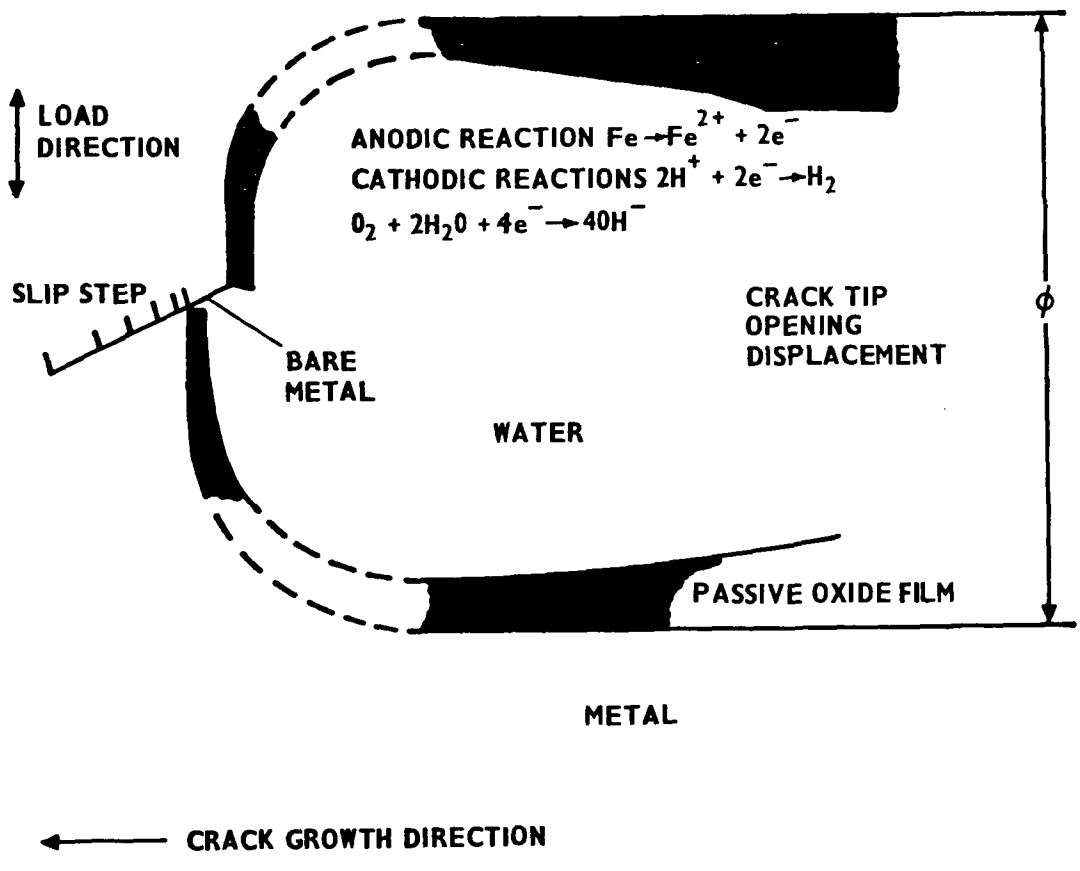

FIG. 8 MODEL OF CRACK TIP DURING CORROSION FATIGUE

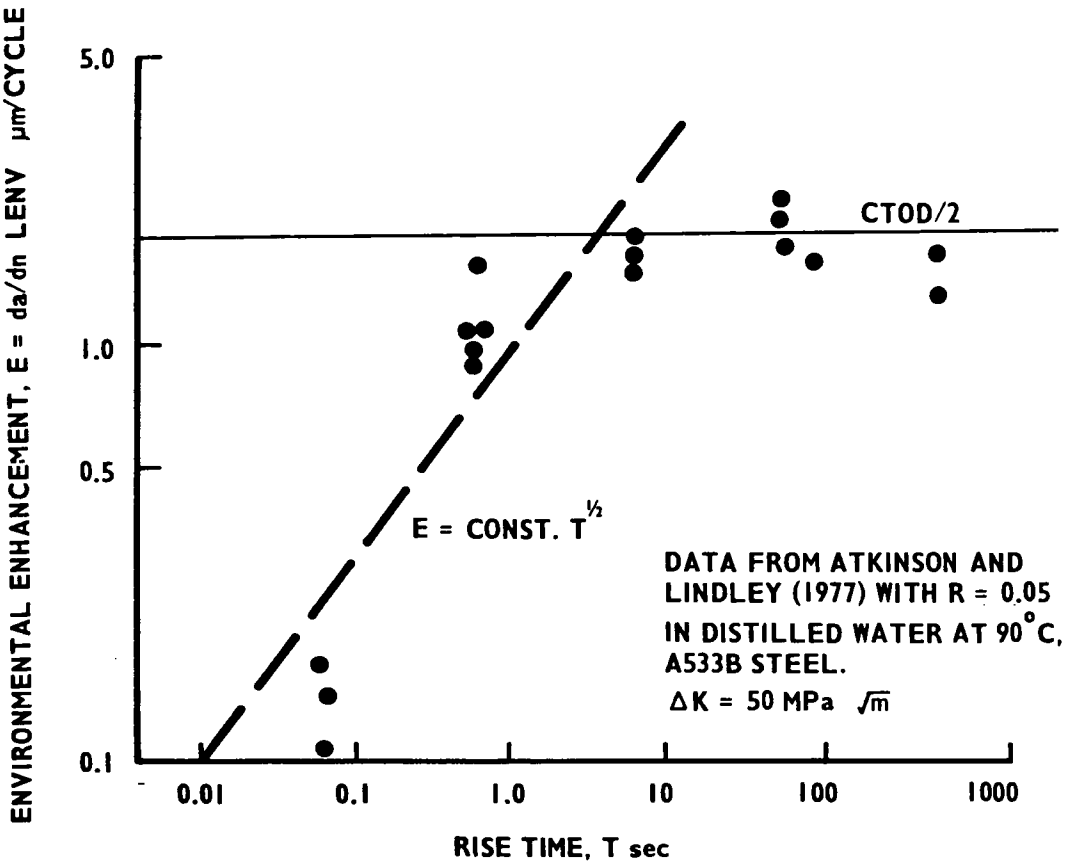

FIG. 9 ENVIRONMENTAL ENHANCEMENT AS A FUNCTION OF RISE TIME

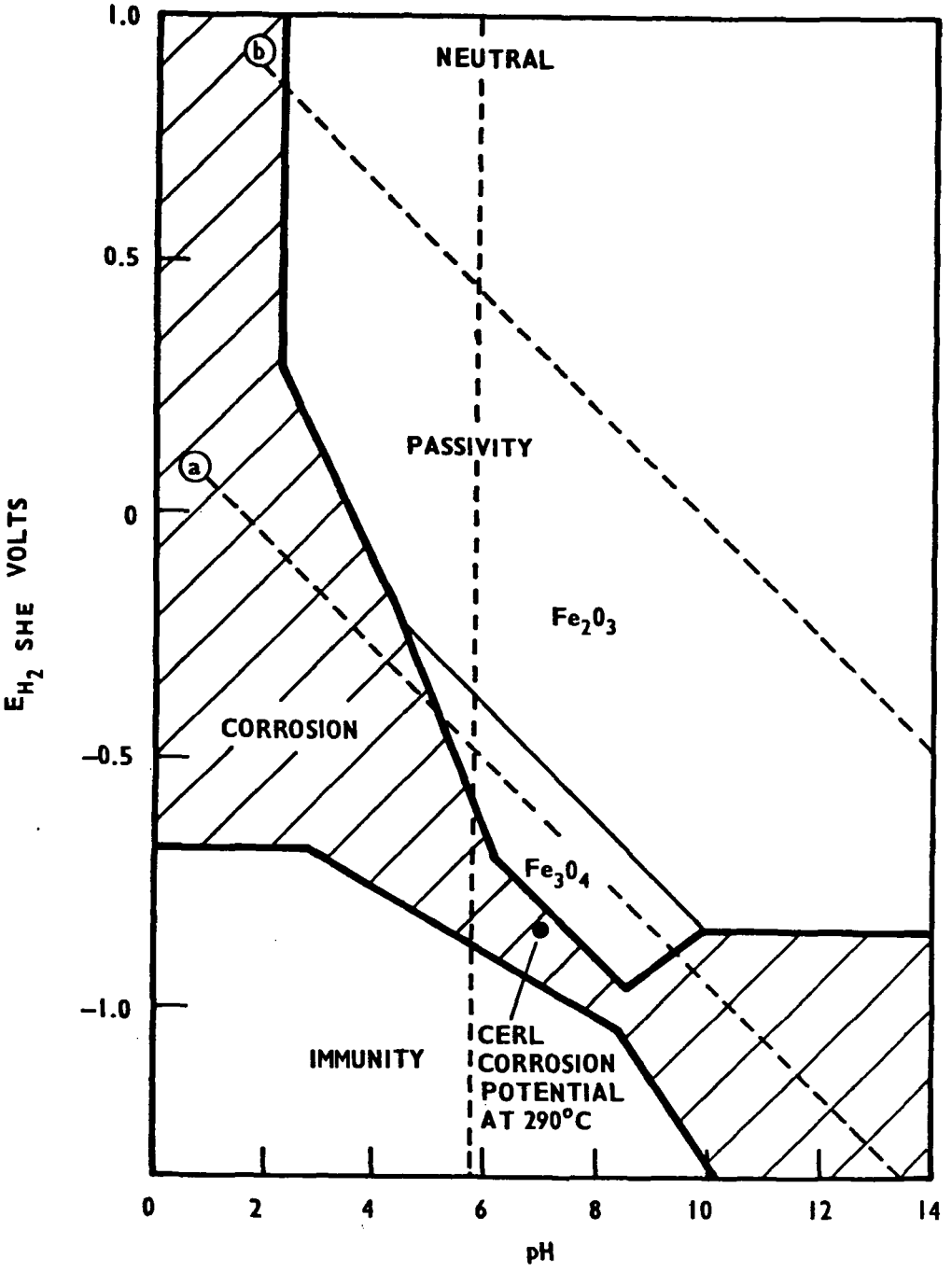

FIG.10 POURBAIX DIAGRAM FOR Fe-H_2O AT 300°C (MANN 1977)

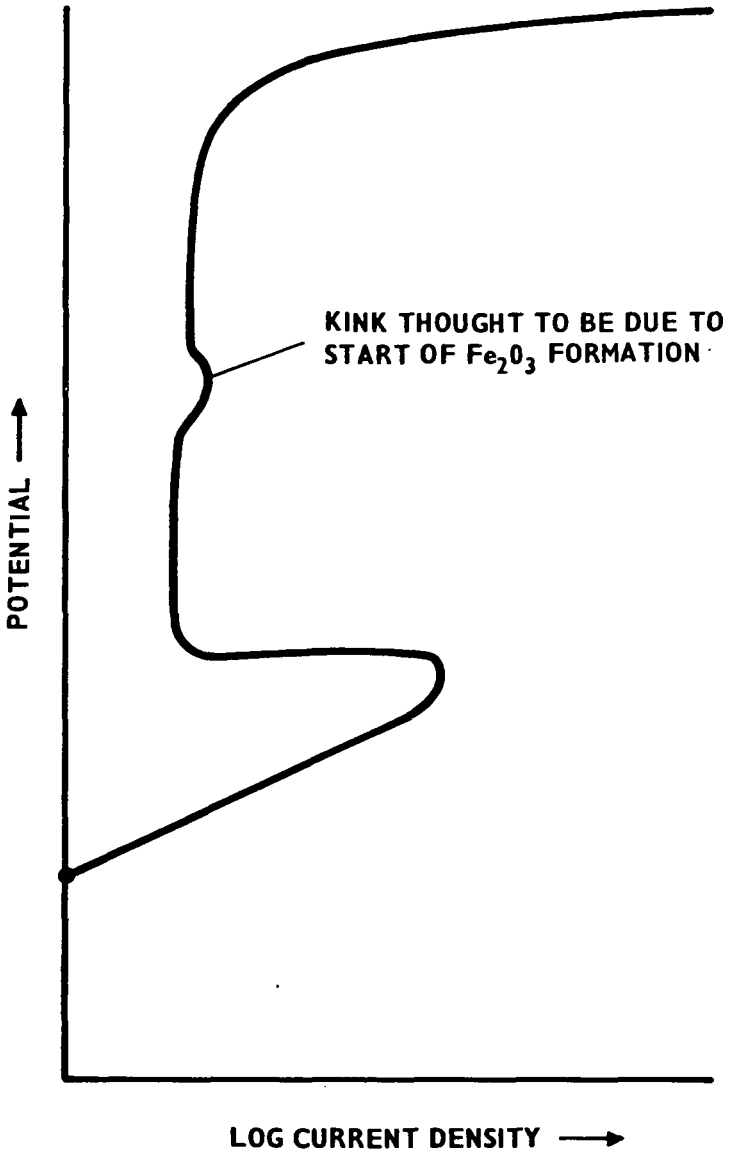

FIG. 11 SCHEMATIC REPRESENTATION OF THE POLARISATION CURVE FOR PURE Fe AT 290°C IN ACIDIC SULPHATE SOLUTION

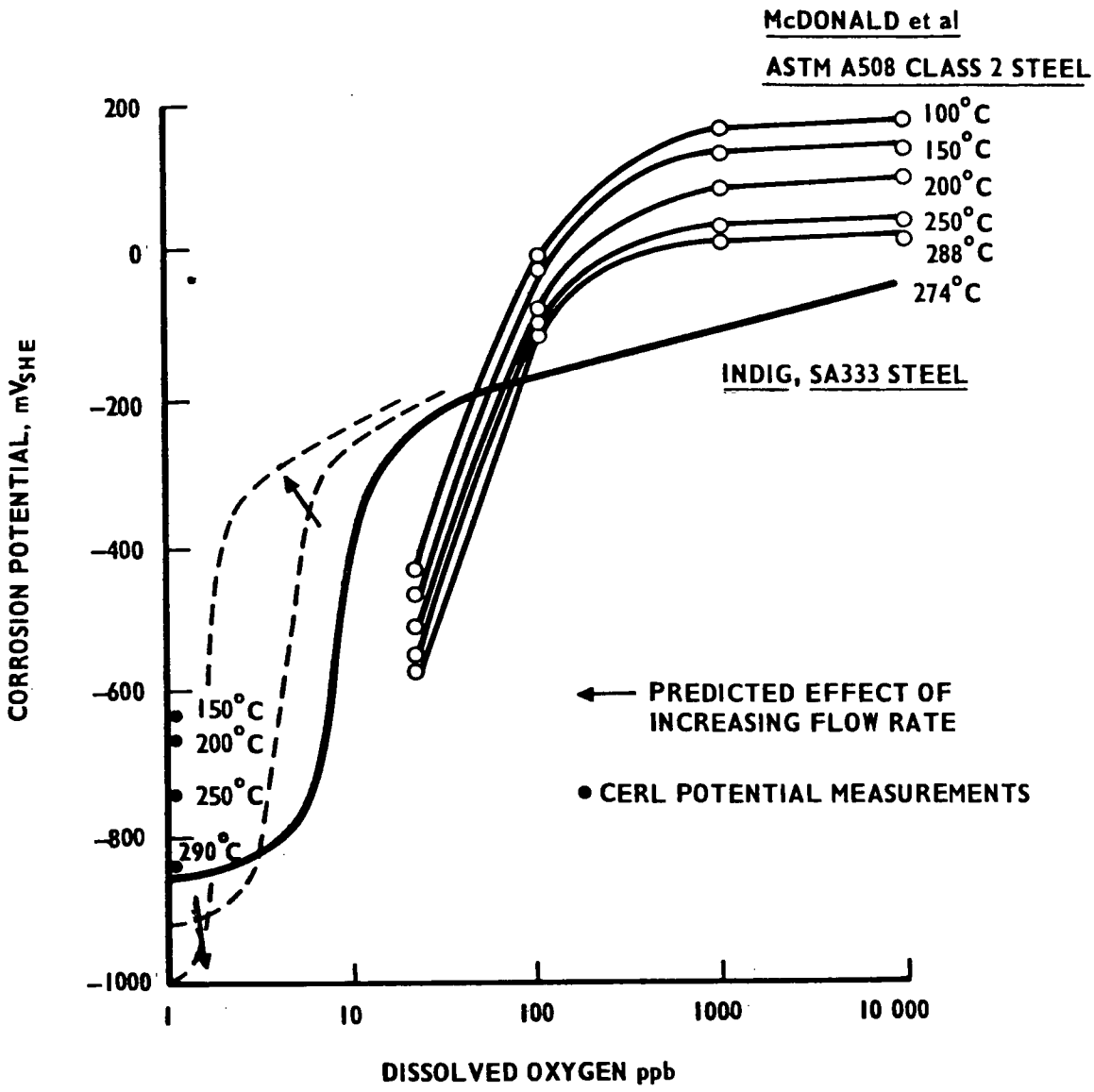

FIG. 12 CORROSION POTENTIALS V DISSOLVED OXYGEN CONTENT FOR CARBON STEELS COMPARED WITH CERL RESULTS

A FATIGUE CRACK GROWTH THEORY BASED UPON ENERGY CONSIDERATIONS

Pietro P. Milella
Comitato Nazionale per l'Energia Nucleare
Roma, Italia

1. Introduction

It is well known how the repeated application of a load over a body containing a crack leads to a progressive growth of the crack itself. It has also been observed that the rate of such a growth is somehow related to both the dimensions of the crack and the amplitude of the load cycling.

This observation has led in the past to the formulation of many empirical formulas aiming to predict the fatigue crack growth rate without any pretense, however, to explain the phenomenon itself. Often such formulas were not only inadeguate but also contradictory.

It was not untill the introduction of Fracture Mechanics in the study of fatigue that the dependence of the growth rate on crack size and stress amplitude was established unequivocally/1/.

In particular the finding that such a rate when plotted versus ΔK_I on a log-log scale was rapresented by a straight line led Paris and Erdogan /2/ to the formulation of the empirical relationship :

$$\frac{da}{dN} = C\,\Delta K_I^n \qquad (1)$$

where n is the slope of the da/dN data on a log-log scale and C a scale factor. Both n and C are material parameters.

Equation (1) though adequate for simple applications, does not explain neither why a crack has to grow under cyclic loads nor what

physical parameters enter in the constant C which is of experimental derivation.

The purpose of this paper is to shed light on the fatigue crack growth process and establish what physical parameters significantly intervene in the phenomenon itself.

2. The energy approach

To fully understand the fatigue crack growth phenomenon it is necessary to search into what happens ahead of a flaw during any loading phase. In the present work such an investigation has been done on an energy base rather than from a geometric stand point which has led to the CTOD based equation /3/ :

$$\frac{da}{dN} = C \frac{\Delta K^2}{E \sigma_{ysc}} \qquad (2)$$

which seems to be more significative than equation (1).

Recolling the Griffith's criterion for fracture /4/ in an ideally brittle material containing a flaw of length 2a under a tensile stress state it can be stated that instability is reached whenever the energy release rate $\mathcal{G}$ approaches a critical value $\mathcal{G}_c$ such that during a virtual crack extension, da, energy is released with the same rate at which it is absorbed:

$$G_c = R \qquad (3)$$

or:

$$\frac{\pi \sigma_c^2 a}{E} = 2 \gamma_s \qquad (4)$$

In an " end fixed " configuration the energy γ_s to form new free surface provides the only mechanism through which energy can be absorbed by the system. Equation (3) and (4) are graphically rapresen

ted in figure 1. Any stress state σ resulting in a $\mathcal{G}$ value lower than $\mathcal{G}_c$ would not produce instability.

It is an " in - out " situation in that a crack of a given length 2a under a stress state σ either becomes unstable or stays like it is.

In real materials the main contribution to the energy absorbtion rate R comes from the energy stored ahead of the crack tip as plastic strain energy. The contribution of the surface energy is now pratically negligible. The resistance R is no longer rapresented by a constant term but becomes a rather complex function of crack length increasing as a increases. The new situation is depicted in figure 2.

The instability condition is now :

$$\frac{\delta G}{\delta a} = \frac{\delta R}{\delta a} \qquad (5)$$

and is rapresented in figure 2 by the tangency point A.

The main difference with respect to ideally brittle materials is that now even though a certain combination of crack size 2a and stress state σ does not result critical (see fig. 2) yet there is sufficient energy in the system to pop the crack up to a point at which $\mathcal{G}$ becomes equal to R and the crack stops. Any further increment would not be possible in that R becomes greater than $\mathcal{G}$. The $\mathcal{G}$ function has been assumed to be the same as for ideally brittle materials. Actually this is only a first approximation since in real materials $\mathcal{G}$ seems to deviate for longer cracks from the straight line condition indicating a more complex dependence on crack size a.

Unloading and than reloading, the crack which stopped earlier now grows again indicating that the previous condition $\mathcal{G} = R$ is no longer satisfied.

If this happens there is only one possible explanation : the volume that yields ahead of the crack tip is not capable, during any reloa-

ding, to absorb energy with the same rate. This forces the crack to grow further to regain the loss in the energy absorbtion rate and establish once again the equilibrium between $\mathcal{G}$ and R through the yielding of new material.

3. Energy lost in the plastic zone

The reason why the material ahead of the crack tip plastically deformed during a load cycle cannot absorb the same quantity of energy in the following cycle is clearly related to the Bauschinger effect.

Because of the sharp stress concentration a region around the crack tip deforms plastically thus impeding the occurrence of a stress singularity. The elastic stress field exists somewhere ahead of the crack tip. According to Irwin /5/ the presence of the plastic zone makes the crack behave as if it were longer. Assuming hereafter that the plastic zone has a circular shape of radius r_p it is as if the actual crack tip were located at the center of that zone as rapresented in figure 3.

To start with it is convenient to consider the material as elastic-plastic, than the stress in the plastic zone is kept equal to the yield stress while the elastic stress field commences at the boundary of that small plastic enclave.

The elastic stress field is rapresented by the well known equations

$$\sigma_x = \frac{K_I}{(2\pi r)^{1/2}} \cos\frac{\vartheta}{2}\left[1 - \sin\frac{3\vartheta}{2}\sin\frac{\vartheta}{2}\right]$$

$$\sigma_y = \frac{K_I}{(2\pi r)^{1/2}} \cos\frac{\vartheta}{2}\left[1 + \sin\frac{3\vartheta}{2}\sin\frac{\vartheta}{2}\right] \qquad (6)$$

where r and ϑ are the polar coordinates of any point close to the

crack tip, the origin being located at the center of the plastic zone which actually becomes the tip of the effective crack (see fig. 3).

Following the Irwin hypothesis /5/ the radius of the plastic zone can be expressed as :

$$r_p = \frac{K_I^2}{2\pi\sigma_{ys}^2} \tag{7}$$

While σ_y in the plastic enclave is kept to the yield value because of the elastic- plastic hypothesis, the strain ε_y is actually increasing as the center of the plastic zone approaced. There will be a distance r_p^* from the origin were ε_y becomes twice the elastic strain ε_e at which yield occurs.

The value of r_p^* can be inferred replacing in equation (7) σ_{ys} with $2\sigma_{ys}$

$$r_p^* = \frac{K^2}{8\pi\sigma_{ys}^2} = \frac{1}{4} r_p \tag{8}$$

The material in the small plastic enclave of radius r_p^* (see fig. 3) undergoes a reverse plastic flow during the unloading of the body containing the crack. This is due to the constraint exerted by the material elastically stressed all around the plastic zone which upon unloading returns to zero strain overwelming and thus forcing the small area plastically deformed to shake down remaining in a state of permanent compressive stress. Figure 4 depicts this situation and the occurrence of the reverse plastic flow. It can be seen that any element deformed beyond $2\varepsilon_e$ (for example point C of figure 4) upon unloading goes back to point B" through a reverse plastic flow C"B". The consequence is that the actual yield stress is now $2\sigma_{ys}$ since the material can be stressed elastically from zero to $2\sigma_{ys}$ without undergoing a plastic deformation. This justifies the value $2\sigma_{ys}$ introduced in equation 7.

Rice /6/ has shown that the effect of a stress reversal attending

load cycling is to generate a small plastic core whose radius is approximately given by equation (6).

During the reloading the element will return to the same deformation but this time instead of following the path OABC (see fig. 4) it will reach point C through the line B"B'BC. In terms of energy this means that the element, as well as any other element in the plastic zone of radius r_p^*, will no longer absorb the energy proportional to the area OAB'O, i.e. the elastic energy.

For any other element outside the area of radius r_p^* but inside the plastic zone (see fig. 3) there will be a reduction in the energy stored during the reloding phase but of a lower magnitude. Finally a point on the border line of the plastic enclave will be stressed elastically from zero up to the yield point with no loss of energy during the load cycling.

To visualize the consequence of such a loss of energy during the reloading it may be convenient to return to the R curve as shown in figure 5. During the first application of the external load there is sufficient energy in the system to pop the crack of a quantity Δa^* such that an equilibrium is reached between $\mathcal{G}$ and R. That point is rapresented in figure 5 by the equality $\mathcal{G}_1 = R_1$. Unloading the system a new crack is left whose half size is $a + \Delta a^*$.

Upon reloading the R curve will start from an initial crack length $a + \Delta a^*$ but since the material is not capable to absorb energy with the same rate as before to the same combination of crack size and stress state σ it will not correspond the previous value R_1 but a smaller one R_1'. The new R curve, indicated in figure 5 as R_{rel}, has been assumed to have the same shape of the initial R curve, i.e. the R curve has been considered invariant /7/.

The loss in the energy absorbtion rate R will be :

$$-\Delta R = \frac{\partial}{\partial a}\left(E_2 - E_1\right) \qquad (9)$$

where E_1 and E_2 are the energies stored in the material during the first cycle and the second one respectively, E_2 being smaller than E_1. To the new size $a + \Delta a^*$ it will correspond a new value R_1' equal to :

$$R_1' = R_1 - \Delta R \tag{10}$$

As it can be seen from figure 5 this shift in the R curve results in a new point of equilibrium between $\mathcal{G}$ and R. To reach it the flaw has to grow further of a quantity Δa so that :

$$\mathcal{G}_2 = R_2 \tag{11}$$

where :

$$\mathcal{G}_2 = \mathcal{G}_1 + \Delta\mathcal{G} \tag{12}$$

Therefore the growth Δa during the reloading cycle is the consequence of the loss of capability to absorb the same amount of energy through a plastic deformation. Such a loss is regained by the growth of the crack and hence by the plastic deformation of new material.

The energy lost in the plastic area can be assessed recolling that in the small central core, in which reverse plastic flow occurs, the material does not absorb energy proportional to the elastic energy $1/2 \cdot \sigma_{ys}\varepsilon_e$. Outside that small area but within the plastic enclave the loss of energy becomes smaller and smaller as the border is approached becoming zero on the border itself.

Assuming a linear distribution from $1/2 \cdot \sigma_{ys}\varepsilon_e$ to zero than the energy lost $E_{2,1}$, the thickness of the material being 1, is :

$$E_{2,1} = 0.2188\,\pi r_p^2 \varepsilon_e \sigma_{ys} \tag{13}$$

4. The shape of the plastic zone after cycling

If, on the one hand, the material around the crack tip in the plastic enclave cannot absorb the same amount of energy inthe following cycle, on the other hand the tensile residual stress field left beyond the plastic enclave provides an absorbtion mechanism that must be taken into consideration in the evaluation of the net energy loss ΔE.

The existence of such a tensile stress field is the consequence of the compressive stresses left in the plastic zone after unloading as previously described. That compressive stress state must be balanced by a tensile stress field. This situation is depicted in figure 6. The tensile residual stress field provides additional plastic deformation around the original plastic zone and hence additional energy absorbtion during the reloading phase when it combines with the elastic stress field given by equations (6) as shown in figure 7. Hahn, Hoagland and Rosenfield /8/ using an etching technique revealed that effectively the global plastic deformation attending crack growth is wider than that corresponding to a monotonic loading.

Since in the reloading cycle the resulting elastic stress distribution is somewhat higher because of the superposition of the tensile residual stress field to the crack tip stress field even the material elastically stressed ahead of the plastic zone will absorb more energy, through an elastic deformation. To infer such an energy absorbtion, both plastic and elastic, the distribution of the residual stress field must be known. Some hypotheses have been made to derive it. To start with the continuous shape of the tensile stress distribution has been approximated by a triangle,

than the field itself has been assumed to span twice the radius r_p of the plastic zone. This hypothesis, which follows the Saint Venant principle, is also consistent with experimental evidences about residual stress fields set up after welding /9, 10/.

The compressive stress distribution within the plastic zone has also been simplified. The final scheme is shown in figure 8.

Under these hypotheses the total compressive residual force $F_{c,r}$ left in the plastic enclave is:

$$F_{c,r} = 0.109\ \pi r_p^2 \sigma_{ys} \cdot 4 \tag{14}$$

while the total tensile residual force $F_{t,r}$ is :

$$F_{t,r} = 0.833\ \pi r_p^2 \sigma_{max} \cdot 4 \tag{15}$$

Since $F_{t,r}$ must be equal to $F_{c,r}$ the value of σ_{max} can be inferred:

$$\sigma_{max} = 0.13\ \sigma_{ys} \tag{16}$$

The distribution of the tensile residual stress field is then :

$$\sigma_{t,r}(s) = 0.13 \left(1 - \frac{s}{2r_p} \right) \sigma_{ys} \tag{17}$$

The origin of the s axis is shown in figure 8.

Since the crack tip stress field ahead of the crack itself is given by equation (6) for $\vartheta = 0$ then :

$$\sigma_y(r) = \sqrt{\frac{r_p}{r}}\ \sigma_{ys} \tag{18}$$

The additional plastic deformation ahead of the original plastic enclave due to the superposition of the residual stress field will extend up to a distance s which satisfies the condition :

$$\sigma_y(r) + \sigma_{t,r}(s) = \sigma_{ys} \tag{19}$$

or :

$$\sqrt{\frac{r_p}{r}} + 0.13\left(1 - \frac{s}{2r_p}\right) = 1 \tag{20}$$

with $r = s + r_p$ (21)

Equation (20) is satisfied for $s = 0.136\ r_p$ (22)

The shape of the global plastic zone attending the load cycling is than given in figure 7 .It can be seen that the additional plastic area drops abruptly to zero from 90° to 180° because of the sharp decrease in the crack tip stress field given by equation (6) for ϑ higher than 90°. The value given by equation (22) is in good agriment with experimental results /8/.

5. Energy lost per cycle

Once the distribution of the tensile stress field is known (see equation (17)) the energy absorbed ahead of the plastic enclave $E_{2,a}$ through the mechanism described in the previous section can be inferred. The value of $E_{2,a}$ is given by :

$$E_{2,a} = 2\,\varepsilon_e\,\sigma_{ys}\int_0^{\pi}\int_0^{2r_p} f(r)\,g(s)\,d\vartheta\,ds \tag{23}$$

where the functions f(r) and g(s) rapresent the distribution of the crack tip stress field and the tensile residual stress field respectively normalized to σ_{ys} , i.e. from equations (18) and (17) :

$$f(r) = \sqrt{\frac{r_p}{r}} \cos\frac{\vartheta}{2}\left[1 + \sin\frac{3\vartheta}{2}\sin\frac{\vartheta}{2}\right]$$
$$g(s) = 0.13\left(1 - \frac{s}{2r_p}\right) \qquad (24)$$

Than the right term of equation (23) becomes :

$$E_{2,a} = 0.2116\pi\, r_p^2 \varepsilon_e \sigma_{ys} \qquad (25)$$

than the total energy lost in the reloading is :

$$E_{2,i} - E_{2,a} = 0.0072\,\pi\, r_p^2 \varepsilon_e \sigma_{ys} \qquad (26)$$

Equation (26) rapresents the value of the difference $E_1 - E_2$ where E_1 and E_2 are the energies absorbed by the material in the first cycle and in the second one. Than the value $-\Delta R$ given by equation (9) can be finally derived :

$$-\Delta R = \frac{\partial}{\partial a}\left(E_2 - E_1\right) = \frac{\partial}{\partial a}\left(7.2\cdot 10^{-3}\pi\, r_p^2 \varepsilon_e \sigma_{ys}\right) \qquad (28)$$

and recolling the expression of r_p given by equation (7) :

$$-\Delta R = 3.6\cdot 10^{-3}\,\frac{\pi a \sigma^4}{E\,\sigma_{ys}^2} \qquad (29)$$

6. Maximum fatigue crack growth

Equation (29) can be used in the evaluation of the maximum fatigue crack growth. It can be seen from figure 5 that for a subcritical crack growth the drop $-\Delta R$ in the Energy Absorbtion Rate subsequent a reloading is always greater than the increase $\Delta \mathcal{G}$ in the

Energy Release Rate. Actually this represents a condition for sub-critical crack growth to occur. The maximum allowable fatigue crack growth can than be inferred by equating :

$$\Delta \mathcal{G} = -\Delta R \tag{30}$$

and recolling the Griffith's expression for $\mathcal{G}$ /4/ and the expression (29) for R equation (30) can be written as :

$$\frac{2\pi\sigma^2\Delta a}{E} = 3.6\cdot10^{-3}\ \frac{\pi a \sigma^4}{E\,\sigma_{ys}^2}$$

from which :

$$\Delta a = 1.8\cdot10^{-3}\ \frac{a\,\sigma^2}{\sigma_{ys}^2}$$

or :

$$\Delta a = 0.57\cdot10^{-3}\left(\frac{\Delta K_Q}{\sigma_{ys}}\right)^2 \tag{31}$$

where $\Delta K_Q = \sigma\sqrt{\pi a}$. Equation (31) rapresents the maximum growth Δa per cycle following the load rising from zero to σ to which K_Q corresponds.

It is of extreme interest to compare equation (31) with the experimental relationship found by Bates and Clark /11/ between the width of the stretched zone at the onset of a rising load fracture after fatiguing and the relative toughness parameter, i.e. ratio between the critical stress intensity factor and the yield stress K_Q/σ_{ys} :

$$\text{Stretched zone width} = 0.85 \cdot 10^{-3} \left(K_Q/\sigma_{ys} \right)^{1.6} \tag{32}$$

The right terms of equatios (31) and (32) are very close to each

other and such a consistency is even more effective considering the approximations made in deriving equation (31) and the fact that Bates and Clark /12/ claimed that the width of the stretched zone is often found with a 50 % uncertainity.

This strongly suggests the physical meaning of that featureless zone observed on the fracture surface between the striations produced by fatigue and the dimple rupture and colled Stretched Zone is actually the maximum fatigue crack growth that a material can experience before it fractures.

On the other hand this also suggests that the energy path followed to derive equation (31) is right.

7. Subcritical crack growth

Equation (31) can be further developed to be applied in the evaluation of the subcritical crack groth rate following a load cycling.

As first the crack size a must be modified to account for the plastic zone which results in an effective crack longer than the physical one as pointed out in section 3. Following the Irwin'shypothesis the increment a_1 in the crack size is equal to half the radius of the plastic zone :

$$a_1 = \frac{1}{2} r_p \tag{33}$$

Equation (7) has been modified and r_p given a more general expression of the form :

$$r_p = \frac{K_I^2}{\pi \alpha \sigma_{ys}^2} \tag{34}$$

intraducing a parameter α which in real situations could not be necessarily equal to 2. Equation (33) thus becomes :

$$a_1 = \frac{a\,\sigma^2}{2\alpha\sigma_{ys}^2 - \sigma^2} \tag{35}$$

The left term of equation (30), $\Delta\mathcal{G}$, considering the effective crack length $a + a_1$ now becomes :

$$\Delta\mathcal{G} = \frac{\pi\sigma^2\Delta a}{E} \quad \frac{4\,\alpha\sigma_{ys}^2}{2\alpha\sigma_{ys}^2 - \sigma^2} \tag{36}$$

The right term, $-\Delta R$, of equation (30) needs not be modified since in the evaluation of $-\Delta R$ it has already been considered the effective plastic zone size. It is rather the whole equation (30) that must be modified.

Such a modification arises from the observation, already pointed out in section 6, that for subcritical crack growth to occur during load cycling it is necessary that upon reloading the increment $\Delta\mathcal{G}$ at which a new equilibrium is reached (see fig. 5) is smaller than the loss $-\Delta R$ in the energy absorbtion rate. Than equation (30) becomes :

$$\Delta\mathcal{G} = -\frac{1}{\beta}\Delta R \tag{37}$$

where β is an adimensional factor greater than 1.

If the R curve where a straight line the ratio :

$$\frac{\Delta\mathcal{G}}{\Delta R} = \frac{1}{\beta} \tag{38}$$

would be invariant and β indipendent on both σ and a.

The more R departs from the straight line condition the more $\Delta\mathcal{G}$

takes over $-\Delta R$ and the ratio (38) increases : β is no longer independent on both σ and a but becomes a function of the tipe :

$$\beta = \frac{\lambda}{(\sigma^2 a)^n} \tag{39}$$

where n is a parameter which depends on the shape of the R curve, i.e. a material parameter, and λ a material parameter which can be determined as follows.

At instability β has to be equal to unity thus satisfying equation (30), than from equation (39) it follows :

$$\lambda = \left(\sigma_{max}^2 a\right)^n \tag{40}$$

where σ_{max} is the maximum stress that can be held by the material containing the crack. Equation (39) becomes :

$$\beta = \frac{(\sigma_{max}^2 a)^n}{(\sigma^2 a)^n} \tag{41}$$

The radius of the plastic zone being expressed according to equation (34), the drop $-\Delta R$ given by equation (29) can be written as:

$$-\Delta R = C\pi \frac{a\sigma^4}{E\alpha^2\sigma_{ys}^2} \tag{42}$$

where $C = 1.44 \cdot 10^{-2}$.

Recolling equations (36), (41) and (42) equation (37) takes the form :

$$\Delta a \frac{4\alpha\sigma_{ys}^2}{2\alpha\sigma_{ys}^2 - \sigma^2} = C \frac{(\sigma^2 a)^{1+n}}{(\sigma_{max}^2 a)^n} \frac{1}{\alpha^2\sigma_{ys}^2}$$

or :

$$\Delta a = C \frac{(\sigma^2 a)^{1+n}}{(\sigma_{max}^2 a)^n} \frac{(2\alpha\sigma_{ys}^2 - \sigma^2)}{4\alpha^3\sigma_{ys}^4} \tag{43}$$

Since the effective stress intensity factor K_I or ΔK_I considering that the half crack length is $a + a_1$ is :

$$K_I^2 = \sigma^2 \pi a \frac{2\alpha\sigma_{ys}^2}{2\alpha\sigma_{ys}^2 - \sigma^2} \tag{44}$$

equation (43) becomes :

$$\Delta a = C \frac{\Delta K_I^{2(1+n)}}{K_{Ic}^{2n}} \frac{(2\alpha\sigma_{ys}^2 - \sigma^2)^{2+n}}{(2\alpha\sigma_{ys}^2 - \sigma_{max}^2)^n} \frac{1}{8\pi\alpha^4\sigma_{ys}^6} \tag{45}$$

8. Conclusion and results

Equation (45) rapresents the fatigue crack growth rate in a material cyclically stressed from zero to σ. The corresponding excursion of the stress intensity factor is ΔK_I. As it can be seen the crack growth rate depends on the toughness K_{Ic} of the material and the yield stress. Since, normally, the tougher the material the lower the yield stress these two parameters tend to balance each other. Such a balance is more or less effective depending on the value of the parameter n. Increasing n the weight of K_{Ic} prevails over σ_{ys} which actually means that in tougher materials K_{Ic} plays a major role than σ_{ys} particularly in the temperature range in which K_{Ic} increases at higher rate than σ_{ys} decreases.

The effective plastic zone size is very important in the fatigue crack growth rate. The higher α, i.e. the smaller the plastic zone size, the lower the rate.

Equation (45) also indicates a slight dependence of the growth rate on the crack length. In facts the maximum stress that a material can withstand, σ_{max}, decreases as the crack length increases. A dependence of the growthrate on the crack size has been effectively observed /13, 14 /.

Figures 9 to 11 show the fatigue crack growth rates predicted by equation (45) (solid line) and the experimental results (solid circles) for 3 different alloys.

The agreement is very good. It is important to note how the experimental results are matched by equation(45) when α is given a value of 2 for 7079 - T6 Aluminum Alloy, 2.2 for 4340 Steel and 3 for Ni Mo V Steel, i.e. a value very close to the theoretical one which according to the Irwin's hypothesis of the plastic zone is 2 (see equation 7).

9. References

1) P.C. Paris,M. Gomez and W.M. Anderson, A Rational Analitic Theory of Fatigue, The Trend in Eng.,13,1961,pp.9-14.

2) P.C. Paris,F. Erdogan, A Critical Analysis of Crack Propagation Lows, Trans. of ASME, Dec. 1963.

3) F.A. Mc Clintock, ASTM STP 415?pp.170 - 174, 1967.

4) A.A. Griffith, The Phenomena of Rupture and Flaw in Solids, Ro. Soc. Phil. Trans.(London),Series A, Vol.221, 1920, pp. 163-198.

5) G.R. Irwin, Plastic Zone Near a Crack and Fracture Toughness, Proc. 7th Sagamore Conf., IV - 63, 1960.

6) J.R. Rice, Amer. Soc. Test.MAt., Spec. tech. Publ. 415,1967,p.247

7) J. Kraft, A.M. Sullivan and R.W. Boyle, Effect of Dimension on Fast Fracture Instability of Notched sheets, Proc.of the Crack prop. Symp. I,Cranfield,1961,pp. 8 - 28.

8) G. Hahn, R.G. Hoagland and A.R. Rosenfield, Local Yielding Attending Fatigue Crack Growth, Metall. Trans., Vol. 3, 1972, pp. 1189 - 1202.

9) K. Masubuchi, Control of Distortion Shrinkage in Welding, WRC Bull.No 149, 1970

10) H. Kihara, K. Masubuchi, T. Kasuda and K. Iida, IIW - X -219-59

11) R. Bates and W. Clark, Fractography and Fracture Mechanics, ASM Trans., June, 1969.

12) W.G. Clark,R.C. Bates, Microscopic Aspect of Fracture Toughness, Scient. Paper 69-1E7-RDAFC-P1, Westinghouse, Dec., 1969.

13) N.E. Frost,L. Pook and K. Denton, Eng. Frac. Mech.,3,109,1971.

14) T.R. Gurney, Metal. COnst.,1, 91, 1968.

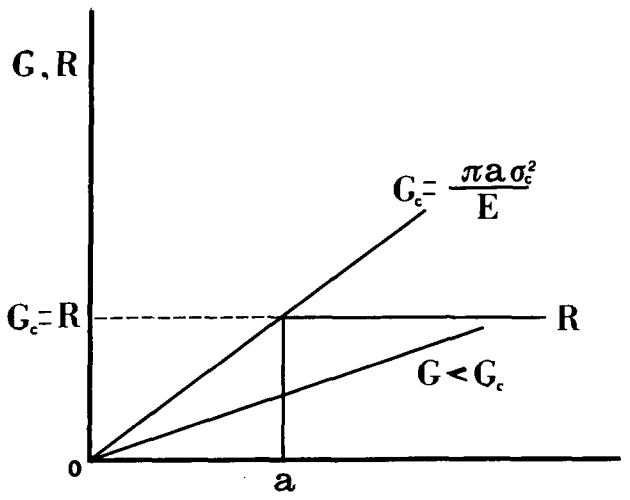

Figure 1. Fracture resistance diagram for an ideally brittle material

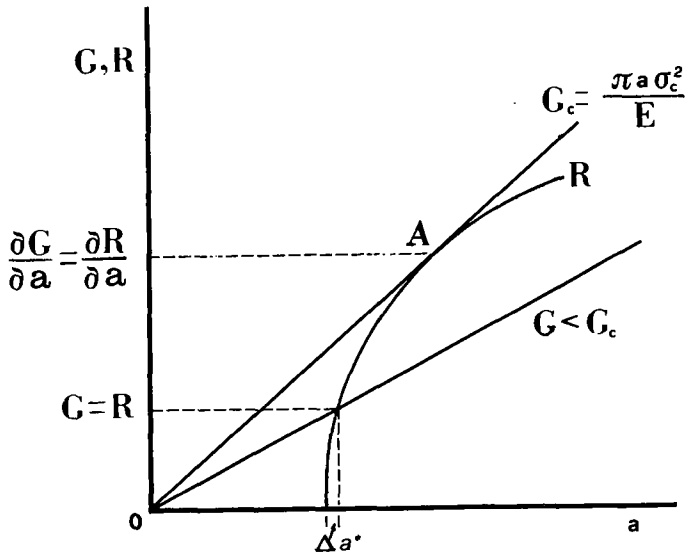

Figure 2. Fracture resistance diagram for a material which exhibits ductility.

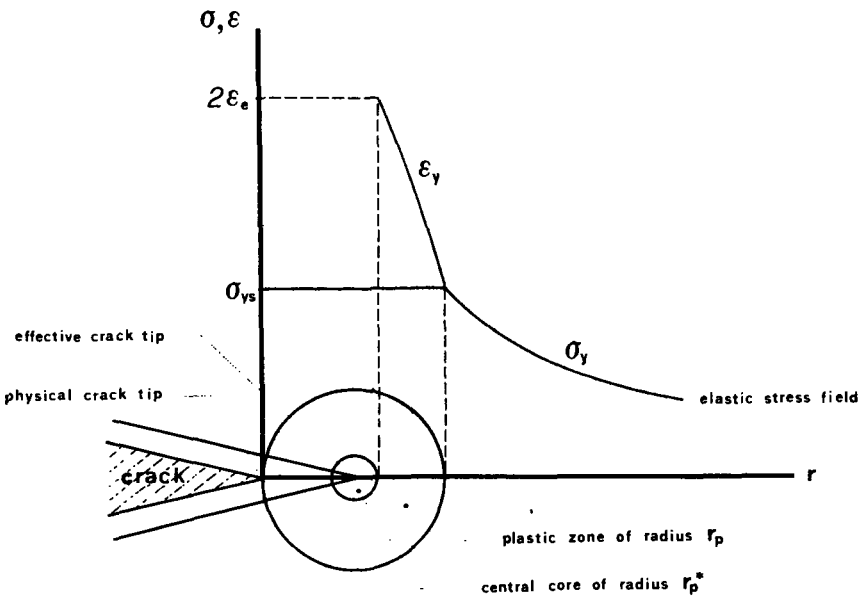

Figure 3. The plastic zone, of radius r_p, makes the crack behave as if it were longer. The effective crack tip is located at the center of the plastic zone. A central core of radius $r_p^* = 1/4\ r_p$ exsists in which the strain exides twice the elastic strain ε_e .

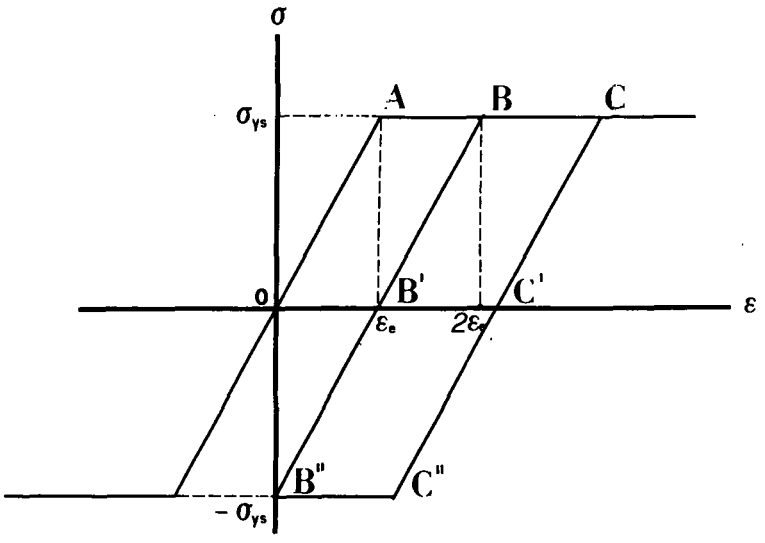

Figure 4. Elements deformed beyond $2\varepsilon_e$ after unloading undergo a reverse plastic flow remaining in a state of permanent compression. Point C, for instance, during the unloading goes to B" trhough CC'C" and the plastic flow C"B".

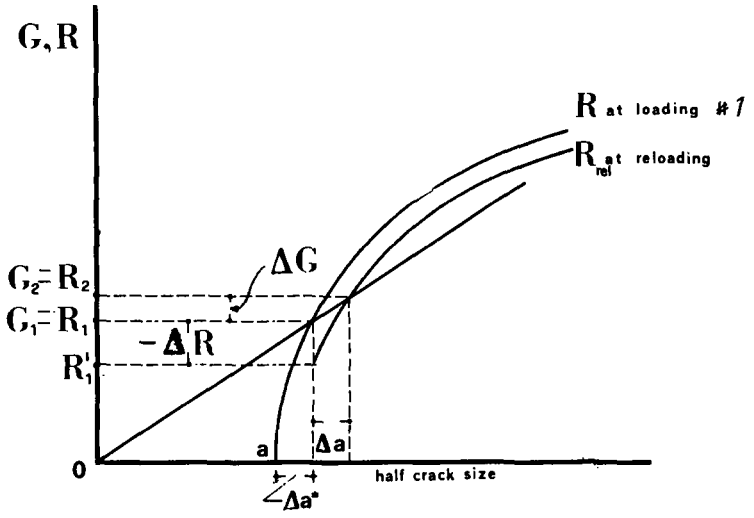

Figure 5. During the first loading the half crack size a increases of a quantity Δa^*. At reloading the R value which corresponds to the new crack $a + \Delta a^*$ is no longer R_1 but R'_1.

Figure 6. Residual compressive stresses at crack tip and tensile stresses beyond the plastic zone set up after unloading.

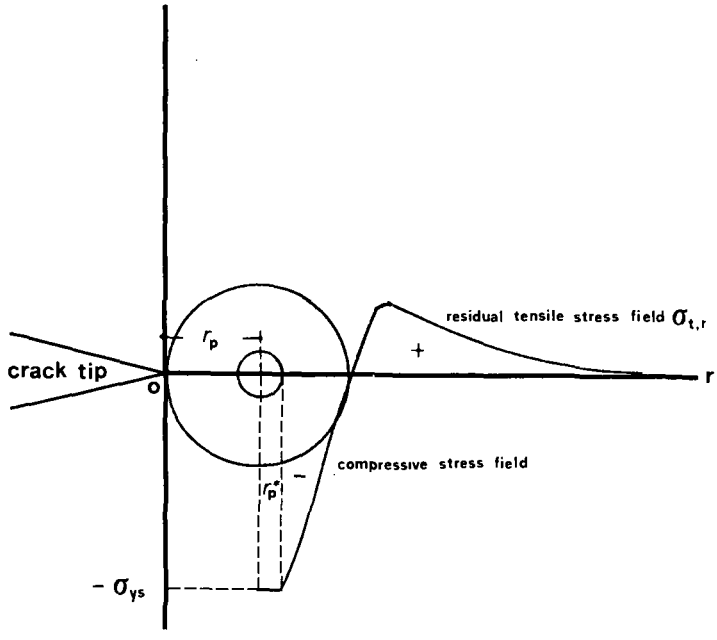

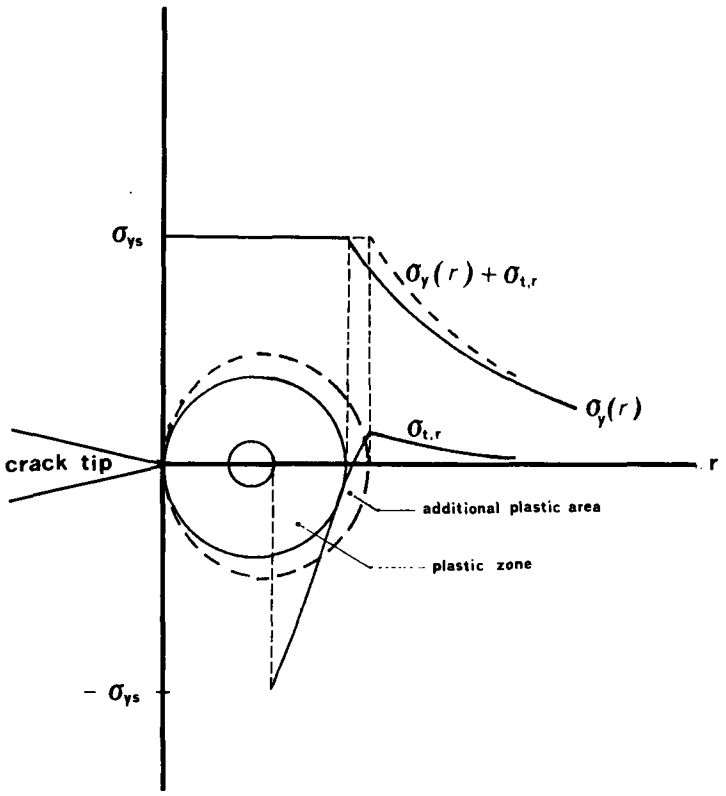

Figure 7. At reloading the residual tensile stress field $\sigma_{t,r}$ combining with the crack tip stress field σ_y provides additional plastic deformation beyond the plastic zone built up in the previous cycle.

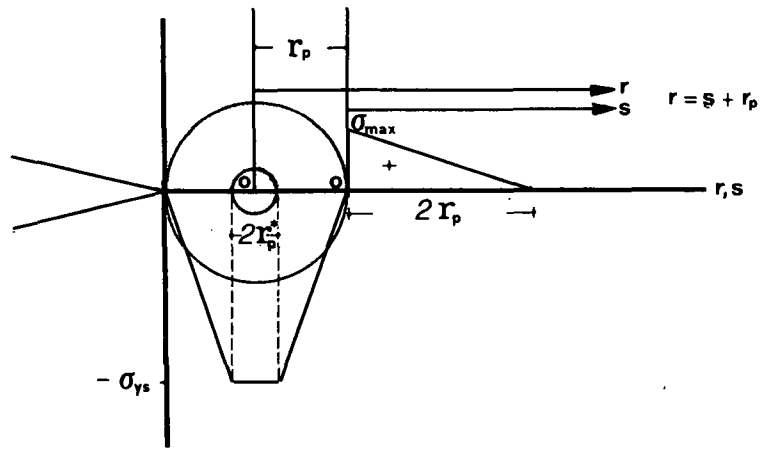

Figure 8. Schematic of residual stress fields used in the calculations.

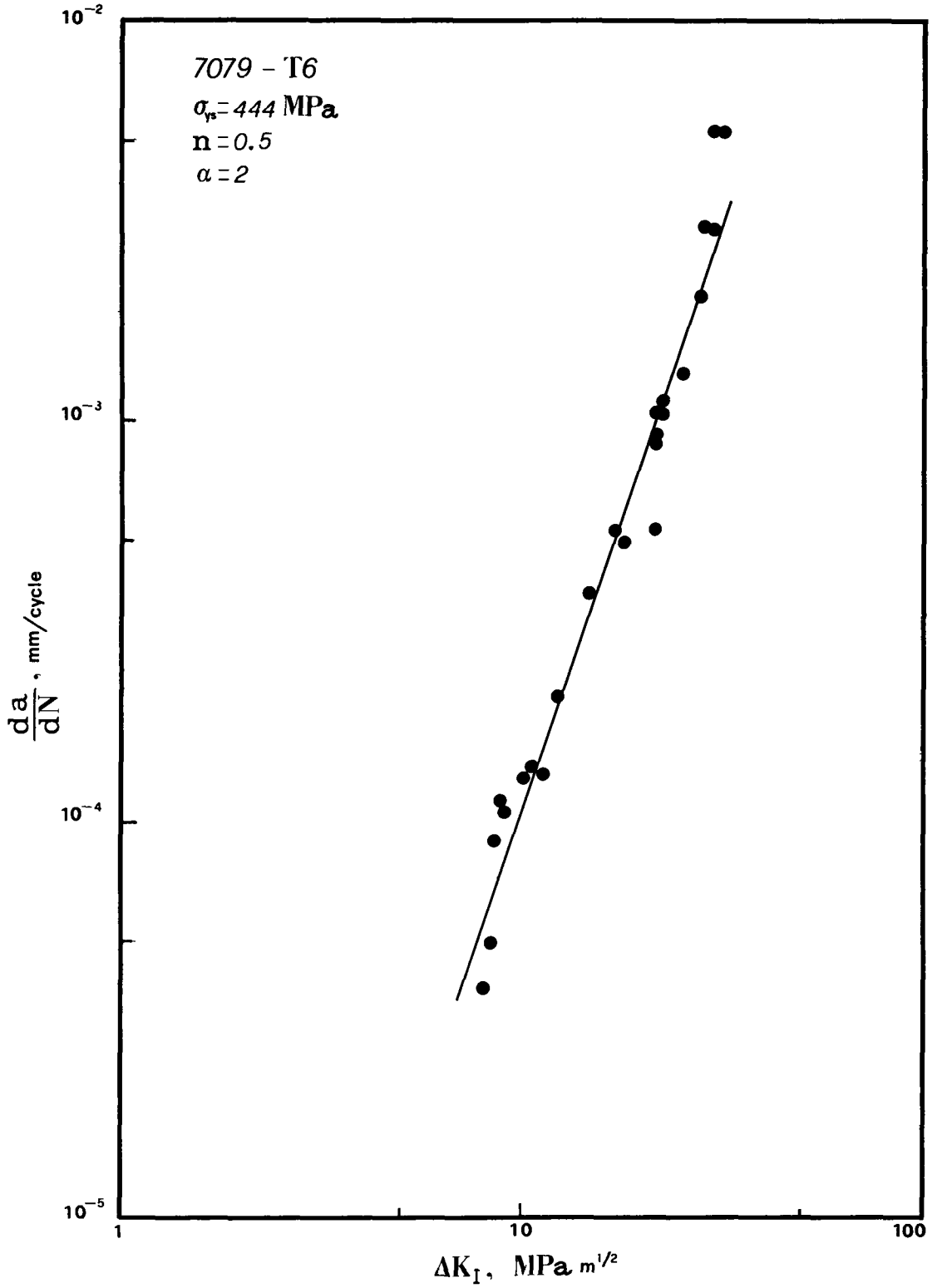

Figure 9. Comparison of fatigue crack growth rate given by eq.(45) and experimental results for 7079 - T6 Aluminum alloy.

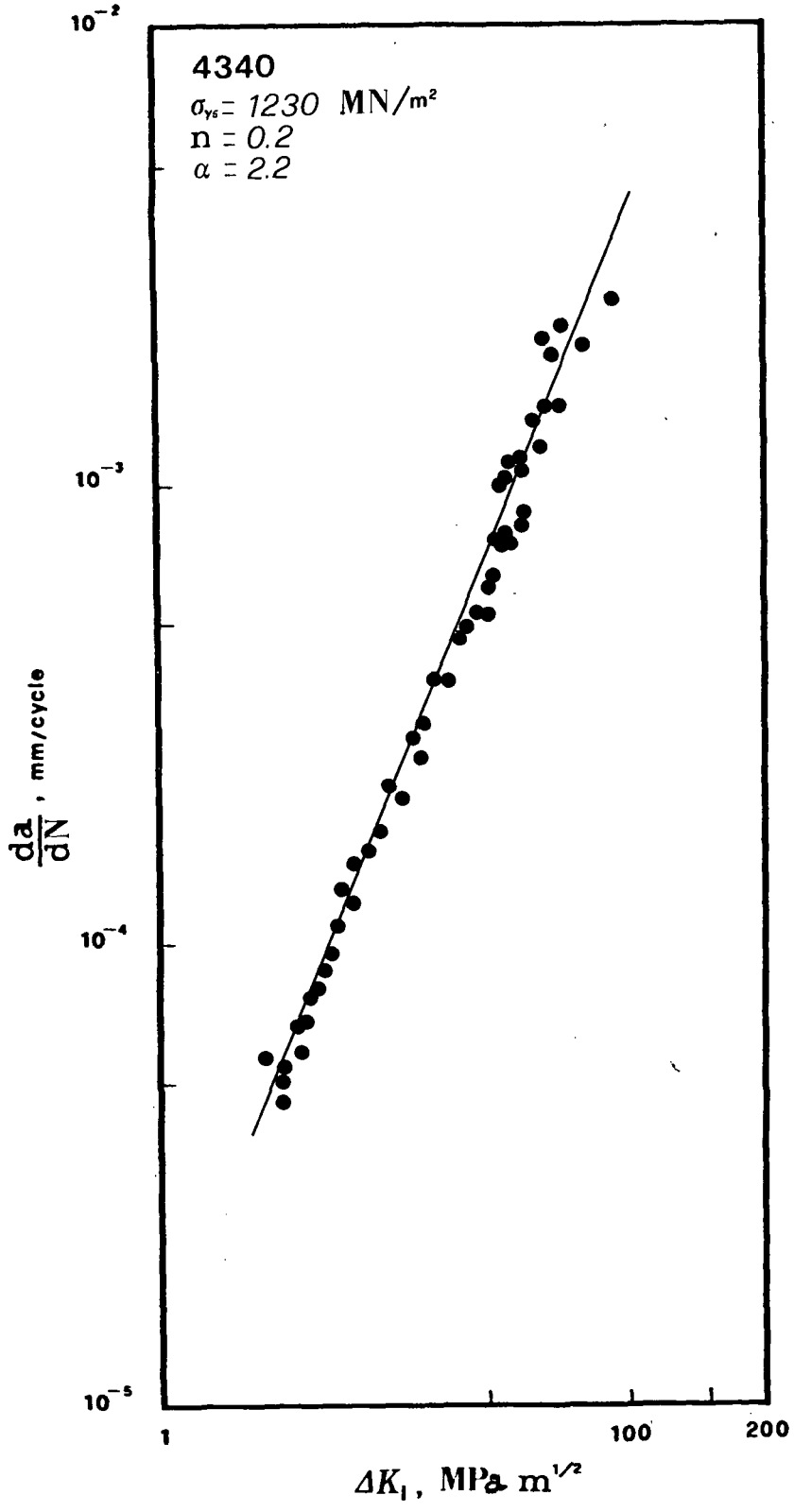

Figure 10. Comparison of fatigue crack growth rate given by eq. (45) and experimental results for 4340 Steel.

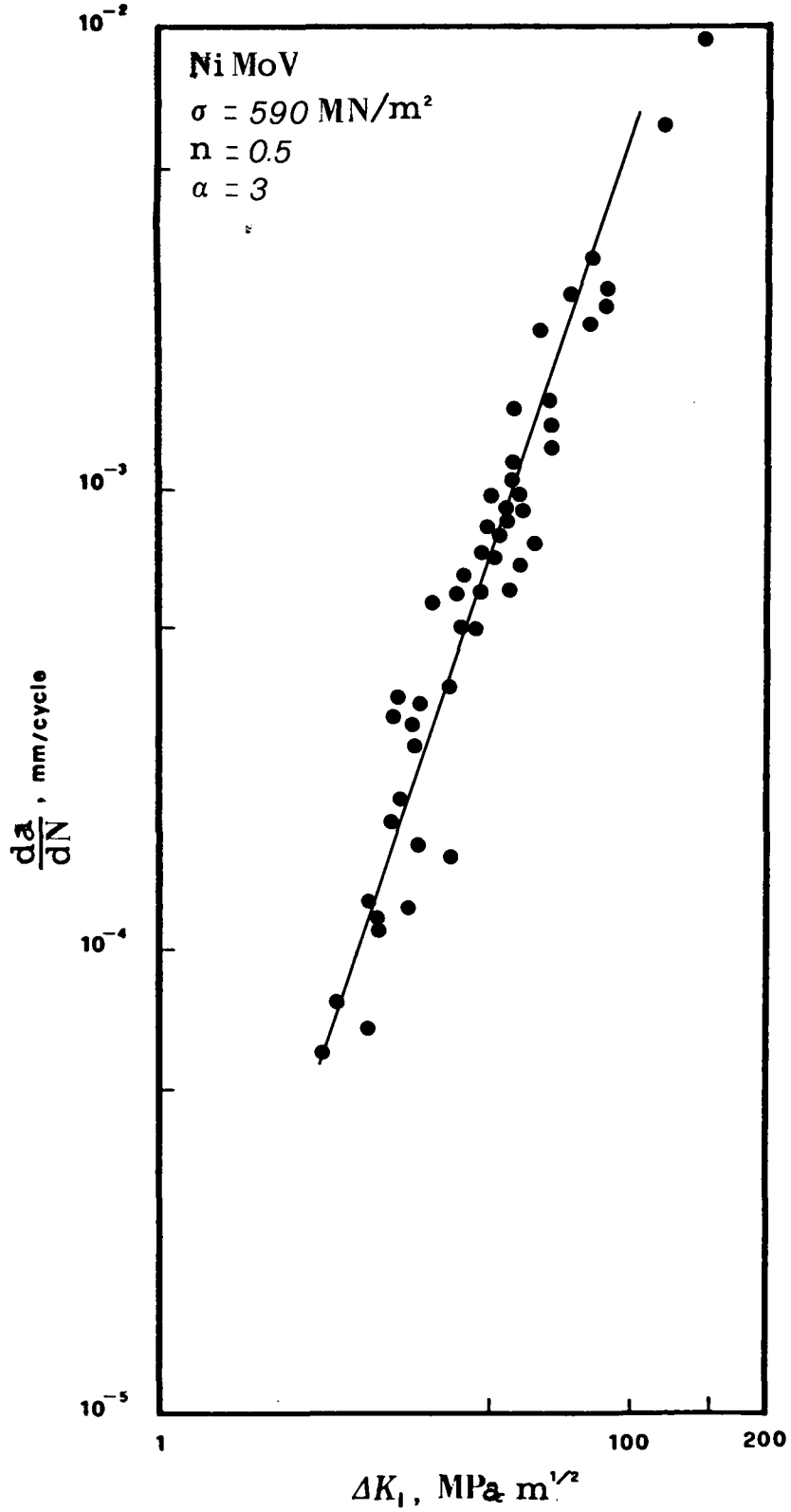

Figure 11. Comparison of fatigue crack growth rate given by eq. (45) and experimental results for NiMoV Steel.